Developing an Effective Die Cooling Technique For Casting Solidification

Velluvakkandi, Navaneeth

A thesis submitted in fulfilment of the Master of Engineering

School of Engineering
Auckland University of Technology
July 2009

Contents

1 Introduction 1

1.1 Expendable mold casting 2

1.1.1 Sand Casting 2

1.1.2 Plaster casting 2

1.1.3 Investments casting 3

1.1.4 Shell molding 3

1.2 Non-expendable mold casting 4

1.2.1 Permanent mold casting 4

1.2.2 Die casting 4

1.2.3 Centrifugal casting 6

1.2.4 Continuous casting 6

1.2.5 Semi-solid metal casting 6

1.3 Shrinkage during solidification 7

1.4 Solidification control 8

1.5 Example of solidification in a product 10

1.6 Affect of air gap on temperature distribution at a typical TT junction. 13

1.7 Metal-Mold Interface 14

1.8 Research objectives 15

1.8.1 Air gap signaling and temperature data acquisition 15

1.8.2 Computer simulation to calculate heat transfer coefficient 15

1.8.3 Micro structure and SDAS measurements 15

2 Literature Review 16

2.1 Air Gap measurements 16

2.2 Interfacial heat transfer coefficients 23

2.2.1 Inverse heat conduction problem concept 23

2.2.2 Difficulties in solving inverse heat transfer problem 25
2.2.3 Theoretical development 27
2.2.4 Formulation of interface element 28
2.2.5 Interface element 29
2.2.6 Factors affecting interfacial heat transfer coefficients 30
2.3 Solidification: Theoretical Background 31
2.3.1 Effect of cooling rate and melt temperature on solidification of aluminium alloy 32
2.3.2 Relationship between microstructure and thermal parameters 33
2.4 Aluminium silicon eutectic modification 35
2.5 Effect of structure on properties 36
2.6 Computer modelling and simulation 37
2.6.1 Modelling of casting processes 37
2.6.2 Modelling of heat transfer mechanism across the casting-mold interface 38
2.6.3 Reverse Engineering 38
2.6.4 Determination of heat transfer coefficient at water cooling 39
2.7 Summary 39
3 Experimental setup 42
3.1 Mold 42
3.2 Chill 42
3.3 Furnace 43
3.4 Methodology 44
3.5 Sources of errors and experimental uncertainty 45
3.6 Air gap indicator 47
3.7 Experiment procedure 51
3.7.1 Melt preparation 51
3.7.2 Thermocouple installation 51

3.7.3 Mold and chill preheating 51
3.7.4 Cooling tank and pump 52
3.7.5 Pouring 52
3.7.6 Chill displacement 52
3.8 Temperature data and air gap signature 54
3.8.1 Temperature data acquisition 54
3.8.2 Manufacturer's uncertainty and calibration 54
3.8.3 Data acquisition uncertainties 55
3.8.4 Installation error 55
3.8.5 Systematic errors for dynamic measurements 55
3.8.6 Distortion at localized temperature field 56
4 Experimental results 57
4.1 Chilling effect on temperature profile 57
4.2 Scenario A: fixed chill without cooling 57
4.3 Scenario B: fixed chill with cooling) 62
4.3.1 Partial Contact 62
4.4 Scenarios C and D - movable chill with cooling 66
4.4.1 Scenario C - movable chills with cooling (displacement on demand) 66
4.4.2 Scenario D - movable chills with cooling (displacement before eutectic) 70
4.5 Summary 74
5 Computer Simulation 76
5.1 Model setup 76
5.2 Water cooling and film coefficients 78
5.3 Solidification simulation 80
5.4 Model adjustment by ProCAST™ inverse optimization 82
5.5 Simulation results and discussion 84

5.5.1 Effect of fixed chill without cooling on heat transfer (Scenario A) 85

5.5.2 Effect of fixed chill with cooling on heat transfer (Scenario B) 87

5.5.3 Effect of movable chill (Displacement on demand) on heat transfer (Scenario C) 89

5.5.4 Effect of movable chill (Displacement before eutectic) on heat transfer (Scenario D) 89

5.6 Summary 96

6 Micro-structural analyses 98

6.1 Overview 98

6.2 Sample preparation 98

6.3 Uncertainties involved in dendrite measurement 101

6.3.1 Cut-off error 101

6.3.2 Image capturing error 102

6.4 Effect of chill conditions on SDAS 103

6.5 Micrographs 105

7 Discussion and analysis 117

7.1 Chill contact duration and casting temperature 117

7.2 Temperature during initial stages of solidification 119

7.3 Effective cooling calculation 121

7.4 Average SDAS at different locations 122

7.5 Porosity 124

7.6 Summary 125

8 Summary of present research and findings 127

8.1 Chapter 1 127

8.2 Chapter 2 127

8.3 Chapter 3 127

8.4 Chapter 4 127

8.5 Chapter 5 127

8.6 Chapter 6 128
9 Conclusion 130
10 Future development 132
Appendices 133
Appendix A Composition of alloy used 133
Appendix B Composition of the mold 133
Appendix C Physical Properties of the mold 134
Appendix D Drawings of mold chill assembly 135
Appendix E Air gap signals 137
Appendix F SDAS vs. Interface distance for different trials 143
References 151

Table of Figures

Figure 1: A typical gravity casting pouring process for steel at 1500 ˚C 1

Figure 2: Sand mold casting..... 2

Figure 3: Investment casting process [2] 3

Figure 4: Low pressure die casting [3]..... 5

Figure 5: High pressure die casting [3]..... 5

Figure 6: Chill placed in casting 7

Figure 7: Mold without solidification control..... 8

Figure 8: Mold with solidification control..... 9

Figure 9: Automotive wheel showing sections and ideal solidification sequence..... 10

Figure 10: Thermal control possibilities for a typical wheel die 11

Figure 11: A cooling chill positioned at a typical thick/thin (TT) junction known as a rim-spoke junction in the case of a wheel..... 11

Figure 12: Hot spot at a typical thick thin (TT) junction 12

Figure 13: FEM simulation of rim spoke junction without air gap using Quick Field... 13

Figure 14: FEM simulation of rim spoke junction with an exaggerated air gap using Quick Field..... 13

Figure 15: Heat flow at metal mold interface [8, 9]..... 14

Figure 16: (a) Upward solidification, (b): Downward solidification, (c): Horizontal solidification. Reproduced from [7]..... 18

Figure 17: Casting-mold surface roughness and temperature distributions (reproduced from [24])..... 20

Figure 18: Schematic of discretisation of the casting–mold interface. T_{me} = melt temperature, T_{mo} = mold temperature 22

Figure 19: Heat transfer through a slab to illustrate the inverse problem [28]. 24

Figure 20: 2D interface element [43]..... 29

Figure 21: Phase diagram for A356 alloy [44] 31

Figure 22: Micro structure of Al-1.8%Cu solidified at cooling rate 0.4 K/s (D=grain size and d=dendrite arm spacing) [46]. 33

Figure 23: Micro structure of Al-1.8%Cu solidified at cooling rate 13 K/s [46]. 33

Figure 24: Initial model predicted by Fleming [47]. 34

Figure 25: Later model predicted by Fleming [47]. 34

Figure 26: Effect of grain modifiers on temperature profile for a given Aluminium silicon alloy [49]. 35

Figure 27: Reverse engineering technique 38

Figure 28: Heat transfer during quenching [58, 60] 39

Figure 29: Dense fused silica mold 42

Figure 30: Copper chill 43

Figure 31; Chill-housing assembly. 43

Figure 32: Crucible in resistance furnace at 710˚C 44

Figure 33: Air gap indicator circuit 47

Figure 34: Strip chart display 48

Figure 35: Casting after 600 secs 49

Figure 36: Casting-mold interface with fixed chill (image taken after 600 sec) 49

Figure 37: Casting mold interface with movable chill (image taken after600 sec) 49

Figure 38: Mold setup with cooling pipes and thermocouples 50

Figure 39: Location of thermocouple within casting and chill. 51

Figure 40: Temperature (˚K) field distortion caused by a thermocouple mounted inside a permanent steel mold [89]. 56

Figure 41: Effect of chill on temperature profile 57

Figure 42: (1) indicates contact and (-1) indicates air gap for Trial A1 59

Figure 43: (1) indicates contact and (-1) indicates air gap for Trial A2 60

Figure 44: (1) indicates contact and (-1) indicates air gap for Trial A3 61

Figure 45: (1) indicates contact and (-1) indicates air gap for Trial B1 63

Figure 46: (1) indicates contact and (-1) indicates air gap for Trial B2 64

Figure 47: (1) indicates contact and (-1) indicates air gap for Trial B3 65

Figure 48: (1) indicates contact and (-1) indicates air gap for Trial C1 67

Figure 49: (1) indicates contact and (-1) indicates air gap for Trial C2 68

Figure 50: (1) indicates contact and (-1) indicates air gap for Trial C3 69

Figure 51: (1) indicates contact and (-1) indicates air gap for Trial D1 71

Figure 52: (1) indicates contact and (-1) indicates air gap for Trial D2 72

Figure 53: (1) indicates contact and (-1) indicates air gap for Trial D3 73

Figure 54: Model setup 76

Figure 55: Model mesh setup revealing fine density at the interface and coarser density at the outskirts. 77

Figure 56: Quenching effect at the copper chill 78

Figure 57: Film coefficient for water cooling 79

Figure 58: Simulation was performed for 600 seconds 81

Figure 59: Flow chart showing simulation methodology 82

Figure 60: History of the objective function used to determine a set of heat transfer coefficients. 83

Figure 61: Variation of IHTCs to fit the experimental temperature profile 84

Figure 62: Variation of cooling curves with changes in IHTCs 84

Figure 63: ProCast calculated heat transfer coefficients for trial A_Average 86

Figure 64: Procast calculated heat transfer coefficient for trial B_Average 88

Figure 65: Procast calculated heat transfer coefficient for Trial C1 90

Figure 66: Procast calculated heat transfer coefficient for Trial C2 91

Figure 67: Procast calculated heat transfer coefficient for Trial C3 92

Figure 68: Procast calculated heat transfer coefficient for Trial D1 93

Figure 69: Procast calculated heat transfer coefficient for Trial D2 94

Figure 70: Procast calculated heat transfer coefficient for Trial D3 95

Figure 71: Combined HTC graph for trial A, B, C and D 97

Figure 72: Cross section of the casting sample 98

Figure 73: Image-Pro™ software used to measure secondary dendrite arm spacing (SDAS). 100

Figure 74: dendrite calculation 101

Figure 75: Casting samples cut into small sizes for microscopic analysis 102

Figure 76: x=distance lost between two consecutive images. 103

Figure 77: SDAS plotted against distance from interface for different chill conditions. 104

Figure 78: Dendrites at 2.5mm from the interface 105

Figure 79: Dendrites at 7.5 mm and 15 mm 105

Figure 80: Dendrites at 37.5 mm and 52.5 mm 105

Figure 81: Dendrites at 2.5mm from the interface 106

Figure 82: Dendrites at 7.5 mm and 15 mm 106

Figure 83: Dendrites at 37.5 mm and 52.5 mm 106

Figure 84: Dendrites at 2.5mm from the interface 107

Figure 85: Dendrites at 7.5 mm and 15 mm 107

Figure 86: Dendrites at 37.5 mm and 52.5 mm 107

Figure 87: Dendrites at 2.5mm from the interface 108

Figure 88: Dendrites at 7.5 mm and 15 mm 108

Figure 89: Dendrites at 37.5 mm and 52.5 mm 108

Figure 90: Dendrites at 2.5mm from the interface 109

Figure 91: Dendrites at 7.5 mm and 15 mm 109

Figure 92: Dendrites at 37.5 mm and 52.5 mm 109

Figure 93: Dendrites at 2.5mm from the interface 110

Figure 94: Dendrites at 7.5 mm and 15 mm 110

Figure 95: Dendrites at 37.5 mm and 52.5 mm 110

Figure 96: Dendrites at 2.5mm from the interface 111

Figure 97: Dendrites at 7.5 mm and 15 mm 111

Figure 98: Dendrites at 37.5 mm and 52.5 mm 111

Figure 99: Dendrites at 2.5mm from the interface 112
Figure 100: Dendrites at 7.5 mm and 15 mm 112
Figure 101: Dendrites at 37.5 mm and 52.5 mm 112
Figure 102: Dendrites at 2.5mm from the interface 113
Figure 103: Dendrites at 7.5 mm and 15 mm 113
Figure 104: Dendrites at 37.5 mm and 52.5 mm 113
Figure 105: Dendrites at 2.5mm from the interface 114
Figure 106: Dendrites at 7.5 mm and 15 mm 114
Figure 107: Dendrites at 37.5 mm and 52.5 mm 114
Figure 108: Dendrites at 2.5mm from the interface 115
Figure 109: Dendrites at 7.5 mm and 15 mm 115
Figure 110: Dendrites at 37.5 mm and 52.5 mm 115
Figure 111: Dendrites at 2.5mm from the interface 116
Figure 112: Dendrites at 7.5 mm and 15 mm 116
Figure 113: Dendrites at 37.5 mm and 52.5 mm 116
Figure 114: casting-chill contact percentage vs. chill conditions 117
Figure 115: Casting temperature after 575 sec 118
Figure 116: Temperature of casting after 50 sec of pouring 119
Figure 117: Temperature of casting after 300 sec of pouring 120
Figure 118: Temperature of casting after 575 sec of pouring 120
Figure 119: Average SDAS at 2.5 mm Vs. Trials 122
Figure 120: Average SDAS at 7.5 mm Vs. Trials 122
Figure 121: Average SDAS at 15 mm Vs. Trials 123
Figure 122: Average SDAS at 37.5 mm Vs. Trials 123
Figure 123: Average SDAS at 52.5 mm Vs. Trials 124
Figure 124: Average pores vs. Exp. Trials 125
Figure 125: HTC vs time showing higher HTC for scenario C and D 128

Figure 126: SDAS at 52.5 mm showing 26% reduction in dendrite sizes for scenario C and 30 % reduction for scenario D compared to scenario B. 129

Figure 127: Average No. of porosities showing 27 % reduction in No. of pores in scenario C and 53 % reduction in scenario D compared to scenario B 129

Figure 128: Properties of dense fused silica mold (reproduced from Pyrotek manual) 134

Figure 129: cooling chill assembly 135

Figure 130: Chill mold assembly 136

Figure 131: Air gap signal for Trial A1 137

Figure 132: Air gap signal for Trial A2 137

Figure 133: Air gap signal for Trial A3 138

Figure 134: Air gap signal for Trial B1 138

Figure 135: Air gap signal for Trial B2 139

Figure 136: Air gap signal for Trial B3 139

Figure 137: Air gap signal for Trial C1 140

Figure 138: Air gap signal for Trial C2 140

Figure 139: Air gap signal for Trial C3 141

Figure 140: Air gap signal for Trial D1 141

Figure 141: Air gap signal for Trial D2 142

Figure 142: Air gap signal for Trial D3 142

Figure 143: Average SDAS vs. Interface Distance for Trial A1 143

Figure 144: Average SDAS vs. Interface Distance for Trial A2 143

Figure 145: Average SDAS vs. Interface Distance for Trial A3 144

Figure 146: Average SDAS vs. Interface Distance for Trial B1 145

Figure 147: Average SDAS vs. Interface Distance for Trial B2 145

Figure 148: Average SDAS vs. Interface Distance for Trial B3 146

Figure 149: Average SDAS vs. Interface Distance for Trial C1 147

Figure 150: Average SDAS vs. Interface Distance for Trial C2 147

Figure 151: Average SDAS vs. Interface Distance for Trial C3 148

Figure 152: Average SDAS vs. Interface Distance for Trial D1 149
Figure 153: Average SDAS vs. Interface Distance for Trial D2 149
Figure 154: Average SDAS vs. Interface Distance for Trial D3 150

ACKNOWLEDGEMENT

Now finally it's time to express my gratitude to those individuals, without whom this project wouldn't have been possible.

Firstly, I would like to express my deepest sense of gratitude to my supervisor Prof. Darius Singh for his patient guidance, encouragement and excellent advice throughout the project.

Next, I would like to thank Rafael Lee for his effort and commitment towards this project.

I would like to thank all fellow researchers at CAMTEC for their guidance and support during the course of this project.

I would also like to thank, various staff of AUT University for their support and valuable inputs to my work.

I would also like to thank Keith and Tevita for their contributions to this project.

Finally, I would like to thank my beloved parents for their endless support during the difficult times of the project.

ABSTRACT

In permanent mold casting, die design for cast aluminium alloy and magnesium alloy products includes a number of high conductivity material cooling blocks (also called channels or cooling circuits) that are aimed to extract heat away from molten metal through direct conduction heat transfer and freeze the casting as quickly as possible in a directional manner. One of the biggest problems during this solidification process occurs when the molten metal naturally shrinks away from the mould as it solidifies. This makes it increasingly difficult to efficiently and effectively cool targeted areas in the casting through conduction, since the direct contact between the solidifying casting and the cooling block is significantly reduced or even lost.

A typical cooling block (termed in this thesis as a "chill") is a cooling circuit that is embedded in a permanent mold (or die) and positioned to enable high heat transfer (effective cooling) to a targeted large section in the casting. If a large volume section in a casting does not cool efficiently and in the correct sequence in the overall product (i.e. solidification first in the furthest part from the sprue inlet followed by successive and ordered solidification towards the sprue inlet, until finally the sprue inlet itself), then it will create a "hot spot" which will create macro-shrinkage in the casting. This can create millions of dollars of waste in terms of casting rejects, lost productivity, and reworks for a given manufacturing company.

When the molten metal solidifies, it shrinks by about 6.6 % for aluminium alloys and 4.0 % for magnesium alloys. This creates an air gap at the casting and mold interface. This air gap causes inefficient, random and isolated pockets of heat transfer from the casting to a contacting chill, which in turn causes a significant variation in the temperature distribution in the casting and die during solidification. A die operating in an incorrect and unstable temperature band will very likely produce adverse secondary effects in the final product such as macro shrinkage, micro shrinkage, hot tearing, gas porosity, or even misruns. This aim of this study is to theoretically understand and experimentally develop a cooling technique that can offset or close up the growing air gap and maintain high heat transfer between the casting and contacting chill, by ensuring that the chill is pushed closer into the casting at specific times during the solidification (and shrinking) process.

A movable copper chill was designed and built to push forward into an insulated mold. The experiments were carried out using commercially available A356 aluminium alloy. The chill was pushed into the casting as it solidified in the mold. Studies were carried out to understand the effect of a movable chill with different cooling conditions compared to a fixed chill. Numerical simulations were conducted using developed boundary conditions in a commercial casting solidification package (ProCAST^{TM}). The boundary condition used to emulate the air gap is a temporally distributed interfacial heat transfer coefficient function between the casting and chill and this is manually calculated using inverse modelling in an in-house developed optimisation package (OPTCAST^{TM}) to compare and validate with experimental data. The resulting sensitivities of the casting due to different chill conditions (i.e. fixed vs. moving) are described through physical phenomenon, metallographic analysis and computational modelling.

Results show that the effective cooling can be increased by 39.2 % by using movable chill with cooling compared to fixed chill with cooling. The percentage of complete contact between the casting and chill has been increased from 10 % in case of fixed chill with cooling to 76% in case of movable chill with cooling. Apart from effectiveness of cooling, the quality of casting produced with new cooling technique has significantly improved. The secondary dendrite arm spacing (SDAS) of the casting produced under the movable chill have be reduced by 26 % compared to fixed chill.

1 Introduction

In the casting manufacturing process, molten metal is poured using gravity or injected vertically using low pressure, or injected horizontally (or vertically) using high pressure and vacuum into a non-expendable or expendable mold or die (as appropriate) and allowed to solidify. This die contains a hollow cavity of the desired product shape including sufficient distortion, machining and finishing tolerances built into the cavity design. Even though there have been significant developments in all manufacturing technologies over the recent years, casting is still one of the most widely adopted manufacturing techniques used to produce complicated shapes which could not be obtained by any other process.

Casting can be broadly divided into two main categories: expendable and non-expendable mold casting. It can also be classified according to the mold material such as sand casting, ceramic casting or metal mold casting and depending on the pouring methods as gravity casting, low pressure die casting and high pressure die casting.

Figure 1: A typical gravity casting pouring process for steel at 1500 ˚C

1.1 Expendable mold casting

Expendable mold casting is where the mold is temporary and cannot be used for producing more than one casting. This includes sand casting, plaster casting, investment casting, and shell molding.

1.1.1 Sand Casting

Sand casting is the most common method of casting which is employed when there is a relatively low number of components required to be produced

Sand casting allows for smaller batches to be made compared to permanent mold casting and at a very reasonable cost. In this type of casting the mold is made out of sand mixed with silica and other additives (binders). However sand can be recycled again in most of the cases with few additional operations.

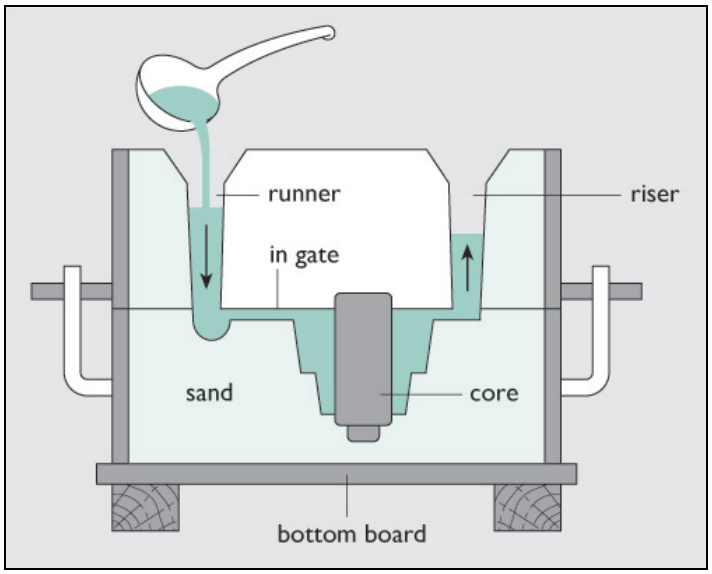

Figure 2: Sand mold casting

1.1.2 Plaster casting

Plaster casting is similar to sand casting except plaster is replaced for sand. Plaster usually consists of gypsum, strengtheners and water. Plaster casting can be an economical replacement for other casting techniques due to the low cost of plaster and mold production. But plaster casting has its own disadvantages since mold quality is dependant on several factors including plaster molding composition, mold pouring procedures, and plaster curing techniques etc. Another problem with plaster casting is that once the mold is used or broken, the plaster cannot be recycled. Plaster casting can be used for non-ferrous metals such as aluminum, copper, zinc and their alloys.

1.1.3 Investments casting

Investments casting is also known as lost wax process in which wax patterns are used to create mold in a refractory material usually ceramic. It is one of the most practiced casting techniques when small sized casting needs to be produced in large quantities. However this process can be used to produce most complicated casting with ease. Compared to die casting, investment casting can be more expensive but it can produce highly intricate components with little machining work to be done [1].

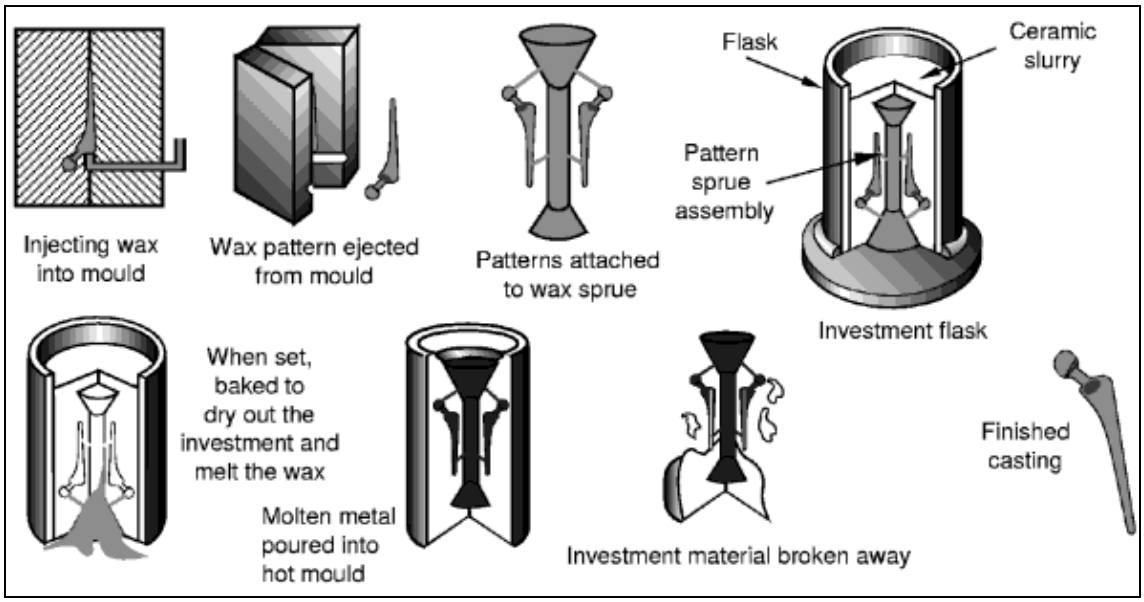

Figure 3: Investment casting process [2]

1.1.4 Shell molding

Shell molding is similar to sand casting; the only difference is that a relatively small amount of resin is used to keep the sand grains together. Shell molding also uses sand with a much smaller grain than green-sand. Usually shell molding is done in a machine called shell molding machine. The molds are made in two pieces that are clamped together for the molding process. Shell molding is used for small parts that require high precision. It is also used to make high-precision molding cores. By this technique most complex shaped castings can be produced at a relatively low cost.

1.2 Non-expendable mold casting

Non expendable mold casting is where a permanent (steel or other similar material) mold is used for casting. This technique includes casting non-ferrous materials like aluminum, magnesium, zinc, or copper based alloys.

Some of the different methods used are permanent mold casting, centrifugal casting continuous casting and low/high pressure die casting.

1.2.1 Permanent mold casting

In permanent mold casting, high production rates (i.e. number of casting shots per hour) can be achieved due to the higher conductivity of the mold material (over sand or plaster) and the instant preparedness of the mold from one to the next. The most common material is steel which is coated with a refractory wash of acetylene, soot, sodium silicate or talc based material before casting. This is to allow a) easy removal of the casting once solidified; b) a particular unnatural solidification direction to occur in the part; c) no chemical reactions to occur between molten alloy and the steel; and d) a longer tool life. Permanent molds have a limited life of between 50,000-150,000 casting shots before wearing out due to repeated fluid flow from incoming molten metal or internal thermal fatigue cracking or both. Worn out molds are replaced or repaired. Castings produced using permanent mold casting show relatively high strength compared to the castings produced by sand casting, due to the higher heat transfer rates and faster solidification times. Typically permanent mold casting is used for manufacturing aluminum, magnesium and copper alloy based products.

1.2.2 Die casting

The die casting process forces molten metal under high pressure (up to 100Mpa gauge pressure) into mold cavities. Most die castings are made from nonferrous metals, specifically zinc, copper, magnesium and aluminum based alloys, but ferrous metal die castings are possible. The die casting method is especially suited for applications where many small to medium sized parts are needed with good detail, a fine surface quality and dimensional accuracy and consistency.

Die casting can be classified as;

1.2.2.1 Low pressure die casting

Figure 4 shows schematic diagram of low pressure die casting. In this process the permanent mold is mounted on a fixed furnace. A tube extends from the mold cavity into the furnace. The molten metal is injected into the fixed permanent mold.

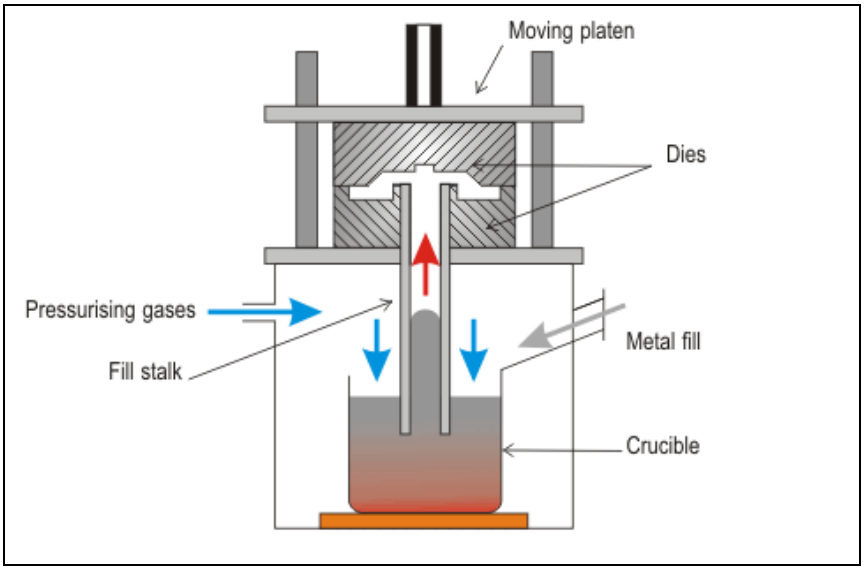

Figure 4: Low pressure die casting [3]

After solidification the part is removed and the mold is prepared for the next casting. This process is more suitable for axis symmetric parts such as an automobile wheel.

1.2.2.2 High pressure die casting

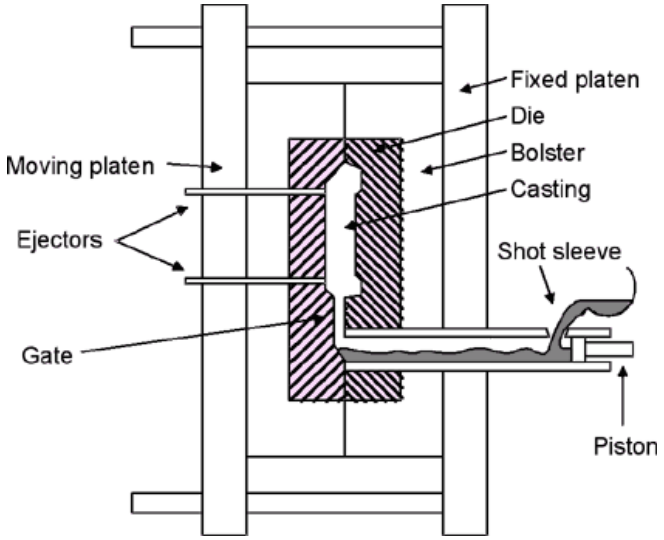

Figure 5: High pressure die casting [3]

In high pressure die casting the molten metal is injected into the mold cavity under pressure. This process is suitable for high production rate and volume production of

dimensionally accurate products with excellent surface finish. Most of the dies used for high pressure die casting are usually water or air cooled. Molten metal usually enters the mold under the action of a hydraulic ram. Slight lubrication is applied on the die after each casting is made.

1.2.3 Centrifugal casting

In centrifugal casting the mold is rotated at a certain speed and molten metal is injected into the die. Centrifugal casting produces its own force using a temporary sand mold held in a spinning chamber at up to 900 N (90 *g*). Semi- and true-centrifugal processing permit 30-50 pieces/hr-mold to be produced, with a practical limit for batch processing of approximately 9000 kg total mass with a typical per-item limit of 2.3-4.5 kg.

1.2.4 Continuous casting

Continuous casting is a refinement of the casting process for the continuous, high-volume production of metal sections with a constant cross-section. Molten metal is poured into an open-ended, water-cooled copper mold, which allows a 'skin' of solid metal to form over the still-liquid centre. The strand, as it is now called, is withdrawn from the mold and passed into a chamber of rollers and water sprays; the rollers support the thin skin of the strand while the sprays remove heat from the strand, gradually solidifying the strand from the outside in. After solidification in the mold the metal is cut to predetermined amount using oxyacetylene torch. Continuous casting is widely used for casting billets because of its low cost associated with production. This method is primarily used for producing steel, aluminum and copper ingots.

1.2.5 Semi-solid metal casting

Semi solid casting is a modification of normal die casting which reduces residual stresses and new oxides formed by turbulence that contribute to porosity in the casting. Rather than using liquid metal as the feed material, semi-solid casting uses a higher viscosity feed material that is partially solid and partially liquid. A modified die casting machine is used to inject the semi-solid slurry into re-usable hardened steel dies. The high viscosity of the semi-solid metal, along with the use of controlled die filling conditions, ensures that the semi-solid metal fills the die in a non-turbulent manner so that porosity can essentially be eliminated. The method is mainly used for casting aluminum and magnesium alloys. The combination of heat treatment controlled cooling

and minimum porosity provides excellent strength and ductility. Other advantages of semi solid casting include the ability to produce complex shaped parts net shape, pressure tightness, tight dimensional tolerances and the ability to cast thin walls [4].

1.3 Shrinkage during solidification

Castings shrink during solidification. Like all other materials, metals shrink volumetrically due to low density. The density of the metal increases gradually as it solidifies. Solidification shrinkage is the term used for contraction.

When the metal changes its phase from liquid to solid it contracts within itself leaving behind cavities in the casting. In order to counter this problem, a riser (excess metal at a head height) is connected to the casting, which continuously feeds the casting during solidification. These risers are cut away from the casting after ejection from the mold. One method is to keep the molten metal in liquid state as long as possible using exothermic sleeves [1].

Another method is to use chills which promote directional solidification by removing heat from specified locations within the casting. A chill is any material that removes heat from the molten metal faster than the mold material. Figure 6 shows a typical chill used in casting.

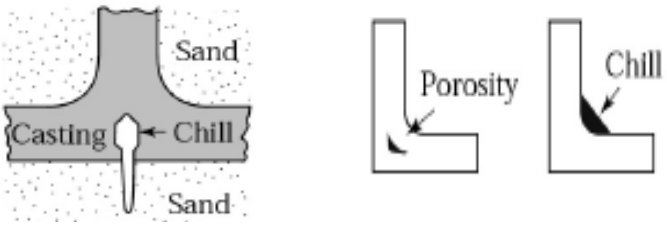

Figure 6: Chill placed in casting

1.4 Solidification control

The castings structure depends on its solidification history; hence it is very important to control the solidification itself. The solidification rate can be controlled either using exothermic materials, chills or by design of the mold. Consider an example of a casting as shown in Figure 8.

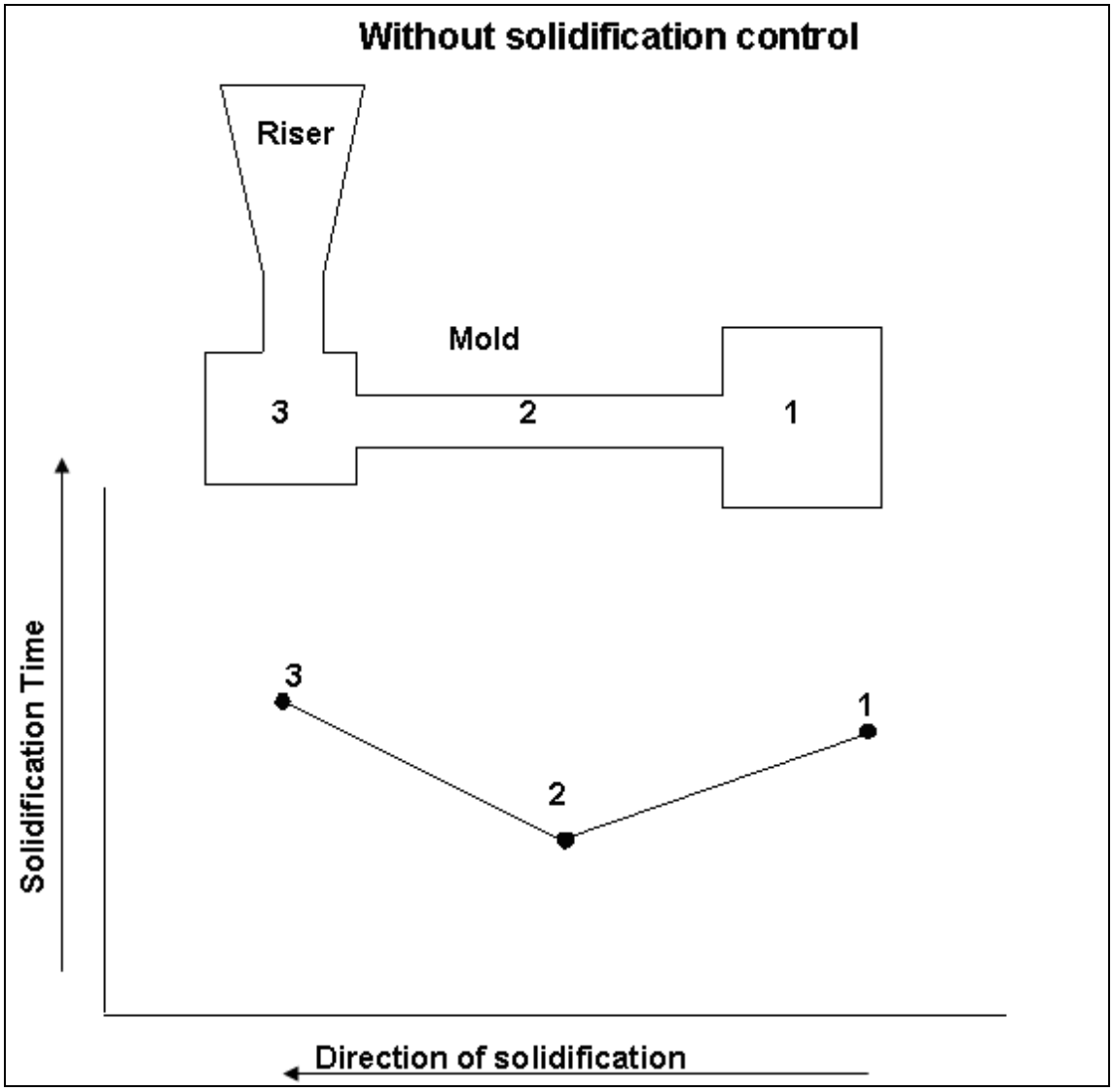

Figure 7: Mold without solidification control

The order of solidification is shown in corresponding graphs. In Figure 8 since section 2 is thinner than section 1 it solidifies quicker than section 1, followed by section 1 and section 3. This pattern of solidification results in a non-unidirectional solidification leading to non-homogenous structure within the casting which could effect significantly on the structural property of the casting. Also in some cases if section 2 solidifies first,

this can block the feed of metal required for filling section 1, resulting in macro-shrinkage.

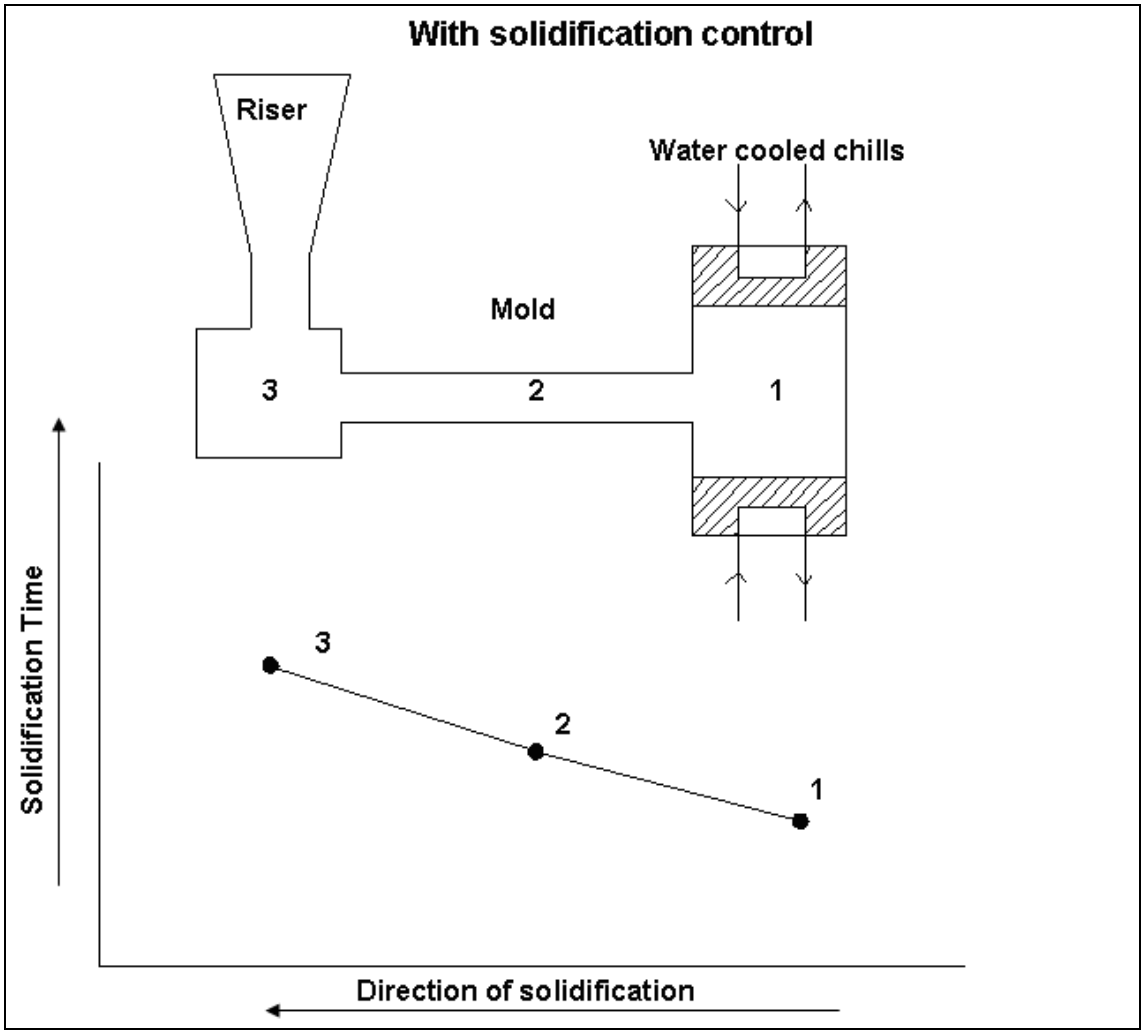

Figure 8: Mold with solidification control

To avoid this, the mold could be installed with cooling chills as shown in Figure 8. The chill extracts the heat from section 1 allowing it solidify first, followed by section 2 and finally the riser section 3. This promotes unidirectional solidification as shown in the corresponding Figure 8.

1.5 Example of solidification in a product

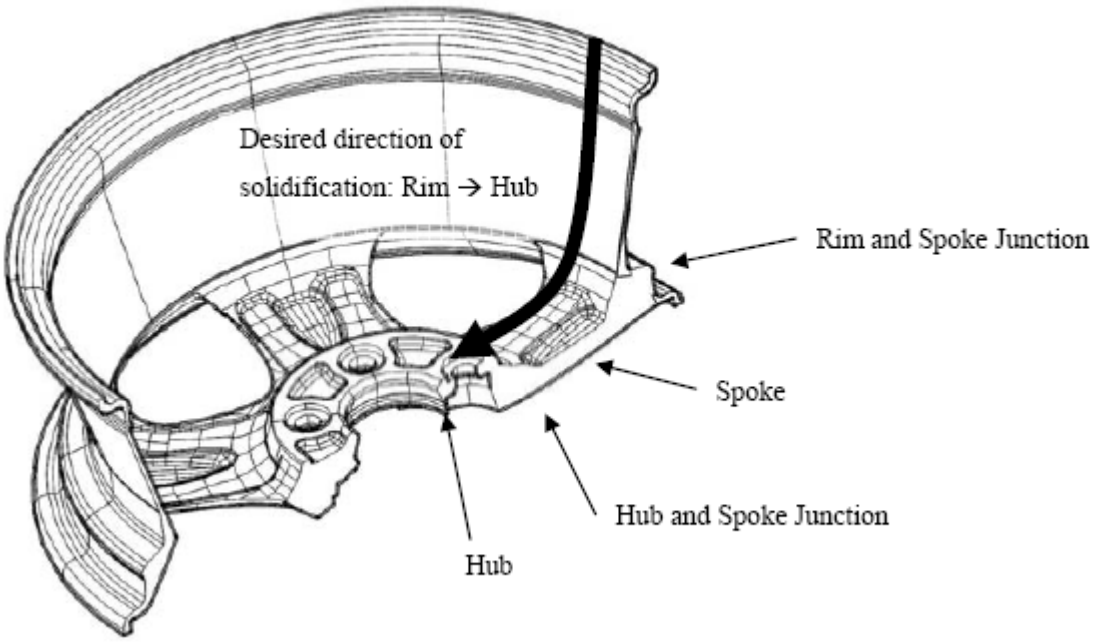

Figure 9: Automotive wheel showing sections and ideal solidification sequence.

This research is inspired by the thermal control of dies used for casting at Ford Motor Company in New Zealand [5, 6]. In some casting components, the design of the casting geometry may naturally induce directional solidification naturally. But in many cases such as an automotive wheel or an engine block, where the geometry is complex, naturally induced progressive solidification becomes impossible. In such cases, it is necessary to thermally control the solidification rate by forced external means, such as a cooling circuit or insulation.

Thermal control of dies can involve a series of cooling circuits targeted to remove heat from strategic locations within the die as shown in Figure 10. Usually air, water, oil or a combination of all is used to effectively control the die temperature. The sequence of solidification can be controlled by varying the cooling circuit activation sequence, cooling fluid flow rate and coolant temperature.

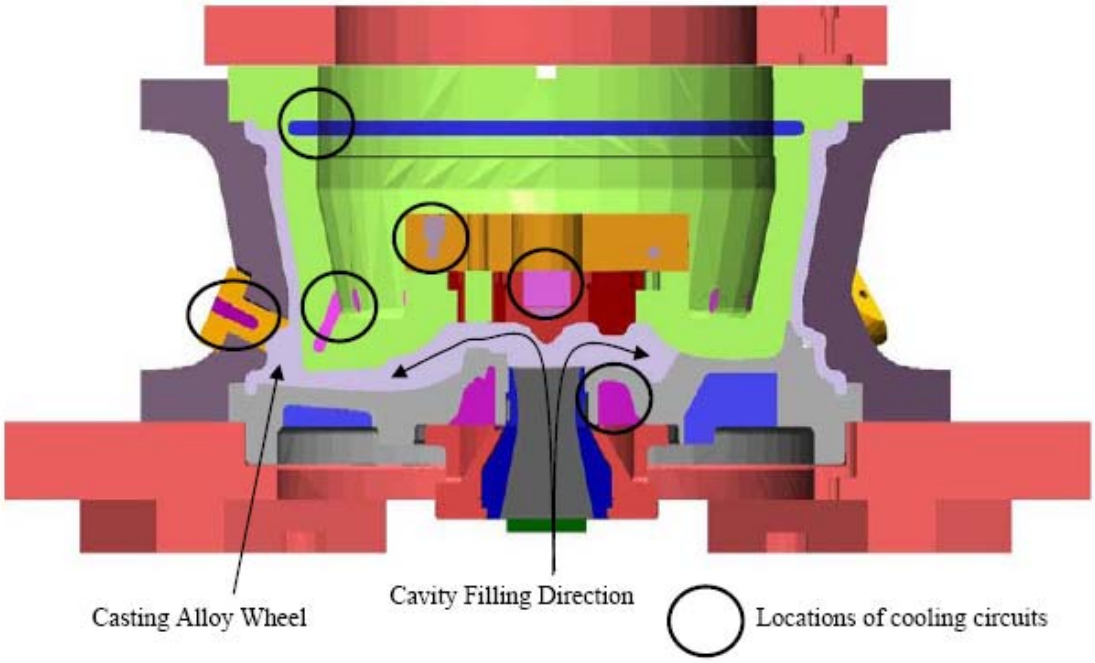

Figure 10: Thermal control possibilities for a typical wheel die

A TT junction (thick-thin junction) can be a rim spoke junction of a casting which is an area where large mass is surrounded by thin sections as shown in Figure 11. This result in non-uniform solidification leaving behind porosity at the rim spoke junction as in Figure 11. This problem can be solved by speeding up the solidification time in that junction by forced cooling. The side die cooling block (called "chill") is a cooling circuit that is targeted to cool typical thick thin junction such as rim- spoke junction.

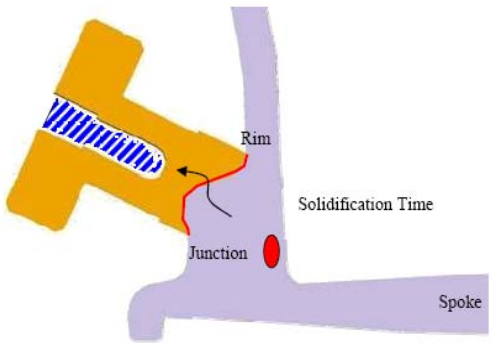

Figure 11: A cooling chill positioned at a typical thick/thin (TT) junction known as a rim-spoke junction in the case of a wheel.

The biggest problem however, occurs when the rim-spoke junction shrinks and moves away from the chill, resulting in an air gap at the casting-chill interface. This air gap

reduces the heat transfer from the casting to the chill consequent making the chill inefficient for the rest of the casting solidification cycle, which can take up to six minutes. If the rim-spoke junction (or any junction involving thin/thick sections in a general casting) is not cooled efficiently and in the correct sequence in the overall casting, this will create a “hot spot” which leads to macro-shrinkage in the casting as shown in Figure 12

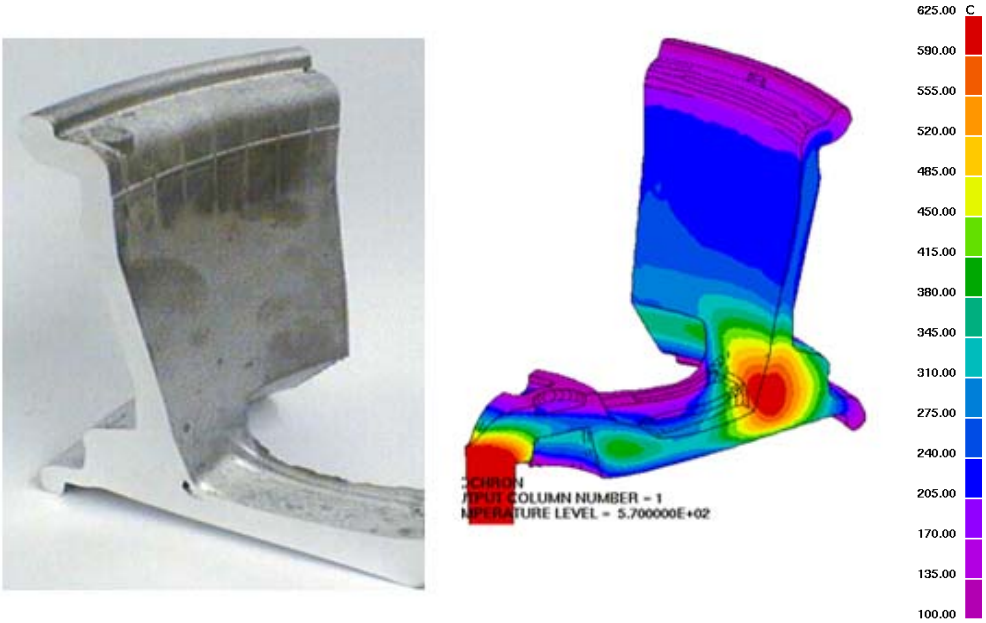

Figure 12: Hot spot at a typical thick thin (TT) junction

1.6 Affect of air gap on temperature distribution at a typical TT junction.

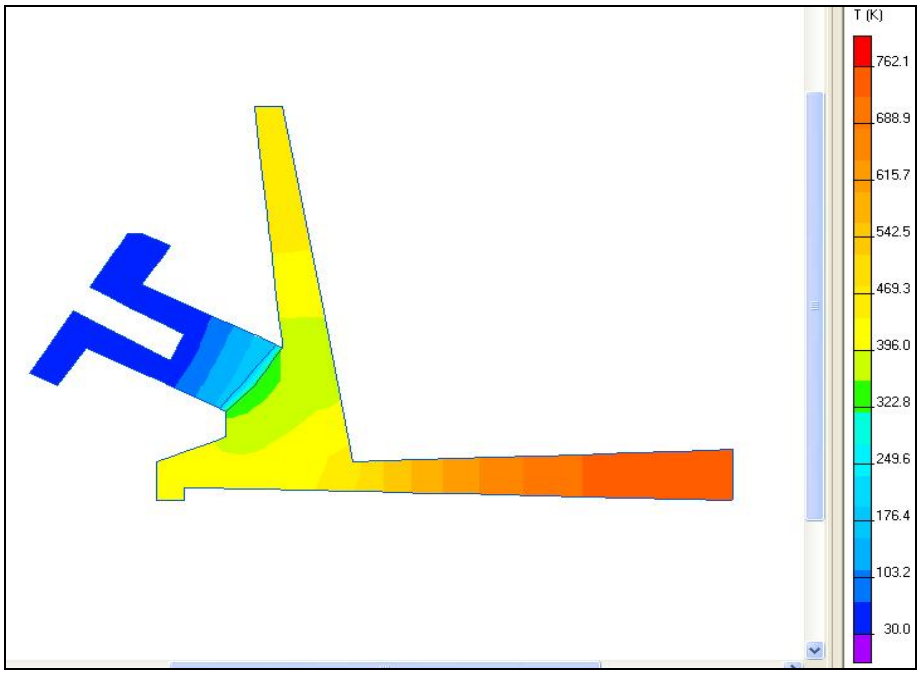

Figure 13: FEM simulation of rim spoke junction without air gap using Quick Field.

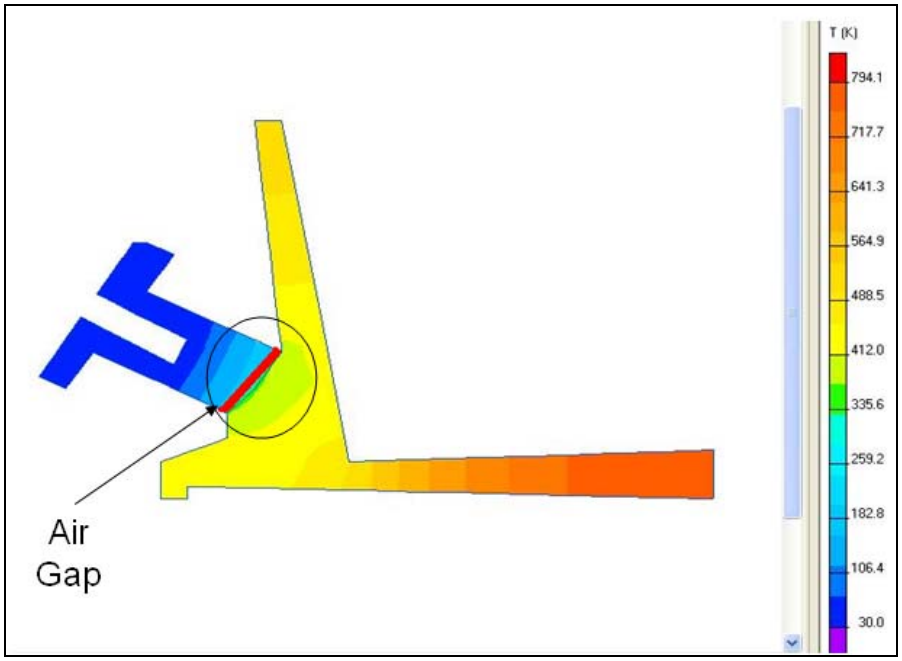

Figure 14: FEM simulation of rim spoke junction with an exaggerated air gap using Quick Field.

Figure 13 and Figure 14 show a finite element simulation of the rim-spoke junction with and without the presence of an air gap. By comparing the temperature profile in both

cases it can be seen that the presence of air gap has a direct influence on the temperature distribution.

1.7 Metal-Mold Interface

The structural integrity of many castings greatly depends on the thermal histories during solidification. A number of analytical and numerical models were developed considering heat transfer and simulation of freezing pattern which has helped in modification of the casting process itself. Hallam and Griffiths [7] developed a model for estimation of interfacial heat transfer coefficients for the aluminum gravity die casting process. They worked to calculate the interfacial heat transfer coefficients from the thermal histories and thermo physical properties. Their work concluded that during solidification of aluminum die casting the majority of resistance to heat flow is attributed to the layer of air trapped between the rough casting and the coating surface and not due to the lower thermal conductivity of the refractory coating.

The surface that appears to be smooth is actually contoured with microscopic cavities and depressions that deviate from an ideal fully contacting smooth surface. Usually, the microscopic deviation is termed as roughness and macroscopic deviation is termed as waviness.

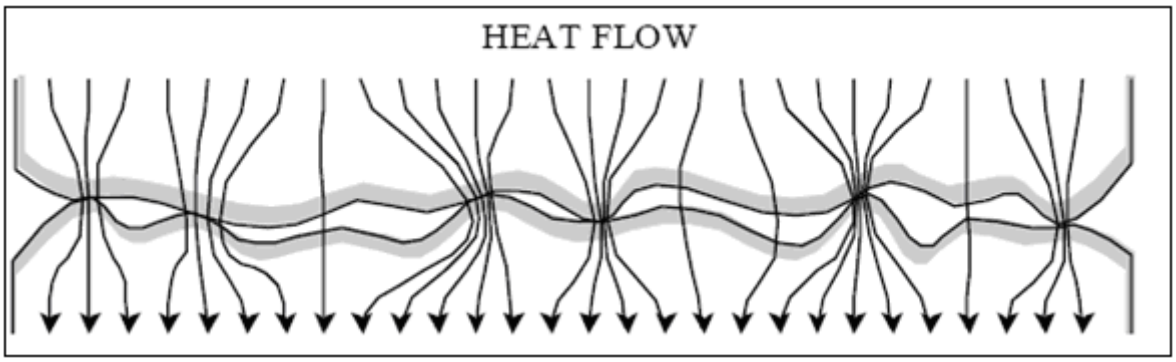

Figure 15: Heat flow at metal mold interface [8, 9]

The area of actual contact is usually considered between the asperities (ups and downs) of one surface on asperities of another surface. Typically, there is some material or fluid in the interstitial space between the contacting surface and the heat is allowed to flow through this interstitial material. Where there is no conducting interstitial material between the interfaces, and then heat transfer could be considered mainly through the physical contact points as shown in Figure 15.

1.8 Research objectives

This research investigates the hypothesis of using a movable chill (that is a cooling circuit that can be pushed closer to the casting as it shrinks away) to increase the casting-mold contact duration thereby increasing the heat transfer between the casting and the chill. This research develops a technique which identifies air gap formation between the casting and the chill and provides a means to push the chill closer into the casting to reduce the air gap.

The main objective of this research is to understand the effect of a movable chill that can be pushed closer to maintain a constant or prolonged contact with the casting as it shrinks away. Development of such a chill will not only improve the heat removal rate from the strategic regions within the casting more effective but also reduce the micro and macro shrinkage and improve the productivity of a given casting by saving the cycle time.

1.8.1 Air gap signaling and temperature data acquisition

The research shall include identifying suitable signaling technique to identify air gap formation. The air gap evolution was important to identify in order to push the chill closer to the casting. The temperature data from the casting and chill is required to have a relationship with the air gap formation.

1.8.2 Computer simulation to calculate heat transfer coefficient

These temperature and air gap obtained from the experiments will be used calculate interfacial heat transfer coefficient (IHTC) by inverse optimization technique. The resulting heat transfer data shall be used to compare the effectiveness of fixed and movable cooling chill blocks.

1.8.3 Micro structure and SDAS measurements

Since the effectiveness of the cooling chill has a direct relationship with the microstructure, it is in interest of the this research to understand the effect of both fixed and movable cooling chills on microstructure or the secondary dendrite arm spacing. Apart from these, it present research also tends to answer the questions such as (i) When is the air gap forming? (ii) How much can we push the chill closer into the casting?

2 Literature Review

In last few decades there has been a great deal of research conducted in air gap measurement, metal-mold interface, thermal contact resistance, interfacial heat transfer, solidification and inverse modeling techniques. Some of the recent works are summarized below.

2.1 Air Gap measurements

When molten metal is poured into the mold, the mold expands and at the same time the cast metal contracts during solidification. This thermal deformation does not significantly affect the thermal conductivity, however it causes a gap formation or decrease in pressure at the casting/mold interface which leads to thermal contact resistance. Thermal contact resistance at the casting-mold interface directly affects the solidification rate in the casting. This thermal contact resistance is directly proportional to the size of the air gap. There have been several works that have been dedicated to understanding air gap formation.

Some investigators used an inverse heat conduction technique to model the heat transfer at the interface as explained in section 2.2.3. Others tried to measure the air gap directly or indirectly by sensors as discussed in this section. In spite of these efforts, a reliable empirical relationship between the air gap size and temperature distribution at the interface has still not been established.

In 1962, Savage [10] proposed a simple explanation of air gap formation in the case of casting ingots. According to his work, the time of air gap formation was taken to be the point, when the inward dishing of the skin due to thermal stresses exceeds the outward bulging due to metal pressure.

Prates and Biloni [11] first suggested the existence of an air gap which affects the heat transfer mechanism at the casting-mold interface. From their work it can be seen that, a combination of restricted wetting ability of molten metal due to surface tension and volumetric contraction during the initial phase of solidification is the main cause of air gap formation.

Ho and Pehlke [12] calculated the interfacial heat transfer coefficient by first estimating the interfacial heat flux using Beck's [13] inverse method based on temperature

measurements within the casting and the chill. In their work, two linear transducers were connected to the mold and the casting respectively. The size of the air gap was then calculated by taking the average of the total deflection of the chill and the casting. The calculated air gap data was later used to estimate heat flux and the interfacial heat transfer coefficient (IHTC) using the inverse method.

Later work by Ho and Pehlke [14] characterized interfacial air gap formation into three physical mechanism states:

1. Conforming contact,
2. Nonconforming contact and
3. Clearance gap.

They also demonstrated two independent ways of determining IHTC:

1. Computer solution of the inverse heat conduction problem using thermocouple measurement.
2. Measurement of air gap size with respect to time and correlating to corresponding IHTC.

Narayan et al [15] proposed a model to compute the interfacial heat transfer coefficient using a model considering both conduction and radiation based on surface roughness characteristics of the casting and the mold.

Griffiths [7] concluded that the initial skin of the casting actually deformed due to thermal stress produced during solidification. The subsequent heat transfer from the casting to the chill would be strongly influenced by the dimension of the interfacial gap resulting from this initial deformation.

Experiments were conducted by Griffiths in different orientations of casting and chills as shown in Figure 16. He found that the upward solidification gave rise to larger values of IHTC than downward solidification for the same alloy. This is due to the fact that during upward solidification the entire casting rests on its own weight due to gravity and can maintain contact pressure on the mold, where as in case of downward and horizontal solidification some portion of the casting withdraws during solidification creating more air gaps and hence lower values of IHTC.

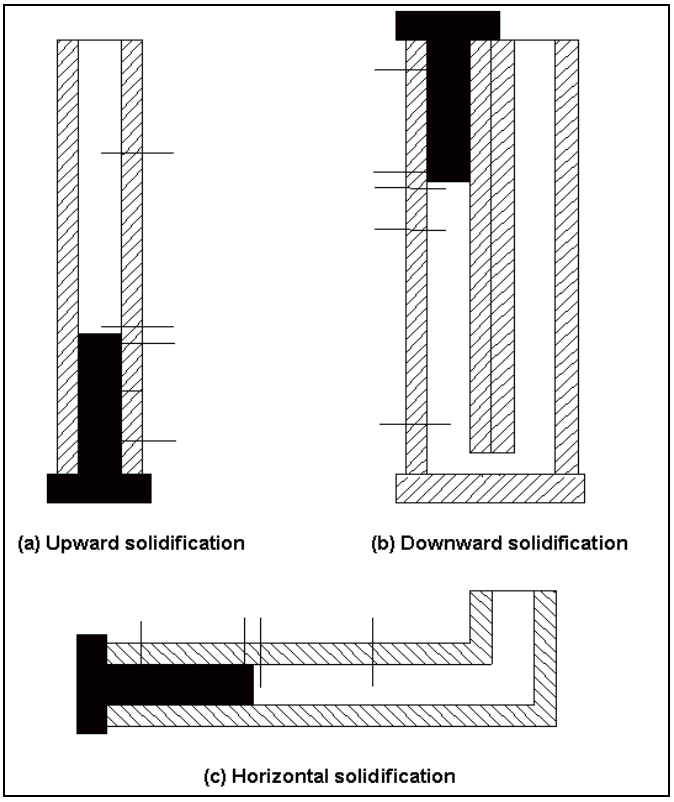

Figure 16: (a) Upward solidification, (b): Downward solidification, (c): Horizontal solidification. Reproduced from [7]

Similar work is reported by Eduardo [16]. He conducted experiments to understand the behaviour of casting-mold heat transfer coefficient in a cylindrical stainless steel chill. He expressed IHTC as a function of time and angular position of casting.

$$h = a.t^{-n} \qquad \textbf{2.1.1}$$

Where h is heat transfer coefficient, a is angular position of the mold, t is time period and n is a constant whose value depends on alloy composition. A similar observation was documented by Santos [17]. His work proposed a relationship between IHTC as a function of time and composition of alloy.

$$h = C_1(t)^{-m} \qquad \textbf{2.1.2}$$

Where C_1 and m are constants whose value depends on alloy composition, chill material and superheat. His work also concluded that the transient heat transfer coefficient profiles increase with increase in melt superheat for horizontal directional solidification. A reverse situation has been observed for vertical upward directional solidification, where the IHTC profiles decrease with increase in melt superheat.

Incropera [18] suggested that increasing contact pressure or reducing the surface roughness can lead to greater contact area thereby reducing the contact resistance. His work also suggested the use of filler material such as helium (which has higher conductivity than air) in between casting and chill to increase IHTC.

More recently use of helium gas as a filler material at the interface has been reported due to its properties such as higher thermal conductivity (5 times than air), non flammable and non toxic. Doutre [19] showed that injecting helium at the interface can reduce solidification time in the case of permanent mold casting. Wan [20] estimated the affect of helium injection on heat transfer coefficient HTC using elementary heat transfer calculations.

Stavros [21] made comparison between effect of air and helium on heat transfer at casting mold interface. He devised a technique to measure the air gap while helium was being injected. His work showed that Helium injection at the metal-mold interface decreases casting-mold separation time. The magnitude of this decrease depends upon the liquid-metal temperature and the mold-surface roughness. The effectiveness of helium on HTC relative to air was found to be elevated with higher mold roughness. Their work suggested a direct relationship between HTC, surface roughness and air gap thickness as shown below.

$$h = \frac{1}{a \times g + b} + c \qquad \textbf{2.1.3}$$

Where h is the IHTC, g is the air gap thickness, a, b and c are constants whose values are a is 1.717×10^{-2} in $W^{-1}m^{2}Kmm^{-1}$, b is $1.018 \times 10^{-3} W^{-1}m^{2}K$ and c is 33.478 $Wm^{-2}K^{-1}$.

Metzloff [22] carried out experiments injecting helium in permanent mold casting in an industrial environment. In this work, helium gas was injected into the mold prior to pouring of molten metal. The introduction of molten metal caused helium to float on top of it (due to the low density of helium with respect to air) along the mold walls, thus increasing the heat transfer at the casting-mold interface. However it was found that injecting helium alone did not make any significant contribution to the overall production time. Further injecting helium just after pouring could lead to bubbler defect (surface porosities) at the interface.

Another method to increase the heat transfer at selected regions within the casting is by applying pressure on the casting while it solidifies in the mold. The effect of "squeeze pins" was demonstrated by Carrig et al [23] to increase the heat transfer at strategic locations within the mold. Their work confirmed that applying pressure to the pins embedded in molds, could affect surface shrinkage and reduce internal shrinkage.

The heat transfer at the casting-mold interface mainly depends on two factors [24]: (i) type of contact surface. (ii) medium in between the contact surface. The contact surface often depends on the surface roughness at the interface. The contact surface at the interface can be treated in any of the following three ways. (i) perfect contact, (ii) imperfect contact. (iii) contact with a gas medium

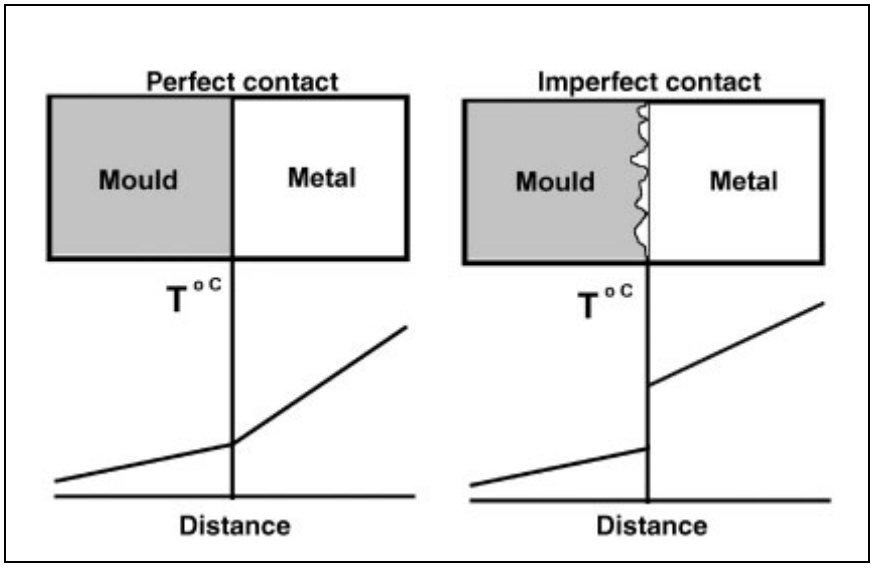

Figure 17: Casting-mold surface roughness and temperature distributions (reproduced from [24])

Perfect contact as mentioned earlier is considered to be ideal, and it can be seen that by application of pressure and surface polishing this can be achieved.

However imperfect contact is mainly when the surfaces are not in complete contact, which is usually due to roughness, coating of the mold or due to lower contact pressure. This resistance occurs until a thick solid layer is formed. In such cases, heat is transferred through contact points and gas gap at the interface. This occurs when the metal is not deformed under metallostatic or external pressure. Due to shrinkage of the deformed metal skin, the heat transfer occurs mainly through a layer of gas at the interface.

In general, heat transfer through this gas gap occurs due to convection, radiation and gas conduction. States of the heat transfer conditions at the interface depend on the Rayleigh (Ra) number and Nusselt (Nu) numbers [25], The Grashof number (Gr) is one of the parameters, which must be the same in two free convective systems for them to be dynamically similar [24].

$$Gr = \frac{g\beta\Delta T d^3}{\nu^2} \qquad \textbf{2.1.4}$$

where g is the gravity, β is thermal expansion coefficient, ΔT is gap temperature difference, d is the length scale and ν is the kinematic viscosity. When $Gr \geq 1$, the viscous force is negligible compared to the buoyancy force and inertial force. Also the inertial forces are negligible. When Grashof's number $Gr \leq 1$ convection occurs when the Rayleigh (Ra) number is more than 1700.

$$Ra = \frac{g\beta\Delta T d^3}{\nu\alpha} = Gr\,\mathrm{Pr} \qquad \textbf{2.1.5}$$

where Pr is the Prandtl number and is defined as follows:

$$\mathrm{Pr} = \frac{\nu}{\alpha} = \frac{C_p \mu}{K_g} \qquad \textbf{2.1.6}$$

where C_p is the heat capacity of gas, K_g is the thermal conductivity of gas, α is the thermal diffusivity, μ and is dynamic viscosity. The Nusselt number (Nu) gives the ratio of actual heat transferred between two parallel plates (gap) at different temperature by moving fluid to the heat transfer that would occur by conduction. It is defined as follows.

$$Nu = \frac{hd}{K_g} \qquad \textbf{2.1.7}$$

where h is the heat transfer coefficient between the interfaces (air or gas gap).

The mechanism of heat transfer at the gap can be divided into five regimes [24, 25].

(i) Conduction regime $Ra < 1000$;

(ii) Asymptotic flow regime $1000 \leq Ra < 10000$;

(iii) Laminar flow regime $10^4 \le Ra < 10^6$;

(iv) Transition flow regime $10^6 \le Ra < 10^7$;

(v) Turbulent flow regime $Ra \ge 10^7$

It is also possible to determine the temperature profile of the casting mold interface using Knudsen number (Kn)

$$Kn = \frac{\lambda}{d} \qquad \textbf{2.1.8}$$

The small value of free mean path λ compared with the size of the gas gap (d), confirms that the temperature profile at the interface of casting can always be assumed linear and continuous [8, 24].

Heat transfer at the interface can also be explained by Fourier's law of heat transfer. The overall heat transfer coefficient at the interface can be calculated assuming that the medium of interface is layer of gas with a thickness (d) as shown in Figure 18.

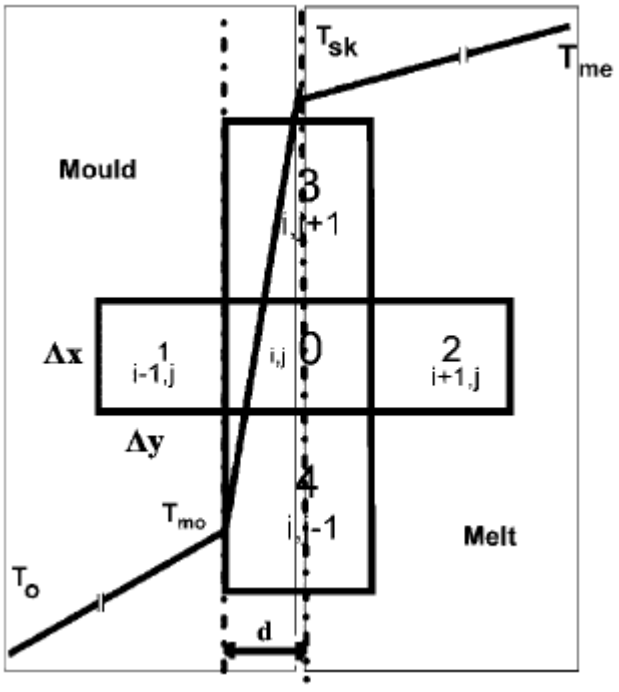

Figure 18: Schematic of discretisation of the casting–mold interface. T_{me} = melt temperature, T_{mo} = mold temperature

$$h_g = \frac{k}{d} \quad \textbf{2.1.9}$$

$$h_t = \frac{q}{A(T_{Cast} - T_{mold})} \quad \textbf{2.1.10}$$

In the equation, A is the interface area, q is the heat flux through the interface, T_{cast} and T_{mold} are the casting and mold temperature respectively.

2.2 Interfacial heat transfer coefficients

Reviewing the past literature, it has been found that there are two methods of determining the interfacial heat transfer coefficients. One method is to measure the size of the air gap and correlating it to appropriate heat transfer coefficients. Another more accurate method is to measure the temperature at different locations in the casting and the chill and using inverse methods to calculate the IHTC.

Using the first method, earlier researchers discovered that both casting and mold move during casting [26]. But it was not until a recently reliable method was adopted to measure the mold and casting simultaneously [16].

The second method is to derive the interfacial heat transfer coefficient (h) using inverse methods.

2.2.1 Inverse heat conduction problem concept

Inverse heat conduction is generally defined as the determination of heat flux from measured transient temperature inside a heat conducting body as defined by Beck [27]. In other words if the heat fluxes or the temperature history at the surface are unknown, we can estimate by solving inverse heat conduction problem from measured temperature histories within the body.

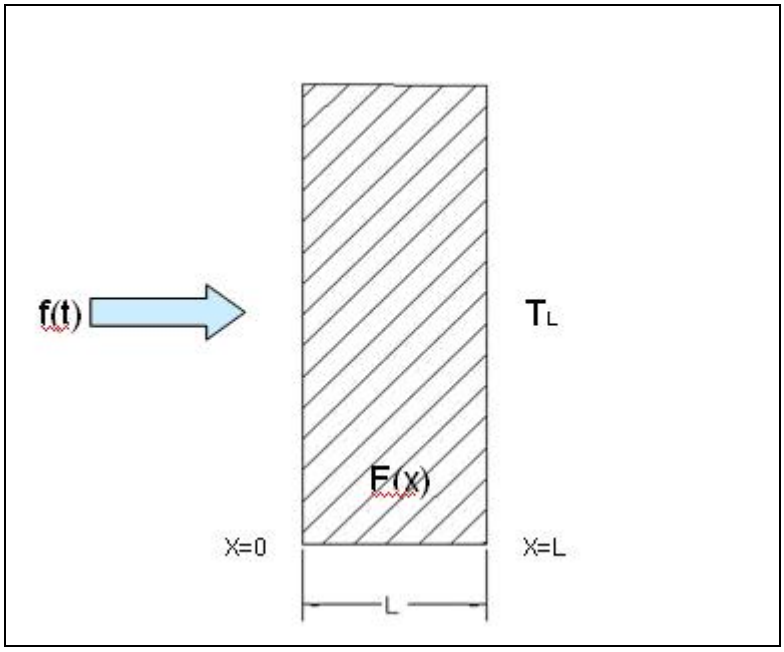

Figure 19: Heat transfer through a slab to illustrate the inverse problem [28].

Before going any further into inverse heat conduction problem, let us understand the difference between direct heat conduction problems and inverse heat conduction problems. Consider a slab with a thickness (L) as shown in Figure 19. The initial temperature distribution in the slab is F(x). For time t>0, a transient heat flux is applied on the boundary X=0, while the boundary X=L is maintained at a constant temperature T_L.

In the case of the direct problem [29, 30],

$$\frac{\partial}{\partial x}\left(K\frac{\partial T}{\partial t}\right)=\rho Cp\frac{\partial T}{\partial t} \qquad \text{in } 0<x<L \qquad \text{for } t>0$$

$$-K\frac{\partial T}{\partial x}=f(t) \qquad \text{at } x=0 \qquad \text{for } t>0$$

$$T=T_L \qquad \text{at } x=L \qquad \text{for } t>0$$

$$T=F(x) \qquad \text{for } t=0 \qquad \text{in } 0<x<L$$

For the above case, the boundary conditions f(t) and T_L, initial condition F(x) and thermo physical properties such as Cp, ρ and K are given. Hence this can be used to

calculate the temperature distribution within the slab T(x, t) as a function of position and time. This is called a direct heat conduction problem.

Now let us consider the same equations where the boundary condition function f(t) at surface x=0 is unknown and all other parameters such as T_L, F(x), Cp, ρ and K in the above equations are known. Now we need to determine the unknown boundary condition f(t). To compensate for the missing data, temperature measurements are taken at different locations (X_{meas}) within the slab and estimated as $T(X_{meas}, t_i)$. Where t_i is time of temperature measurements (i=1, 2,……, I) over a specified time interval of $0<t\leq t_f$. The equations can now be written as;

$\frac{\partial}{\partial x}\left(K\frac{\partial T}{\partial t}\right)=\rho Cp\frac{\partial T}{\partial t}$	in 0<x<L	for $0<t\leq t_f$
$-K\frac{\partial T}{\partial x}=f(t)=?$ **Unknown**	at x=0	for $0<t\leq t_f$
$T=T_L$	at x=L	for $0<t\leq t_f$
$T=F(x)$	for t=0	in 0<x<L

Where t_f is the final time. This is called an inverse heat conduction problem aimed to estimate an unknown surface condition. It must be noted that the solution by inverse heat conduction problems can only be estimated, not determined since there could be errors associated while measuring the temperature within the body. Moreover acquiring temperature data at infinitesimal points is challenging and the solution is often not unique given specific initial conditions.

The major difference between direct and inverse method is that in direct problems the causes are given, the effect is determined; where as in the inverse problem the effect is given, and the cause is estimated [29].

2.2.2 Difficulties in solving inverse heat transfer problem

Inverse heat transfer problems are often referred to as ill posed problems. To explain this let us consider a semi infinite solid ($0 < x < \infty$) initially at zero temperature.

For time t>0, the boundary surface at x=0 is subjected to a periodically varying heat flux in the form

$$q(t) = q_0 Cos\omega t \qquad \textbf{2.2.1}$$

where, q_0 and ω are the amplitude and frequency of the oscillation of the heat flux respectively, and t is the time variable after the transient have passed, the quasi-stationary temperature distribution in the solid can be given by [29, 31]

$$T(x,t) = \frac{q_0}{K}\sqrt{\frac{\alpha}{\omega}}\exp\left(-x\sqrt{\frac{\omega}{2\alpha}}\right)\cos\left(\omega t - x\sqrt{\frac{\omega}{2\alpha}} - \frac{\pi}{4}\right) \qquad \textbf{2.2.2}$$

where α the thermal diffusivity and K is the thermal conductivity of the solid.

Equation 2.2.2 illustrates that the temperature response is lagged with respect to the heat flux excitation at the surface of the body, and such lagging is more pronounced for the points located deeper inside the body. This lag in temperature indicates the need for measurements to be taken just after the application of heat flux, if such heat flux has to be estimated.

The amplitude for the temperature oscillation at any location, $|\Delta T(x)|$ is obtained by setting Cos(0)=1 in equation 2.2.2. Hence,

$$|\Delta T(x)| = \frac{q_0}{K}\sqrt{\frac{\alpha}{\omega}}\exp\left(-x\sqrt{\frac{\omega}{2\alpha}}\right) \qquad \textbf{2.2.3}$$

From Equation 2.2.3 it can be seen that $|\Delta T(x)|$ attenuates exponentially with increasing frequency (ω). On the other hand, if the amplitude of the surface heat flux, q_0 is to be estimated by utilizing directly the measured temperature at an interior points, any measurement error on $|\Delta T(x)|$ will be magnified exponentially with the depth x and with frequency ω, as shown below

$$q_0 = K|\Delta T(x)|\sqrt{\frac{\omega}{\alpha}}\exp\left(x\sqrt{\frac{\omega}{2\alpha}}\right) \qquad \textbf{2.2.4}$$

From equation 2.2.4 it can be seen that the heat flux q_0 it is important to locate the temperature sensors such that the amplitude of the temperature oscillation is much

greater than the measurement errors. Otherwise it would be a challenge to distinguish if the measured temperature oscillation is due to a change in boundary heat flux or due to measurement errors, resulting in non-uniqueness of the inverse problem solution.

The above discussion supported by the equations proves that the accuracy of the solution estimated by inverse heat transfer problem depends on accuracy of the measured temperature.

There have been several methods developed in the recent past to solve the inverse heat transfer problem, since its widespread applications in the quenching industry. Few significant works are summarized below.

Method	**Researchers**
1. Exact Solution Technique	Burggraf [32],
2. Inversion of Duhamel's integral	Stolz [33], Beck [13]
3. Laplace transformation techniques	Sparrow [34],Imber [35]
4. Control volume method	Taler [36]
5. Finite difference method	Beck [37], , Blackwell [38]
6. Finite element method	Hore [39], Bass [40], Ling [41],

Table 1

2.2.3 Theoretical development

In this section, a brief discussion is made on the algorithm developed by Beck to determine the IHTC at the casting-mold interface based on non-linear estimation method. This is one of the widely used methods to estimate the IHTC since it improves computational stability by using future time steps. Non-linear approximation is obtained by minimising the below function using sum of least square approximation [7, 13]

$$F(h) = \sum_{j=1}^{J} \sum_{i=1}^{I} \left(\theta_{j,i}^{m} - \theta_{j,i}^{c} \right)^{2} \qquad \textbf{2.2.5}$$

where $\theta^m_{j,i}$ and $\theta^c_{j,i}$ are measured and calculated temperature respectively at jth temperature measurement location in ith time step and h is the heat transfer coefficient. By mathematical deduction equation 2.2.5 can be written as below.

$$\Delta h_{l+1} = \frac{\sum_{j=1}^{J}\sum_{i=1}^{I}\left(\theta^m_{j,l+1} - \theta^c_{j,l+1}\right)\phi_{j,l+1}}{\sum_{j=1}^{J}\sum_{i=0}^{I}\phi^2_{j,l+1}} \qquad \textbf{2.2.6}$$

where,

$$h_{l+1} = h_l + \Delta h_{J+1} \qquad \textbf{2.2.7}$$

$$\phi_{j,i} = \frac{\partial \theta^c_{j,i}}{\partial h_i} \qquad \textbf{2.2.8}$$

The iteration is continued until convergence which is defined by:

$$\frac{\Delta h_{l+i}}{h_{l+1}} < \varepsilon \qquad \textbf{2.2.9}$$

2.2.4 Formulation of interface element

Heat transfer in gap is by convection and as the air gap widens, the heat transfer coefficient becomes affected. Hence an interface element needs to be used between the casting and mould to accommodate the developing changes in the interface condition. A coincident node method is one of the techniques applied to account for casting mould interfacial heat transfer.

The governing differential equation in Cartesian coordinate system can be written as [42];

$$\frac{\partial}{\partial x}\left[k\frac{\partial T}{\partial x}\right] + \frac{\partial}{\partial y}\left[k\frac{\partial T}{\partial y}\right] = \rho Cp\frac{dT}{dt} \qquad \textbf{2.2.10}$$

By variational formulation and suitable shape function, equation 2.3.10 can be written as;

$$[K]^e\{T_i\} + [C]^e\{T_i\} = \{F\}^e \qquad \textbf{2.2.11}$$

where $[K]^e$ is conductivity matrix, $[C]^e$ is capacitance matrix, T_i is the time derivatives at the nodal temperature and $\{F\}^e$ is the thermal load vector.

2.2.5 Interface element

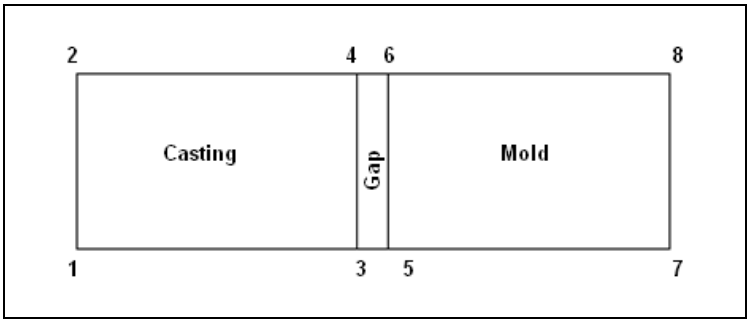

Figure 20: 2D interface element [43]

Interfacial heat transfer at the casting mold interface can be calculated by the coincidental node technique by constructing a virtual conductivity matrix for the gap element. From Figure 20 it can be seen that nodes 3, 5, 4 and 6 are coincident node with same spatial co-ordinates [42, 43].

$$[K]_{Gap} = h \int_{3,4} N^T \left(T_{metal} - T_{mold}\right) d\Gamma \qquad \textbf{2.2.12}$$

2.2.6 Factors affecting interfacial heat transfer coefficients

Die coating thickness; Initial value of heat transfer coefficient decreases with increase in die coat thickness. Insulating chills and pads; Insulation pads will reduce IHTC where as chills will enhance its value. Casting geometry; in areas where there is a continuous contact between the mold and casting IHTC will be higher. For example, bottom part of the casting. Pouring temperature; Increase in melt temperature will certainly increase the initial IHTC. Surface Roughness; Smooth surface will have less thermal contact resistance hence increase in IHTC. Alloy composition; Alloy with higher freezing range will have higher IHTC. Metallo-static pressure; Increase in metallo-static pressure reduces the air gap hence better IHTC. Mold Temperature; higher mold temperature gives higher IHTC variation at the first stage of solidification.

2.3 Solidification: Theoretical Background

Since aluminium alloy A356 is used in this experiment it is important to discuss the solidification characteristics.

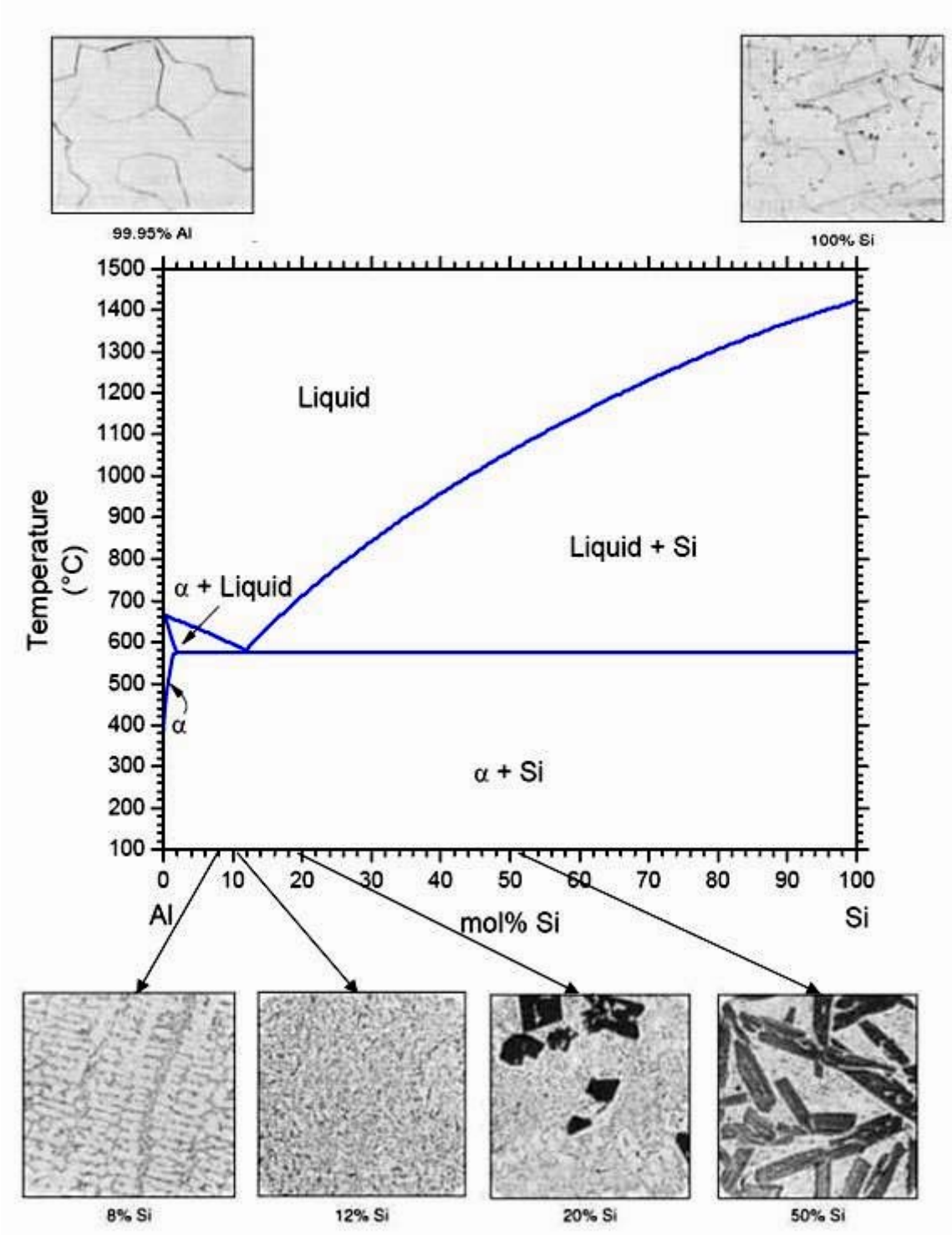

Figure 21: Phase diagram for A356 alloy [44]

Figure 21 shows a typical phase diagram for A356 with micrographs of representative structures. A356 mainly consists of silicon (6.5-7%) and magnesium (0.3-0.4%) as the main constituent. The presence of silicon content in aluminium improves heat treatable properties and with addition of magnesium increases fluidity. The eutectic temperature of aluminium silicon alloy is 577˚C. The microstructure of 99.5 % wt aluminium has an equi-axed structure of pure metal. Addition of 8 % wt silicon shows long tree-like dendrites of primary alpha solid solution surrounded by the eutectic pool.

2.3.1 Effect of cooling rate and melt temperature on solidification of aluminium alloy

Two key factors in casting processing that are responsible for the formation of structure and the quality of any casting are.

1. Cooling rate
2. Melt temperature

The cooling rate is closely connected to the solidification rate, which can be defined either as the velocity of solidification rate, (i.e. the velocity of the solidification front) or the as the liquid-solid phase transformation rate, measured in units of m/sec or s^{-1}.

Generally, the microstructure is refined by increasing the heat extraction and corresponding increase in solidification rate. In fundamental and theoretical studies, casting structure is often represented as unidirectional and columnar, with grains or branches represented by cylinders with rounded tips. In fact the microstructure of commercial alloy casting consists of dendrite equi-axed grains [45]. The microstructure is therefore considered on two levels: grain size and dendrite arm spacing.

The grain size is a function of several parameters, the most important of which are nucleation rate and growth rate. The nucleation rate depends on the amount of energy required for the creation of a new phase structure and new surface area. Therefore the nucleation rate can be affected by the melt under cooling below the liquidus (which gives a direct thermodynamic stimulus for nucleation, decreasing the critical size of the solidification nucleus) [45].

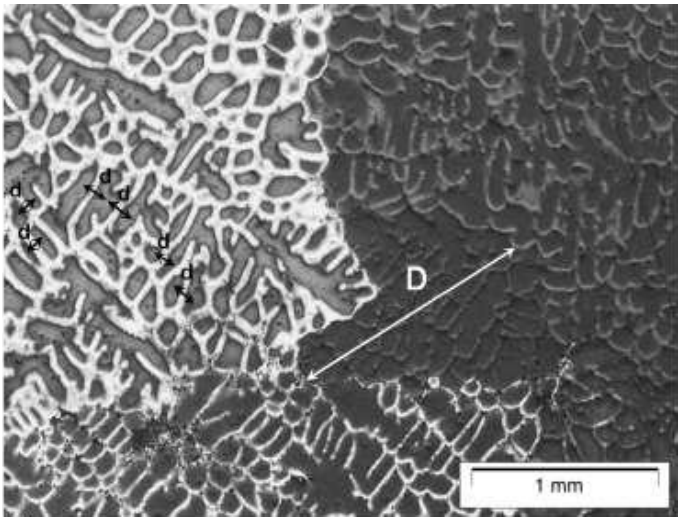

Figure 22: Micro structure of Al-1.8%Cu solidified at cooling rate 0.4 K/s (D=grain size and d=dendrite arm spacing) [46].

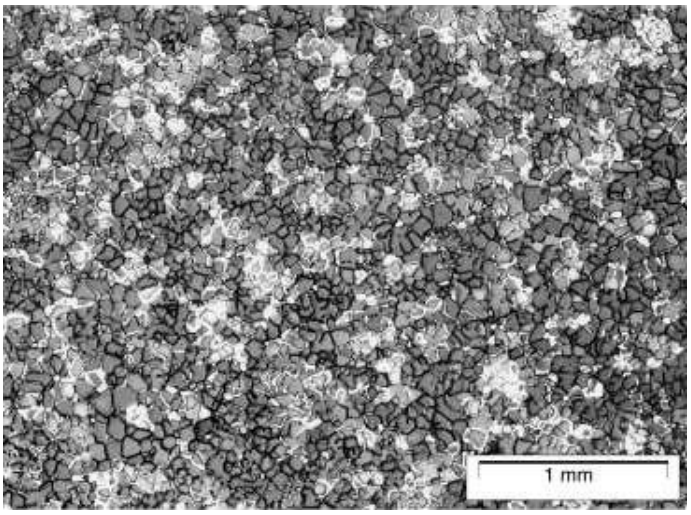

Figure 23: Micro structure of Al-1.8%Cu solidified at cooling rate 13 K/s [46].

2.3.2 Relationship between microstructure and thermal parameters

Fleming [47] established a power relationship between the thermal parameters and secondary dendrite arm spacing. His hypothesis suggested that a longer solidification time results in slow cooling rate hence allowing enough time for remelt for dendrite arm spacing. This results in large sized dendrite arms with large dendrite arm spacing.

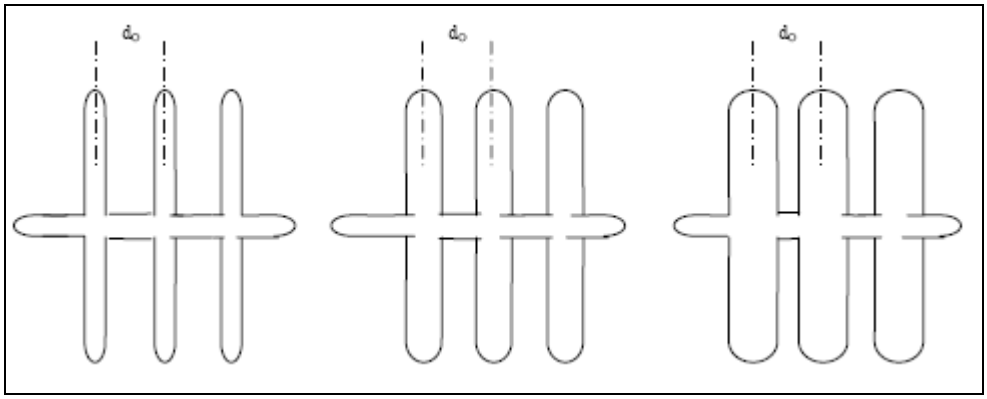

Figure 24: Initial model predicted by Fleming [47].

Fleming initially suggested that as the solidification progresses the dendrite arm spacing (d_o) remains constant but the grain size increases as shown in Figure 24. But later publications suggested that the dendrite arm spacing varies with the solidification rate. He suggested that the dendrite arm spacing (d_f) at the end of solidification was much larger than the initial dendrite (d_o) as shown in Figure 25.

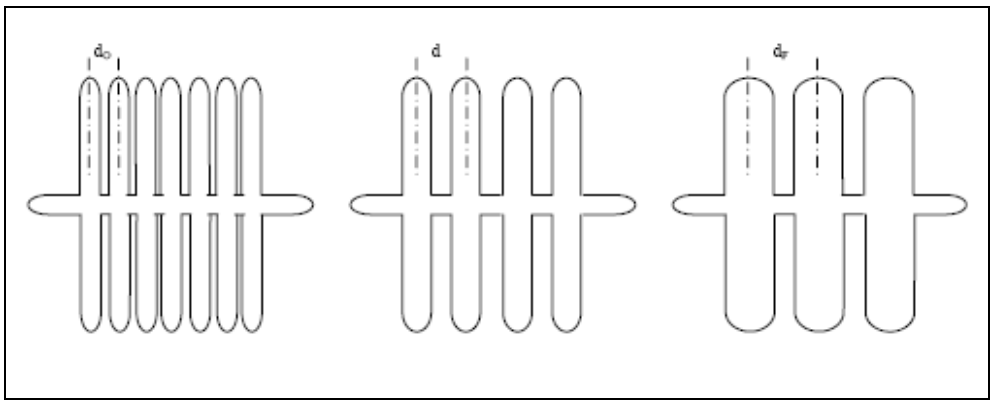

Figure 25: Later model predicted by Fleming [47].

Based on diffusion controlled coarsening model, Fleming suggested a relationship between the solidification time and final dendrite arm spacing as shown in equation 2.3.1

$$d = A \times \theta_f^a \qquad \textbf{2.3.1}$$

where A is the alloy specific constant, θ_f is the local solidification time and a is the alloy specific exponent.

This equation was later modified by Kirkwood [48] where an additional parameters of M was introduced known as coarsening parameter as shown in equation 2.3.2

$$\lambda_2 = K(Mt_f)^{1/3} \qquad \textbf{2.3.2}$$

where λ_2 is secondary dendrite arm spacing, K is alloy specific constant and M is the coarsening parameter.

2.4 Aluminium silicon eutectic modification

The properties of aluminium silicon eutectoid can be affected by modifying the form of eutectic. The fineness of the grain can be either naturally increased by the cooling rate or by addition of chemical modifiers. Sodium, calcium, antimony and strontium are commercially used chemical modifiers during solidification. Sodium is the most favourable modifier but its effects are transient due to oxidation and vapour pressure loss[49]. Strontium is less transient compared to sodium but it less influential for modification under slow solidification rate. The addition of modifying elements to aluminium silicon alloys results in finer lamellar and fibrous eutectic structures.

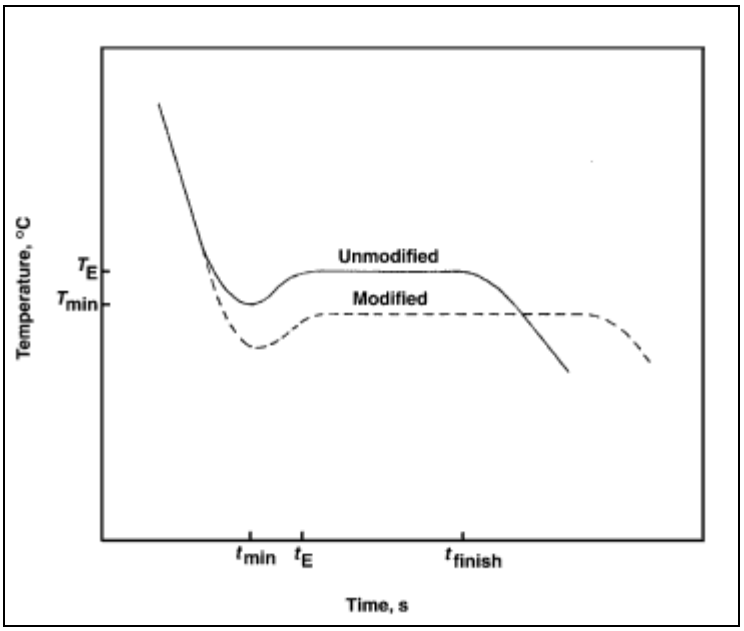

Figure 26: Effect of grain modifiers on temperature profile for a given Aluminium silicon alloy [49].

It is seen that modified structures displays higher tensile strength and ductility compared to unmodified structures. Temperature profile variation of a small aluminium silicon alloy sample solidified with modified and unmodified eutectic structure is shown in Figure 26. It can be seen that the presence of additives increases the rate of solidification consistently.

2.5 Effect of structure on properties

Mechanical properties of aluminium silicon alloys are principally controlled by the cast structure. Porosity and micro-shrinkage in aluminium castings limit the mechanical properties of the alloys. It is well known that the secondary dendrite arm spacing of the alloys decreases with increase in cooling rate and their hardness, tensile strength, percentage elongation and impact energy also increases. Since the structure has a direct relationship with the mechanical properties, investigators have found different methods to improve the microstructure. Adding modifier and refiner as discussed in previous section to the melt is a common method of achieving better quality micro-structure and have been adopted by several investigators [50, 51]. Power ultrasound [52] and electromagnetic stirring [53] have also been used to refine the microstructure of alloys. Another method of improving the microstructure of the solidifying metal is to cool it at a faster rate. This method not only improves the microstructure but also reduces the porosity and reduces solidification time (improve productivity) to a considerable level.

2.6 Computer modelling and simulation

Even though the casting dates back to around 5000 years it is only recently with the advancement in technology, that it is being thoroughly understood. Like any other complex problems casting involves several phenomena like;

1. Fluid mechanics with phase change,
2. Shrinkage and porosity,
3. Macro-segregation in alloys,
4. Heat transfer between the mold and casting,
5. Thermal stress in solidifying ingot.

Considering a few of the above phenomena, while solidification analysis makes modelling extremely sophisticated. Adding to this, the geometries of industrial castings are complicated to analyse and requires 3D modelling.

Numerical techniques developed to solve problems related to casting dates back to 1940s [54], but not until the last 15 years with the development of computational fluid dynamics and numerical heat transfer based software packages, has it is been well understood. Earlier computer programs were based on finite difference method (FDM) and in more recent years the finite element method (FEM) has also developed

2.6.1 Modelling of casting processes

While analysing casting process two difficulties encountered are [55];

1. The air gap at the casting-mold interface during solidification needs to be modelled to obtain the correct thermal response of the system. This effort is often complicated by the lack of understanding of the predominant modes of heat transfer across the gap as discussed in section 1.7 [56].
2. A material constitutive model capable of predicting the liquid-solid mechanical behaviour of metals needs to be developed. This problem is complicated by the fact that material properties at high temperatures are usually unavailable [57].

2.6.2 Modelling of heat transfer mechanism across the casting-mold interface

Numerical simulation in metal casting has developed well with some of the commercially available computer software packages like MagmaSoft^{TM}, ProCAST^{TM}, dieCas^{TM} and Novacast ^{TM}. In each case, after the analysis, there is a requirement to examine the result and to assess whether the design needs to be improved. So the design process is iterative, based on trial and error.

2.6.3 Reverse Engineering

Reverse engineering is a technique which is used to calibrate the experimental result with the numerical estimation. In a thermal problem usually are modelled by differential and integral equation using thermal properties involving k, Cp, ρ etc. and the solution depends on initial and boundary conditions. The temperature distribution in the body is found by known causes such as boundary and initial conditions. But in case where either boundary or initial conditions are unknown an iterative process is adapted based on trial and error.

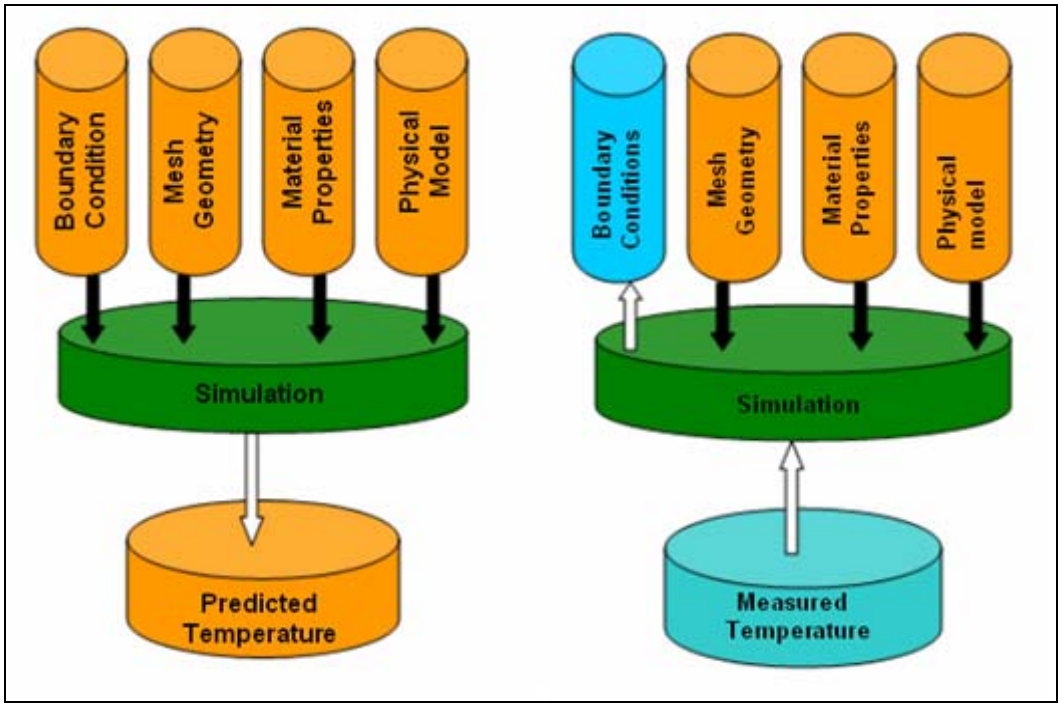

Figure 27: Reverse engineering technique

2.6.4 Determination of heat transfer coefficient at water cooling

The ability to measure temperature data for modelling the heat transfer into air or water channels inside parts of the mold is an important parameter for this experiment. During water cooling cycle during solidification the casting is rapidly cooled from 600˚C to 300˚C at a specified time. Water cooling is a challenging part of computer modelling since the water changes its phase from liquid to steam for a limited period. A quenching approach is used to solve this problem. According to this approach, the first stage is called film boiling when a vapour film blanket is formed on the surface of the component [58-60].

The cooling rate to the casting is usually low during film boiling, because heat is transferred from the chill to water through conduction in the vapour film. The second stage is called nucleate boiling when the vapour film breaks and the chill makes a direct contact with water. The temperature of the chill drops suddenly at this stage. The third stage is called boil cooling when the heat transfer is reduced and dominated by the convective mode. This approach is widely used in inverse modelling to calculate HTC during quenching.

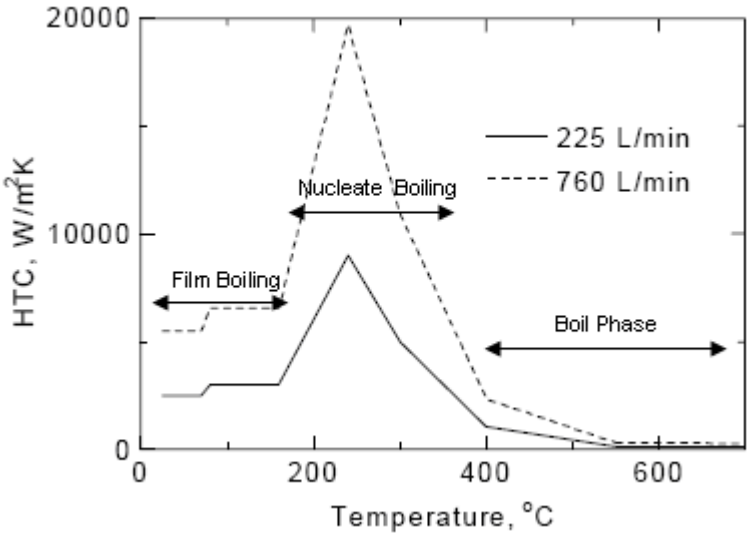

Figure 28: Heat transfer during quenching [58, 60]

2.7 Summary

In this chapter, works carried out by previous investigators related to air gap formation, interfacial heat transfer, effect of cooling on microstructure and finite element

modelling of air gap have been discussed. These previous work have provided a base for the current research. The below table summarises the contributions made by different investigators on heat transfer under different conditions.

Parameter	Summary of effects on heat transfer	Researchers
Casting and mold geometry	Dependent on mold thickness, concavity of casting. Thin mold, Limiting heat flow is the volumetric heat capacity (ρCp) of the mold. Thick mold: Limiting heat flow is the thermal conductivity (k) of the mold. h is higher at bottom of casting than top due to buoyancy.	Nguyen *et al* .[61] Gunasegaram *et al.* [62] Sully [26] Durham and Berry [63] Sun [64] Prates [11] Bishop *et al.* [65] Ayers [9]
Mold surface roughness	h is inversely proportional to a fractional power of chill surface roughness (i.e. increase in surface roughness from 0.018-0.291 μm decreases h by 17%).	Muojekwu et al. [66] Ho and Pehlke [14] Prates and Biloni [67]
Initial mold temperature	Higher mold temperature maintains a longer high initial stage of h.	Gunasegaram et al. [62] Michel at al. [68] Muojekwu et al [66]
Initial molten metal temperature	Increase in superheat achieves higher initial value of h, which remains high for a longer period.	Muojekwu et al. [66] Schmidt and Svensson [69] Prates and Billoni [67]
Contact pressure	Higher pressure leads to more contact between casting/mold interface, reduced air gap, and therefore, higher h.	Carrol et al. [70] Krishnan and Sharma [71] Nishida, Matsubara [61] Rapier et al. [72]
Alloy composition	Longer freezing range alloys have higher initial h. For Al-Si alloys, h increases with	Muojekwu et al.[66] Bamburger and Prinz [73] Wang [74]

	decreasing Si content.	
External cooling	h dependent more on air flow rate (from 0-1200l/min) than impingement distance. h ∞ water spray velocity and water impingement density. Decreasing cooling medium (e.g. air, water) temperature increases maximum value of h.	•Nguyen et al. [75] Lerner and Westendorf [76] Nara [77] Langlais et al. [78] Yeh and Jong [79] Fletcher et al. [80] Bamburger and Prinz [73]
Air/Gas Gap Formation	Larger air/gas gap gives lower h value. Gap forms after eutectic of A356 is reached – h is lowered. Gap growth rate (and hence h reduction rate) is inversely proportional to mold temperature. Air/Gas gap values up to 0.4 mm detected giving h = 150 W/m2K (for A356 castings in sand molds).	Poirier and Poirier [81] Krishnan and Sharma [71] Gunasegaram et al. [82] Santos [17] Eduardo [16] Nguyen et al. [75] Ho and Pehlke [14] Nishida et al. [61] Kulkarni [83]
Helium injection	Heat transfer can be increased with injecting helium along the air gap. Effectiveness of helium injection tested in an industrial environment	Argyropoulos [84] Wan [20] Stavros [21] Metzloff [22]

3 Experimental setup

3.1 Mold

A 3D model of the pattern required to make the mold was printed using a Z crop rapid prototyping machine (manufactured by Z Corp). The pattern was placed in a wooden box and a plaster pattern replica was made. A dense fused silica mold was made using this plaster replica. The DFS mold was then heated to 400 C to remove the moisture (curing). A thin layer of boron nitride was coated for quick release of casting from the mold. The composition and physical properties of the mold are illustrated in the appendix D.

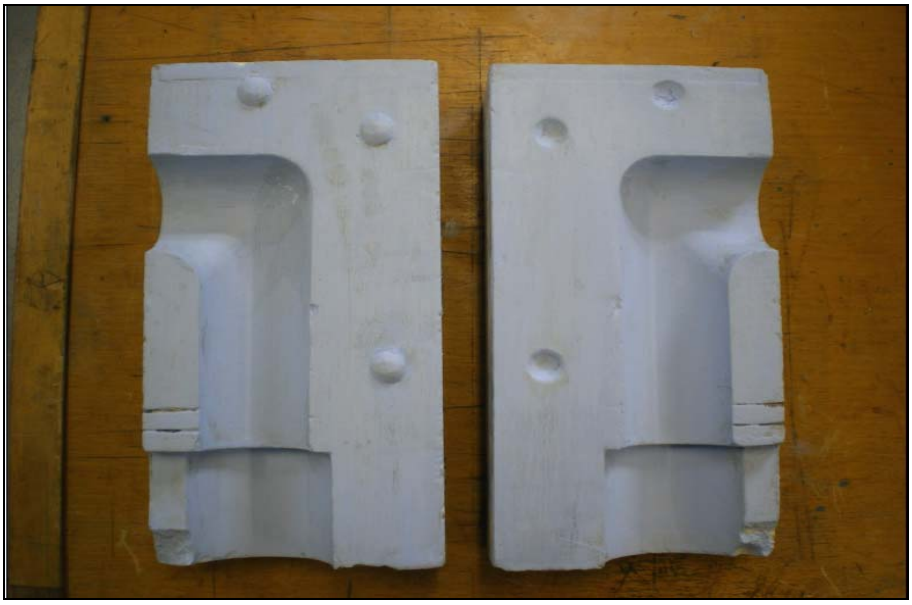

Figure 29: Dense fused silica mold

3.2 Chill

The spot water cooling circuit or "chill" was made up of copper with a push screw mechanism. The chilled is designed to push a maximum of 3 mm into the casting. Two thermocouple holes of 1.5 mm diameter were made in the copper chill at a distance of 10 mm each. The screw was threaded with a pitch of 2.54 mm. The entire chill pushed forward by 2.54mm per revolutions of the screw. The screw was brush coated with copper gel in order to avoid jamming or seizing resulting from thermal expansion at higher temperature. The detailed drawings of the mold and chill assembly are shown in the appendix

Figure 30: Copper chill

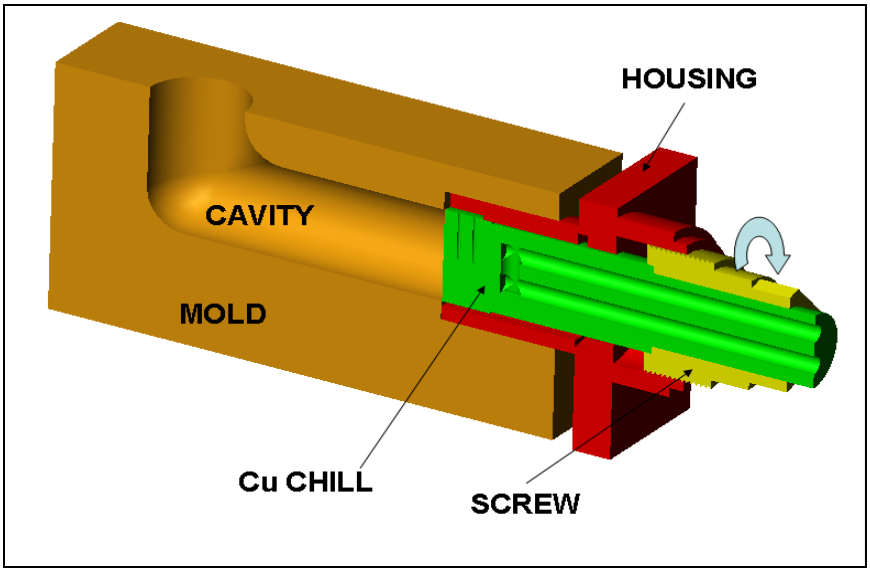

Figure 31; Chill-housing assembly.

3.3 Furnace

The metal was heated in a resistance furnace (4KVA 17amp 230V) located at AUT University as shown in Figure 32.

Figure 32: Crucible in resistance furnace at 710˚C

3.4 Methodology

The methodology adopted in these experiments was to generally ensure consistency in data collection, accuracy in temperature readings and a good understanding of the various cooling scenarios in order to provide the maximum opportunity to reveal any differences in the casting. The order of operations was:

1. Carry out casting trials on different cooling conditions.

2. Record the temperature histories from the thermocouples and the corresponding air gap signature from contact measurements of each casting under different cooling scenarios.

3. Relate the temperature and air gap data with microstructure data by measuring the secondary dendrite arm spacing (SDAS) at various distances in the casting from the chill.

4. Iteratively develop boundary conditions to determine the heat transfer coefficients at the casting/chill interface of the computer model to simulate a close representation of the solidification under each cooling scenario.

5. Relate the temperature, air gap, and heat transfer coefficient and microstructure data to validate the effectiveness of the chill under different scenarios.

The casting trials were carried out in four conditions and with three trials under each condition for repeatability.

Condition A	Fixed chill without cooling
Condition B	Fixed chill with cooling
Condition C	Movable chill with cooling (Displacement on demand)
Condition D	Movable chill with cooling (Displacement before eutectic)

Table 2: Four cooling conditions used in this study

	Fixed	Movable	No cool	Cool
A	**X**		**X**	
B	**X**			**X**
C		**X**		**X**
D		**X**		**X**

Table 3: Matrix of conditions used in this study

There was no condition required for a movable chill without cooling since the aim of the study was to determine an extreme difference in the solidification performance in the casting rather than to fine tune subtle differences in the context of other noisy variables such as thermocouples, melt temperature, mold temperature, ambient temperature, melt quality etc.

3.5 Sources of errors and experimental uncertainty

A one dimensional heat conduction model was created for calculation. After pouring the first thermocouple (positioned in the cavity) took at least 4 seconds to indicate the temperature of the molten metal. This happened due to the fact that metal freezes as it touches the thermocouple. Also the thermocouples were coated with a lubricant and ceramic spray to enable their reuse, however, this also created a lag in the speed of response. In order to minimise this problem a thin layer of copper paste was applied on the thermocouple to provide better sensitivity. The time resolution for data acquisition was 1 second, hence a lag effect was relatively insignificant.

The position of thermocouple was accurately measured in the case of the fixed chill (scenarios A and B). Where as in case of the movable chill, since the casting was pushed to a maximum of 2 mm, there was a variation in the thermocouple position. A preliminary experiment was conducted to reveal some practicalities and constraints of the study and accuracies of thermocouple placements and it was determined that there was a relatively low variation in temperature reading when thermocouples were placed at 5 mm and 10 mm from the casting/chill interface. This difference was estimated to be less significant after eutectic temperature had been reached. However, in general the accuracy of the thermocouples was $\pm 1^0$C.

Based on literature review the following formula is used to calculate the error band for the measured experimental temperature [85]. The approximation for the error of the entire measurement system at 650^{o}C (representing the upper temperature limit) was given by

$$\delta T_{650} = \sqrt{\delta_{ref}^2 + \delta_{zero}^2 + \delta_{lin}^2 + \delta_{DL+C}^2 + \delta_{dry-block}^2 + \delta_{TC}^2 + \delta_{gradient}^2} \qquad \textbf{3.5.1}$$

$$\delta T_{650} = \sqrt{(0.5)^2 + (1)^2 + (0.3)^2 + (1.1)^2 + (0.005 \times 650)^2 + (0.005 \times 650)^2 + (0.1)^2}$$

$$= 4.9\ ^\circ\text{C}$$

The approximation for the error at 450^{o}C (representing the lower temperature limit)

$$\delta T_{450} = \sqrt{\delta_{ref}^2 + \delta_{zero}^2 + \delta_{lin}^2 + \delta_{DL+C}^2 + \delta_{dry-block}^2 + \delta_{TC}^2 + \delta_{gradient}^2} \qquad \textbf{3.5.2}$$

$$\delta T_{450} = \sqrt{(0.5)^2 + (1)^2 + (0.3)^2 + (1.1)^2 + (0.005 \times 450)^2 + (0.005 \times 450)^2 + (0.1)^2}$$

$$= 3.6^\circ\text{C}$$

After the initial trials, it was decided to install one thermocouple into the molten metal instead of two since the temperature histories recorded by both were relatively similar. Also it was important to preserve the casting samples for micro structural analysis. So re-melting the castings to reuse the thermocouple was not an option.

3.6 Air gap indicator

To sense the air gap formation at the interface a simple electronic circuit was used as shown in Figure 33. A small amount of voltage of 1.5 V was passed from the casting to the chill. The circuit was then connected to a computer through a data logger which measures voltage and display using strip chart display software as shown in Figure 34. This enabled in process monitoring of the air gap formation at the casting chill interface. This information was utilized to determine when to move the chill closer to the casting.

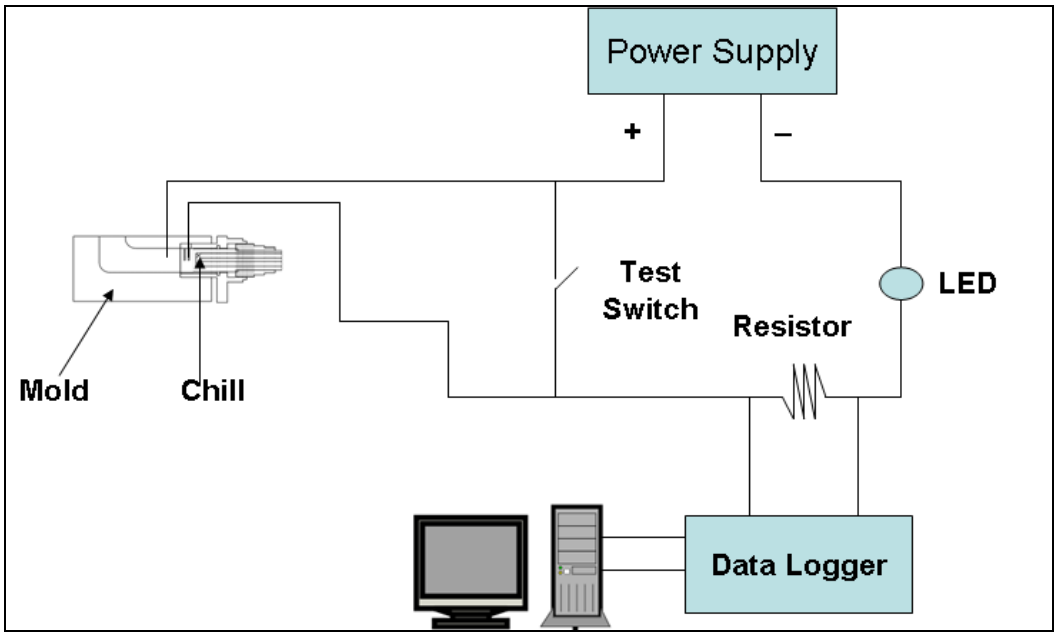

Figure 33: Air gap indicator circuit

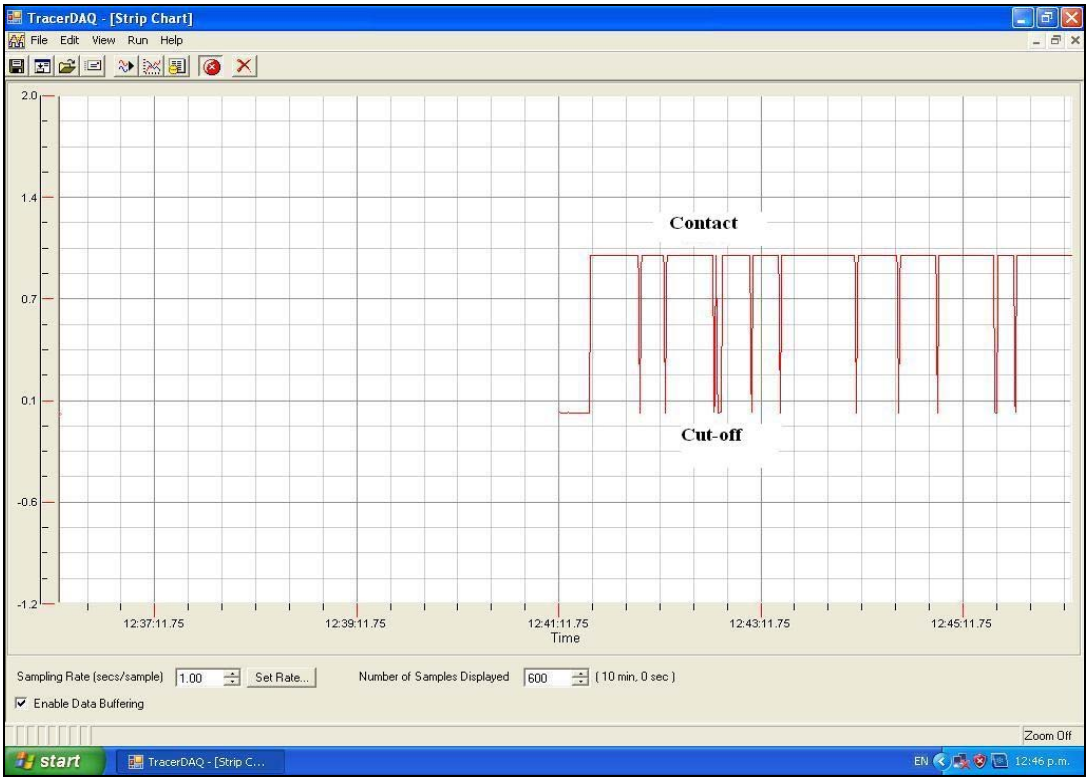

Figure 34: Strip chart display

This system of air gap detection is based on the assumption that the surface of the chill and the casting are perfectly flat. It is also understood and assumed that even though air gaps may form in isolated and non-uniform pockets between the casting/chill interfaces, that the detection method described above is based only on complete cutoff (i.e. a fully developed air gap only). The chill was pushed forward (for scenarios C and D) after complete cut-off was detected. Precautions were taken to avoid any short circuit through the cooling channel.

Figure 36 shows the air gap formation between the casting and the chill, which was produced under scenario B. This air gap was minimised by moving the chill closer in scenarios C and D as shown in Figure 37.

Figure 35: Casting after 600 secs

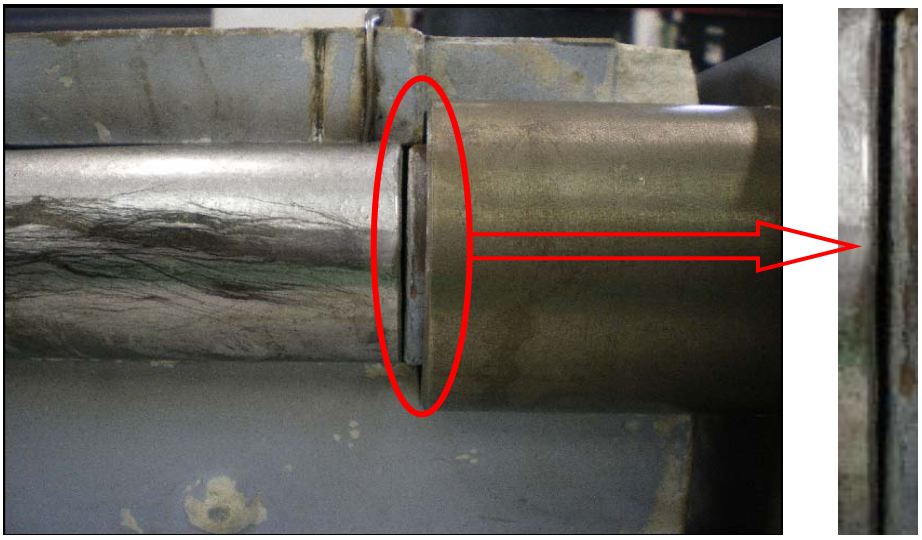

Figure 36: Casting-mold interface with fixed chill (image taken after 600 sec)

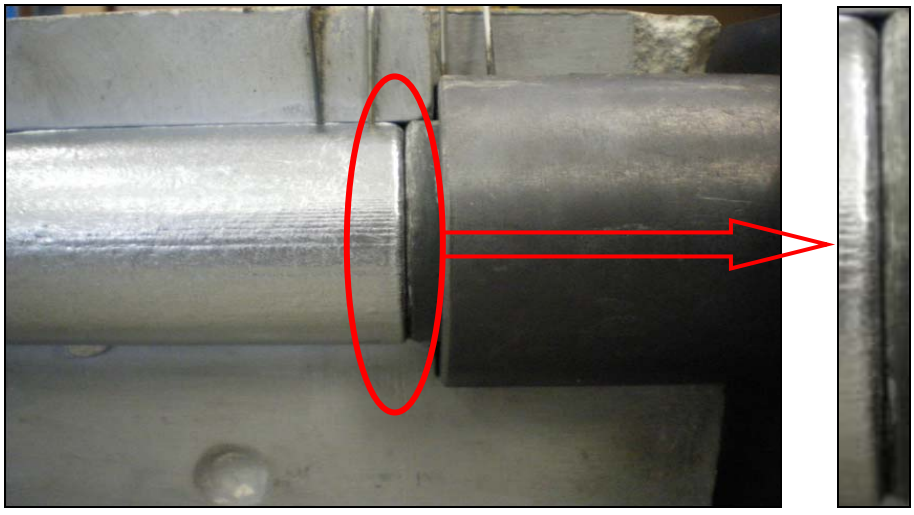

Figure 37: Casting mold interface with movable chill (image taken after600 sec)

Figure 38 shows the mold chill assembly connected to the cooling water pipes and thermocouples. The mold was held together by two F-clamps.

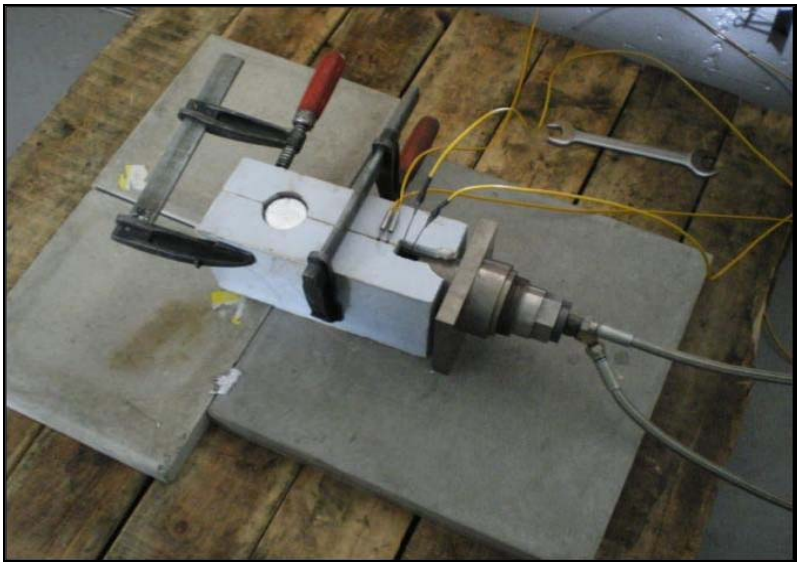

Figure 38: Mold setup with cooling pipes and thermocouples

3.7 Experiment procedure

This section briefly describes the operating procedure for conducting the casting trials.

3.7.1 Melt preparation

Commercially available aluminium A356 (7% wt Si, 0.3% wt Mg) was sectioned into small sizes and was melted in a crucible using a resistance furnace as shown in Figure 32. The melt temperature was carefully monitored for repeatability. The oxide layer at the top of the liquid metal was removed to ensure consistent quality metal entered the mold.

3.7.2 Thermocouple installation

Two 1.5 mm diameter type-K thermocouples were inserted into holes drilled in the copper chill and one 1.5 mm type-K thermocouple was inserted into the cavity. The thermocouple tips in the chill were coated with copper paste to ensure consistent contact between the tip and the chill. The thermocouples were located at a distance of 5 mm away from the interface in the casting and at 5 mm and 10 mm away from the interface in the copper chill as shown in Figure 39.

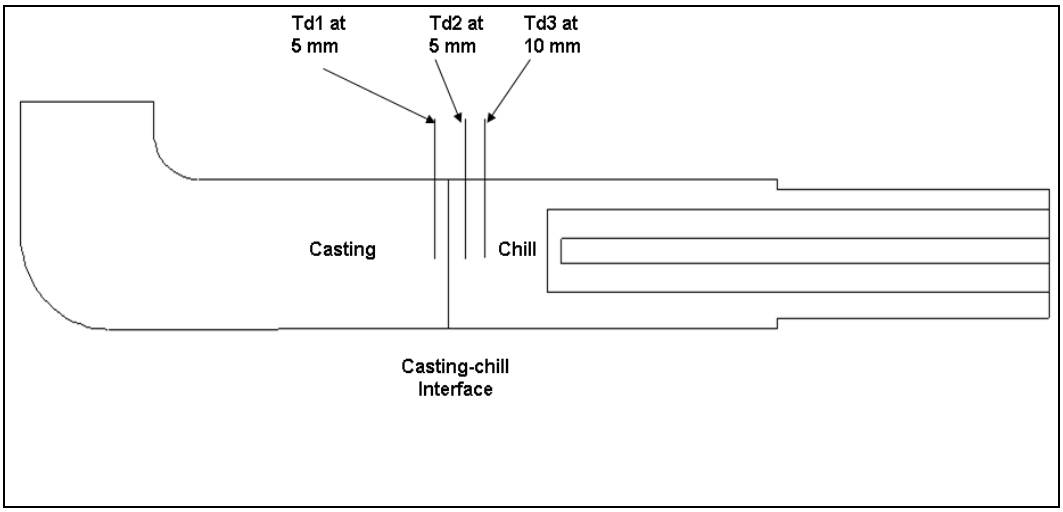

Figure 39: Location of thermocouple within casting and chill.

3.7.3 Mold and chill preheating

As described in previous sections, the mold and chill were simultaneously preheated to 190˚C. Since the thermal conductivity of mold and chill differs hence it was difficult to

maintain an equilibrium temperature. For maintaining a close temperature relation between the mold and chill the following procedure was adopted.

1. Heat mold and chill to 300˚C.

2. Record the temperature at which the difference in temperature is minimum.

3. After few initial trials it was found that the temperature of mold and chill are close at 190˚C. Hence this was maintained for remaining trials.

Also, heating both mold and chill to 300˚C initially provided enough time for experimental tasks such as connecting thermocouples, air gap electronic circuit and cooling water pipes to the chill during trials.

3.7.4 Cooling tank and pump

The cooling water for the chill was supplied from a 45 litre water tank by a 0.5 horse power pump. The water flow rate was measured using a float type flow meter. The water flow rate was maintained to 5.5 litre /min for each trial. This flow rate is considered to be optimum for the given size of the cooling channel beyond which increases in flow do not affect the heat transfer and cooling rate any further [86]. Instead, the dominating heat transfer media and mechanism would shift to the thermo physical properties of the surrounding materials or other such factor.

3.7.5 Pouring

The molten metal was carefully taken out of the furnace using a surface layer sweeping back motion into the hand ladle and then was carefully poured into the mold. The cooling water supply was activated shortly after pouring. The previously activated temperature and air gap data acquisition systems were triggered to acquire the data.

3.7.6 Chill displacement

In case of scenarios C and D with the movable chill, the screw connected to the chill was turned according to predefined graduations along the chill housing. The maximum distance the chill could move into the casting was 5 mm. However in this investigation, the maximum displacement was limited to 2.5 mm. Displacement beyond this value could alter the dimensions of the casting significantly as well as affect machining tolerances of industrial products such as wheel rim and engine castings.

Anticipating the possibility of screw jamming due to thermal expansion, a small layer of Loctite™ anti seizing agent was applied on the screw. This allowed smooth turning of the screw at high temperatures.

3.8 Temperature data and air gap signature

In this section the temperature data acquisition and air gap signal charts for different trial scenarios are presented and discussed.

3.8.1 Temperature data acquisition

In order to accurately estimate the interfacial heat transfer coefficient (IHTC), it is very important to reduce the errors in temperature measurements. Thermocouples must be installed in such a way so that errors are negligible. Investigations were carried out to understand the best way to locate thermocouples in the mold by literature review.

Ideally for permanent moulds, the length of the thermocouple should be situated perpendicular to the isotherms. This configuration reduces the error and allows better flexibility to install thermocouples closer to the interface.

Apart from configuration errors, completely eliminating installation error is very challenging and can be impractical. However, for inverse calculation small errors in temperature measurement could be significant since these could be amplified resulting in large deviations between experimental and simulated results.

Some of the main sources of errors pertaining to temperature data measuring are discussed below.

3.8.2 Manufacturer's uncertainty and calibration

Like any other sensors, commercially available thermocouples are produced with certain manufacturing uncertainties. These errors result from the manufacturing process and assembly of the thermocouples. Commercially available thermocouples come are produced with prefabricated units that can readily installed at the point where temperature measurements are to be made. However manufacturers usually specify the temperature range and percentage of accuracy that the thermocouple could be used. These errors could be avoided by standard calibration techniques [87] as illustrated below.

Thermocouple calibration is generally classified as (i) Calibration at fixed point and (ii) Calibration by comparing to other standard temperature measuring devices such as thermometer or resistance thermometers. In fixed point thermocouple calibration, the

thermocouple reading is compared with the medium of known temperature such as freezing point of water. This method is adopted to calibrate the thermocouples used in the present research.

3.8.3 Data acquisition uncertainties

These are data reduction errors, which include those errors that relates to round-off or to transferring thermocouple voltage outputs to a digital data acquisition system [88]. Briefly, when the thermocouple acquires a voltage values, it compares this to a corresponding predefined thermocouple junction temperature for each voltage values. This is accomplished experimentally by correlating curves for temperature value. These curves are fitted empirically which corresponds to a certain degree of uncertainty associated with them.

3.8.4 Installation error

These are the errors which include uncertainties due to the intrusive nature of the thermocouple installation and distortion at the area where the temperature needs to be measured [89]. Tolerance involved in locating the thermocouple within the solid medium, as well as the heat loss through the thermocouple leads are considered to be important while during installation.

When installing thermocouples within a material, a difference in dimension between the drilled hole and the diameter of the thermocouple results in a gap which causes errors in the measurements being made. In order to avoid this, a filler material is applied between these gaps. Usually a copper paste is filled in the drilled hole before inserting the thermocouple.

3.8.5 Systematic errors for dynamic measurements

A dynamic or transient temperature measurement can be described as the measurement which is collected while the temperature at the sensor location is still varying as a function of time. During transient temperature measurement, the heat flux and the boundary conditions of the medium keeps changing which further adds to the uncertainty of the measurement been made.

3.8.6 Distortion at localized temperature field

As discussed earlier, in order to measure the temperature within a material, a hole needs to be made at a suitable location. This hole however distorts the homogeneity of the material. The presence of cavity within a solid body, whose contents have differing material properties than the surrounding medium, has been shown to induce distortions in a local thermal field around this cavity. This concern is more prominent when transient temperature measurement needs to be collected from medium such as molten aluminium. The presence of a thermocouple could lead to non- homogeneity in the local temperature field within the molten metal [89].

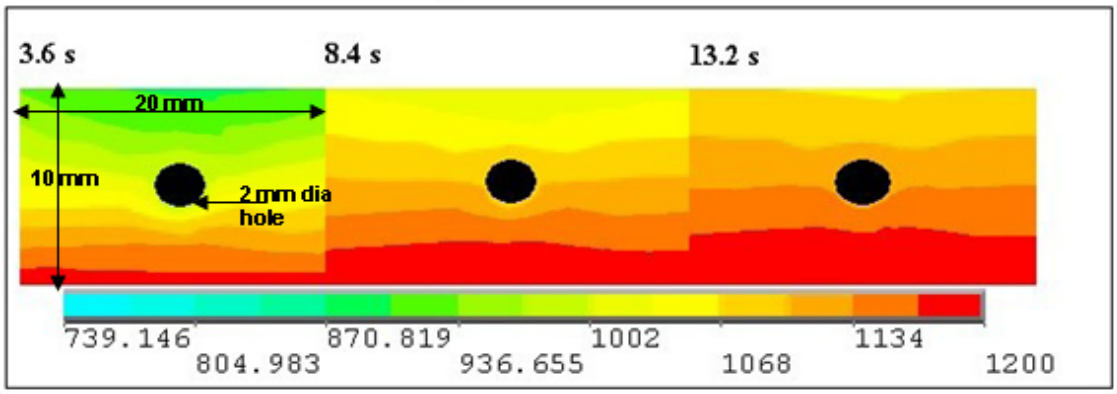

Figure 40: Temperature (˚K) field distortion caused by a thermocouple mounted inside a permanent steel mold [89].

4 Experimental results

4.1 Chilling effect on temperature profile

In trial scenarios C and D (movable chills), the temperature profile shows a rapid step down in temperature whenever the chill is re-engaged (i.e. brought back into contact) with the casting. The temperature profile at some location where the air gap occurs, the temperature gradually increases followed by suddenly drops as shown in Figure 41. This effect is mainly attributed to the displacement of the chill.

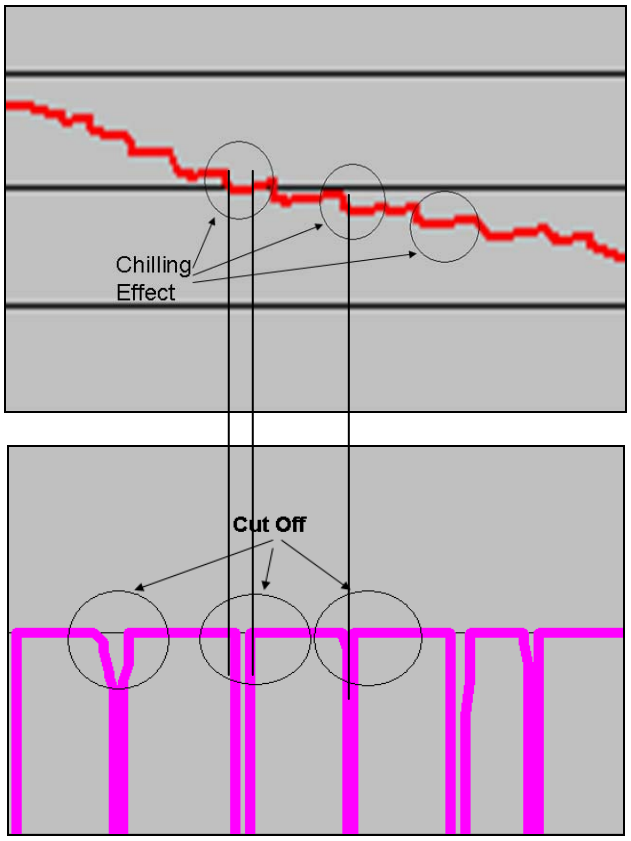

Figure 41: Effect of chill on temperature profile

A direct relationship between the temperature profile and air gap signature can be seen from Figure 41.

4.2 Scenario A: fixed chill without cooling

Figure 42 to Figure 44 shows temperature and air gap profiles of the fixed chill without cooling water supply. Even though most commercially used spot cooling circuits are either water or air cooled, it was important from the current research perspective to compare the effect of the chill without cooling media so as to provide an extreme set of data points and a baseline solidification profile. It is evident from the air gap signature

profiles that the first complete signal "cut-off" between the casting and the chill occurred at 233 seconds, 224 seconds and 230 seconds for trials A1, A2 and A3 respectively. After this period the chill became ineffective in removing the heat from the casting.

The air gap measuring circuit in this experiment only indicates the complete isolation of casting from the chill; however there is a possibility of isolated micro air gap evolution prior to this period since there could be a drop in pressure between the chill and the casting.

Also an effort was made to measure the total air gap between the castings and chill at the end of each scenario an experiment (i.e. after 600 seconds). This was done by moving the chill closer to the casting until the circuit was restored. Hence the total air gaps found at the end of the scenario A trials were 0.9 mm, 0.98 mm and 1.1 mm for trial A1, A2 and A3 respectively.

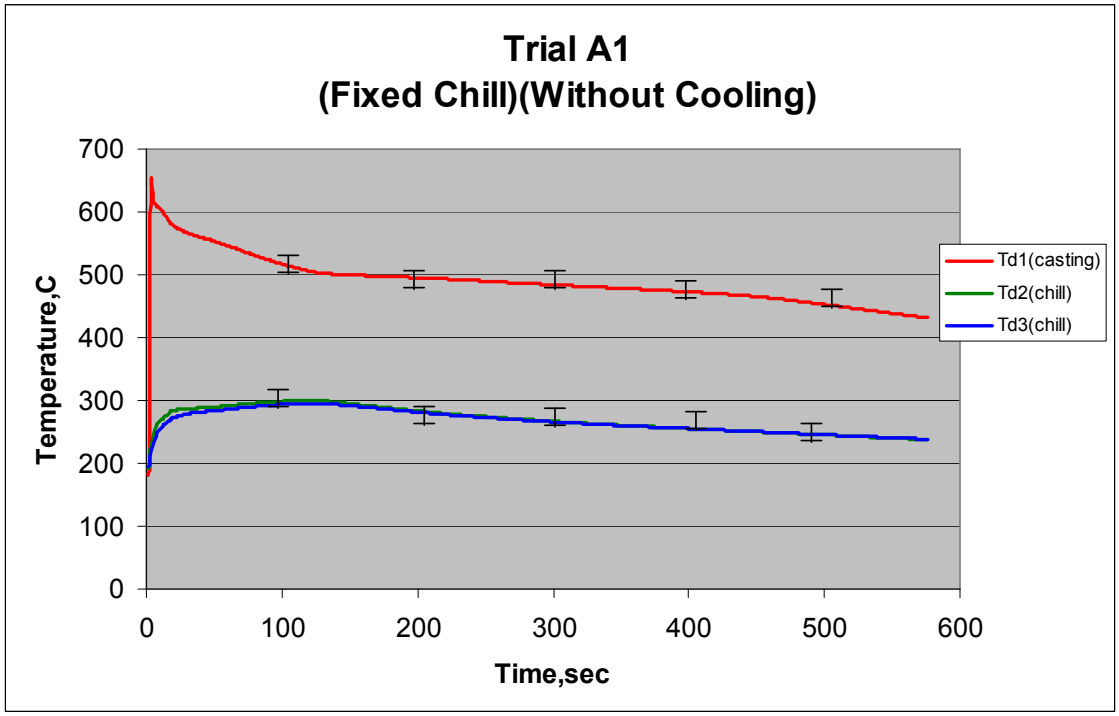

Voltage vs. Time

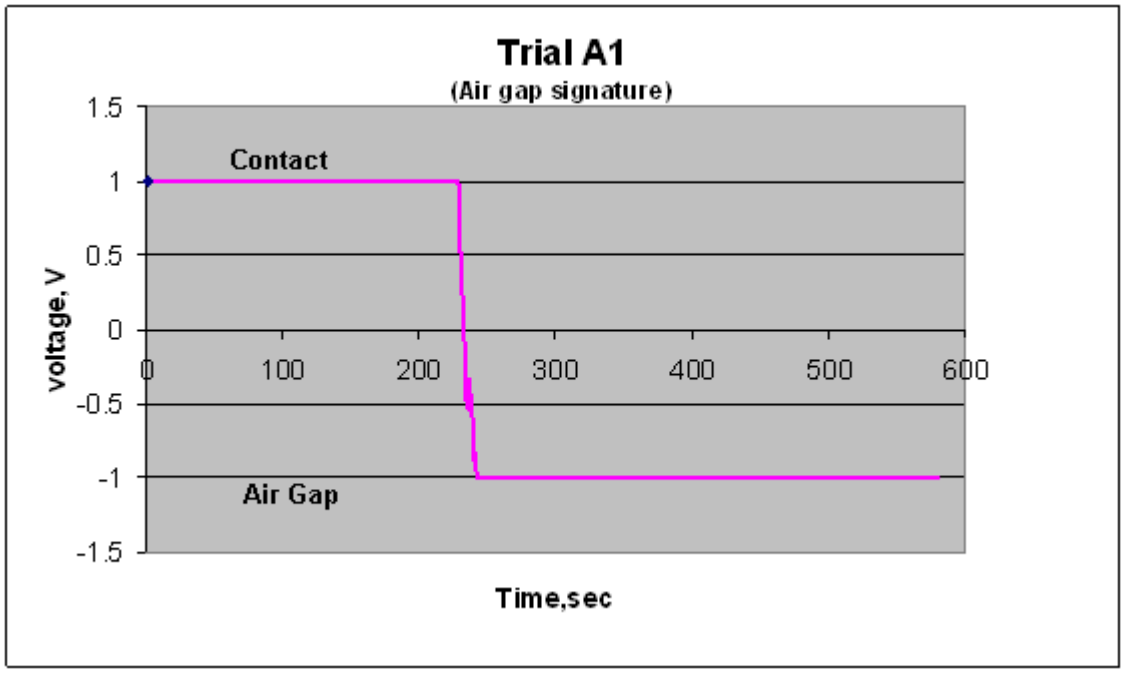

Figure 42: (1) indicates contact and (-1) indicates air gap for Trial A1

Melt Temperature	Initial mold Temp	Initial chill Temp	Total contact of chill with casting	First air gap Cut-off time	Time to reach 540 ˚C	Total Air Gap
652.4˚C	182.3˚C	192.4˚C	40 %	233 sec	67 sec	0.9 mm

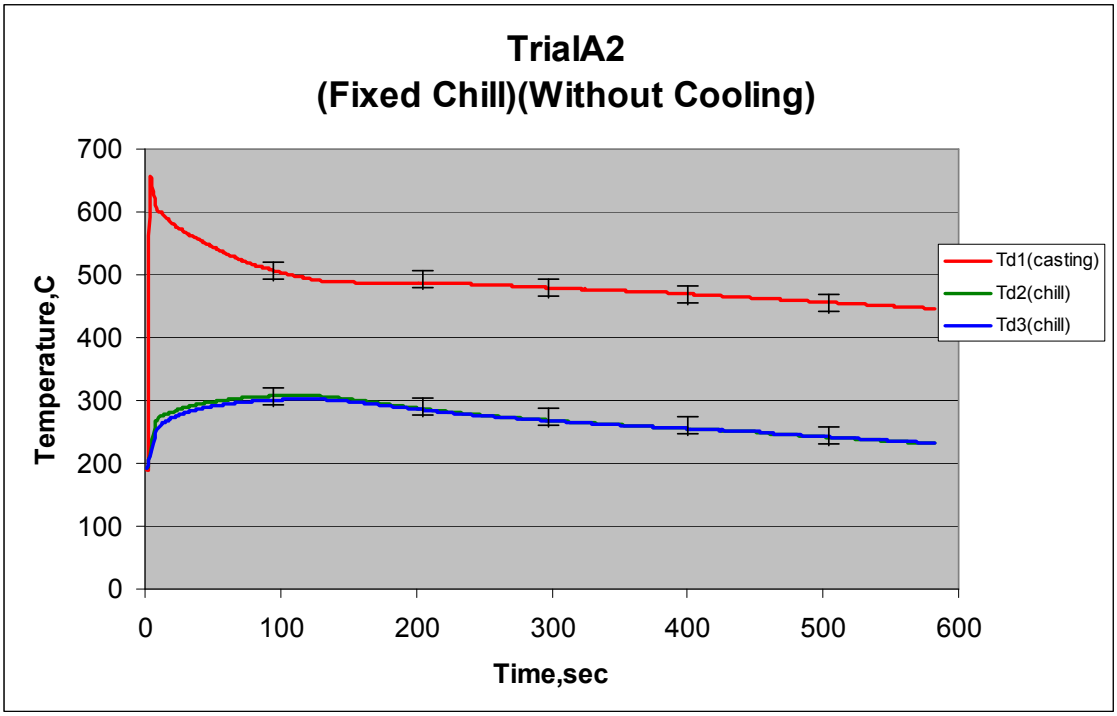

Voltage vs. Time

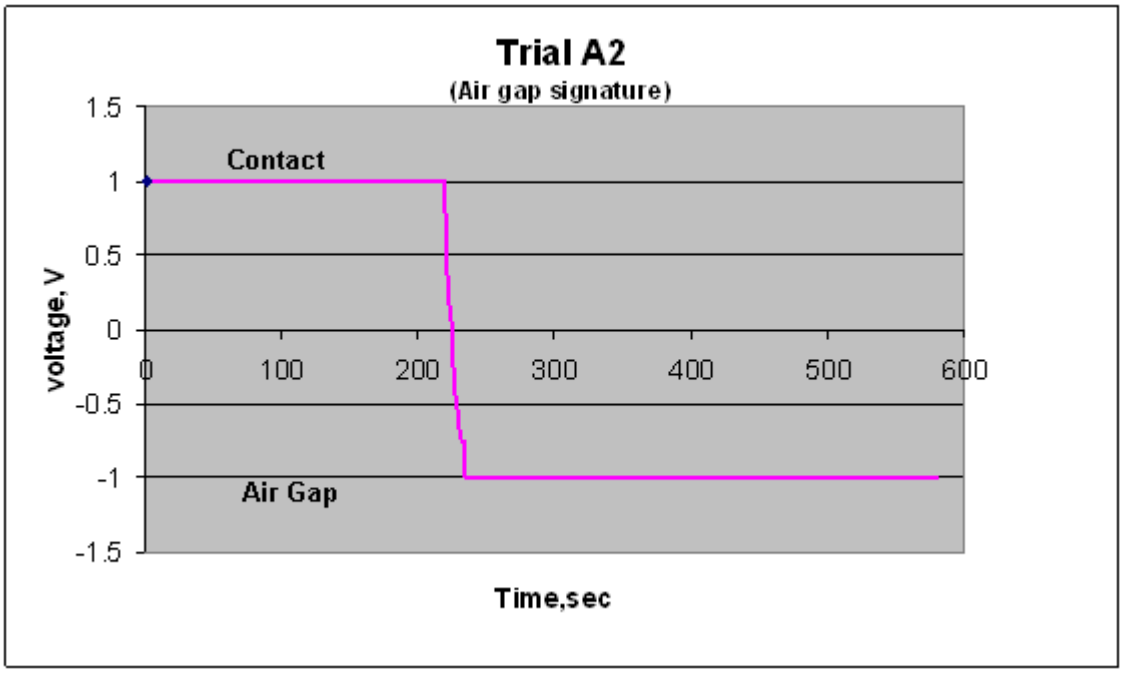

Figure 43: (1) indicates contact and (-1) indicates air gap for Trial A2

Melt Temperature	Initial mold Temp	Initial chill Temp	Total contact of chill with casting	First air gap Cut-off time	Time to reach 540 ˚C	Total Air Gap
653.6˚C	181.4˚C	192.5˚C	38.6 %	224 sec	53 sec	0.9 mm

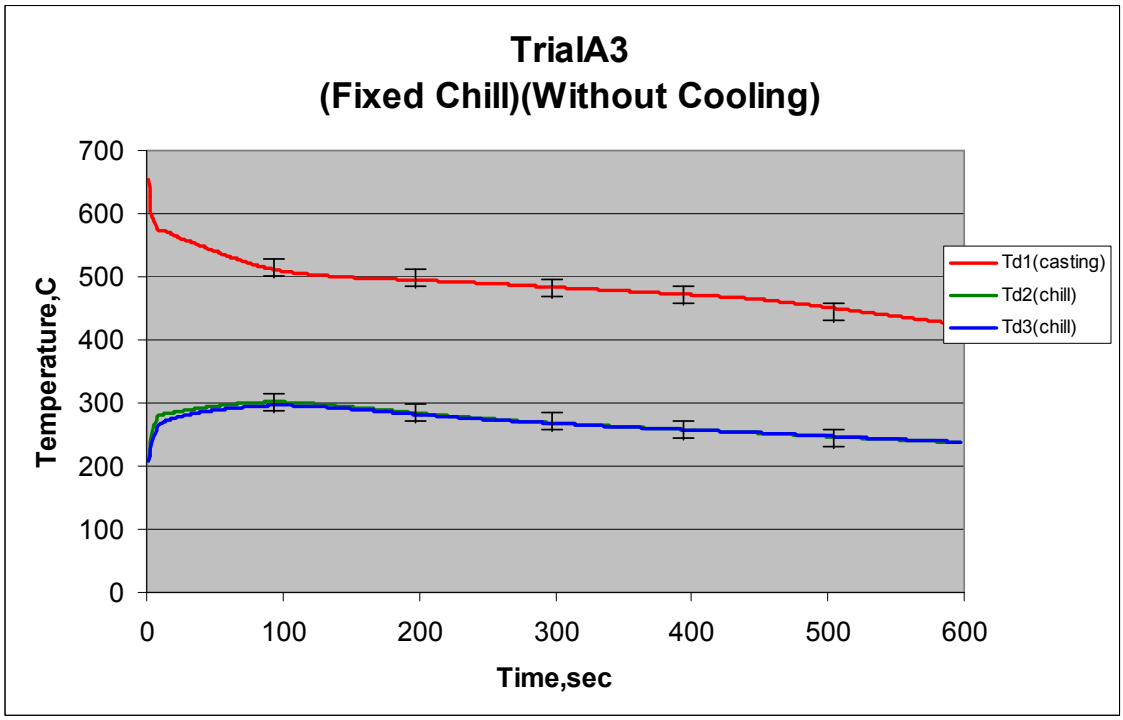

Voltage vs. Time

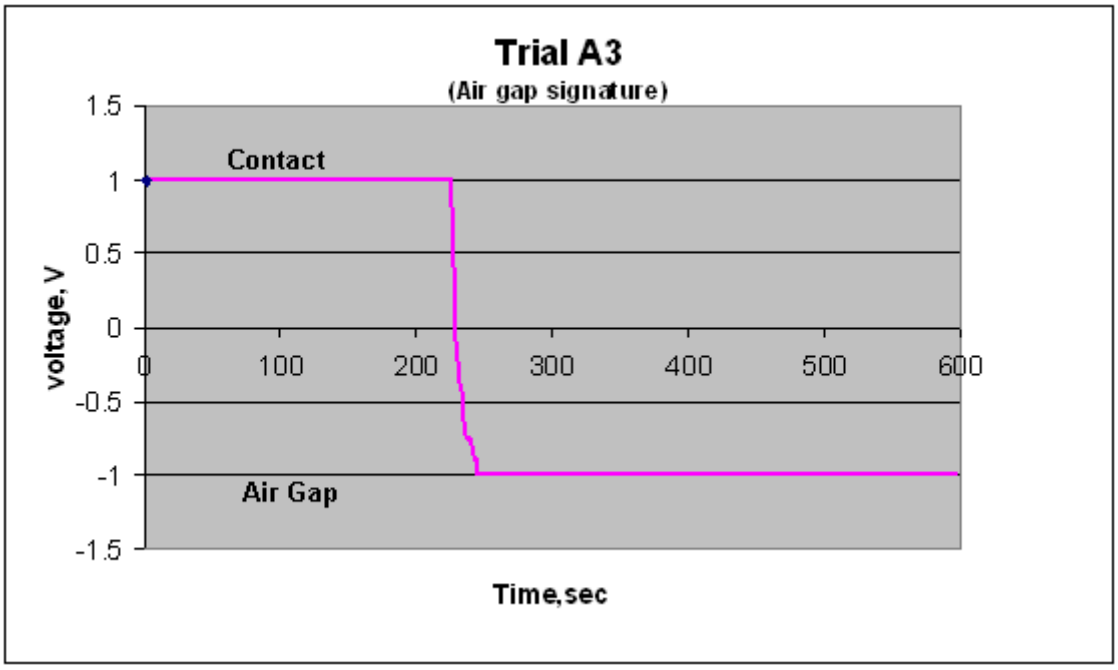

Figure 44: (1) indicates contact and (-1) indicates air gap for Trial A3

Melt Temperature	Initial mold Temp	Initial chill Temp	Total contact of chill with casting	First air gap Cut-off time	Time to reach 540 ˚C	Total Air Gap
654.4˚C	181.6˚C	194.2˚C	38.5 %	229 sec	50 sec	1.1 mm

4.3 Scenario B: fixed chill with cooling)

Figure 45 to Figure 47 show temperature and air gap profiles of a fixed chill with water cooling. Most commercially used spot cooling circuits are provided with either water or air cooling. The main idea of these chills is to extract heat from strategic locations within the casting so that solidification can occur in a desired sequence (see Figure 8). But the chill can become ineffective due to the presence of an air gap. It is evident from the air gap graph that in scenario B, the air gap occurs at 45 seconds, 38 seconds and 46 seconds after pouring in trials B1, B2 and B3 respectively. This is a significantly faster formation of the air gap than observed in scenario A (i.e. between 224-233 seconds). While this may not seem intuitive at first, an explanation is made here that as the molten metal comes into contact with the water cooled chill, a surface layer (skin) of metal freezes instantly and starts to shrink away from the chill. This more rapidly formed air gap makes the remaining solidification inefficient or less than potentially optimum.

Results show that the fixed chill with cooling (scenario B) is less effective than the fixed chill without cooling (scenario A). This observation was also made by Lee, Singh and Chen through changes in shrinkage defects in industrial castings due to the effectiveness of the chill, although the differences were not quantified from an air gap perspective [90]. In scenario B, the air gap isolated the casting from the chill during an earlier stage. The total air gap found at the end of the solidification cycle (i.e. after 600 seconds) was 0.74 mm, 0.93 mm and 0.90 mm for trials B1, B2 and B3 respectively.

4.3.1 Partial Contact

During air gap data acquisition for scenario B the strip chart recorder showed voltage fluctuations when the air gap was occurring. This is because the air gap circuit behaves as a resistance circuit with a variable resistance at the interface. The circuit resistance changes as the metal moves away from the chill as the air gap evolves. However a complete cut-off was recorded nearly after approximately 150 seconds. The temperature profile shows a similar reaction to the air gap signal. Similar phenomena were seen for a number of repeatability and reliability experiments for confirmation.

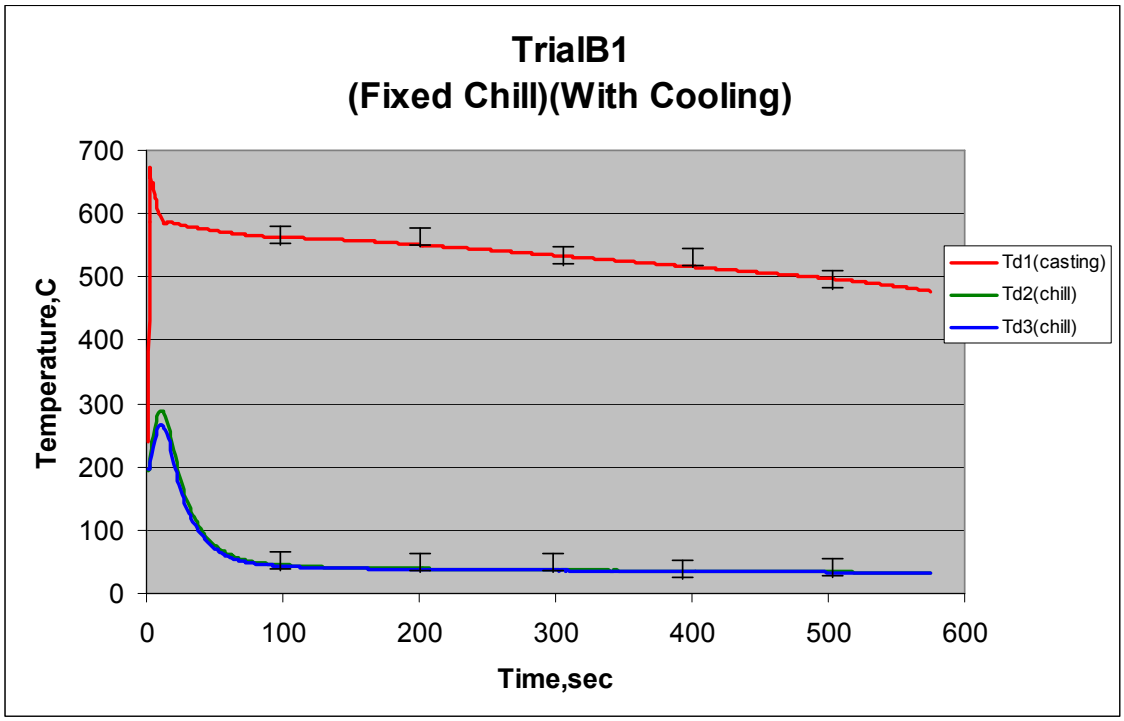

Voltage vs. Time

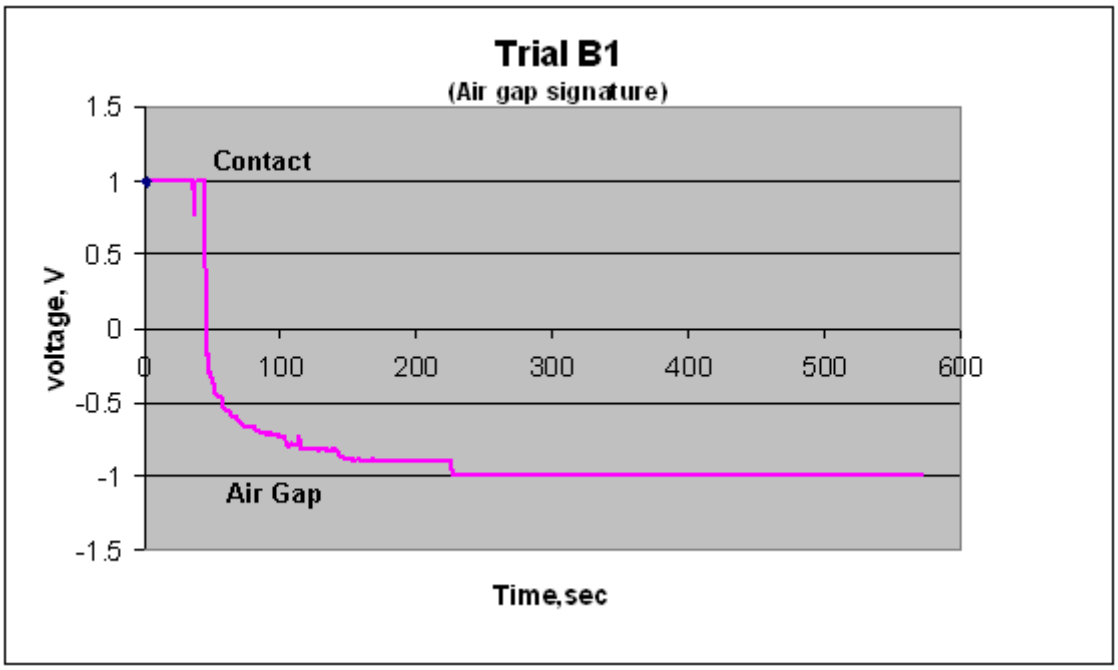

Figure 45: (1) indicates contact and (-1) indicates air gap for Trial B1

Melt Temperature	Initial mold Temp	Initial chill Temp	Total contact of chill with casting	First air gap Cut-off time	Time to reach 540 ˚C	Total Air Gap
669.8˚C	185.7˚C	194.9˚C	7.8 %	45 sec	265 sec	0.7 mm

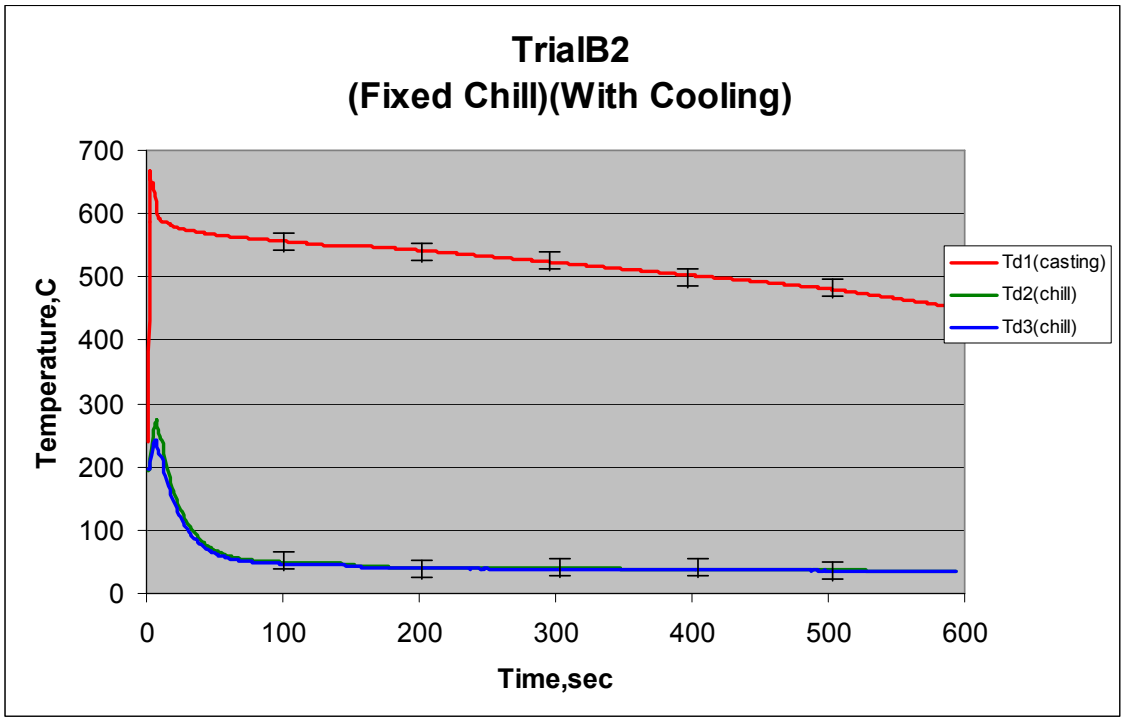

Voltage vs. Time

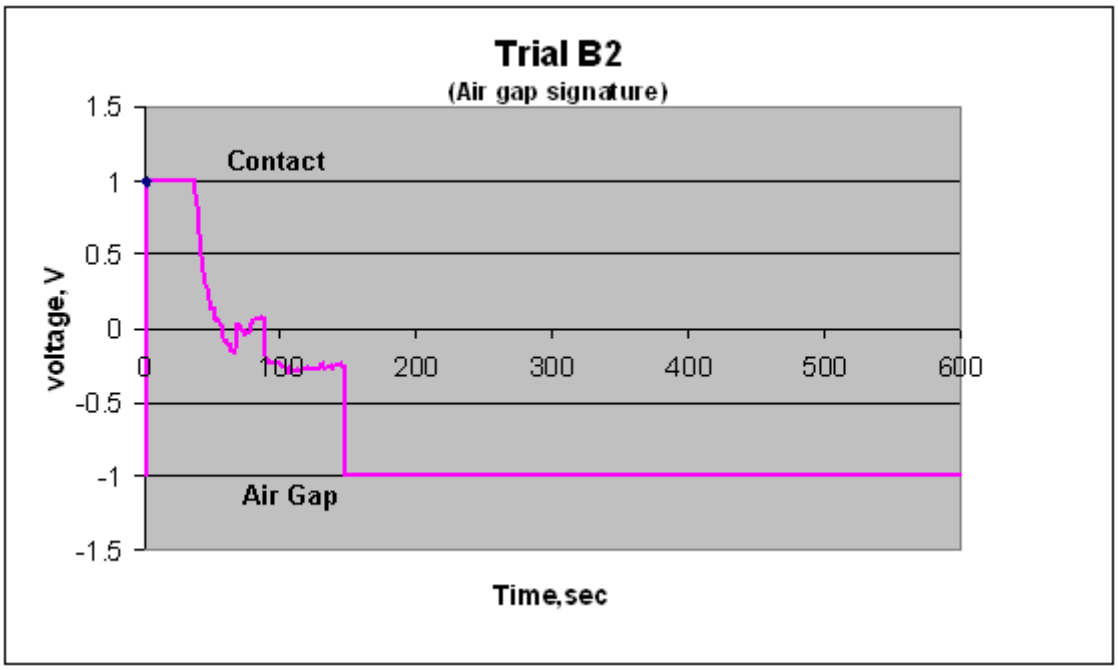

Figure 46: (1) indicates contact and (-1) indicates air gap for Trial B2

Melt Temperature	Initial mold Temp	Initial chill Temp	Total contact of chill with casting	First air gap Cut-off time	Time to reach 540 ˚C	Total Air Gap
665.4˚C	188.3˚C	193.2˚C	6.8 %	38 sec	211 sec	0.9 mm

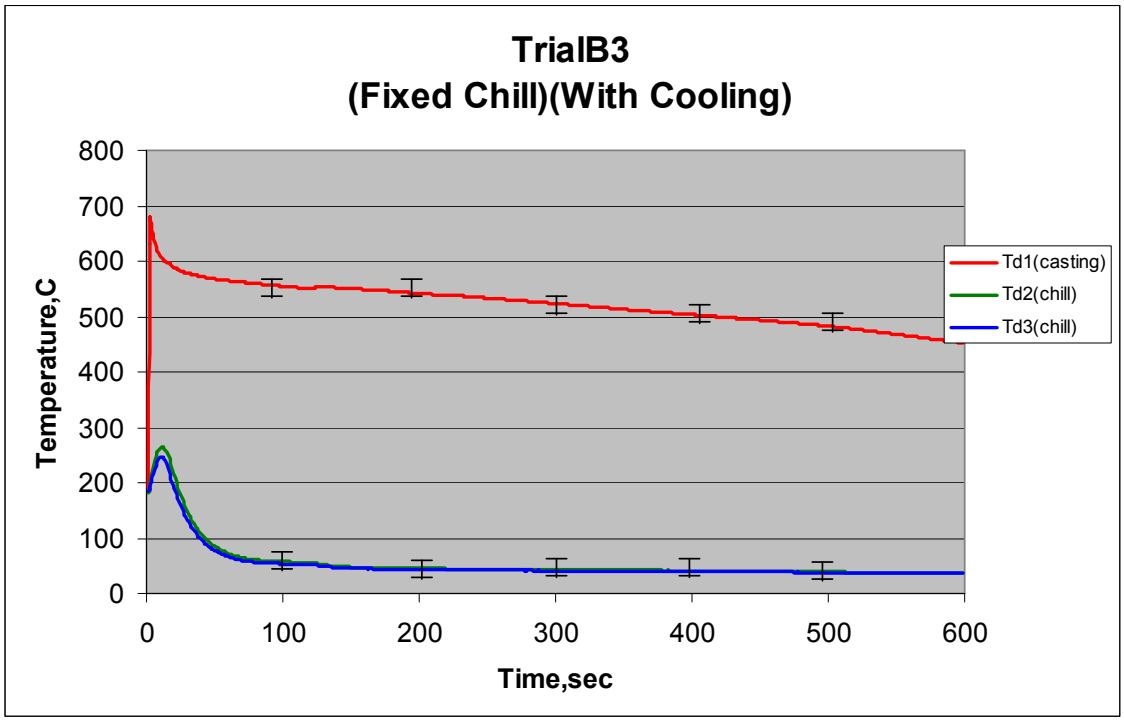

Voltage vs. Time

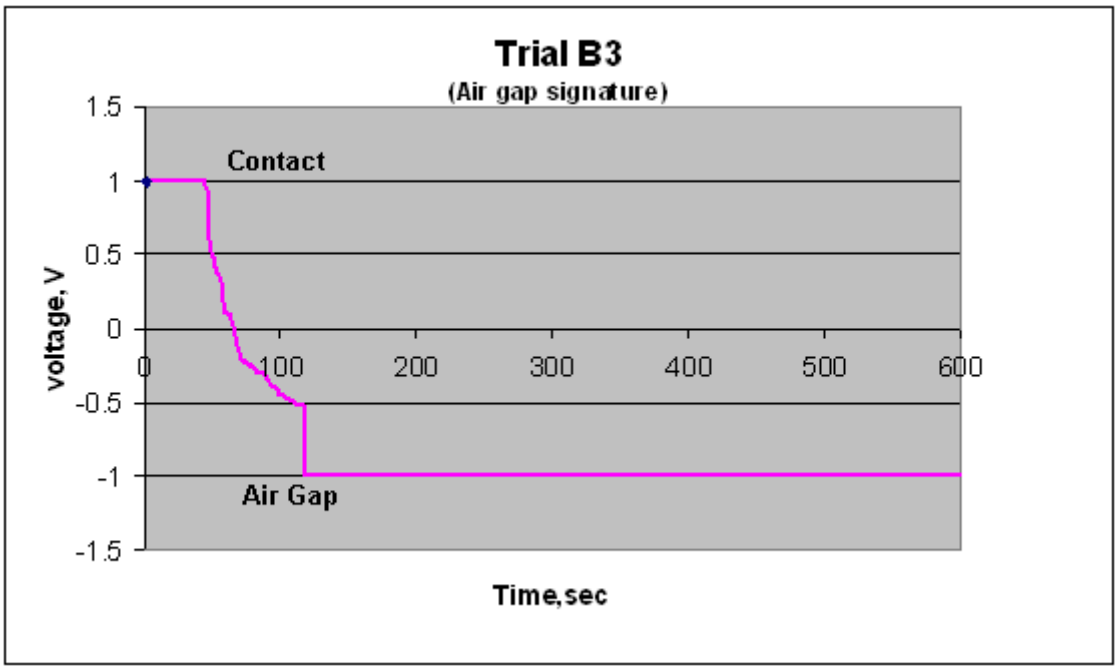

Figure 47: (1) indicates contact and (-1) indicates air gap for Trial B3

Melt Temperature	Initial mold Temp	Initial chill Temp	Total contact of chill with casting	First air gap Cut-off time	Time to reach 540 ˚C	Total Air Gap
679.2˚C	181.3˚C	194.5˚C	16.6%	45 sec	208sec	0.9 mm

4.4 Scenarios C and D - movable chill with cooling

The idea of movable chills is to close the air gap as it evolves. After few initial experiments, it was decided to divide the experimental trials into two different conditions based on displacement.

The principle of movable chills is to close the air gap as it evolves. After few preliminary experiments, it was decided to divide the experimental trials into two different scenarios based on displacement:

- Displacement on demand
- Displacement on eutectic.

4.4.1 Scenario C - movable chills with cooling (displacement on demand)

Figure 48 to Figure 50 shows temperature and air gap profiles of a movable chill with cooling (displacement on demand). In this series of trials the chill was moved forward to maintain contact as the air gap evolved. In other words the chill was pushed forward as the circuit was initially or partially broken.

It is evident from the corresponding air gap graphs that the first cut-off took place at 25 seconds, 22 seconds and 35 seconds for trial C1, C2 and C3 respectively. The faster times were due to the chill being immediately brought into contact with casting to facilitate optimum heat transfer throughout the solidification cycle. The corresponding temperature graphs also reveal high heat extraction rates and rapid losses in temperature in the measured part of the casting. The chill was displaced to 0.9 mm, 1 mm and 1.1 mm for trials C1, C2 and C3 respectively.

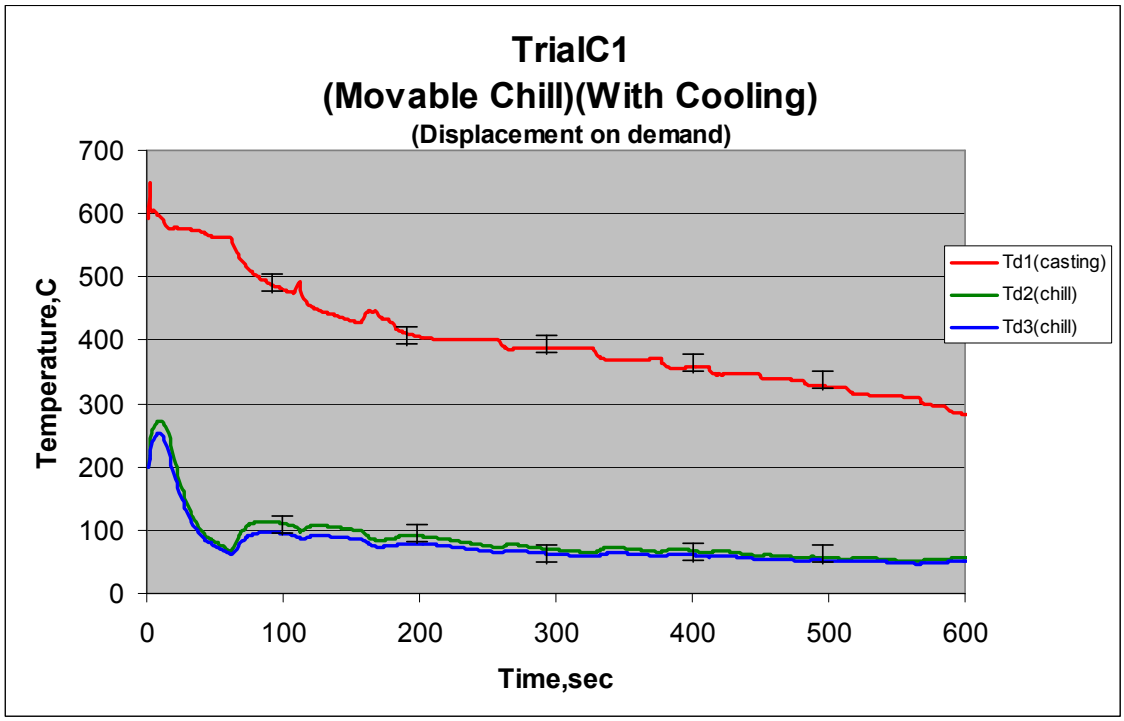

Voltage vs. Time

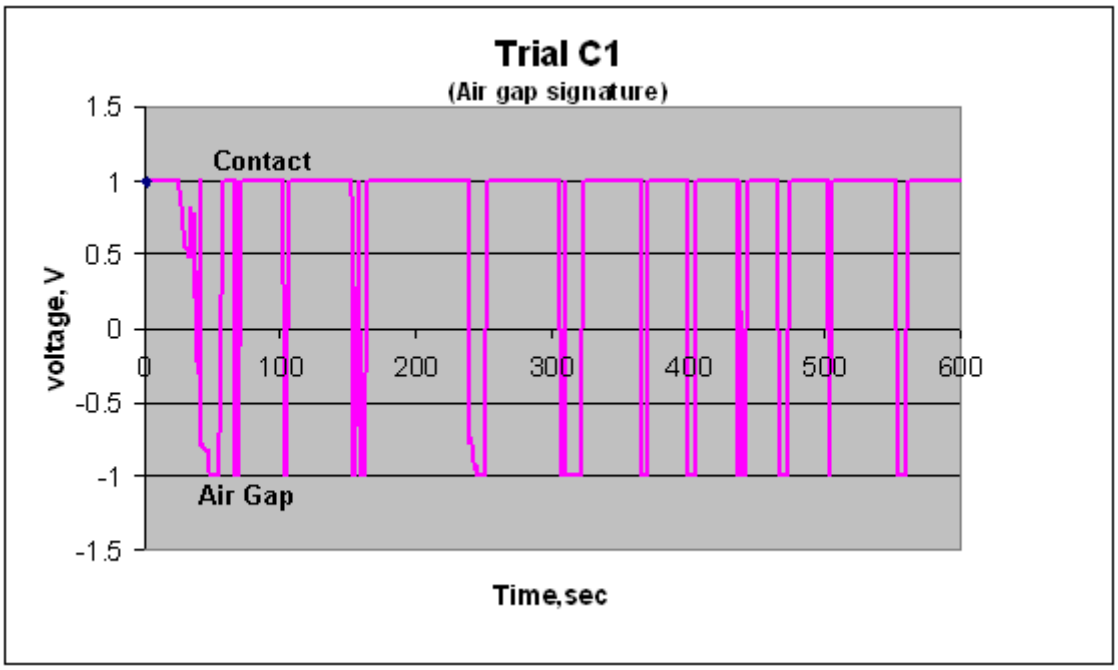

Figure 48: (1) indicates contact and (-1) indicates air gap for Trial C1

Melt Temperature	Initial mold Temp	Initial chill Temp	Total contact of chill with casting	First air gap Cut-off time	Time to reach 540 ˚C	Total chill Displacement
648.2˚C	183.3˚C	191.4˚C	85.6 %	25 sec	65 sec	0.9 mm

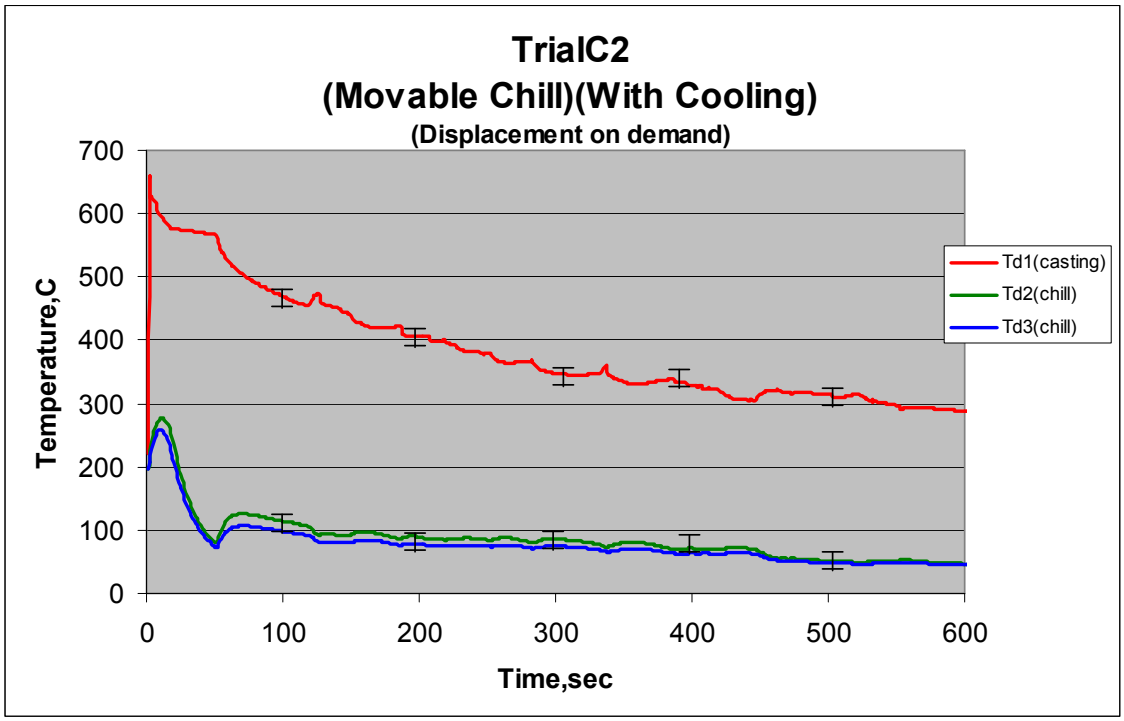

Voltage vs. Time

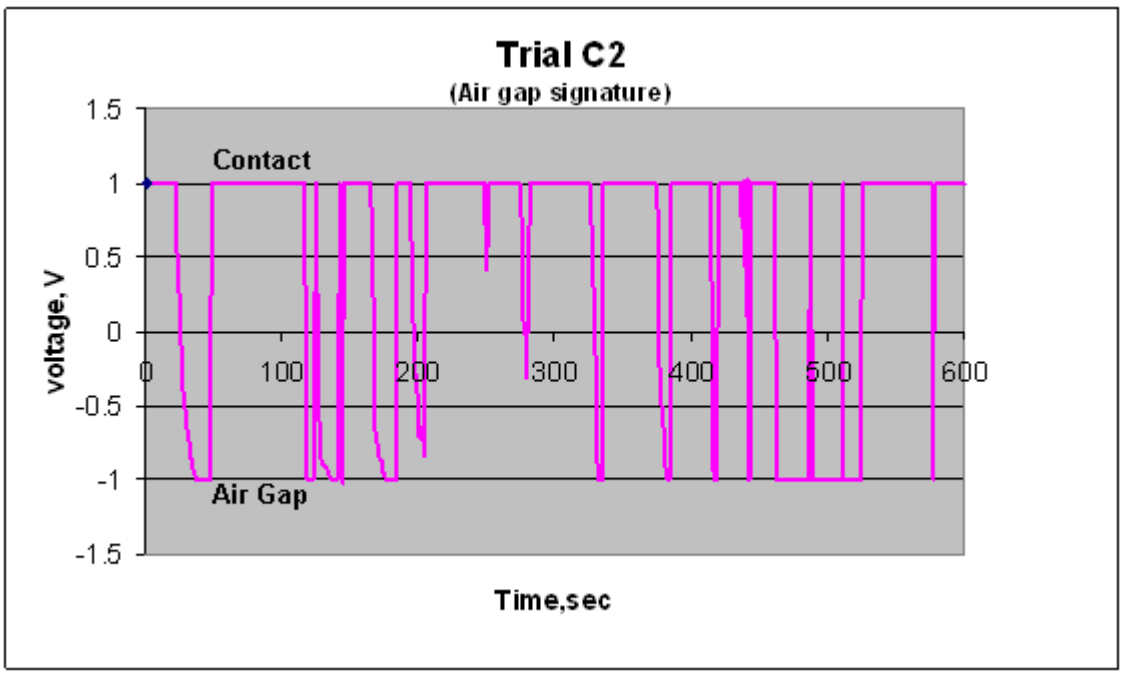

Figure 49: (1) indicates contact and (-1) indicates air gap for Trial C2

Melt Temperature	Initial mold Temp	Initial chill Temp	Total contact of chill with casting	First air gap Cut-off time	Time to reach 540 ˚C	Total chill Displacement
655.2˚C	181.3˚C	192.4˚C	73.1 %	22 sec	54 sec	1 mm

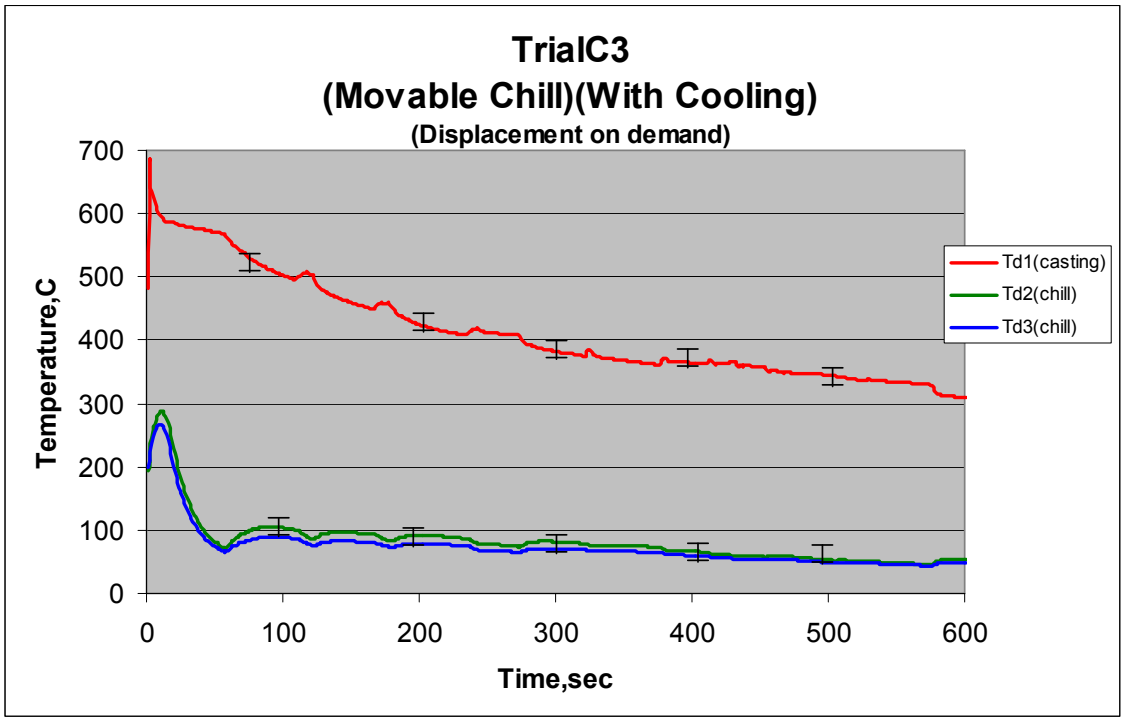

Voltage vs. Time

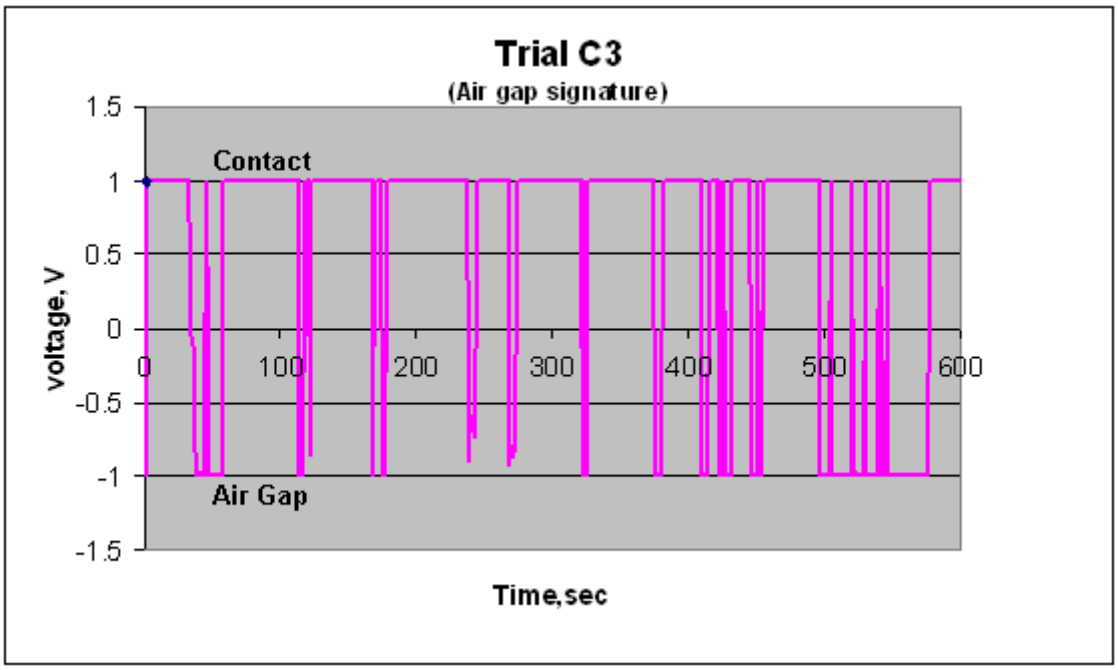

Figure 50: (1) indicates contact and (-1) indicates air gap for Trial C3

Melt Temperature	Initial mold Temp	Initial chill Temp	Total contact of chill with casting	First air gap Cut-off time	Time to reach 540 ˚C	Total chill Displacement
683.4˚C	185.3˚C	193.4˚C	71.8 %	33 sec	70 sec	1.1 mm

4.4.2 Scenario D - movable chills with cooling (displacement before eutectic)

From the literature review it was understood that faster cooling before eutectic temperature could lead to significant improvements in the dendrite arm spacing thereby improving the quality and mechanical properties of the casting. Also in scenario C it was found that the air gap evolves before the eutectic temperature (577˚C) which reduces the heat transfer between the chill and the casting.

To counter this it was decided to give an initial displacement of 0.35 mm before eutectic temperature thereby increasing the heat transfer at this duration. This delayed the evolution of first air gap up to a certain period of time. Also a constant force of 5 N was applied at the end of a chill to maintain a close contact with the chill.

In scenario D trials experiments, the chill was pushed to a total distance of 2.5 mm into the casting to maintain a constant contact. This is due to the fact that the chill was easier to push into the aluminium at plastic state (semi-liquid) before eutectic temperature. It can be seen from the temperature profile that by this method the casting has been cooled at a faster rate compared with the other conditions scenarios.

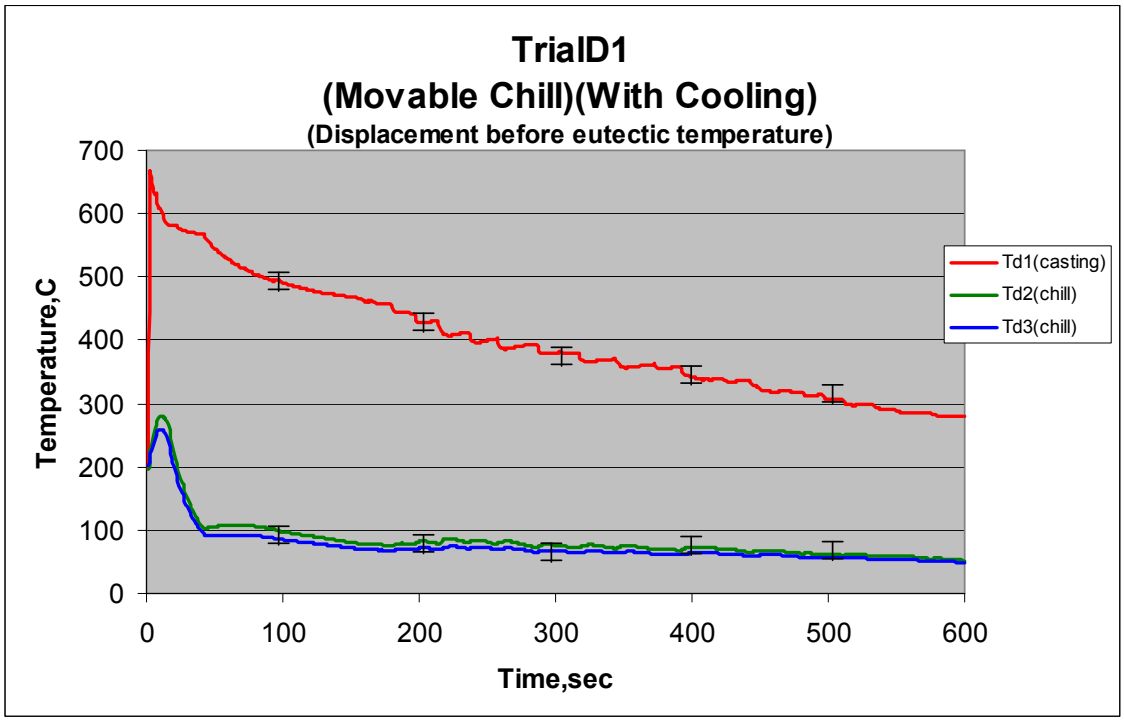

Voltage vs. Time

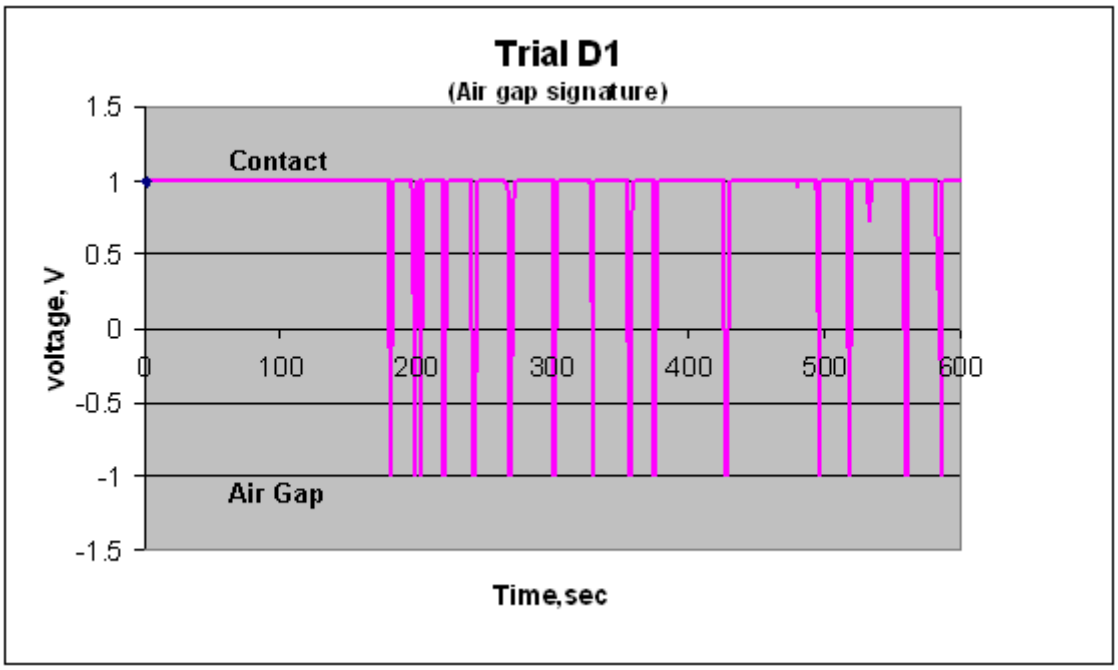

Figure 51: (1) indicates contact and (-1) indicates air gap for Trial D1

Melt Temperature	Initial mold Temp	Initial chill Temp	Total contact of chill with casting	First air gap Cut-off time	Time to reach 540 ˚C	Total chill Displacement
655˚C	184.5˚C	197.3˚C	95.8 %	185 sec	52 sec	2.5 mm

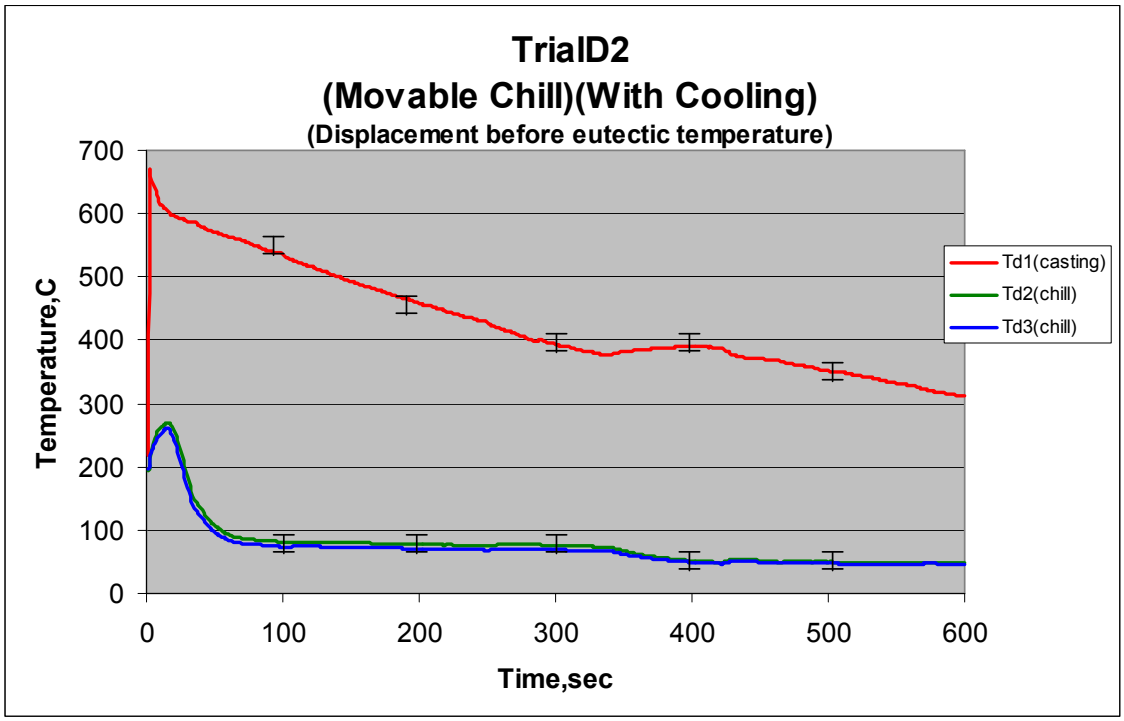

Voltage vs. Time

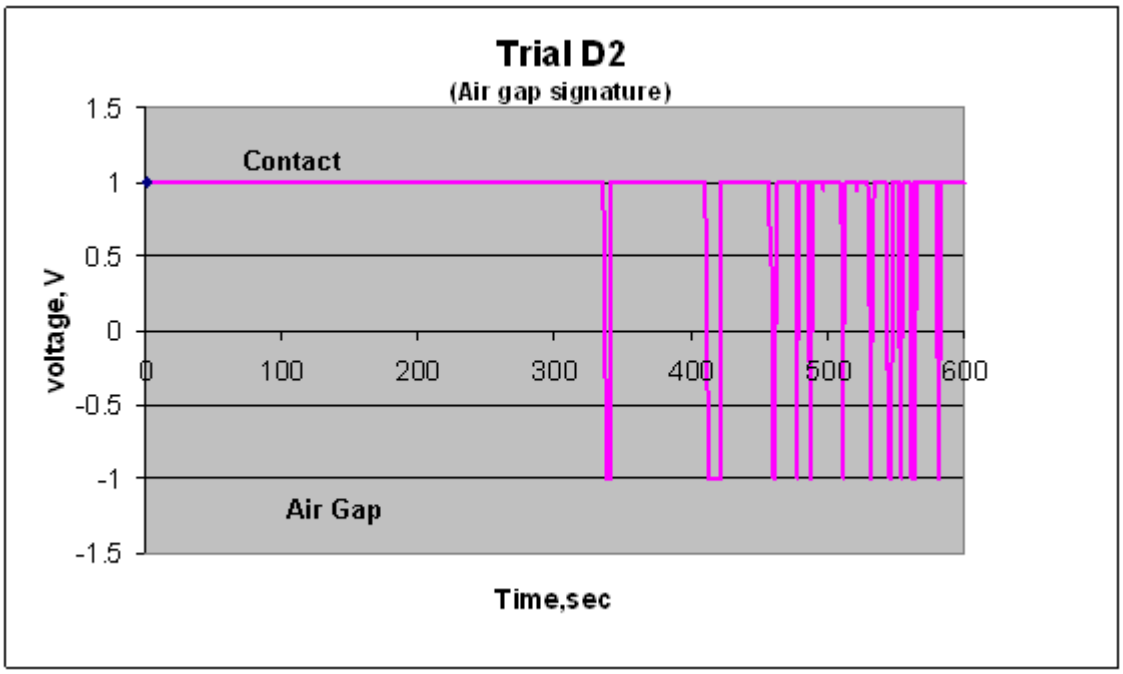

Figure 52: (1) indicates contact and (-1) indicates air gap for Trial D2

Melt Temperature	Initial mold Temp	Initial chill Temp	Total contact of chill with casting	First air gap Cut-off time	Time to reach 540 ˚C	Total chill Displacement
658.2˚C	185.4˚C	191.3˚C	95.3 %	341 sec	90 sec	2.3 mm

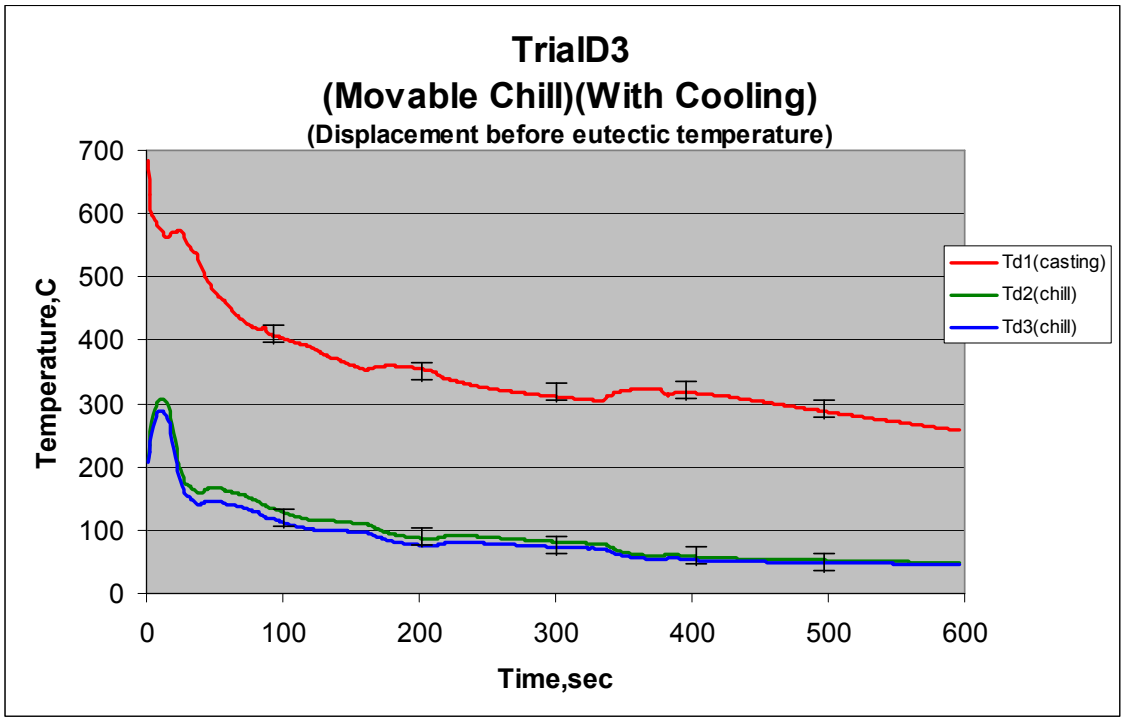

Voltage vs. Time

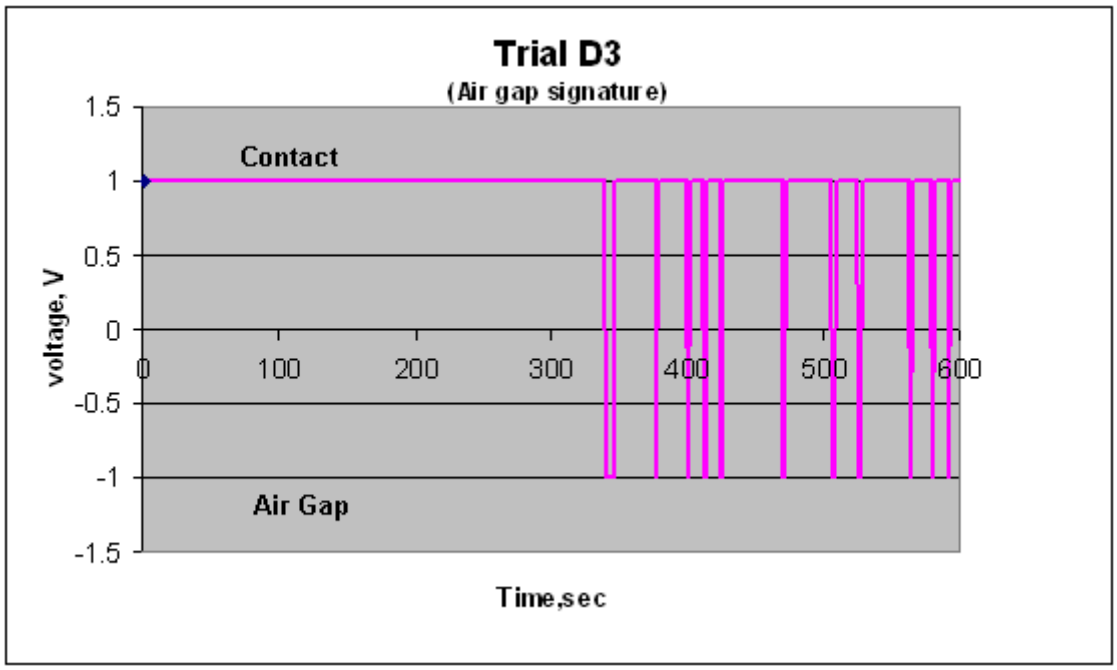

Figure 53: (1) indicates contact and (-1) indicates air gap for Trial D3

Melt Temperature	Initial mold Temp	Initial chill Temp	Total contact of chill with casting	First air gap Cut-off time	Time to reach 540 ˚C	Total chill Displacement
659.3˚C	183.5˚C	193.5˚C	96.1 %	340 sec	35 sec	2.8 mm

4.5 Summary

Experimental trials were carried out by casting an elbow shape in to a ceramic mold water cooled using a copper chill. The casting was allowed to solidify under different chill conditions (fixed and movable). Three thermocouples were located within the chill and casting to record the thermal history of the solidifying casting. An air gap signalling circuit was built which displays and records air gap formation between the chill and casting. The temperature data was related to the corresponding air gap signal and are presented from Figure 42 to Figure 53. Uncertainties associated with the experimental trials are discussed in section 3.8.1.

The below table summarises different experimental scenario;

Trial Id.	Melt Temperature	Initial mold Temp	Initial chill Temp	Total contact of chill with casting	First air gap Cut-off time	Time to reach 540 ˚C	Total Air Gap
Trial A1	**652.4˚C**	**182.3˚C**	**192.4˚C**	**40 %**	**233 sec**	**67 sec**	**0.9 mm**
Trial A2	**653.6˚C**	**181.4˚C**	**192.5˚C**	**38.6 %**	**224 sec**	**53 sec**	**0.9 mm**
Trial A3	**654.4˚C**	**181.6˚C**	**194.2˚C**	**38.5 %**	**229 sec**	**50 sec**	**1.1 mm**
Trial B1	**669.8˚C**	**185.7˚C**	**194.9˚C**	**7.8 %**	**45 sec**	**265 sec**	**0.7 mm**
Trial B2	**665.4˚C**	**188.3˚C**	**193.2˚C**	**6.8 %**	**38 sec**	**211 sec**	**0.9 mm**
Trial B3	**679.2˚C**	**181.3˚C**	**194.5˚C**	**16.6%**	**45 sec**	**208sec**	**0.9 mm**

Trial C1	**648.2˚C**	**183.3˚C**	**191.4˚C**	**85.6 %**	**25 sec**	**65 sec**	**0.9 mm**
Trial C2	**655.2˚C**	**181.3˚C**	**192.4˚C**	**73.1 %**	**22 sec**	**54 sec**	**1 mm**
Trial C3	**683.4˚C**	**185.3˚C**	**193.4˚C**	**71.8 %**	**33 sec**	**70 sec**	**1.1 mm**
Trial D1	**655˚C**	**184.5˚C**	**197.3˚C**	**95.8 %**	**185 sec**	**52 sec**	**2.5 mm**
Trial D2	**658.2˚C**	**185.4˚C**	**191.3˚C**	**95.3 %**	**341 sec**	**90 sec**	**2.3 mm**
Trial D3	**659.3˚C**	**183.5˚C**	**193.5˚C**	**96.1 %**	**340 sec**	**35 sec**	**2.8 mm**

Table 4: Summary of temperature and air gap signal acquisition

5 Computer Simulation

5.1 Model setup

A finite element model was created using ProCAST™ to simulate the solidification process of the casting.

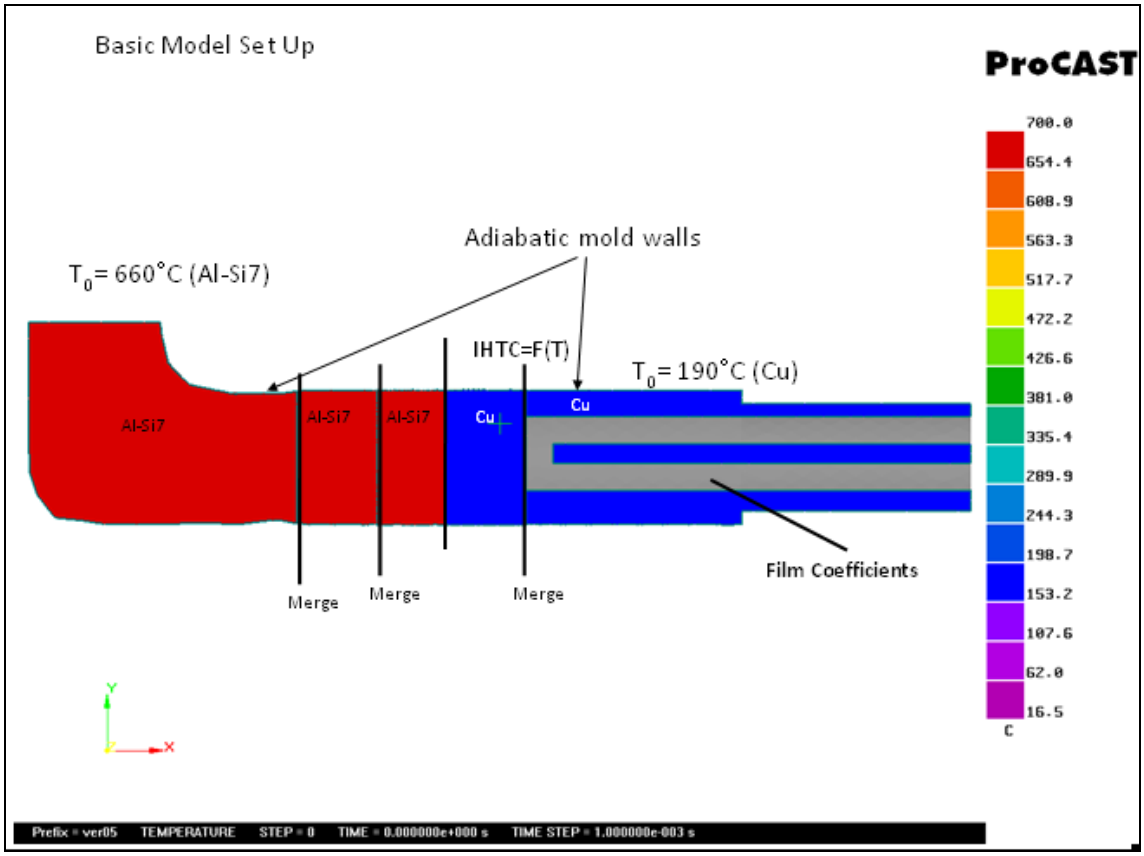

Figure 54: Model setup

The model setup is as shown in the figure above. The initial melt temperature was maintained at 660˚C. Pure copper was chosen as the chill material and was initially set at 190˚C as was measured during the experiments. The mold and chill surface was assigned adiabatic to simulate one dimensional heat flow. The cooling water effect was simulated by assigning a constant film coefficient at the cooling channels (i.e. the effects of film, nucleate and boiling were factored into a single film coefficient value taken from calculations and literature [85]). For initial trials the film coefficient was set to be constant, however, this was later varied to simulate the measured temperature data. A fine mesh density (1 mm) was chosen at the casting-chill interface. The mesh density was also refined to 1 mm size at the thermocouple location to increase the accuracy of

the calculations. However mesh density was coarse (5-8 mm size) for the remaining part of the casting and chill.

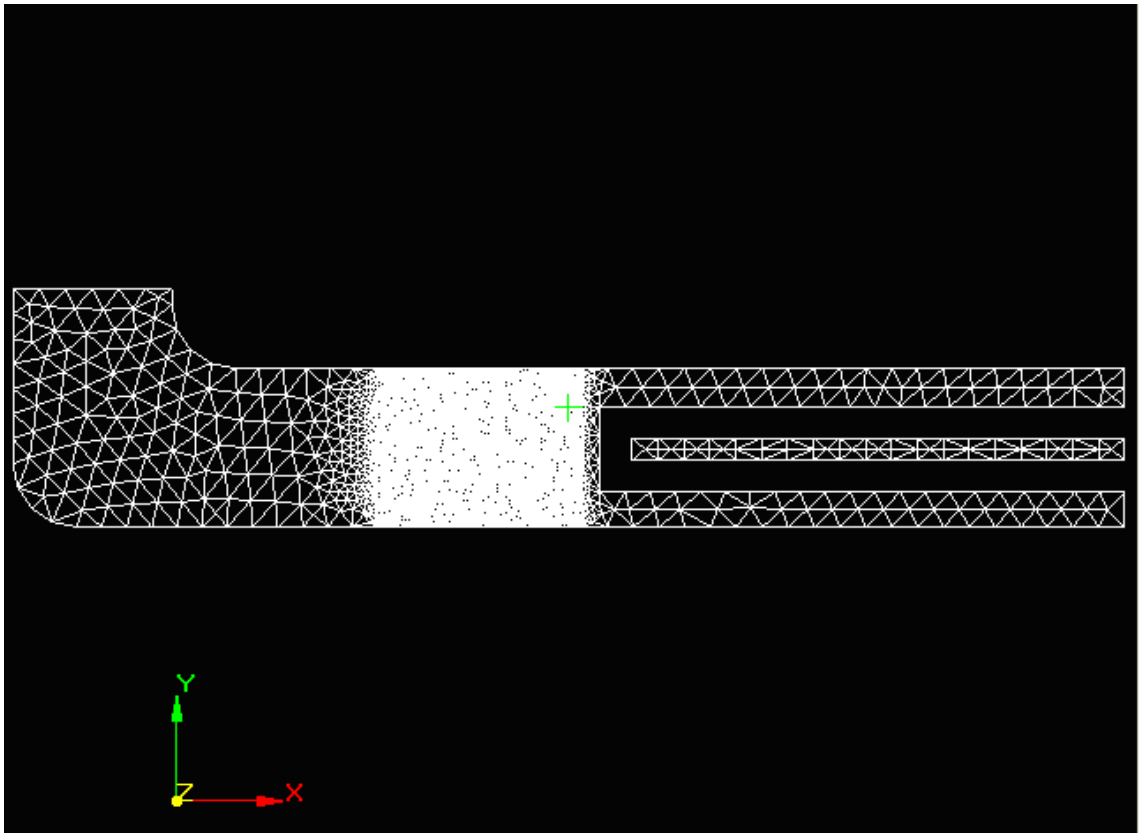

Figure 55: Model mesh setup revealing fine density at the interface and coarser density at the outskirts.

Mesh Data	
Number of Materials	Aluminium A356 and pure copper
Total number of nodes	4565
Total number of Elements	8726
Element type	2D Triangular
Mesh size at interface and thermocouple locations	1 mm
Mesh size at rest of the casting and chill	5-8 mm

Initial Conditions	
Melt Temperature	660˚C
Initial Chill Temperature	190˚C
Mold	Adiabatic

Table 5: Simulation data

5.2 Water cooling and film coefficients

Before numerically calculating the heat transfer coefficients, it is required to determine the effect of cooling water on the chill. Iterations were carried out initially to determine the appropriate film coefficient which could be compared with the measured data. Due to high thermal conductivity of copper the cooling water produces a quenching effect on the chill as shown in Figure 56. As discussed in section 2.6.4, a film boiling approach is used to solve this problem. From the initial iterations it was determined that this effect could be simulated by rapidly increasing the film coefficient from 0 to 8000 W/m^2K for a small fraction of time as shown in Figure 57. However the film coefficient was maintained constant of 8000 W/m^2K for the remaining period.

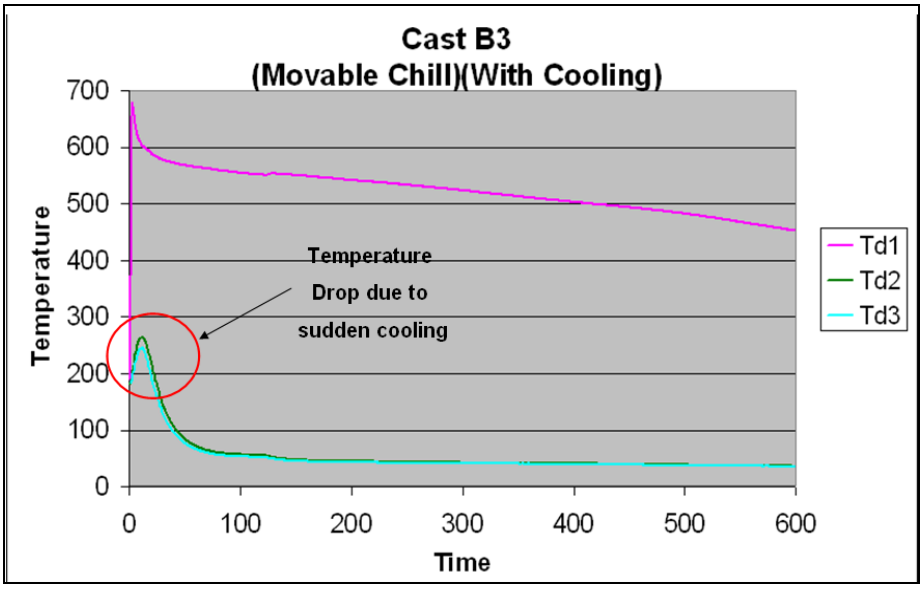

Figure 56: Quenching effect at the copper chill

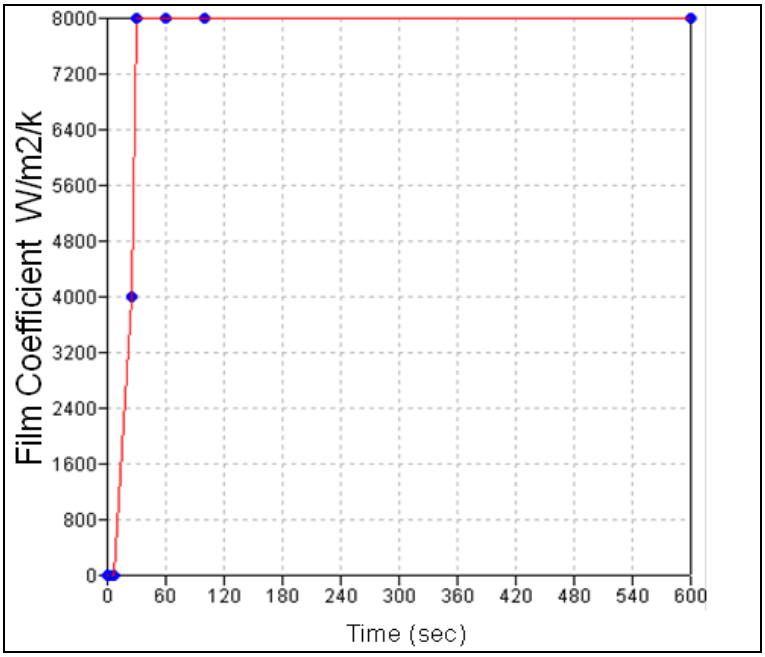

Figure 57: Film coefficient for water cooling

Two nodes 1502 and 3954 were selected at a distance of 5 mm from the interface as in the experiment. These nodes were closest to the thermocouples Td1 and Td2.

5.3 Solidification simulation

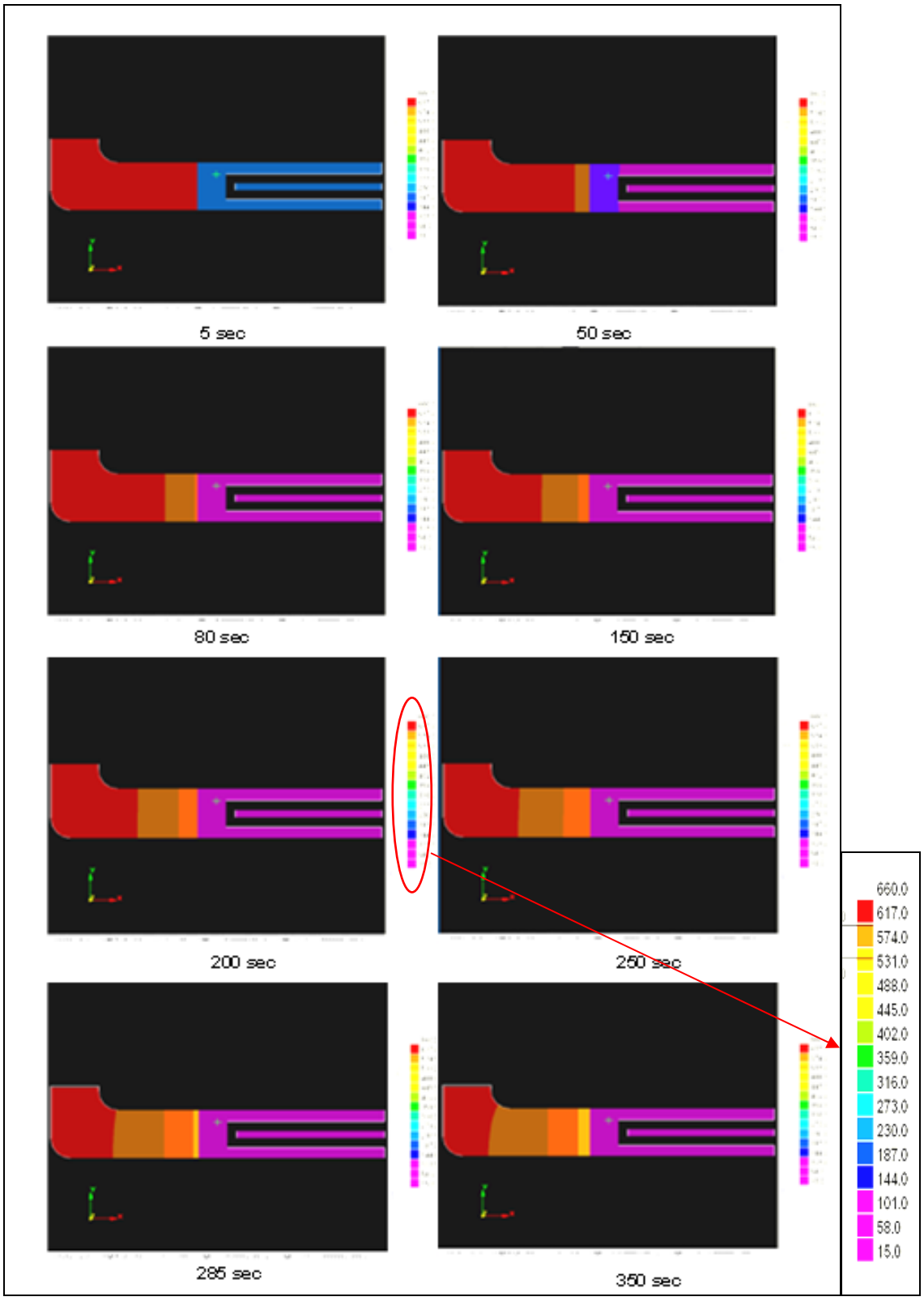

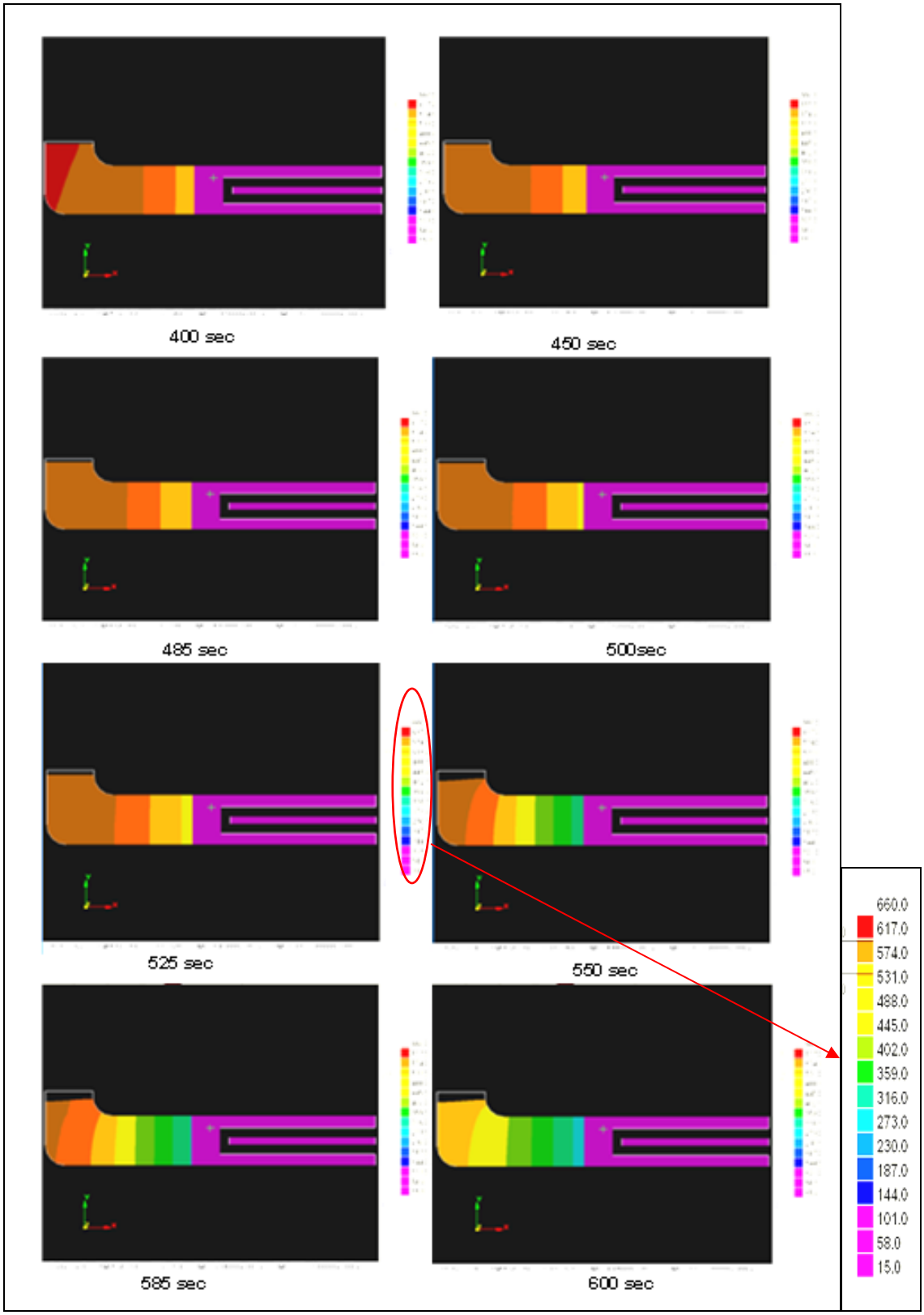

Figure 58: Simulation was performed for 600 seconds

5.4 Model adjustment by ProCAST™ inverse optimization

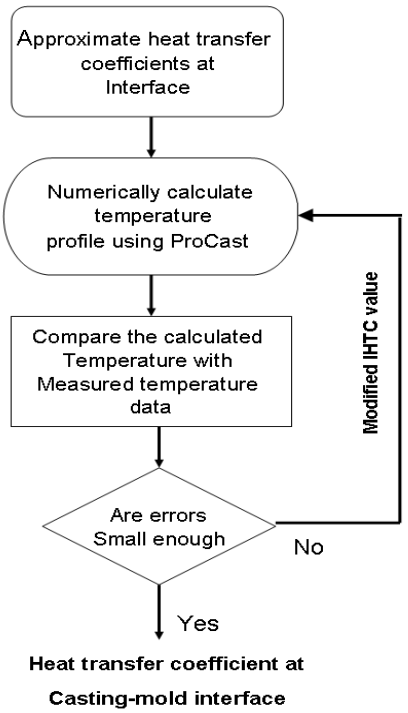

Figure 59: Flow chart showing simulation methodology

Heat transfer coefficients were calculated by an inverse analysis approach. An initial heat transfer coefficient was guessed at the interface to calculate the temperature profile at nodes 1502 and 3954 (representing thermocouples Td1 and Td2 respectively). These calculated temperature profiles were then compared with experimentally measured temperature profiles as shown in Figure 62. Heat transfer coefficients with respect to time and temperature were appropriately adjusted to obtain a close match between the experimental and simulated temperature curve. Several iterations were performed to obtain a close match between the calculated model data and the experimental data.

The initial heat transfer coefficient was chosen from preliminary modelling and by using a trial and error approach. Although heat transfer between the casting and the chill depends on several parameters, temperature was considered as a dominant variable. The objective function for optimisation was defined as;

$$F(x) = \sum_{j=1}^{M} \sum_{i=1}^{N} (T_{i,j}^{\text{model}} - T_{i,j}^{\text{experimental}})^2 \qquad \textbf{5.4.1}$$

Where $T_{i,j}^{model}$ and $T_{i,j}^{experimental}$ are the measured and experimental temperature at the jth time step for the ith thermocouple. Iterations were performed to minimise f(x).

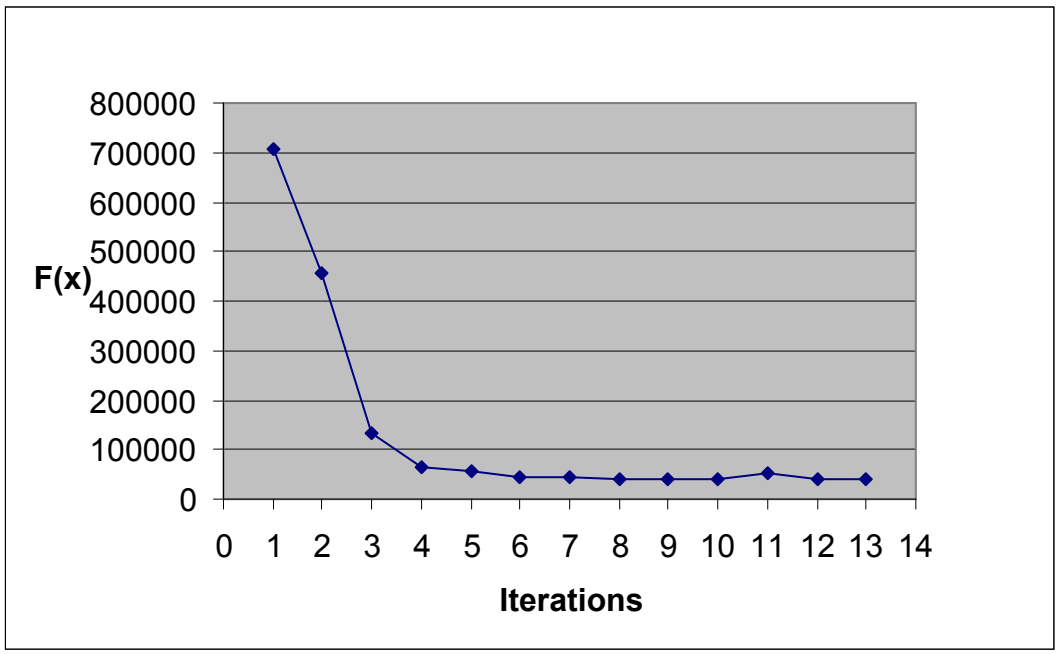

Figure 60: History of the objective function used to determine a set of heat transfer coefficients.

The simulated temperature curves were shifted by varying the time based heat transfer coefficients as shown in Figure 61. The heat transfer coefficients at which the objective function was minimum was chosen as the defining heat transfer at the interface. The optimisation problem was constrained by ensuring that the design variable were monotonic (i.e. decrease in heat transfer coefficient with decreasing temperature). This constrain can be mathematically represented as;

$$G_k(x) = h(T_k) - h(T_{k+1}) \leq 0 \qquad \textbf{5.4.2}$$

where *k* is a counter ranging from 1 to the number of discrete points in the HTC curve. In this special case, *k* was also used to identify the constraint number. This particular type of constraint was enforced to represent the decrease in heat transfer with decreasing temperature at the interface, due to air gap formation between the casting and chill during solidification.

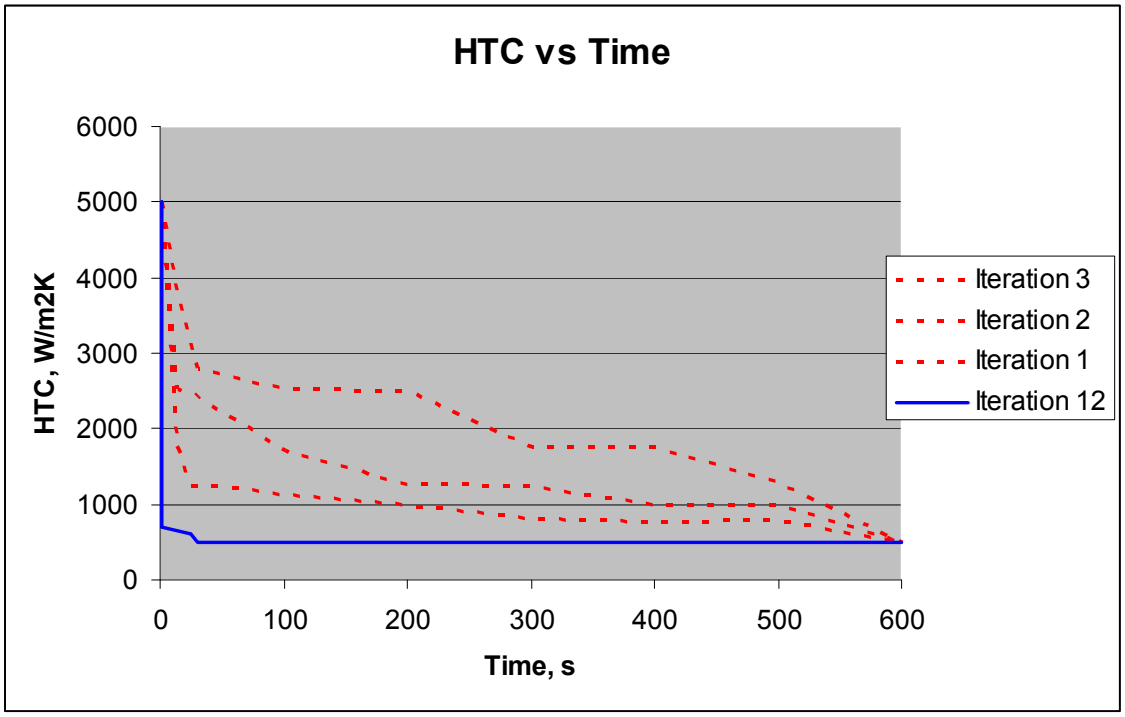

Figure 61: Variation of IHTCs to fit the experimental temperature profile

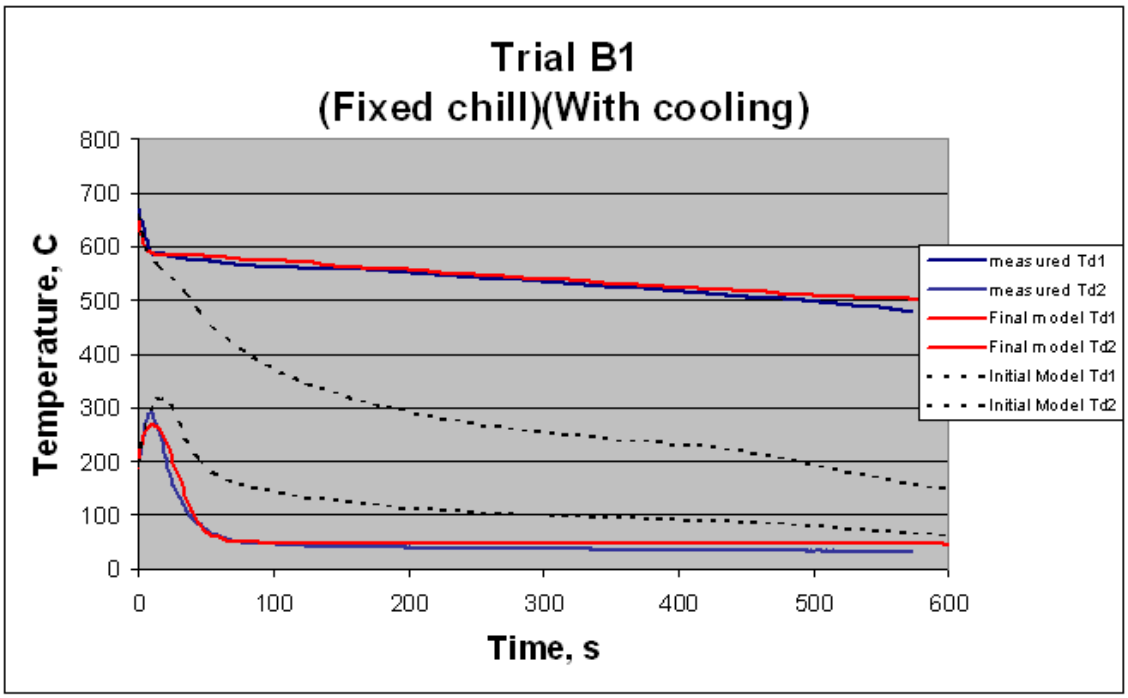

Figure 62: Variation of cooling curves with changes in IHTCs

5.5 Simulation results and discussion

The heat transfer coefficients were obtained and were plotted against time. The heat transfer values which gave the best fit between the measured and calculated data were chosen as the heat transfer coefficient at the interface. Simulation was performed on all

the 12 casting samples (i.e. four scenarios with three repeated trials each) and is presented below.

In this section the effect of different chill conditions on heat transfer is discussed. In this research heat transfer simulations are used as a tool to show the effectiveness of movable chills compare to other chill conditions. For scenarios A and B, an average temperature graph taken from each of the three experiments respectively was chosen for curve matching. Subsequently, optimisation of heat transfer was performed based on the averaged temperatures to calculate time based heat transfer coefficients.

5.5.1 Effect of fixed chill without cooling on heat transfer (Scenario A)

In this scenario, the heat transfer coefficient commences at 5000 W/m²K due to full initial contact between the chill and molten metal, but then decreases as the casting solidifies. In this case, the heat transfer coefficient decreases after the first cut-off (i.e. approximately 230 seconds). In other words the heat transfer rate decreases after the air gap is formed. This indicates that the chill is inefficient for remaining duration of solidification.

Measured vs. Simulated temperature data

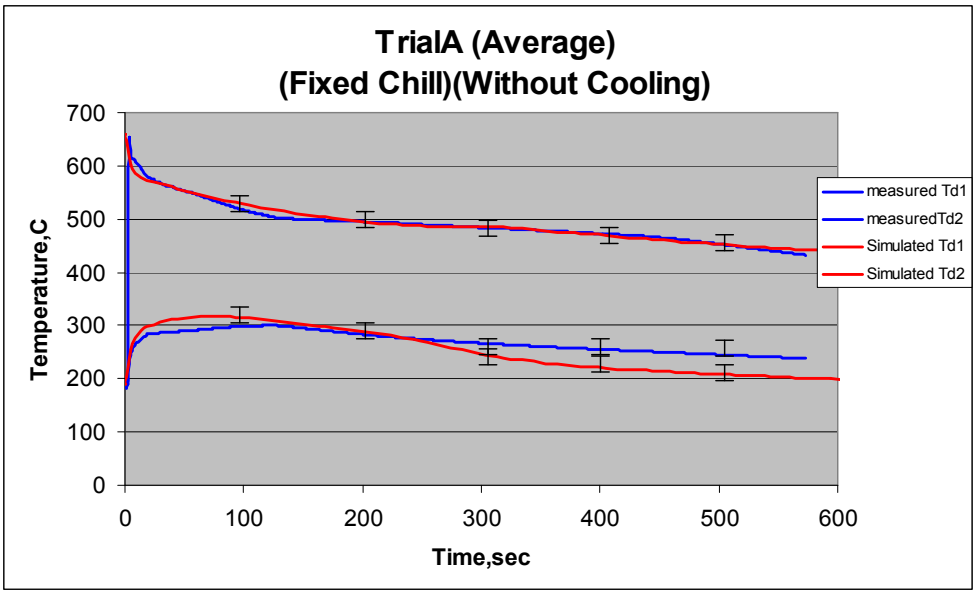

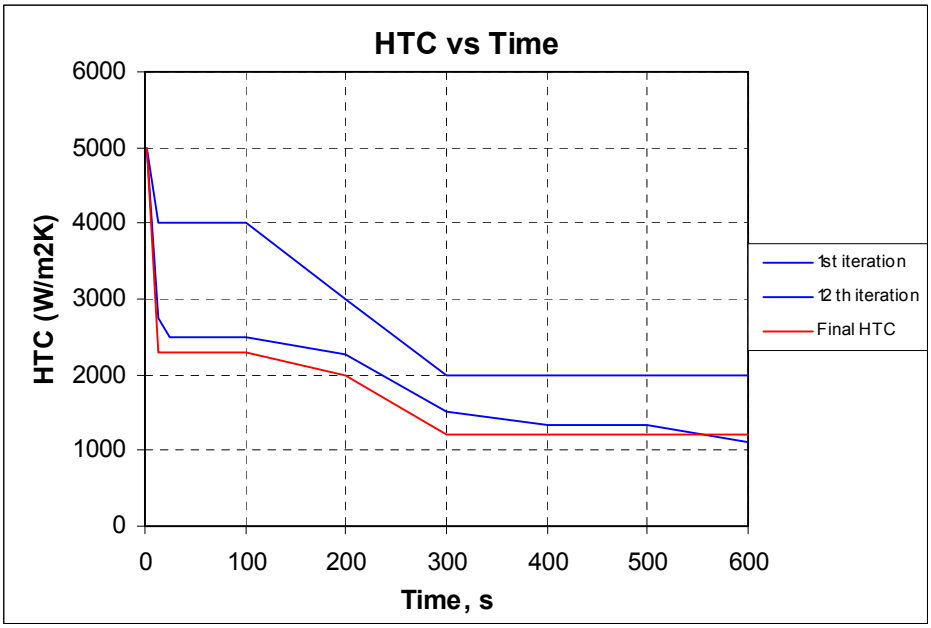

Figure 63: ProCast calculated heat transfer coefficients for trial A_Average

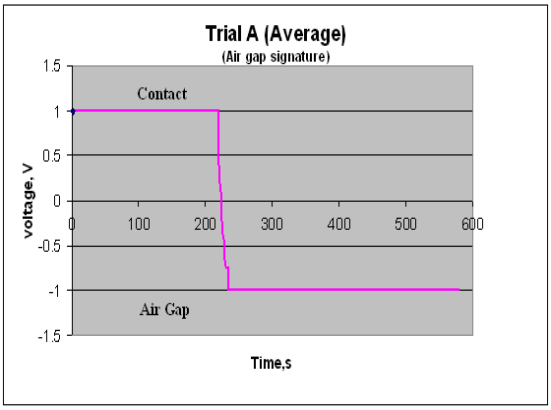

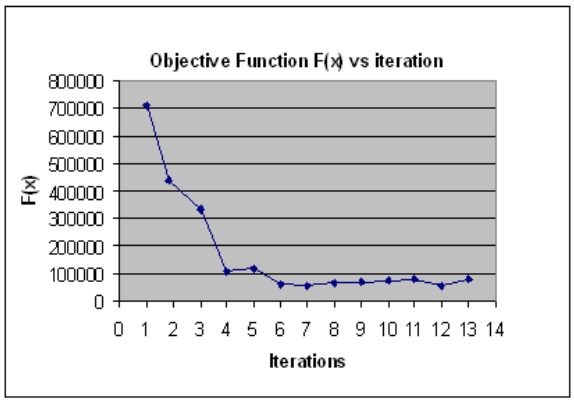

5.5.2 Effect of fixed chill with cooling on heat transfer (Scenario B)

Similar to the previous case the heat transfer coefficient begins at 5000 W/m²K but decreases suddenly after the air gap is formed (i.e. after 30 seconds of pouring). The heat transfer coefficient is lowered to 500 W/m²K. The overall interfacial heat transfer in this chill condition is less than scenario A trials. This confirms previous discussions about an instant surface layer (skin) forming at the chill interface, thus enabling natural shrinkage to occur in the casting earlier than in scenario A with no cooling.

Measured vs. Simulated temperature data

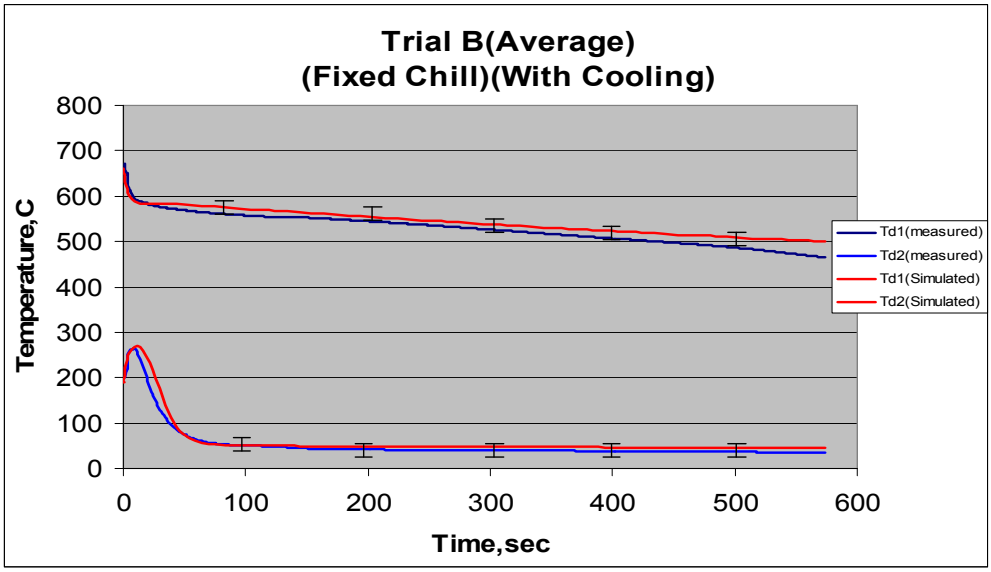

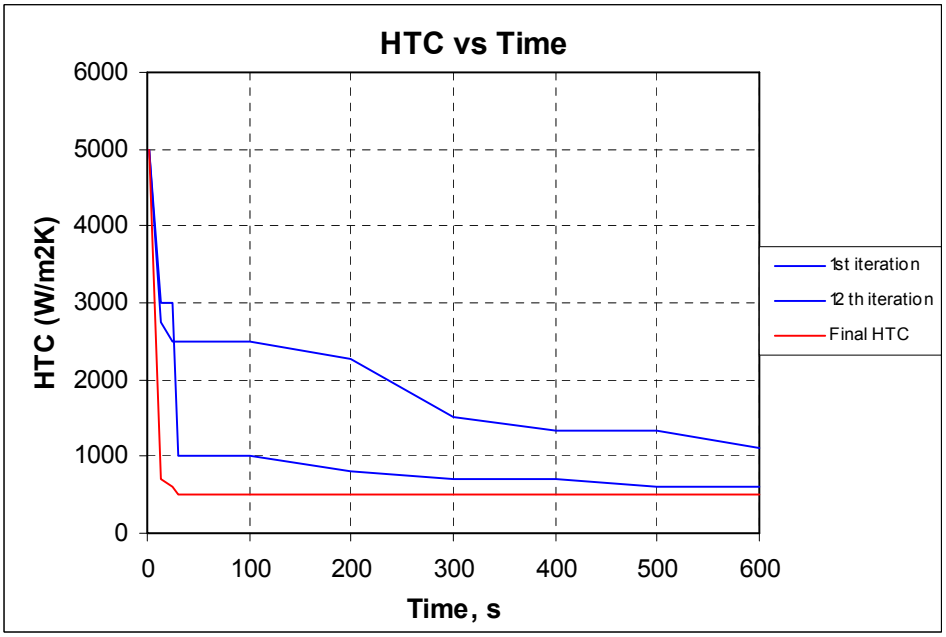

Figure 64: Procast calculated heat transfer coefficient for trial B_Average

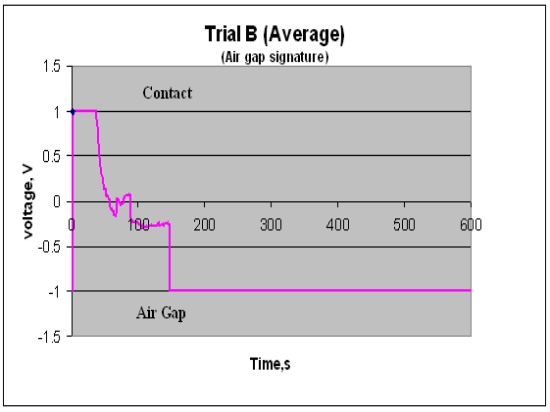

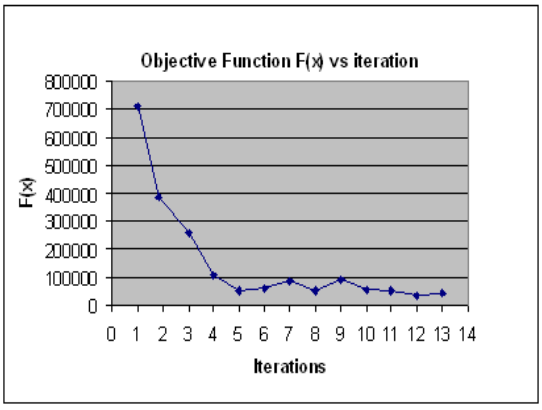

5.5.3 Effect of movable chill (Displacement on demand) on heat transfer (Scenario C)

In the case of movable chills with cooling, as in scenario B, the heat transfer coefficient falls below 1000 W/m²K because of the air gap. As the chill is moved forward to restore the contact between the castings and chill the heat transfer coefficient increases to nearly 1900 W/m²K. To simulate the heat transfer at the exact instant of chill displacement, a number of input heat transfer coefficients were applied.

5.5.4 Effect of movable chill (Displacement before eutectic) on heat transfer (Scenario D)

As in this case the chill is continuously pushed and a continuous contact is maintained between the casting and the chill the initial heat transfer is relatively high compared to chill displacement on demand. The heat transfer coefficient before 100 seconds is maintained above 2200 W/m²K. More importantly the heat transfer is more prominent during the period of dendrite growth.

Measured vs. Simulated temperature data

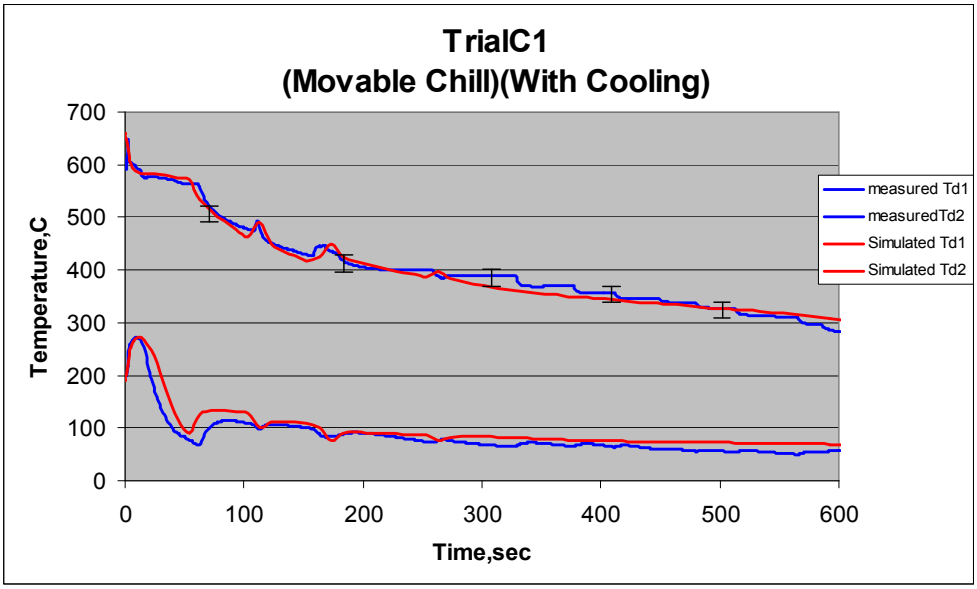

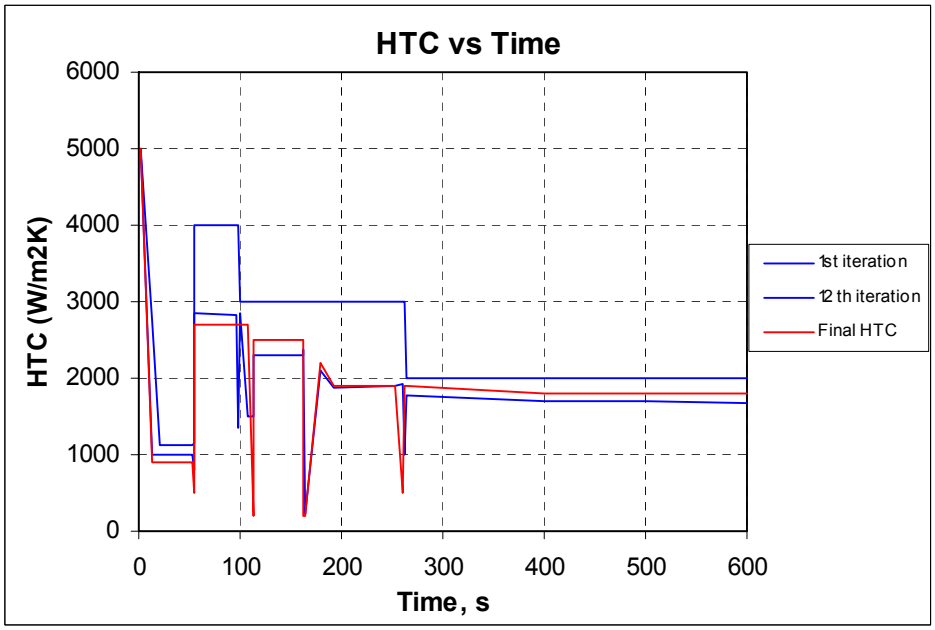

Figure 65: Procast calculated heat transfer coefficient for Trial C1

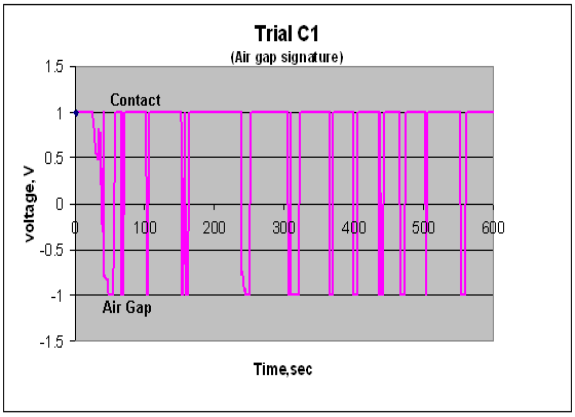

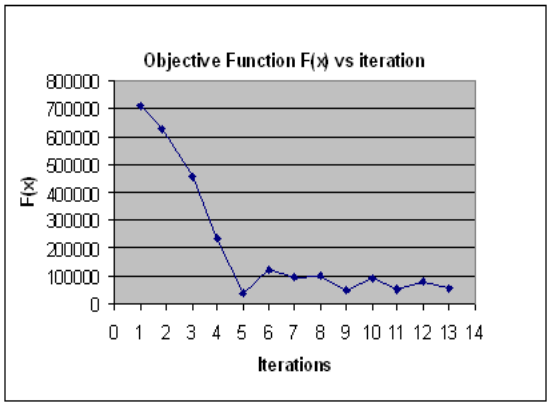

Measured vs. Simulated temperature data

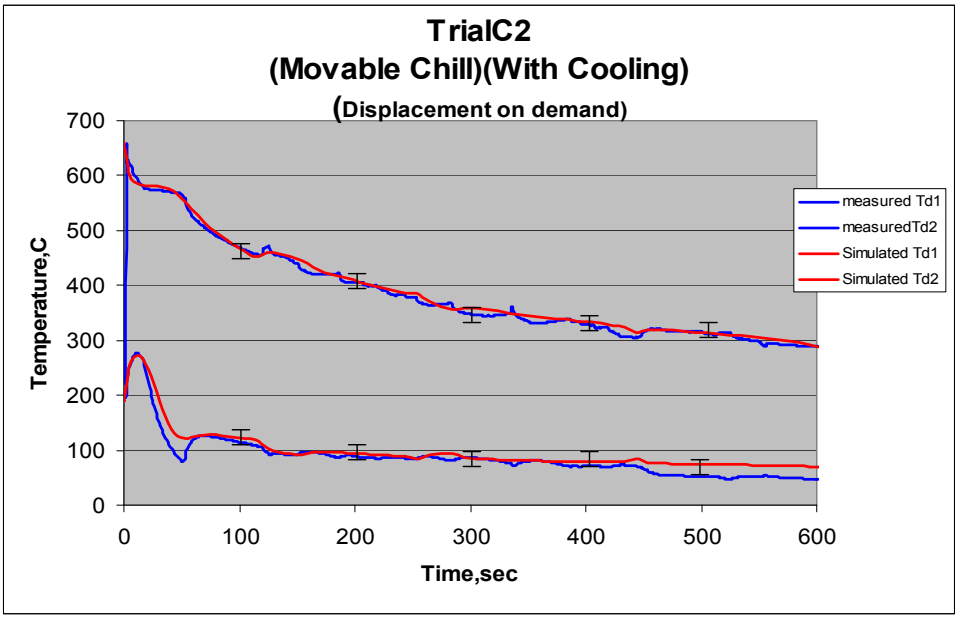

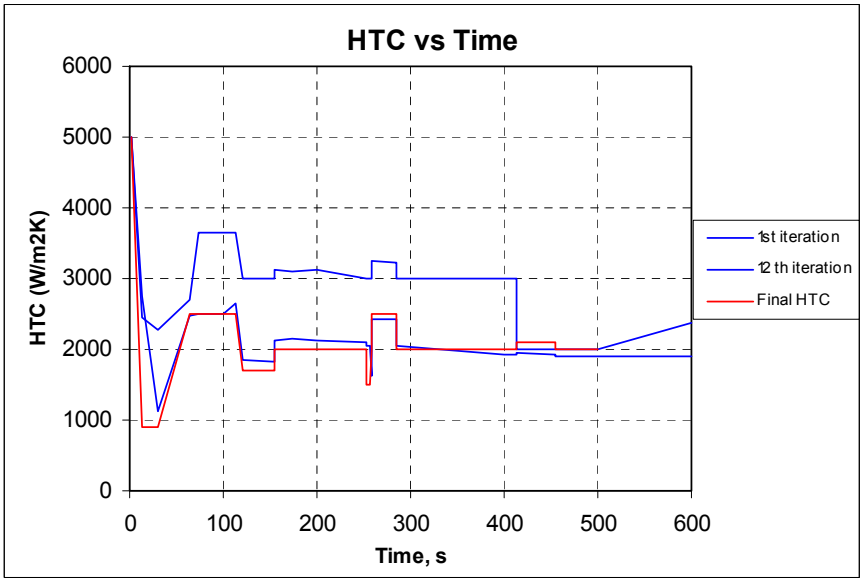

Figure 66: Procast calculated heat transfer coefficient for Trial C2

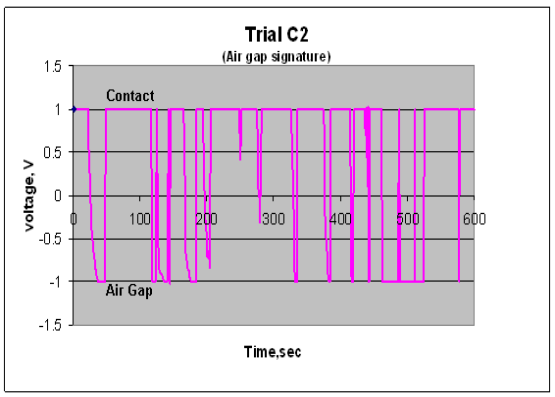

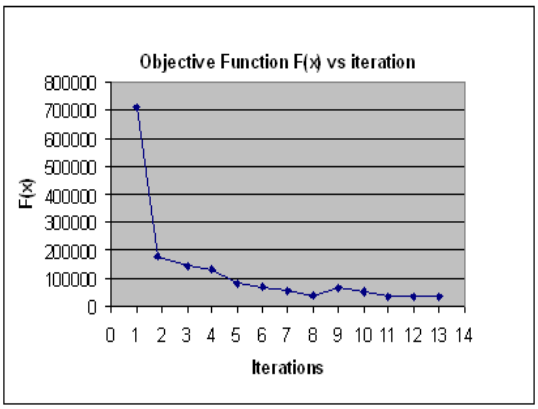

Measured vs. Simulated temperature data

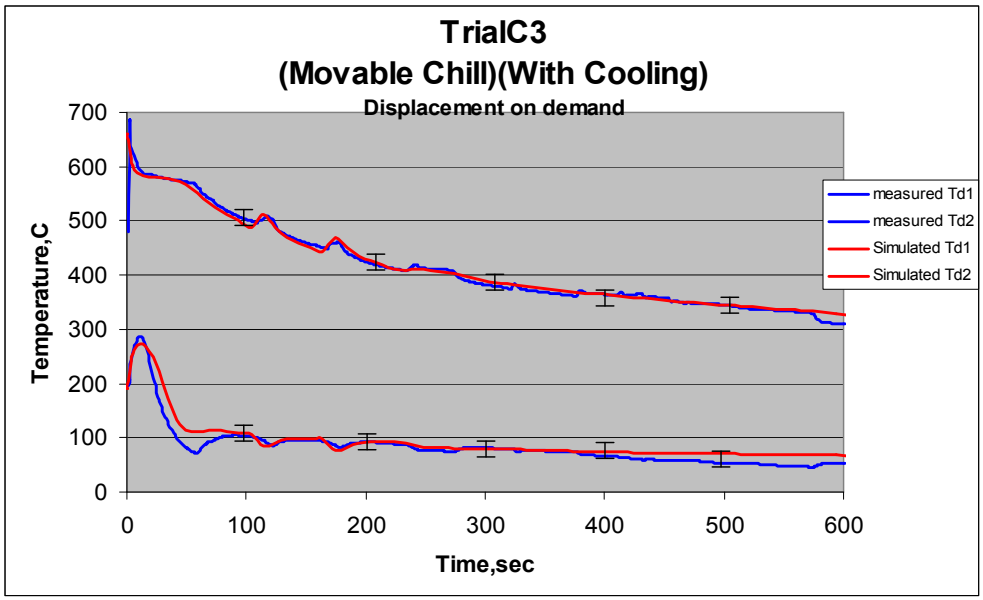

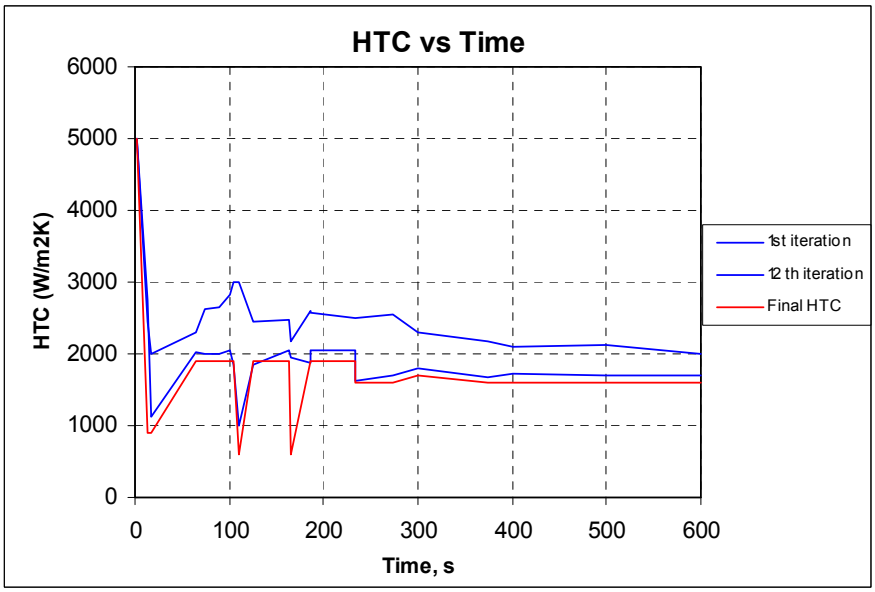

Figure 67: Procast calculated heat transfer coefficient for Trial C3

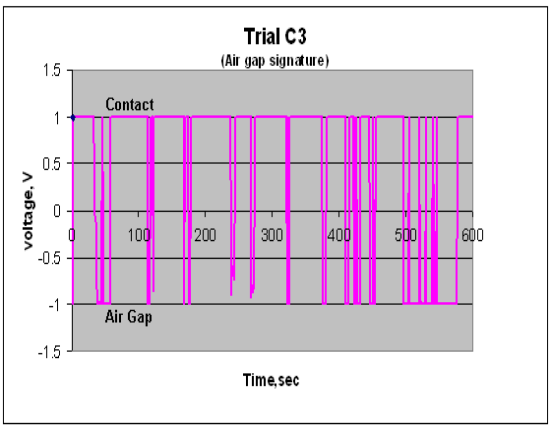

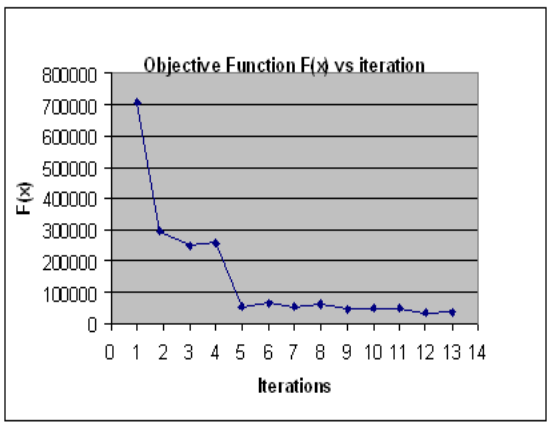

Measured vs. Simulated temperature data

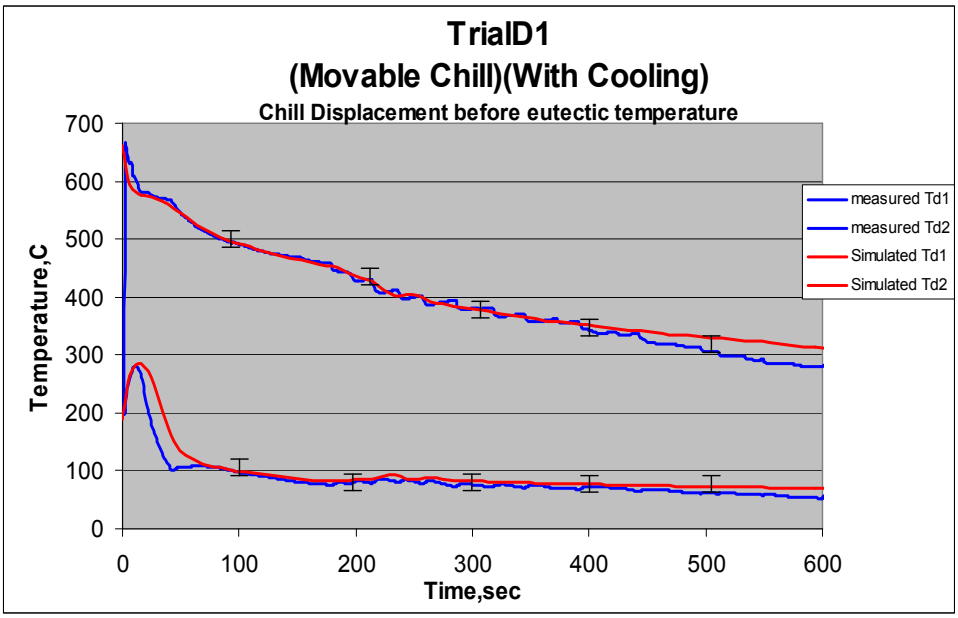

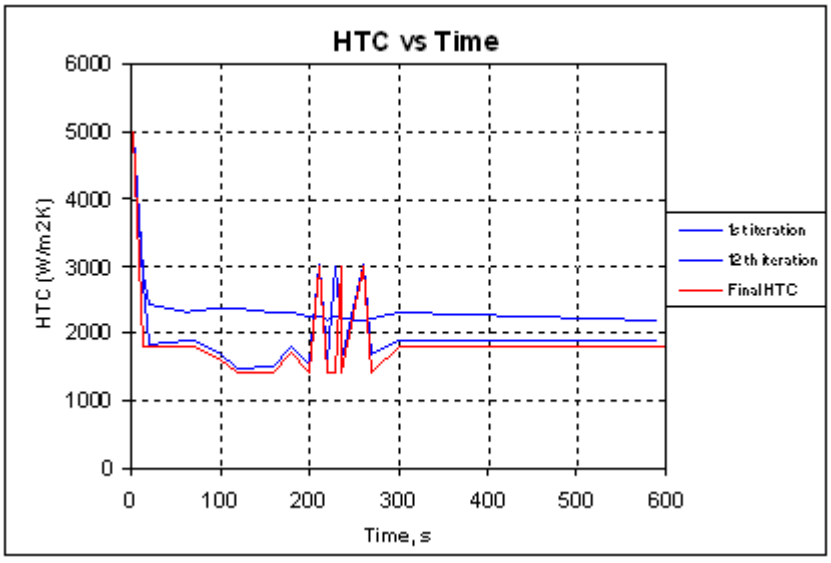

Figure 68: Procast calculated heat transfer coefficient for Trial D1

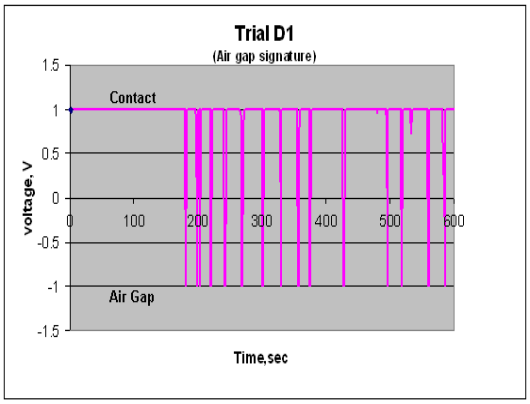

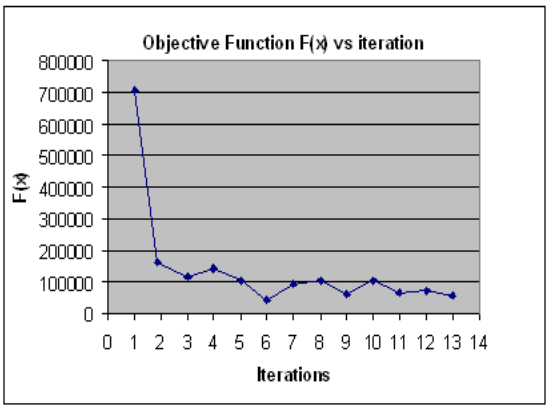

Measured vs. Simulated temperature data

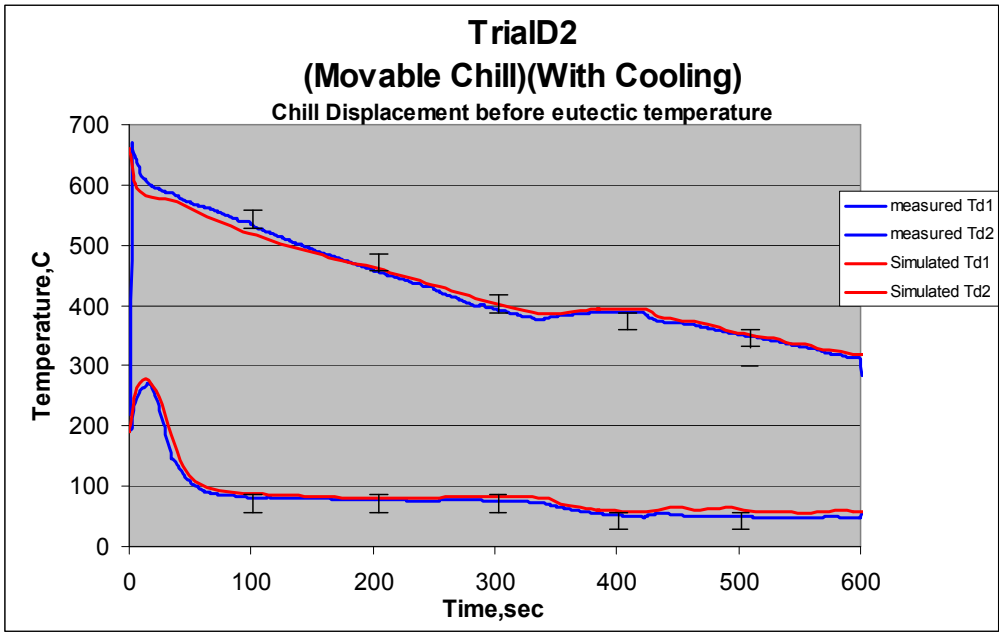

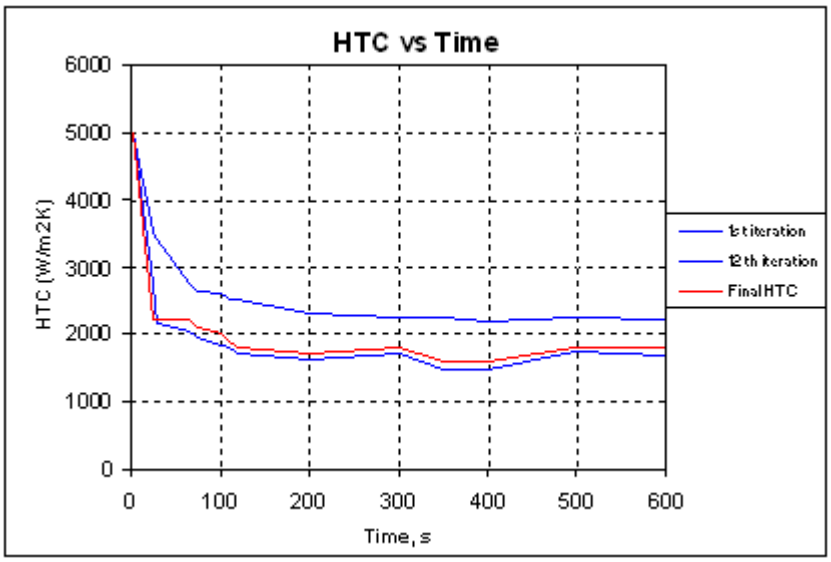

Figure 69: Procast calculated heat transfer coefficient for Trial D2

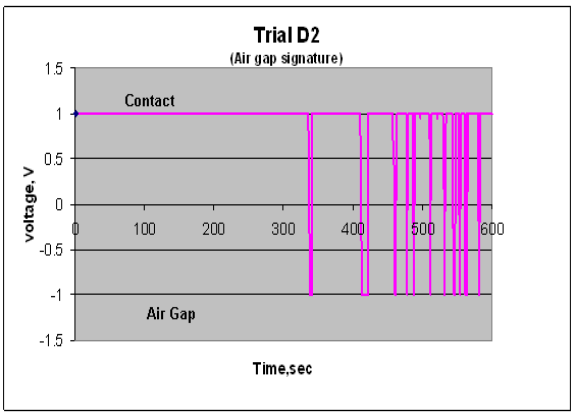

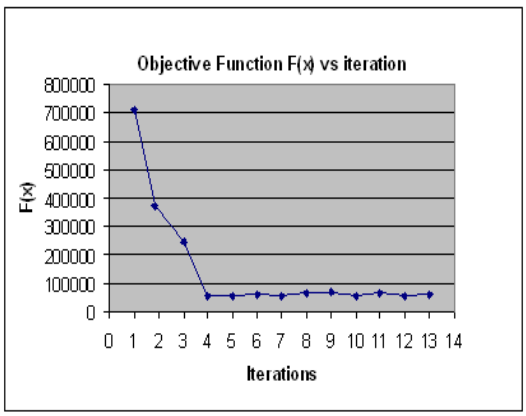

Measured vs. Simulated temperature data

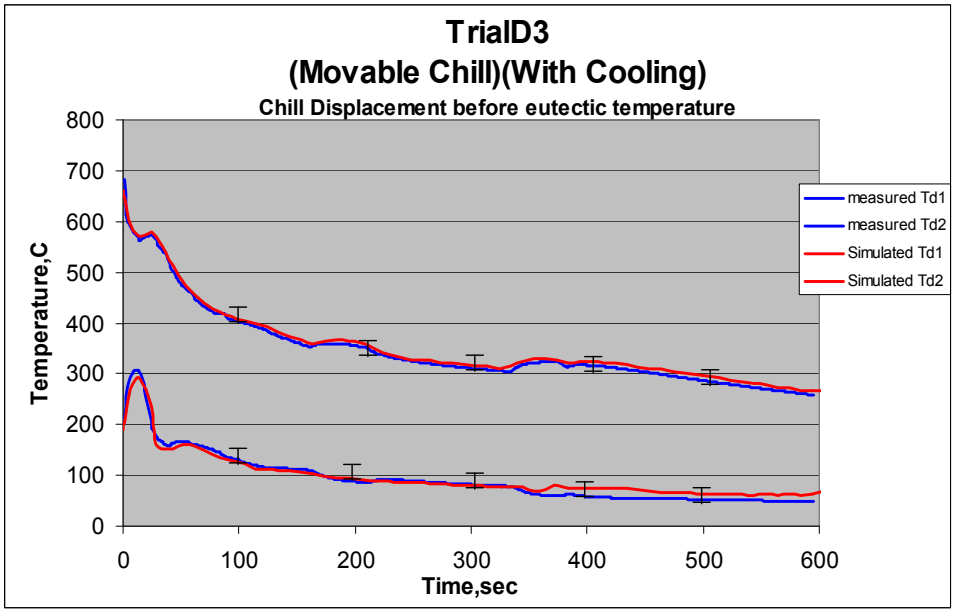

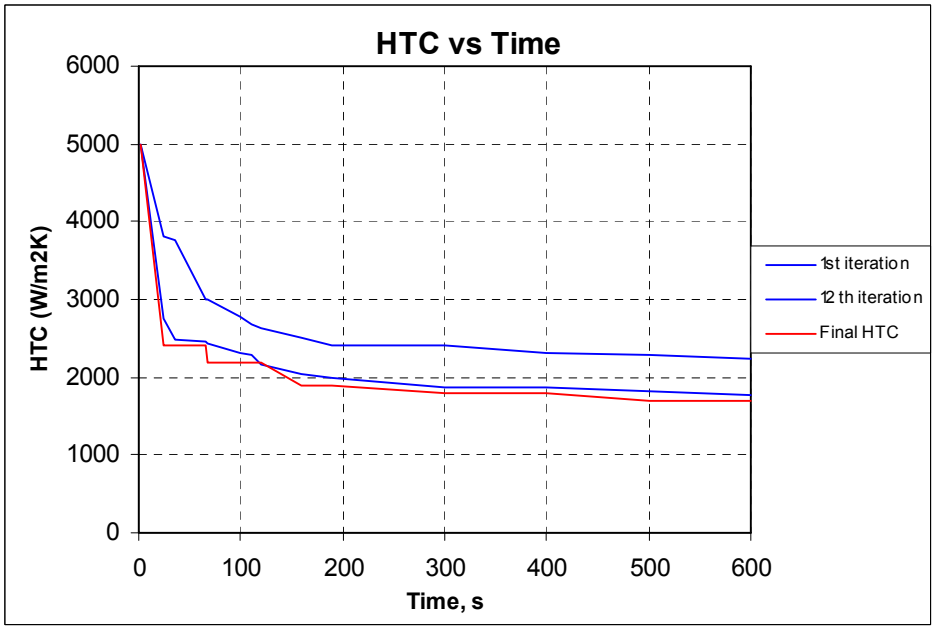

Figure 70: Procast calculated heat transfer coefficient for Trial D3

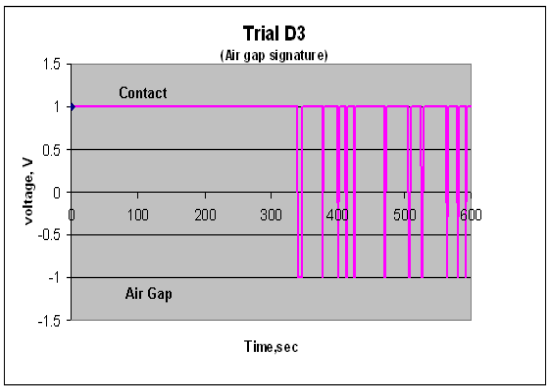

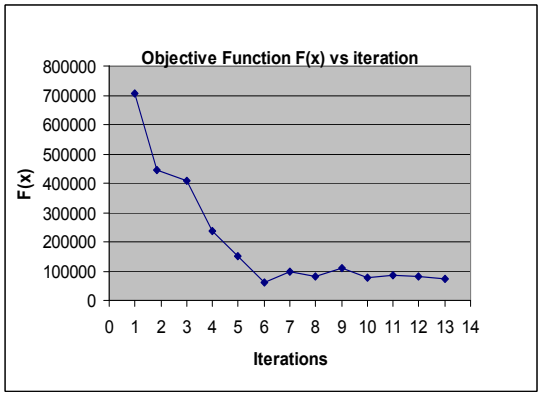

Under each trial number of iterations were performed and the best fit (i.e summation of error is minimum) was chosen as the final result.

5.6 Summary

A finite element model is made using ProCAST^{TM} to simulate solidification. An initial heat transfer value was guessed and later optimised to determine the interfacial heat transfer coefficient between the casting and the chill. An inverse optimisation technique was adopted for the same. The objective function value was calculated for every trial. The least value of objective function is chosen as the optimized result as shown in the below table.

Trial Id.	ith iteration for optimised result	Total percentage of air gap	HTC after 50 seconds W/m²K	HTC after 100 seconds W/m²K	HTC after 300 seconds W/m²K	HTC after 500 seconds W/m²K
Trial A_average	12	39.8%	2200	2200	1200	1200
Trial B_average	11	11.4%	200	200	200	200
Trial C1	8	85.6%	1200	2800	1800	2000
Trial C2	7	73.1%	1200	2400	2000	2000
Trial C3	5	71.8%	1100	1900	1800	1800
Trial D1	6	95.8%	1800	1700	1700	1800
Trial D2	8	95.3%	2300	2000	1800	1800
Trial D3	7	96.1%	2400	2200	1900	1900

Table 6: Summary of simulation result

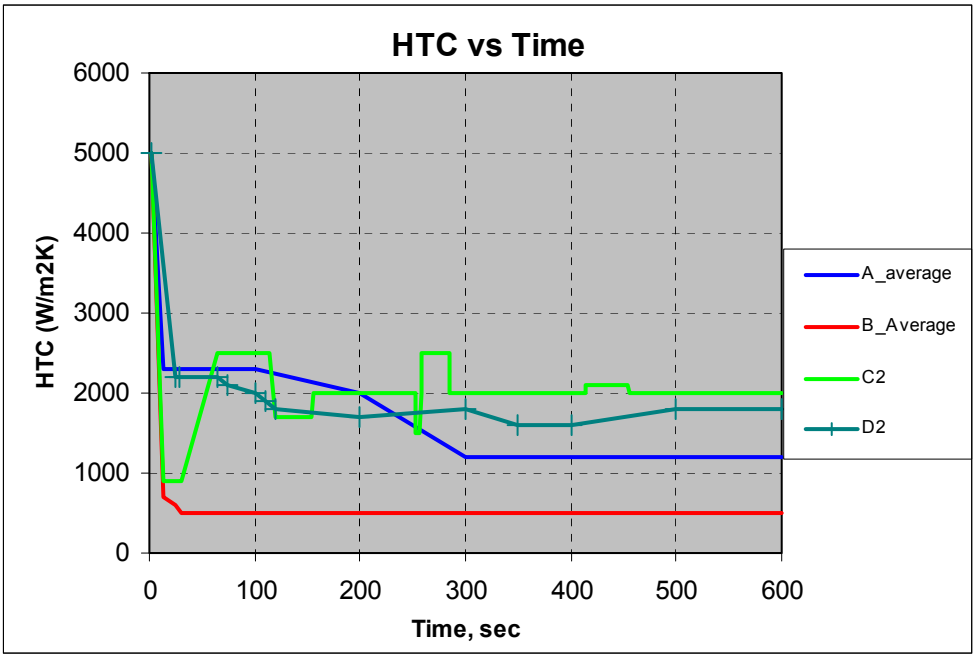

Figure 71: Combined HTC graph for trial A, B, C and D

Figure 71 shows the comparison of HTC for scenario A, B, C and D. The best result of C and D is plotted in this graph. The result indicates the following;

1. The interfacial heat transfer coefficient is found to be high in scenarios C and D where the chill is pushed closer to the casting as it solidifies compared to scenarios A and B.

2. Initial heat transfer rate is maintained in condition D where the chill is maintained in contact with the casting during initial stages of solidification.

6 Micro-structural analyses

6.1 Overview

As discussed in section 2.3.1 the secondary dendrite arm spacing (SDAS) has direct relationship with the cooling rate, hence it is important to measure the difference in SDAS for a particular cooling to demonstrate the effectiveness of the cooling chill.

6.2 Sample preparation

The casting samples under each series were cut at a distance of 5mm, 15mm, 30mm, 45 mm and 60 mm respectively from the interface. The samples were marked according to the method used for cooling and distance from interface as shown in table below.

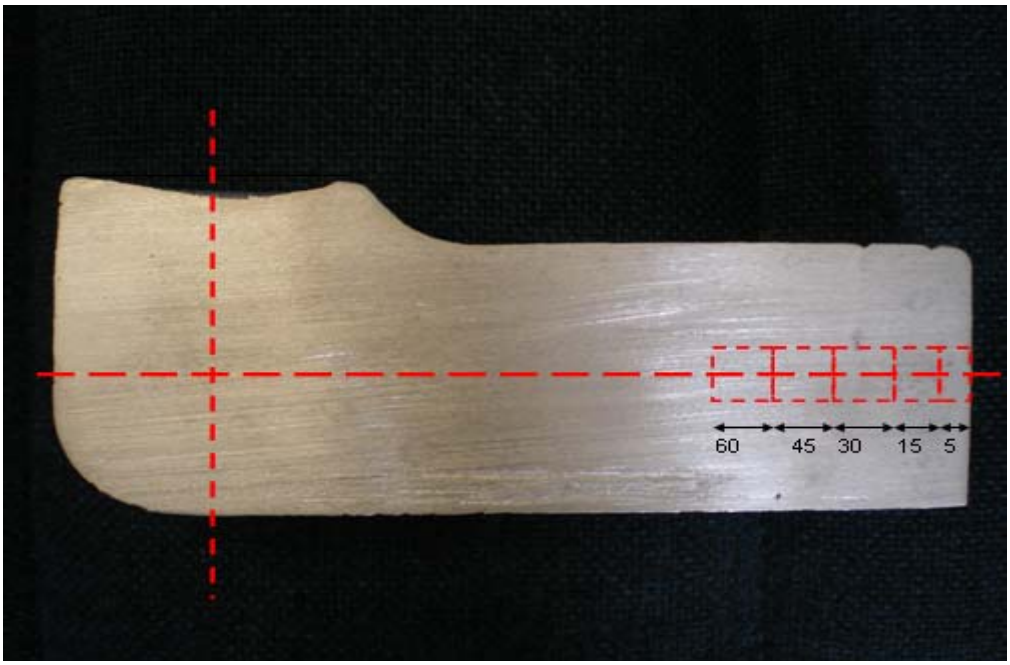

Figure 72: Cross section of the casting sample

Trial Id	Sample Id	Cooling Method	Distance From Chill
A1	A105	SCENARIO A Fixed Chill Without cooling water	5mm
	A115		15mm
	A130		30mm
	A145		45mm

	A160		60mm
B1	B105	SCENARIO B Fixed Chill With Cooling	5mm
	B115		15mm
	B130		30mm
	B145		45mm
	B160		60mm
C1	C105	SCENARIO C Movable chill with cooling(On-Demand Displacement)	5mm
	C115		15mm
	C130		30mm
	C145		45mm
	C160		60mm
D1	D105	SCENARIO D Movable chill with cooling(Displacement before eutectic temperature)	5mm
	D115		15mm
	D130		30mm
	D145		45mm
	D160		60mm

Table 7

A similar pattern is followed for Trial 2 and Trial 3 for the same condition of experiments. To determine the changes in SDAS along its length, the castings were cut parallel to the axis as shown in Figure 72. The samples were cut into rectangular pieces of 15mm X 10 mm. The samples were then mounted using a Bakelite mount. The samples were marked and polished using different grits using an automatic polishing machine in METlab at AUT University. The samples were then washed with soap water, spirit and dried using a standard hair dryer.

The samples were then mounted on the optical microscope and connected to a computer. The samples closer to the chill i.e.: A105, B205, C305 etc were observed under higher magnification (20 times) whereas samples away from the chill face were observed at lower magnification (5 times). This is because the preliminary observations showed that the dendrite closer to the chill was relatively finer compared to the dendrite located away from the chill. The dendrites were observed at different distance from the chill and images were captured at each distance. Image-Pro™ software was then used to measure the dendrite spacing as shown in Figure 73

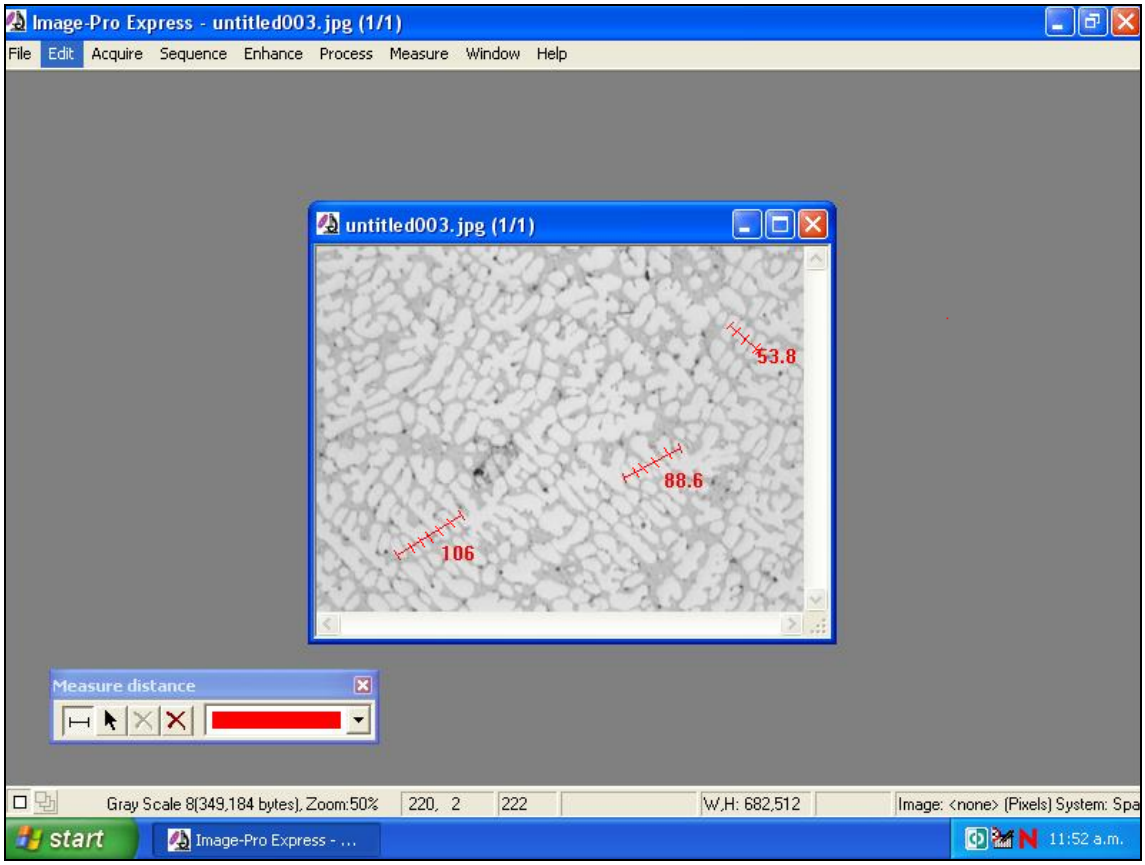

Figure 73: Image-Pro™ software used to measure secondary dendrite arm spacing (SDAS).

The SDAS was measured and tabulated in terms of pixels and was later converted into micrometer length scale using spread a sheet as shown in Figure 74. Three SDAS measurements were chosen in each sample distance from the chill and an average SDAS was calculated and plotted.

	AV	AW	AX	AY	AZ	BA	BB	BC	BD	BE	BF	BG	BH	BI	BJ	BK	BL	BM	BN	BO	BP	BQ
11																						
12																						
13	Dentrite Branch 2					No.	Dentrite Branch 3							No.	Avg Dent1	Avg Dent2	Avg Dent3	SDAS in µm	SDAS in µm	SDAS in µm	Average	Distance
14	25.3	23.1	22.3	21.7		6	20.9	21.7	21.8	21.6	27.3	19.4		6	23.63	23.00	22.12	11.81	11.50	11.06	11.46	1
15	31.8	32.1	28	25.3	27.4	7	32.3	34.3	28.9	29.8	34.7	35.8	32.1	7	31.60	30.07	32.56	15.80	15.04	16.26	15.70	2.5
16	20.2	23.4				4	19.7	20.4	23.7	22.7	25.3			5	20.99	22.73	22.36	43.18	46.76	46.01	45.32	7.5
17	29.9	33.8	32.9			5	28.4	35.3	32.9	29.9	33			5	33.42	31.82	31.90	68.77	65.47	65.64	66.63	22.5
18	31.6	33.9	36.8			5	33.8	32.9	38.9	34.6	27.4			5	33.86	32.70	33.52	69.67	67.28	68.97	68.64	37.5
19	34.8	32.9	42.2	37.4		6	35	33.4	36.2	33.8	39.4	37.2		6	37.43	36.27	35.83	77.02	74.62	73.73	75.13	52.5
20																						
21																						
22																						
23																						
24																						
25																						
26																						
27																						
28																						
29																						
30																						
31																						
32																						
33																						
34																						
35																						
36																						
37																						
38																						
39																						
40																						
41																						
42																						
43																						
44																						
45																						
46																						
47																						
48																						
49																						
50																						
51																						
52																						
53																						
54																						
55																						
56																						
57																						
58																						
59																						

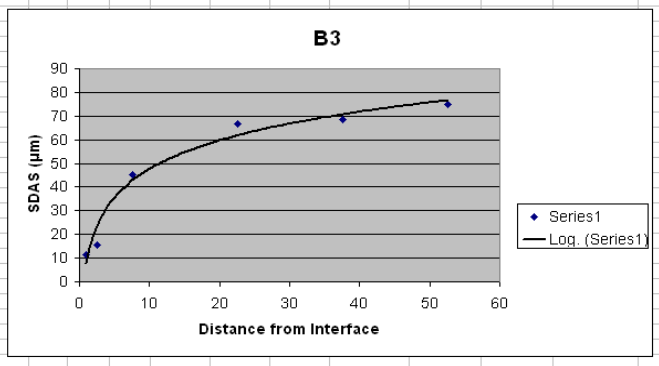

Figure 74: dendrite calculation

6.3 *Uncertainties involved in dendrite measurement*

During secondary dendrite arm spacing measurements, the following errors were minimised to improve the accuracy of the results.

6.3.1 Cut-off error

When the casting samples were sectioned microscopic analysis some a part of length was lost to cutting. These errors are referred to as cut-off errors. Figure 75 illustrates cut-off errors. Where a, b, and c are the length of the samples along the axis. X1 and X2 are the cut-off errors. These errors need to be added to the length for locating the exact distance of dendrites from the interface. These errors are calculated as explained below.

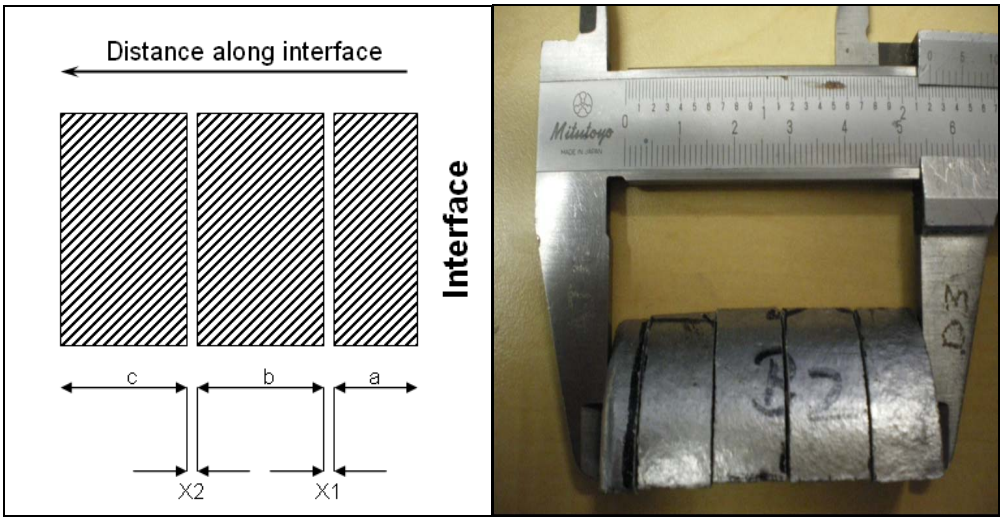

Figure 75: Casting samples cut into small sizes for microscopic analysis

Total length of the sample before cut=60.1 mm

Total length of sample after cut=55.7 mm

Length lost due to cutting= $60.1\text{mm} - 55.7\text{mm} = 4.4\text{mm}$

Length lost during each cut (X1, X2) $= \frac{4.4}{4} = 1.1\text{mm}$

There for a length of 1.1mm was added to the total length to locate the dendrites from the interface.

6.3.2 Image capturing error

During image capturing a specimen needed to be manually shifted along its length. Due to this a small portion of the image was lost between two consecutive images. From the prospective of this research it was very important to locate fixed distances from the interface. From Figure 76, it is seen that there exists a small loss of length at the interface of two pictures. Even though this distance is very small it can cause a significant error at images taken at larger distances from the interface.

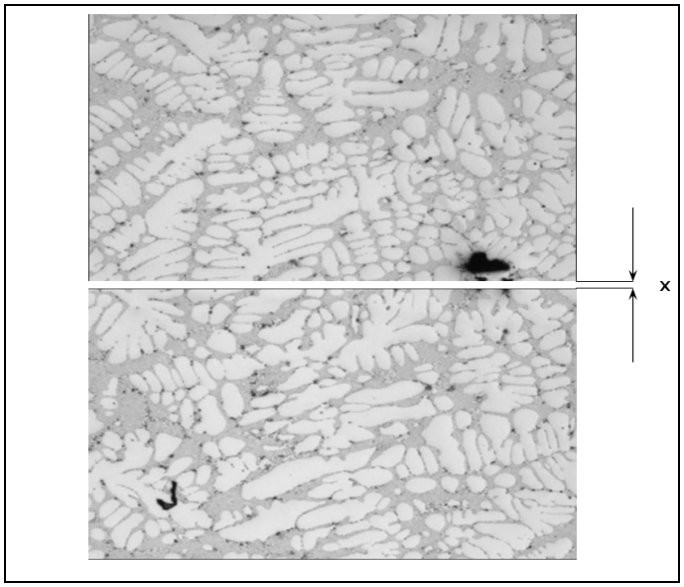

Figure 76: x=distance lost between two consecutive images.

This kind of error was minimised by adding a fixed percentage of length between two consecutive images while calculating the distance from the chill interface. The microstructure for each trial at fixed location from the chill is shown in section 6.5

6.4 Effect of chill conditions on SDAS

As discussed in earlier sections the SDAS has a direct relationship with cooling. The secondary dendrites are observed to be finer at the chill interface and gradually increase away from the interface. It is very important for in this research to analyse and quantify the affects of the movable chill when compared to fixed chills. Figure 78 to figure 113 show microstructure of the casting taken at fixed distance from the chill.

In order to clearly identify the effectiveness of different chill conditions on the SDAS, a graph was plotted between SDAS and distance from the interface for each casting sample. A logarithmic trend line of best fit was drawn over the measured dendrite value as shown in Figure 77. From this figure it can be seen that averaged dendrites in scenario B of trial (fixed chill with cooling) is much higher than rest of the trials. This is due to the fact that the cooling rates of castings produced under scenario B trials are much lower than other scenarios as a result of air gap formation at the beginning of the cooling cycle.

Figure 77: SDAS plotted against distance from interface for different chill conditions.

It is clear from the above figure that the average dendrite arm spacing can be reduced using movable chills. The average SDAS in scenario B (fixed chill with cooling) at 52.5 mm was 76.4 µm which is much higher than average SDAS in scenario C (movable chill on demand) and scenario D (movable chills on eutectic) which is found to be 55.6 µm and 53.5 µm respectively. This difference is a result of faster cooling rates using movable chills. There is also a significant difference in SDAS between scenario C and scenario D especially at dendrites away from the interface. The average SDAS at a distance of 2.5 mm for scenario C and D are found to be 12.5 µm and 11.3 µm respectively. Even though this difference is small, it is due to faster cooling before eutectic temperature in scenario D. The average SDAS at a distance of 55mm for scenario C and D are found to be 55.7 µm and 51.4 µm respectively. This difference is significant.

6.5 Micrographs

Cast A1: Fixed chill without cooling

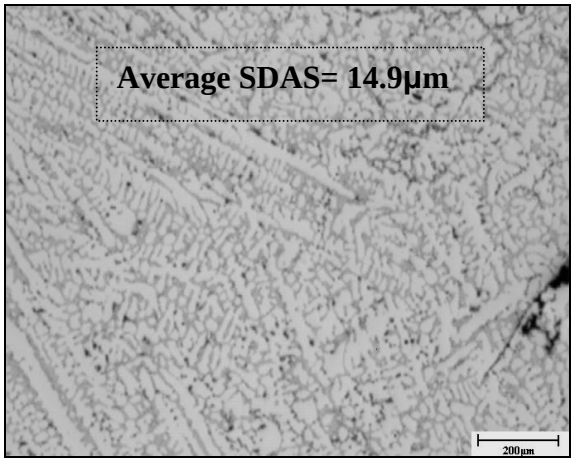

Figure 78: Dendrites at 2.5mm from the interface

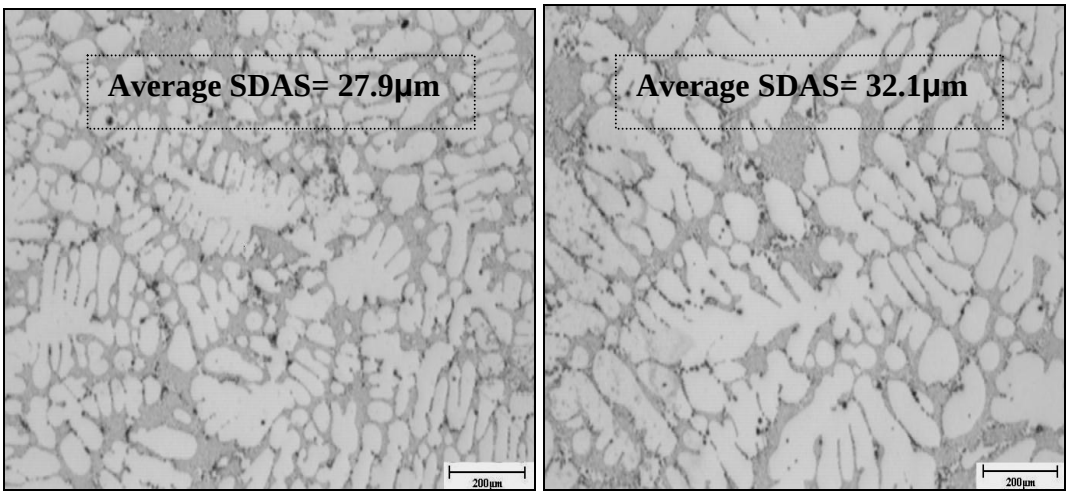

Figure 79: Dendrites at 7.5 mm and 15 mm

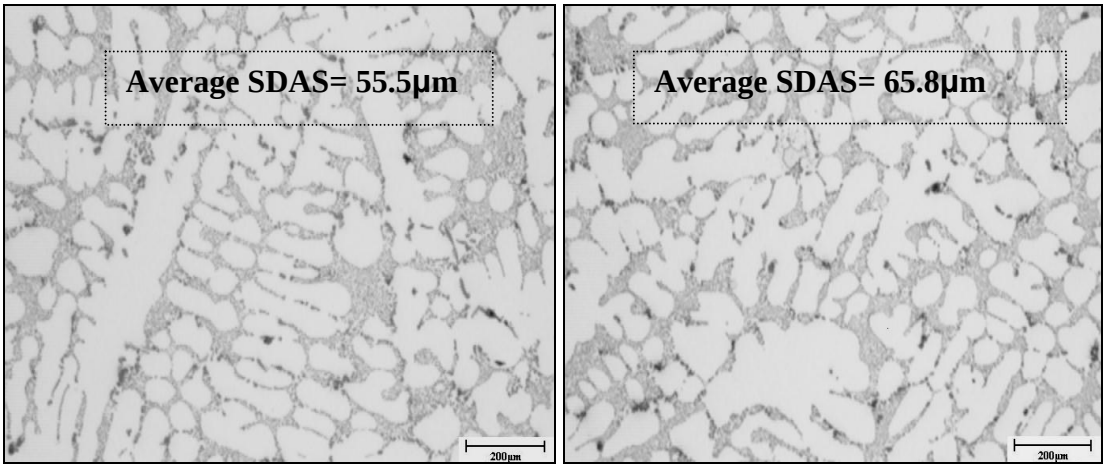

Figure 80: Dendrites at 37.5 mm and 52.5 mm

Cast A2: Fixed chill without cooling

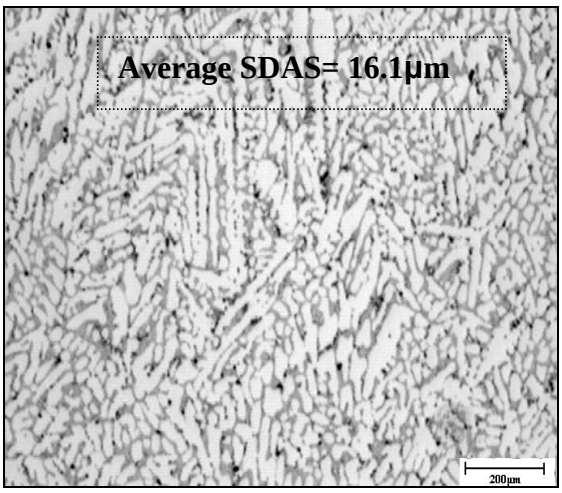

Figure 81: Dendrites at 2.5mm from the interface

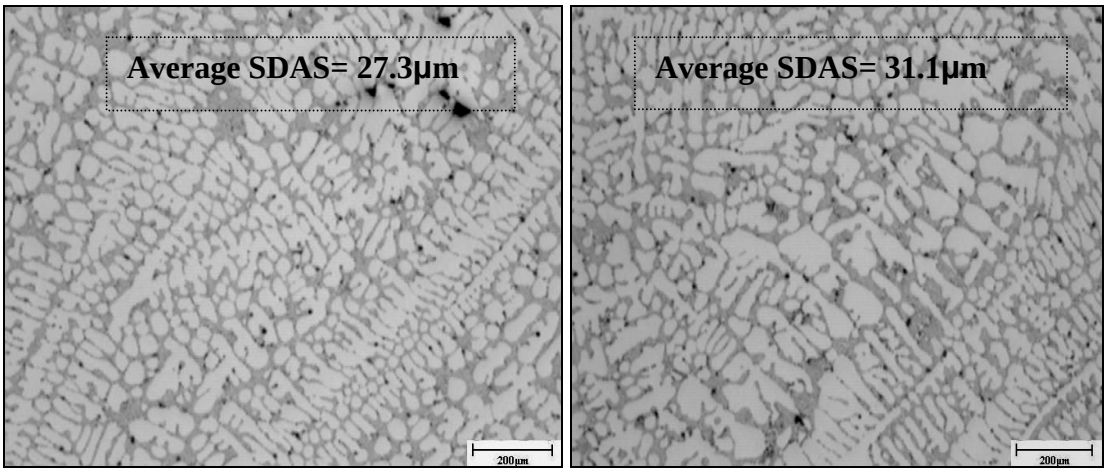

Figure 82: Dendrites at 7.5 mm and 15 mm

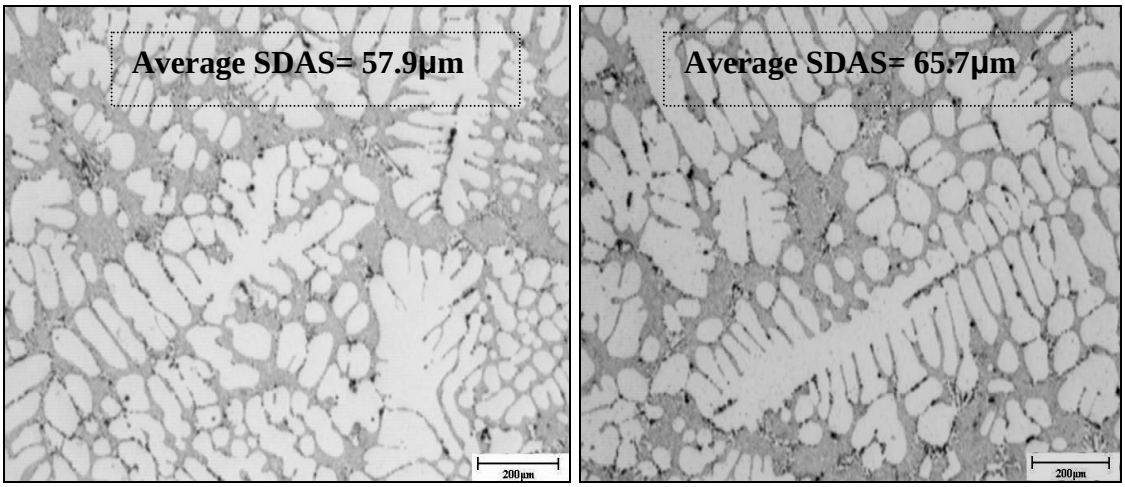

Figure 83: Dendrites at 37.5 mm and 52.5 mm

Cast A3: Fixed chill without cooling

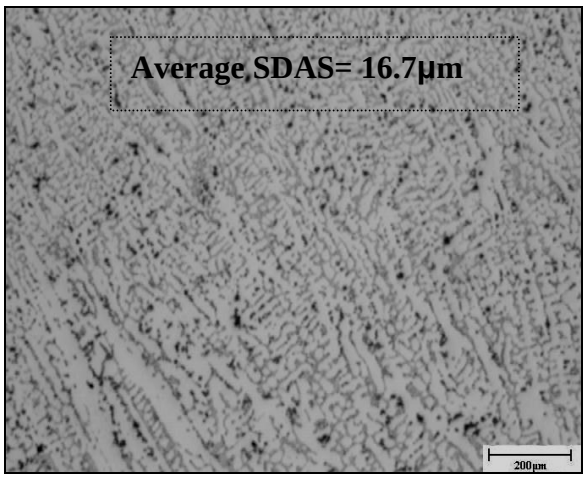

Figure 84: Dendrites at 2.5mm from the interface

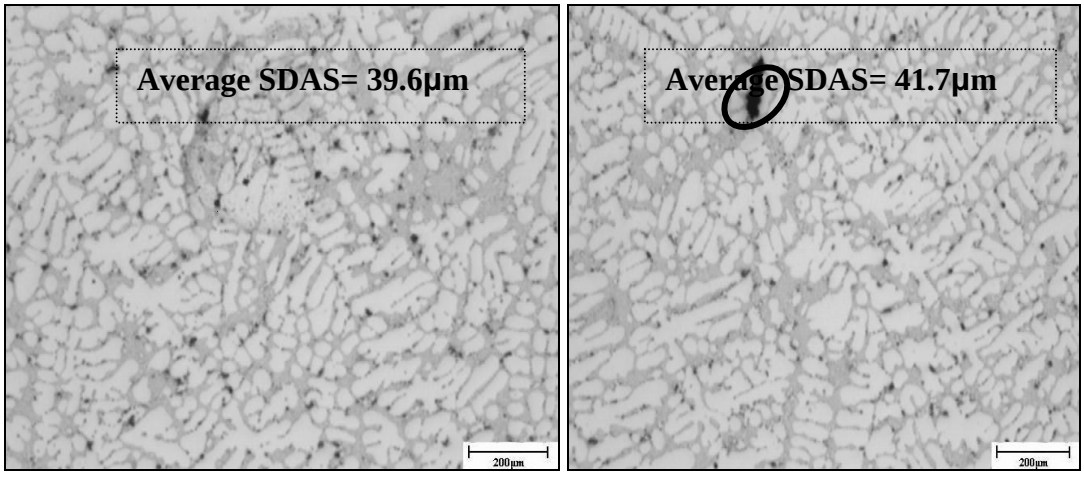

Figure 85: Dendrites at 7.5 mm and 15 mm

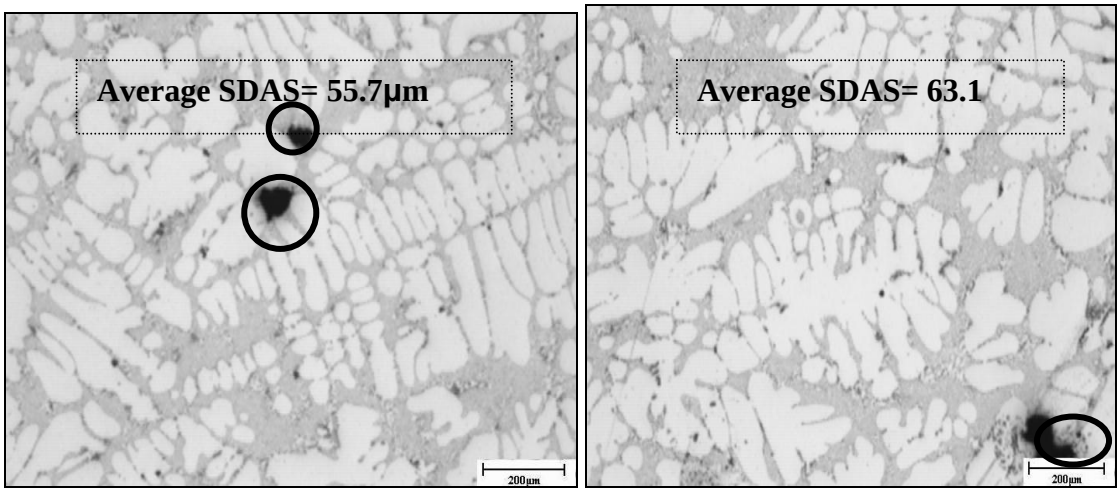

Figure 86: Dendrites at 37.5 mm and 52.5 mm

Cast B1: Fixed chill with cooling

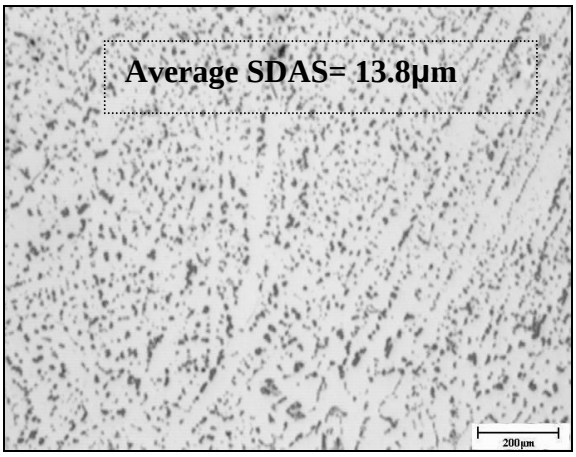

Figure 87: Dendrites at 2.5mm from the interface

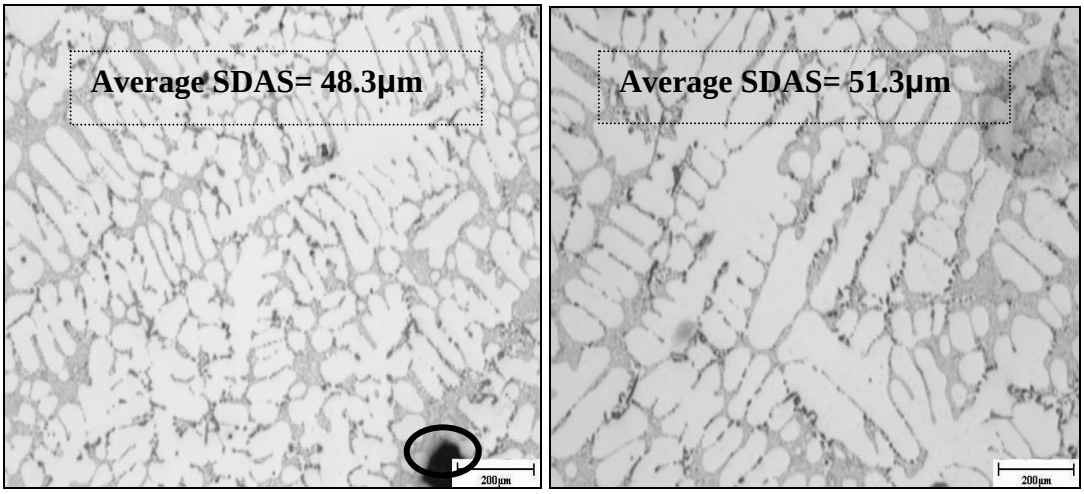

Figure 88: Dendrites at 7.5 mm and 15 mm

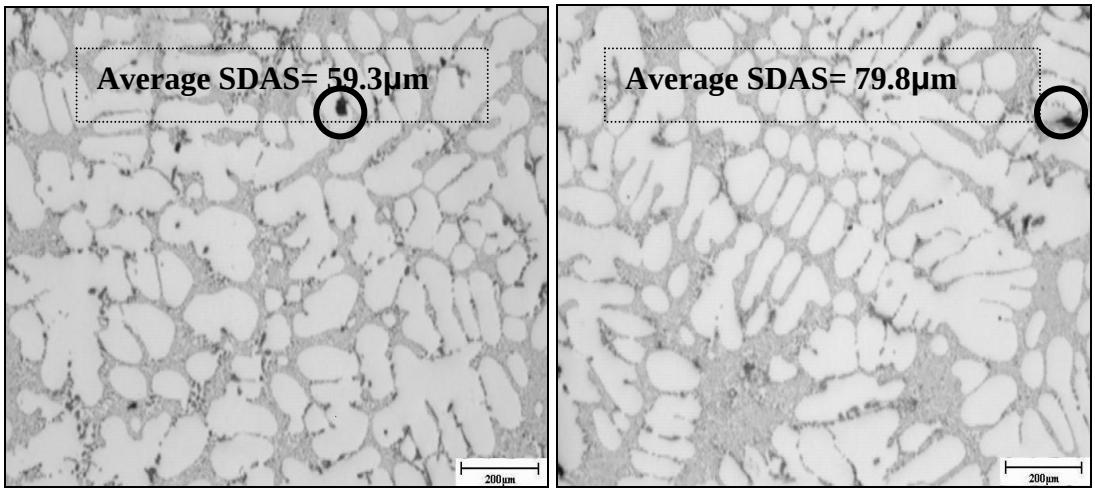

Figure 89: Dendrites at 37.5 mm and 52.5 mm

Cast B2: Fixed chill with cooling

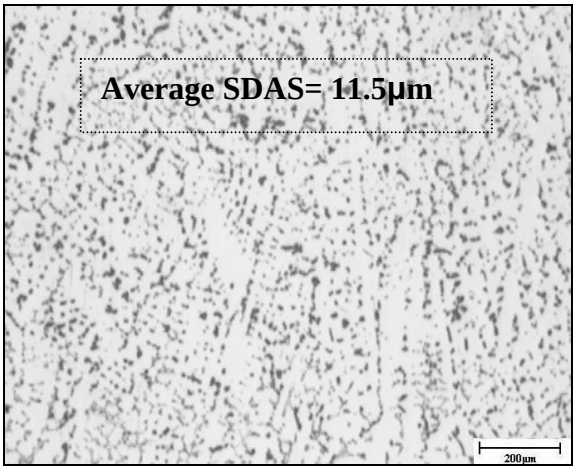

Figure 90: Dendrites at 2.5mm from the interface

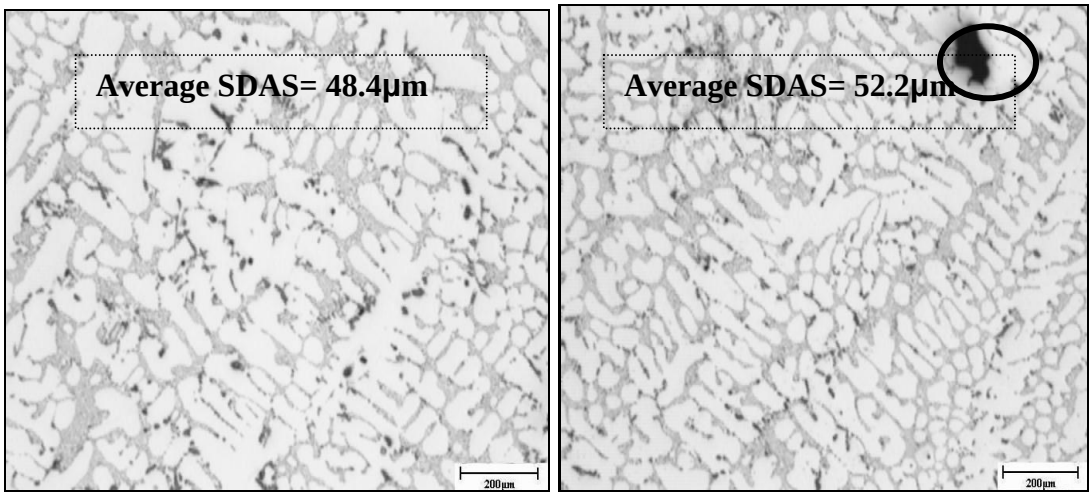

Figure 91: Dendrites at 7.5 mm and 15 mm

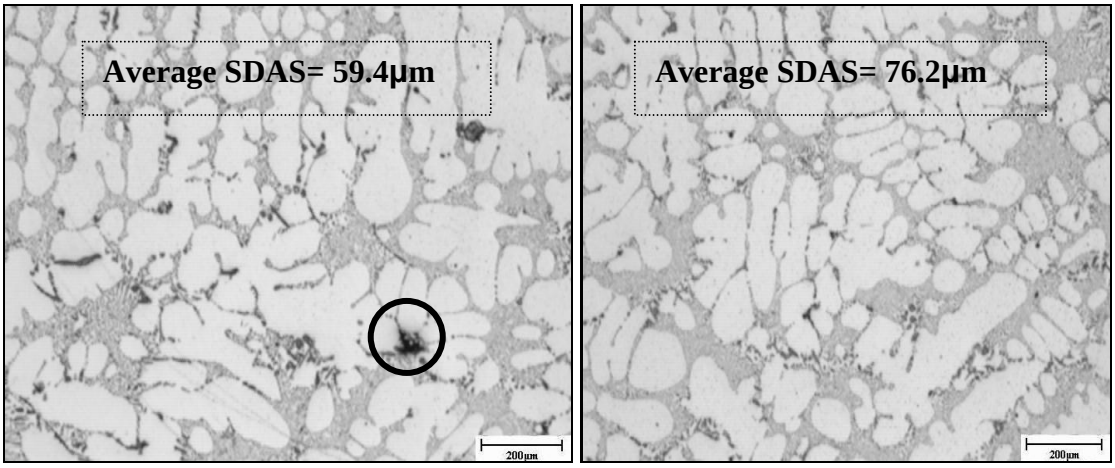

Figure 92: Dendrites at 37.5 mm and 52.5 mm

Cast B3: Fixed chill with cooling

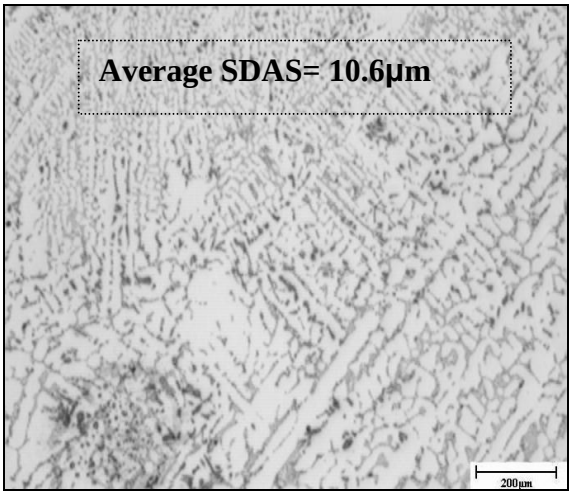

Figure 93: Dendrites at 2.5mm from the interface

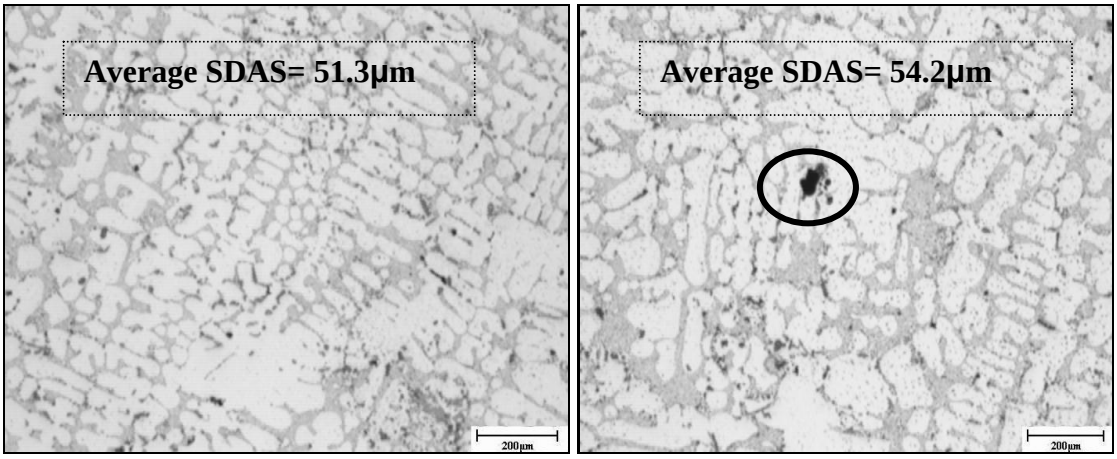

Figure 94: Dendrites at 7.5 mm and 15 mm

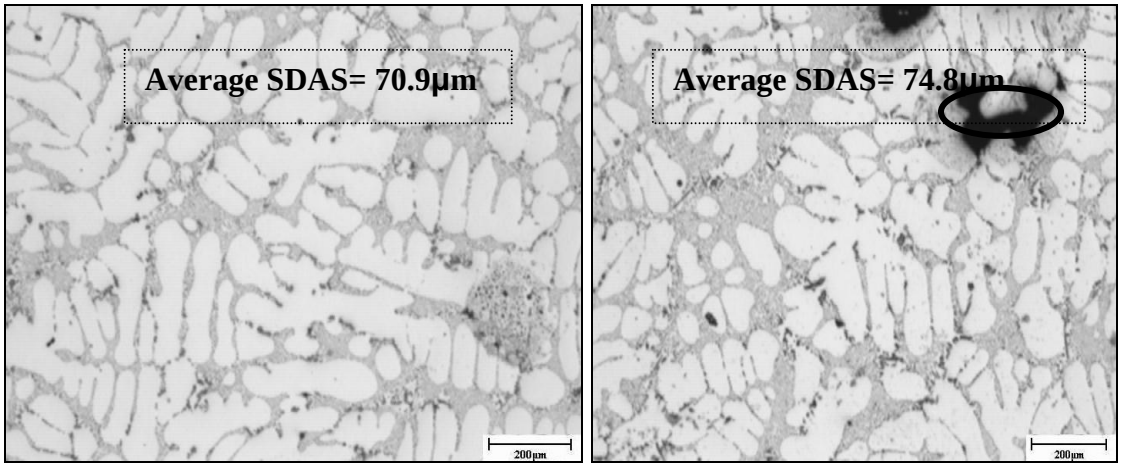

Figure 95: Dendrites at 37.5 mm and 52.5 mm

CastC1: Movable chill with cooling

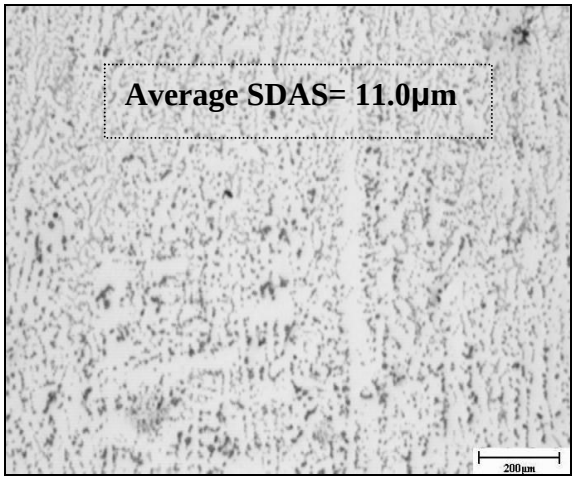

Figure 96: Dendrites at 2.5mm from the interface

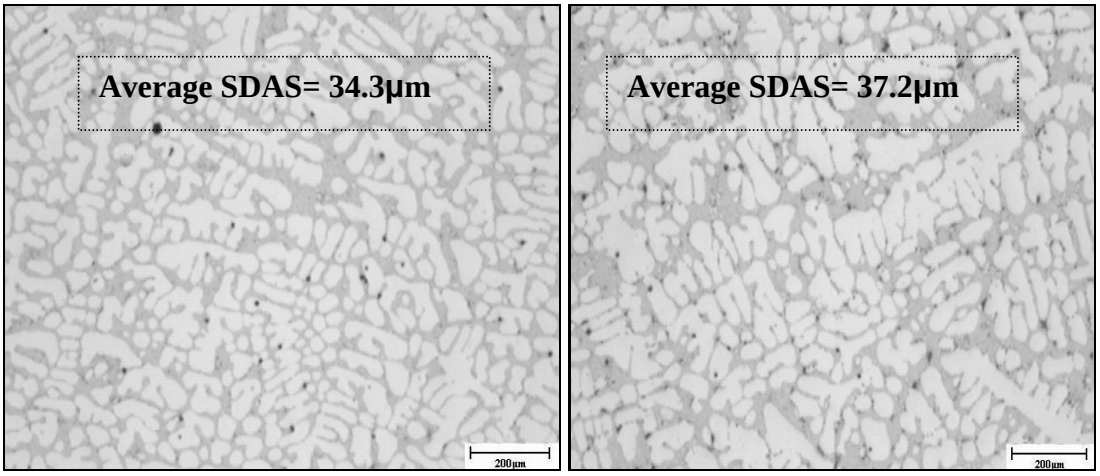

Figure 97: Dendrites at 7.5 mm and 15 mm

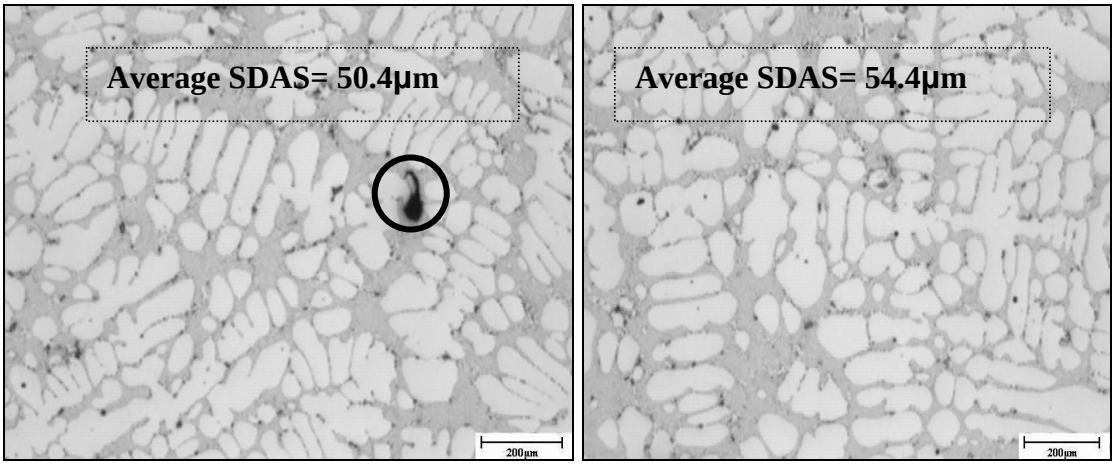

Figure 98: Dendrites at 37.5 mm and 52.5 mm

CastC2: Movable chill with cooling

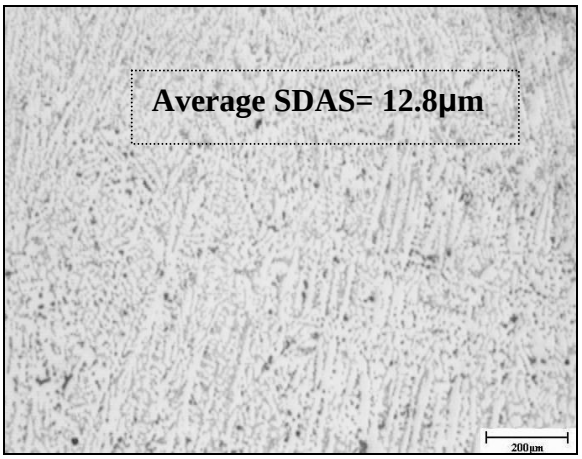

Figure 99: Dendrites at 2.5mm from the interface

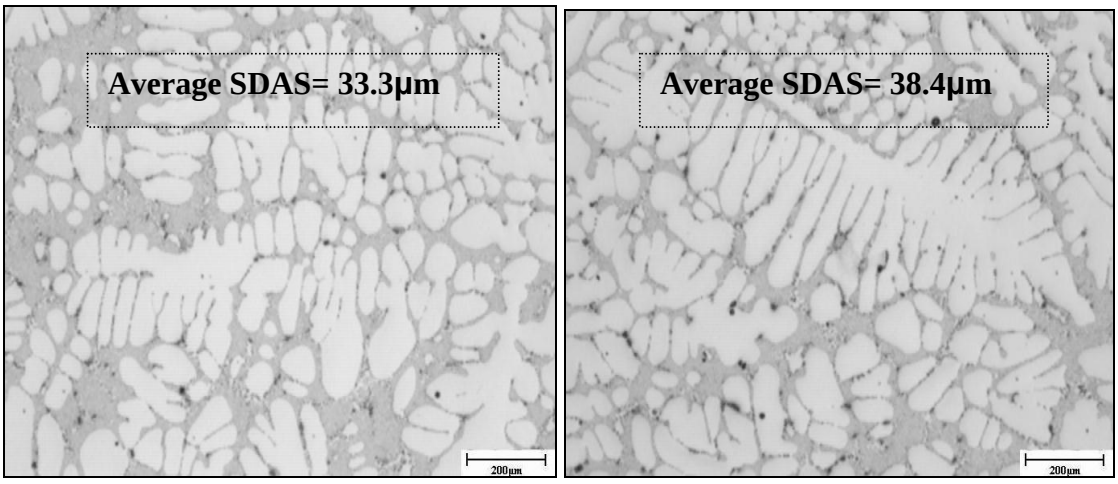

Figure 100: Dendrites at 7.5 mm and 15 mm

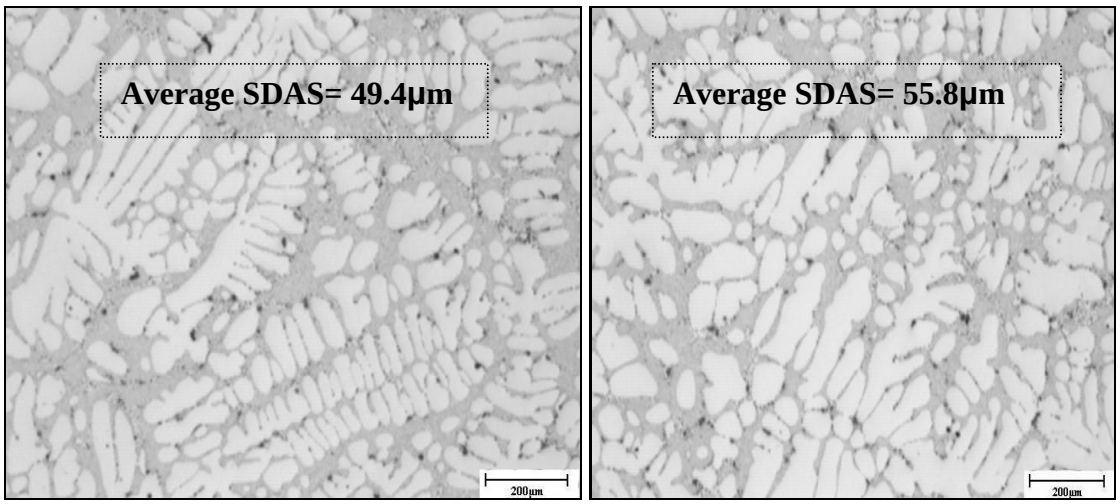

Figure 101: Dendrites at 37.5 mm and 52.5 mm

CastC3: Movable chill with cooling

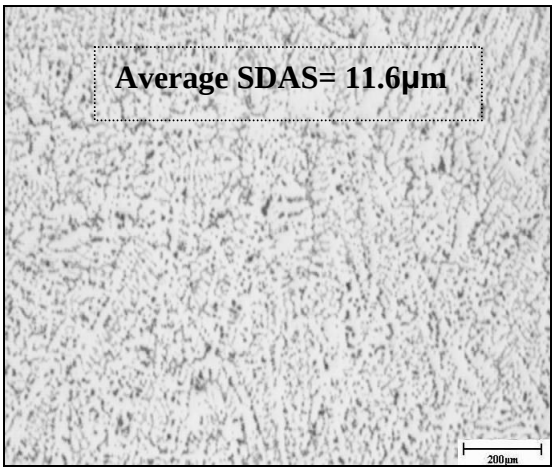

Figure 102: Dendrites at 2.5mm from the interface

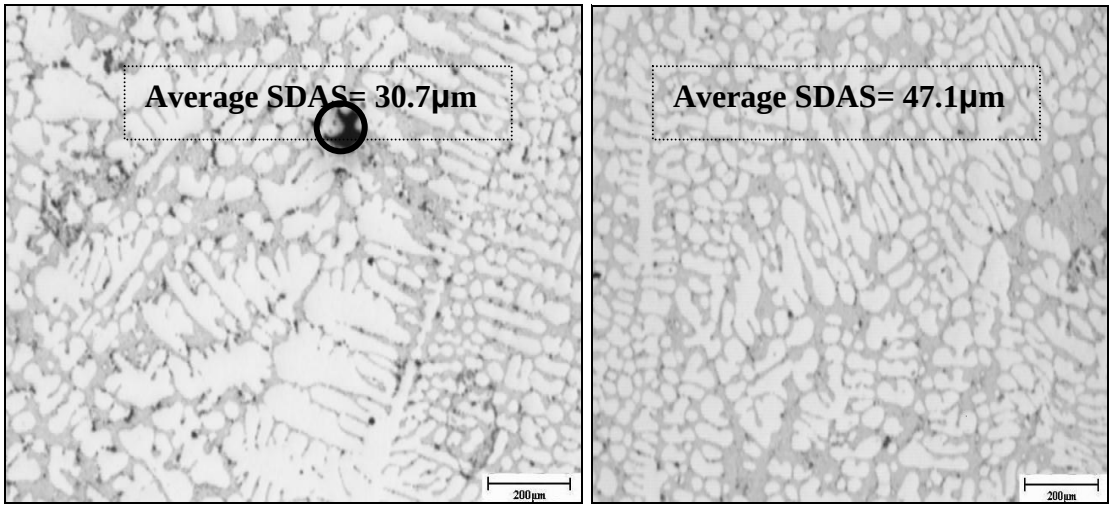

Figure 103: Dendrites at 7.5 mm and 15 mm

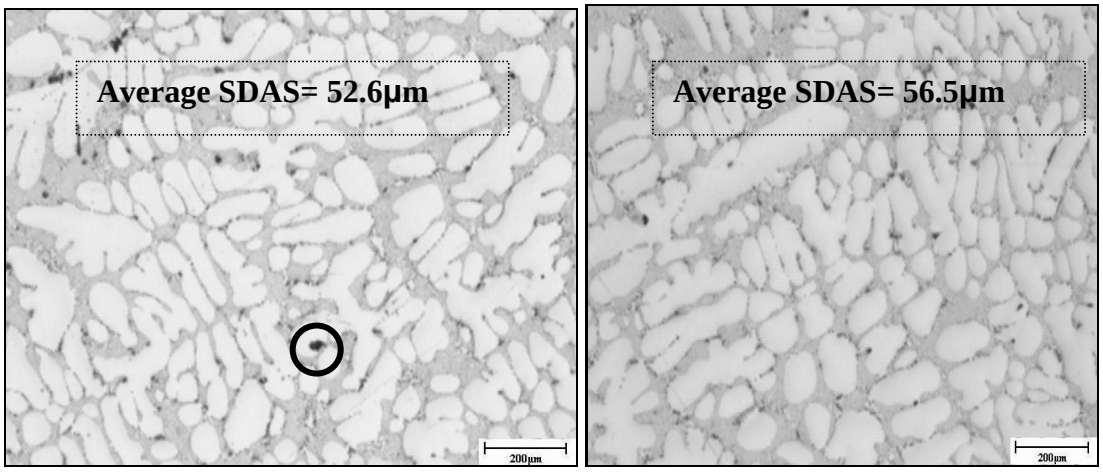

Figure 104: Dendrites at 37.5 mm and 52.5 mm

CastD1: Movable chill with cooling

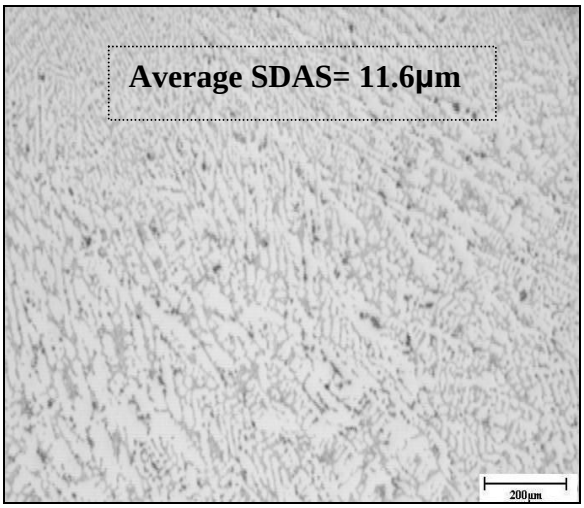

Figure 105: Dendrites at 2.5mm from the interface

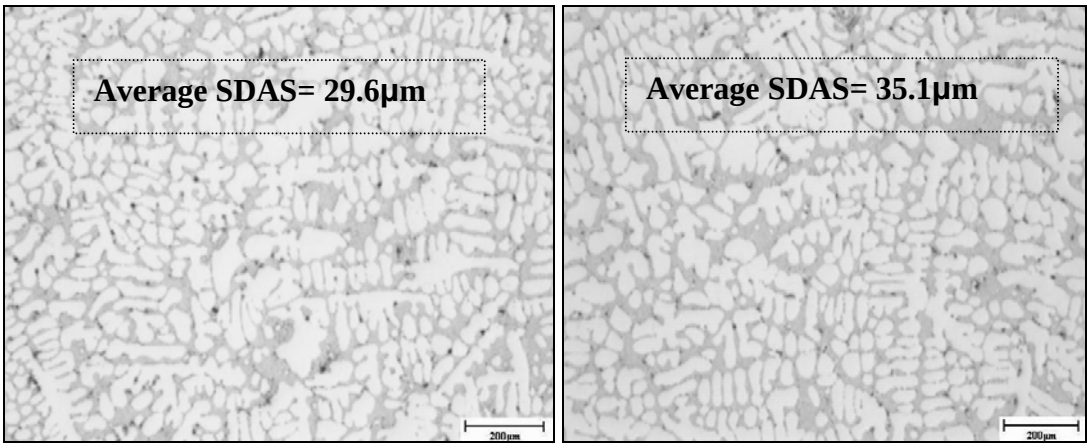

Figure 106: Dendrites at 7.5 mm and 15 mm

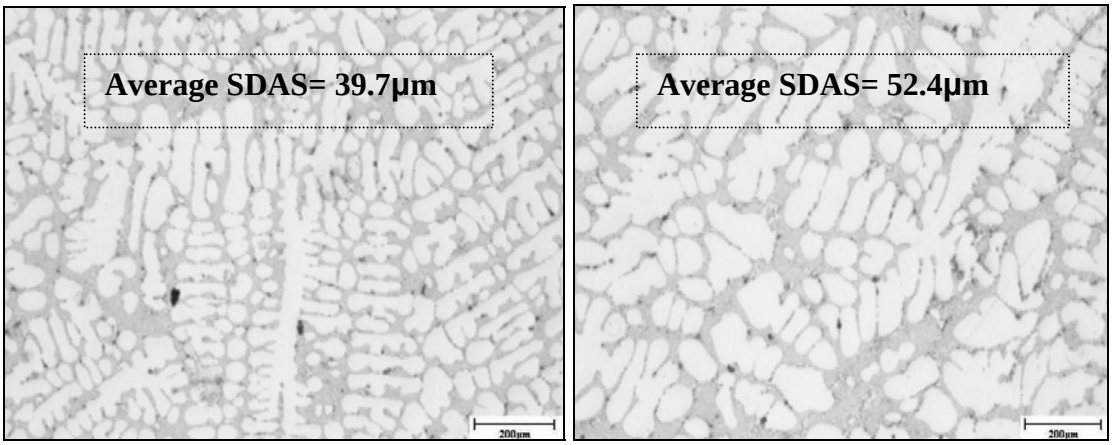

Figure 107: Dendrites at 37.5 mm and 52.5 mm

CastD2: Movable chill with cooling

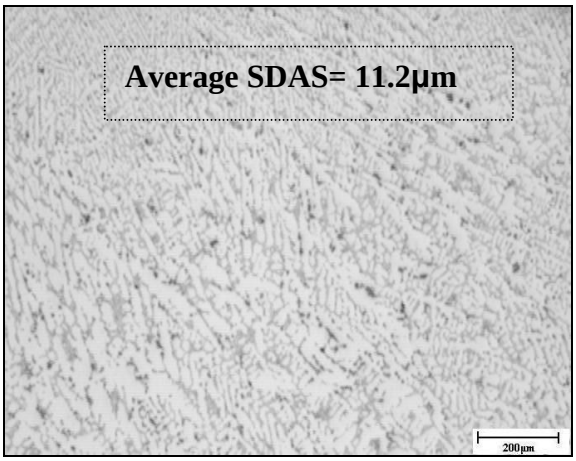

Figure 108: Dendrites at 2.5mm from the interface

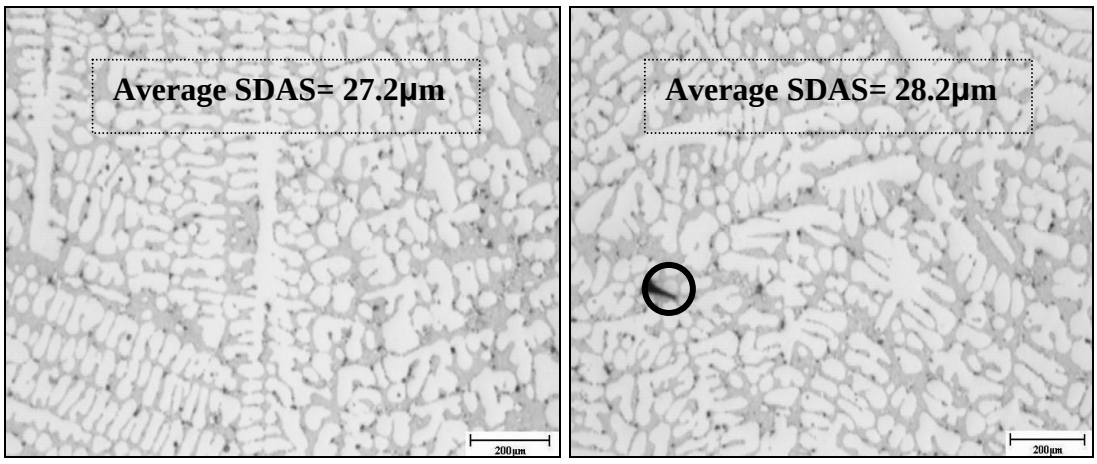

Figure 109: Dendrites at 7.5 mm and 15 mm

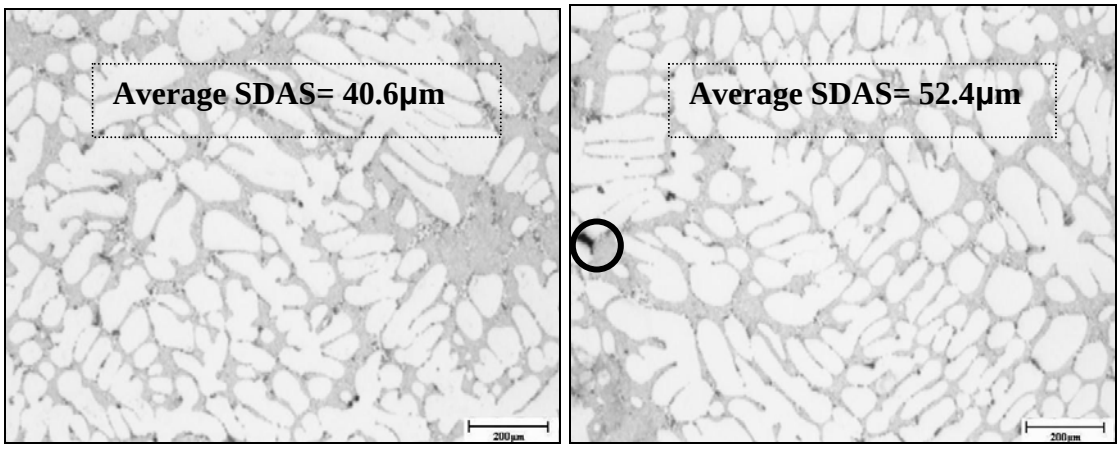

Figure 110: Dendrites at 37.5 mm and 52.5 mm

CastD3: Movable chill with cooling

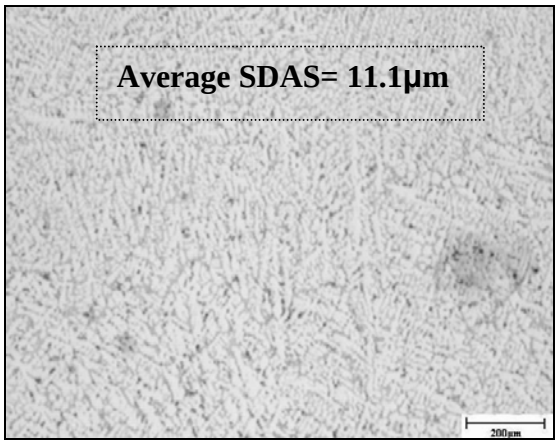

Figure 111: Dendrites at 2.5mm from the interface

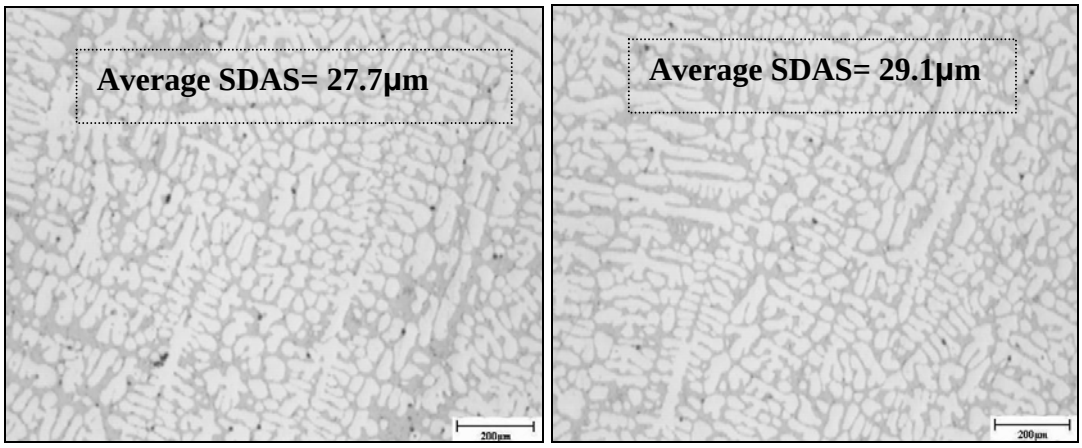

Figure 112: Dendrites at 7.5 mm and 15 mm

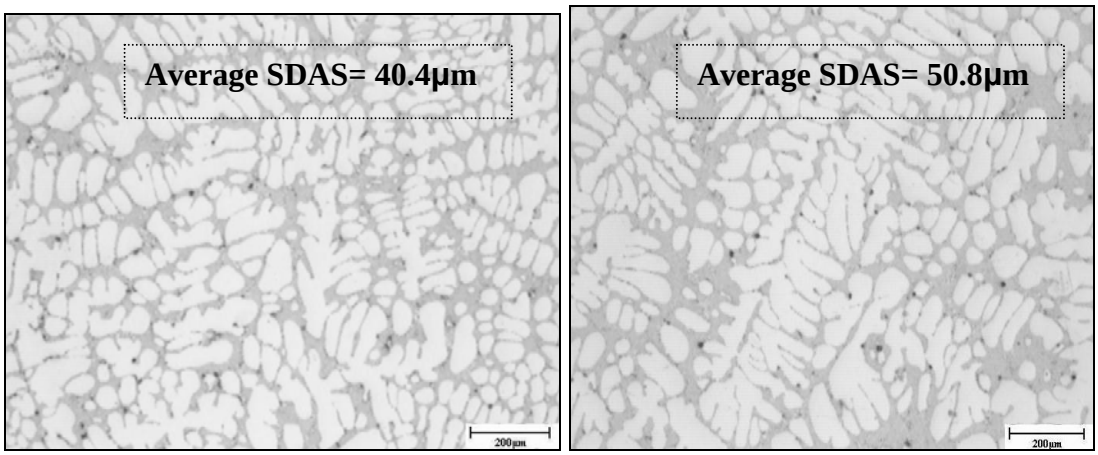

Figure 113: Dendrites at 37.5 mm and 52.5 mm

7 Discussion and analysis

7.1 Chill contact duration and casting temperature

It can be seen that from Figure 114 the chill contact duration for trials in scenario C is over 70% and for trials in scenario D is over 90 %. Another key observation is that percentage of contact for trials in scenario B ("fixed chill with cooling") is significantly lower than other chill conditions and in particular trials in scenario A (fixed chill without cooling).

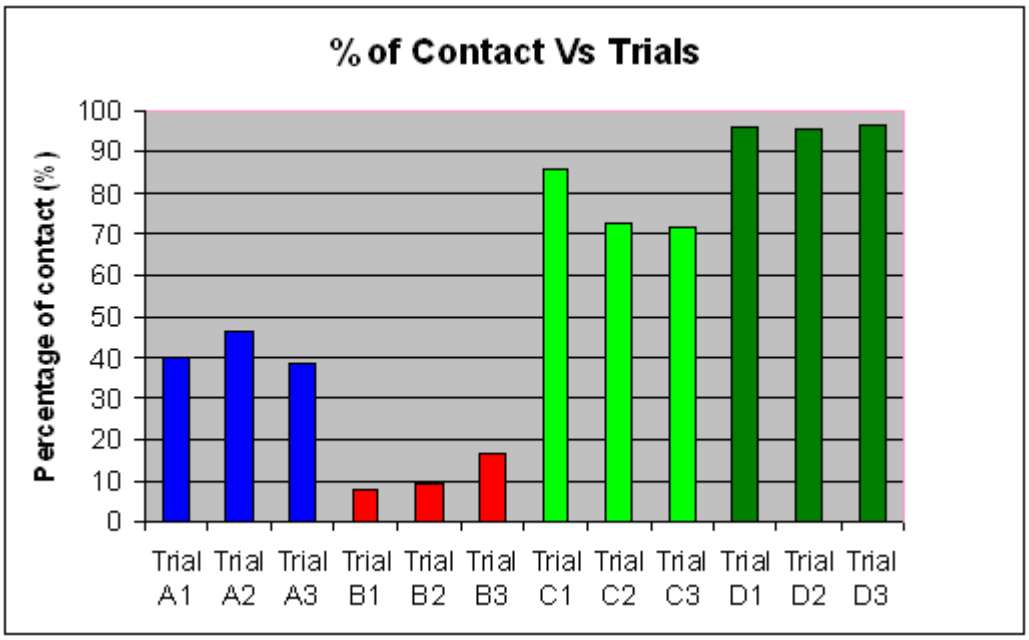

Figure 114: casting-chill contact percentage vs. chill conditions

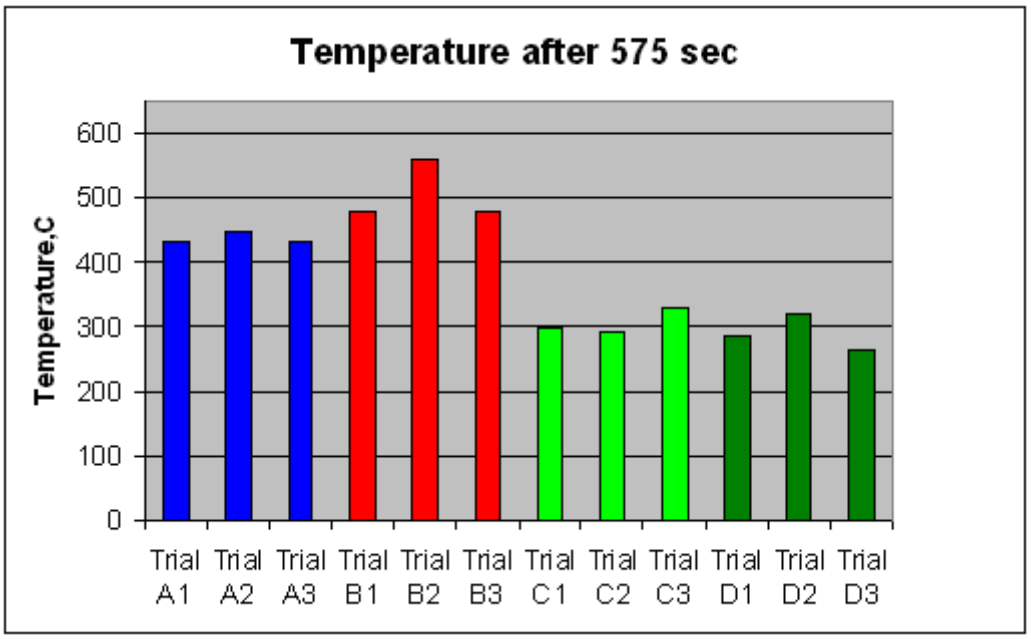

Figure 115: Casting temperature after 575 sec

The temperature of casting shows an inverse relationship with casting-chill contact duration (i.e. the higher the contact time the lower the temperature). Trials in scenario B show higher temperatures at 575 sec is found to be above 450 ˚C where as the movable chills have been capable of reducing the temperature below 300 ˚C for the same time duration. This is significant since this reduces solidification time thereby decreasing production time for a give casting.

7.2 Temperature during initial stages of solidification

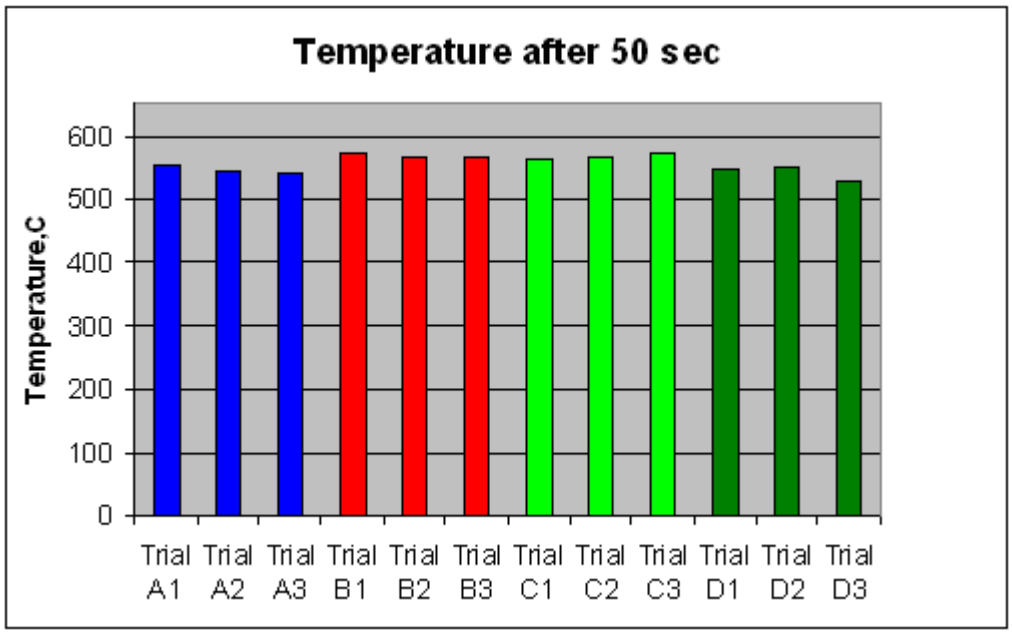

Figure 116: Temperature of casting after 50 sec of pouring

Figure 116 shows temperature of the casting after 50 seconds from pouring. It can be seen that the casting under scenario D has a faster rate of cooling compared to scenarios B and C. There is relatively less difference in temperature under scenarios B and C since in both cases the air gap initialisation took place at 30 seconds. But in case of scenario D the chill was in contact with the casting hence the there is a relatively faster cooling at the initial stages of solidification. Figure 117 shows temperature of the casting after 300 seconds of pouring. The temperature of the casting under scenarios C and D are below 400 ˚C.

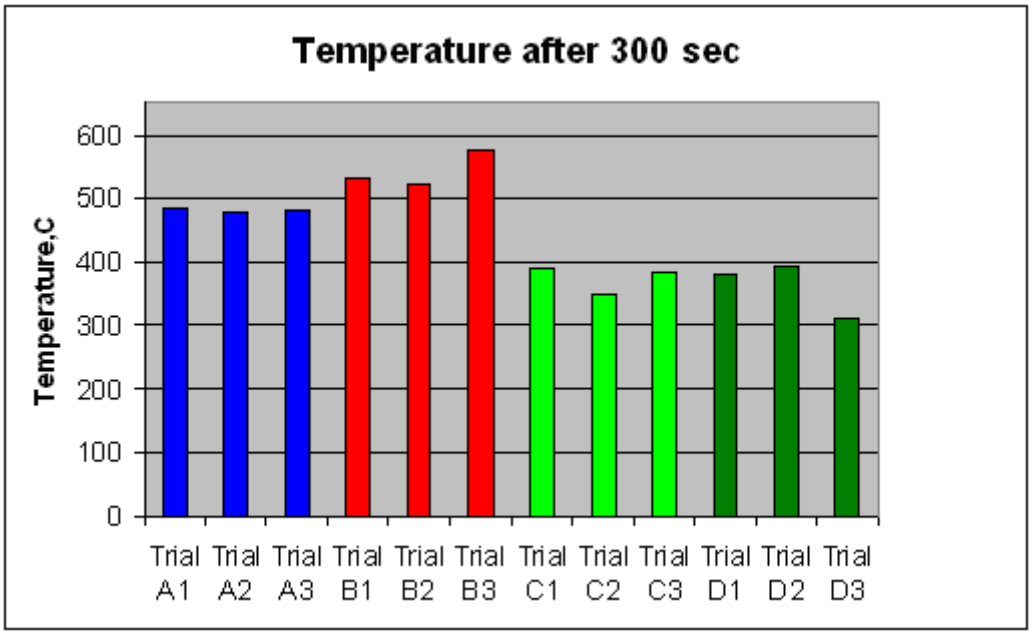

Figure 117: Temperature of casting after 300 sec of pouring

Figure 118 shows the casting temperatures under scenarios C and D at the end of 575 seconds to be below 300 ˚C whereas castings under scenarios A and C are above 400˚C. The differences in temperatures are due to the higher contact time the chill is maintained with the solidifying casting to reduce the air gap.

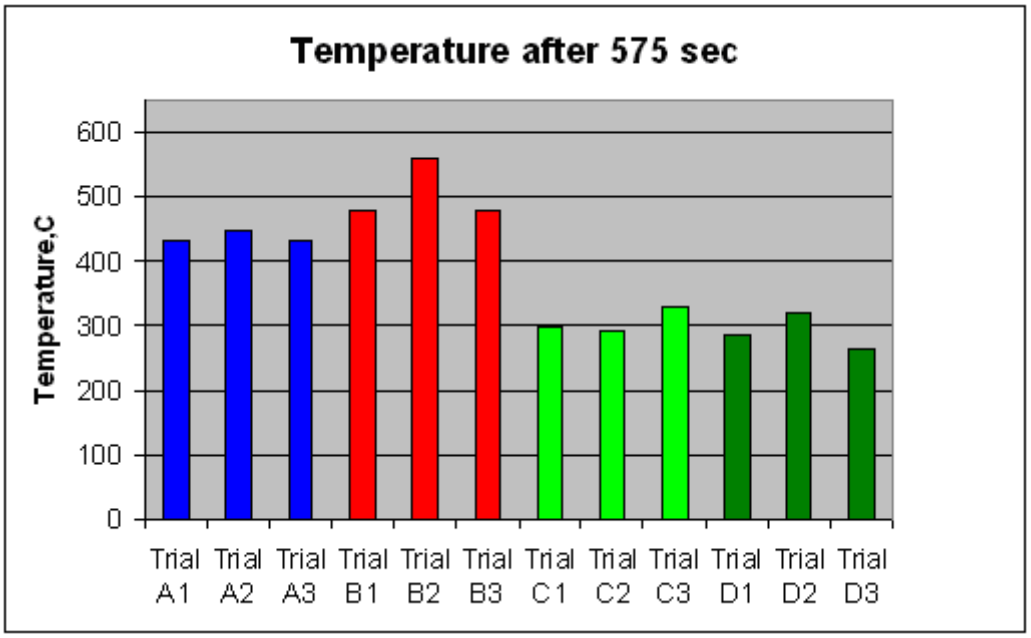

Figure 118: Temperature of casting after 575 sec of pouring

7.3 Effective cooling calculation

This section describes the effective cooling calculation for various cooling scenarios.

To calculate cooling effectiveness of each chill condition an average temperature at 575 seconds is calculated as shown below;

For scenario A

$$A_{avg_temp} = \frac{A1_{575} + A2_{575} + A3_{575}}{3} = \frac{431.9 + 445.2 + 430.7}{3} = 436.6^{\circ}\mathrm{C} \qquad \textbf{7.3.1}$$

For scenario B

$$B_{avg_temp} = \frac{B1_{575} + B2_{575} + B3_{575}}{3} = \frac{477.8 + 557.8 + 477.8}{3} = 504.45^{\circ}\mathrm{C} \qquad 7.3.2$$

For scenario C

$$C_{avg_temp} = \frac{C1_{575} + C2_{575} + C3_{575}}{3} = \frac{297.7 + 292.4 + 329.2}{3} = 306.4^{\circ}\mathrm{C} \qquad 7.3.3$$

For scenario D

$$D_{avg_temp} = \frac{D1_{575} + D2_{575} + D3_{575}}{3} = \frac{285 + 319.7 + 263.6}{3} = 289.4^{\circ}\mathrm{C} \qquad 7.3.4$$

To make a direct comparison of cooling effectiveness between scenario C and D is made with scenario B;

Effectiveness of cooling under scenario C;

$$E_{eff} = \frac{B_{avg_temp} - C_{avg_temp}}{B_{avg_temp}} \times 100 = \frac{504.5 - 306.4}{504.5} \times 100 = 39.2\% \qquad \textbf{7.3.5}$$

Effectiveness of cooling under scenario D;

$$E_{eff} = \frac{B_{avg_temp} - D_{avg_temp}}{B_{avg_temp}} \times 100 = \frac{504.5 - 289.4}{504.5} \times 100 = 42.6\% \qquad \textbf{7.3.6}$$

The above calculations indicate that the scenario C and D are 39.2 % and 42.6 % more effective compared to scenario B.

7.4 Average SDAS at different locations

Below graphs compares the average SDAS between different chill scenarios with the respect to fixed distance from the chill end.

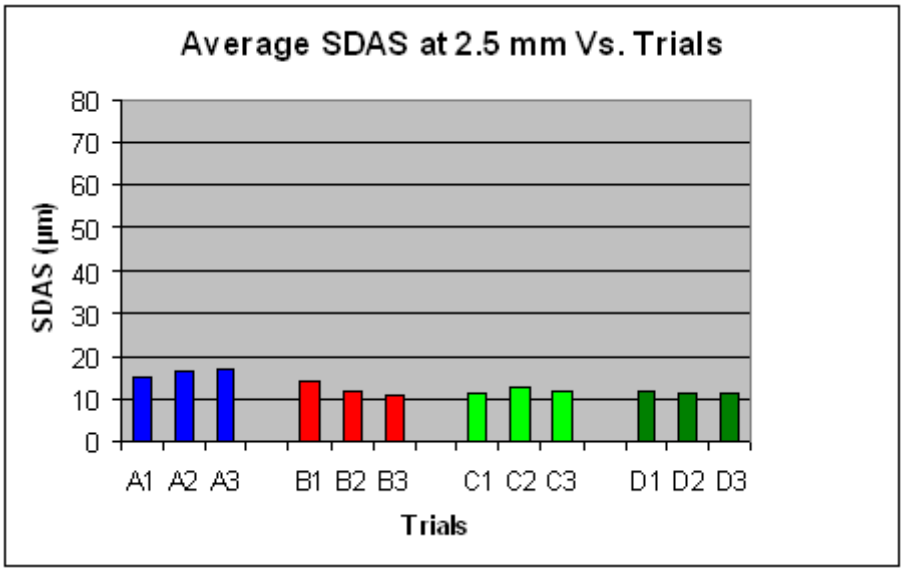

Figure 119: Average SDAS at 2.5 mm Vs. Trials

From Figure 119 it can be seen that at a distance of 2.5 mm from the chill end there is no significant difference in SDAS in scenario C and D. This suggests that effect of pushing the chill closer before eutectic temperature could not considerably reduce the SDAS.

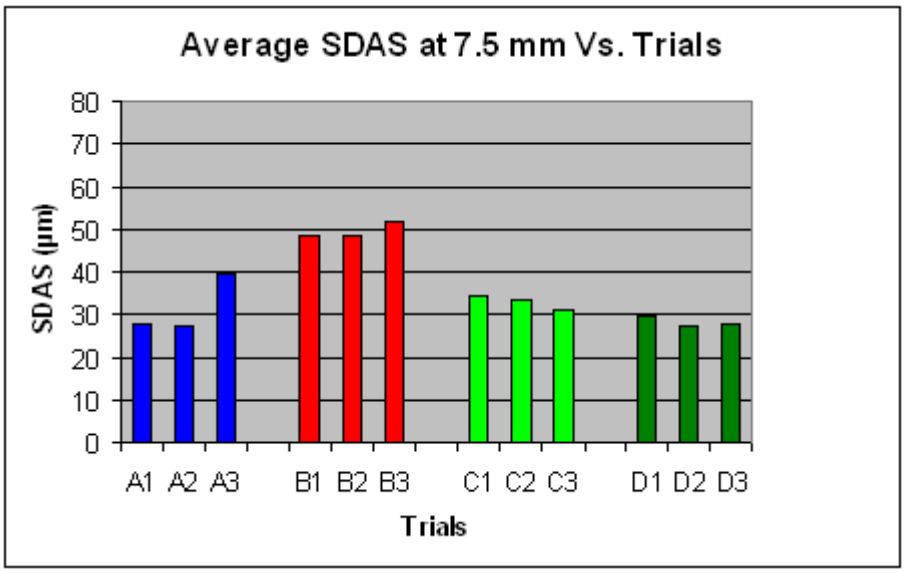

Figure 120: Average SDAS at 7.5 mm Vs. Trials

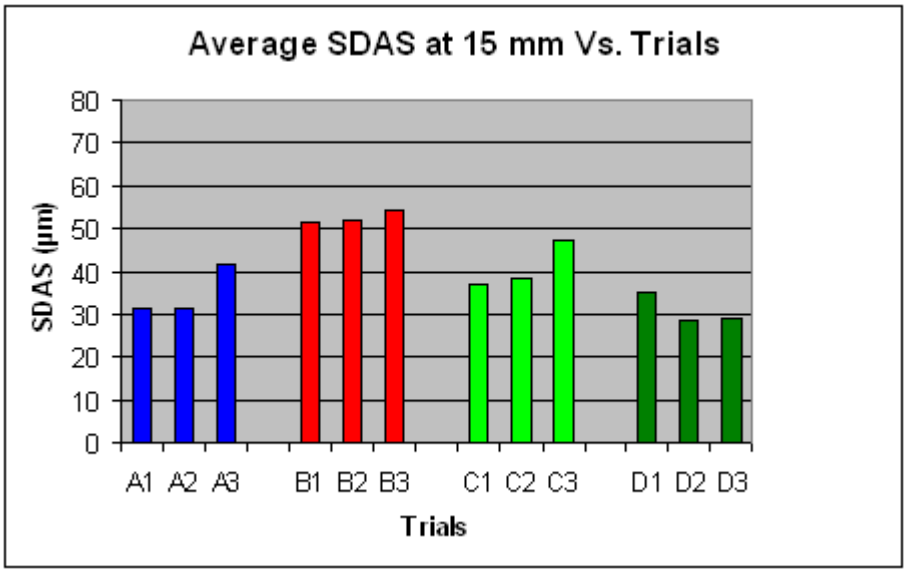

Figure 121: Average SDAS at 15 mm Vs. Trials

From Figure 121 it can be seen that there exists a significant SDAS reduction at a distance of 15 mm from the chill end.

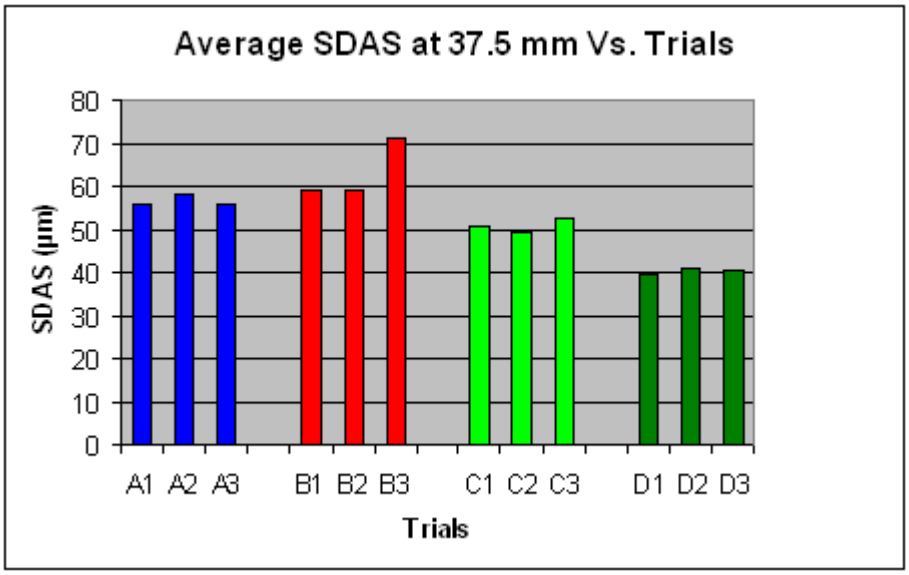

Figure 122: Average SDAS at 37.5 mm Vs. Trials

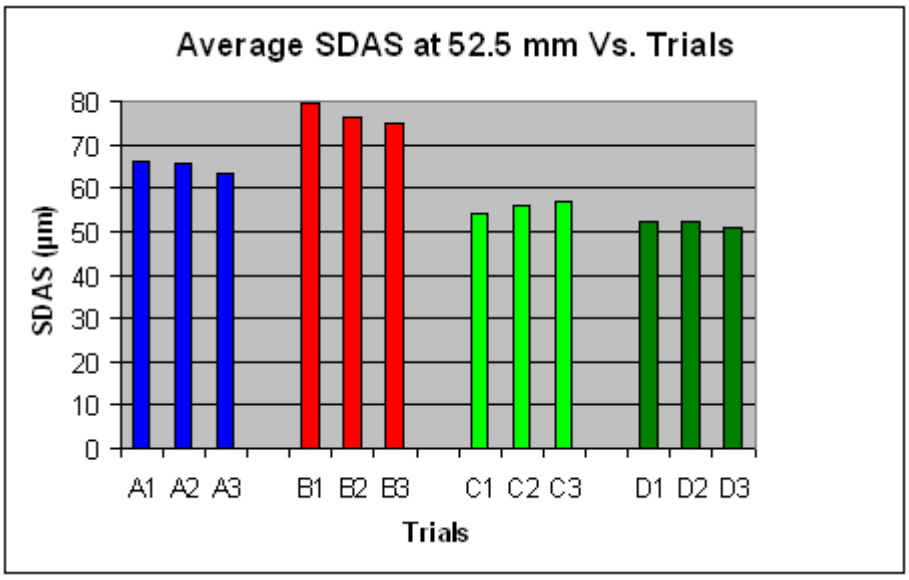

Figure 123: Average SDAS at 52.5 mm Vs. Trials

Figure 123 clearly shows the difference between scenario A, B, C and D. It can be concluded that the in scenario C and D the SDAS has reduced by 26 % compared to scenario B.

7.5 Porosity

It is in interest of this research to measure the quality of castings produced under different chill scenarios. Hence a measurement of porosity was used indicate the quality. The pores greater than 10 µm were located within a 500 µm X 500 µm area at predetermined locations within the casting. The pores were counted and tabulated as follows.

Experimental Condition	**Number of pores at 2.50 mm (>10 µm)**	**Number of pores at 7.50 mm (>10 µm)**	**Number of pores at 15.0 mm (>10 µm)**	**Number of pores at 37.5 mm (>10 µm)**	**Number of pores at 52.5 mm (>10 µm)**
A1	35	67	59	38	40
A2	42	71	76	37	42
A3	38	45	29	37	34

B1	45	88	78	49	53
B2	49	83	78	46	49
B3	52	60	77	58	51
C1	38	35	58	45	35
C2	36	37	43	44	39
C3	38	32	55	52	31
D1	34	41	32	31	29
D2	31	40	32	30	32
D3	28	29	18	33	30

Table 8: Porosity measurements in each casting sample.

Figure 124 shows the average number of pores measured at selected locations within the castings produced under different conditions. It can be seen that the average numbers of pores are much higher in condition B than condition C and D.

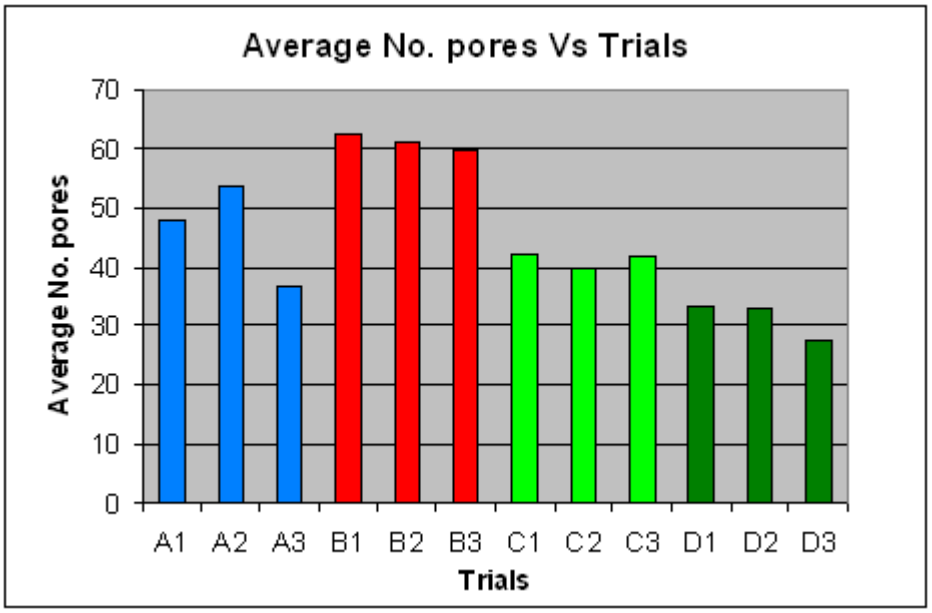

Figure 124: Average pores vs. Exp. Trials

7.6 Summary

A comparison is made between the percentage of contact time and the casting temperature. It is confirmed that the higher the contact times between the casting and chill, the lower the casting temperature. The temperature of castings produced under

experiment scenarios C and D have been significantly reduced by the movable chill by maintaining an effective contact. Chill scenario B was expected to the cool the casting faster than scenario A since scenario B was water-cooled. However, it was discovered from the temperature graphs that scenario B became ineffective due to the rapid formation of an initial air gap, providing an insulating barrier against further fast solidification.

Porosity measurements were performed to measure the quality of castings produced under each condition. It was found that castings produced under scenarios C and D had less porosity compared to casting produced under scenarios A and B. It was also found that porosity can be further reduced by moving the chill before eutectic temperature is reached in scenario D. Hence it could be concluded that the overall quality of the casting can be improved by enabling effective, continuous and sustained heat transfer through the technique of movable chills.

8 Summary of present research and findings

8.1 Chapter 1

Chapter 1 discusses the introduction to casting and casting techniques. This chapter also describes the problems that are associated with solidification. Unidirectional solidification can be achieved by proper cooling techniques. This chapter also identifies the problems with the conventional cooling circuit that is used to control the solidification of Ford automotive wheels (which is the motive behind the present research).

8.2 Chapter 2

In chapter 2 previous works relating to air gap measurements, interfacial heat transfer coefficients, solidification and computer simulation by different researchers have be studied and described. This chapter provided valuable information regarding the size of the air gap that could occur in a given casting sample. It also gave a significant understanding about the techniques other researchers have adopted.

8.3 Chapter 3

Chapter 3 describes the experimental setup such as mold, chill, thermocouple installation, measurement error and calibration techniques etc. This section describes the methodology in which the casting trials were carried out.

8.4 Chapter 4

Chapter 4 presents the temperature data and air gap signal data obtained from the temperature data logger and the air gap signal indicator. It shows a direct comparison between the temperature curve and the air gap curve. A relationship can be observed from either curve. The raw temperature obtained from the data logger was combined with the errors and are plotted with error bands.

8.5 Chapter 5

After obtaining the temperature a computer model was created using a finite element casting simulation package ProCAST^{TM}. An inverse optimization method (OPTCAST^{TM}) is used to calculate the interfacial heat transfer coefficient using the measured temperature from chapter 4. The resulting heat transfer curve is then plotted and compared along with temperature and air gap signal. From chapter 5 it can be

concluded that there has been a significant higher rate of heat transfer in scenario C and D compared to scenario B.

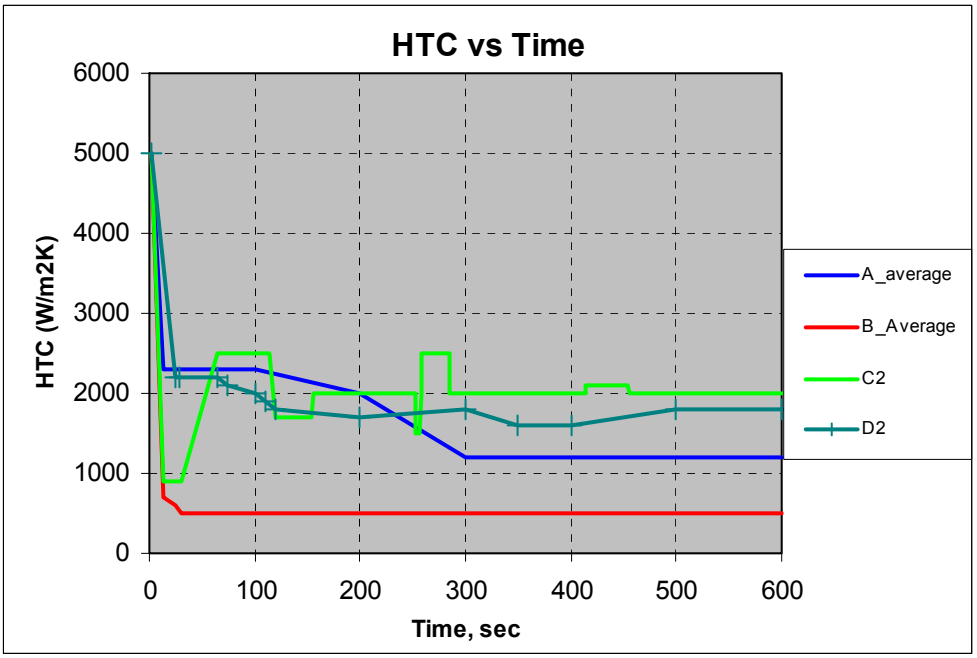

Figure 125: HTC vs time showing higher HTC for scenario C and D

8.6 Chapter 6

It is well known that the faster cooling rate of aluminium silicon alloys can effectively reduce the size of the SDAS. From the current research point of view it is important to demonstrate the effect of effectiveness by new cooling technique on SDAS for the test casting samples. The given casting samples were cut into small pieces and their SDAS measurement were taken and presented in this chapter. It can be observed from the SDAS data that the size of the DAS has reduced by above 26.6 % in scenario C and 30.2 % in D compared to scenario B. Also number of porosity within a given area of the sample was used as a measure to indicate the quality of castings produced under improved cooling technique (scenario C and D).

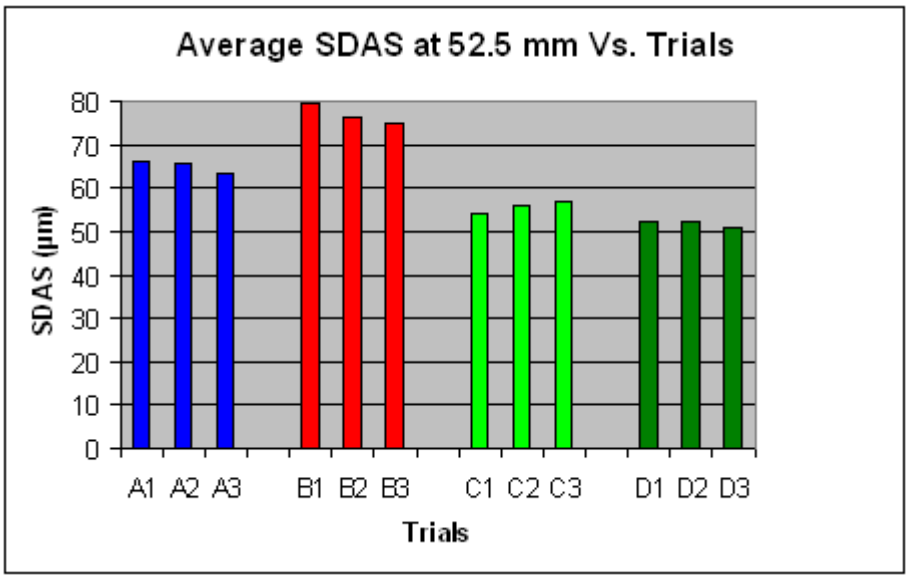

Figure 126: SDAS at 52.5 mm showing 26% reduction in dendrite sizes for scenario C and 30 % reduction for scenario D compared to scenario B.

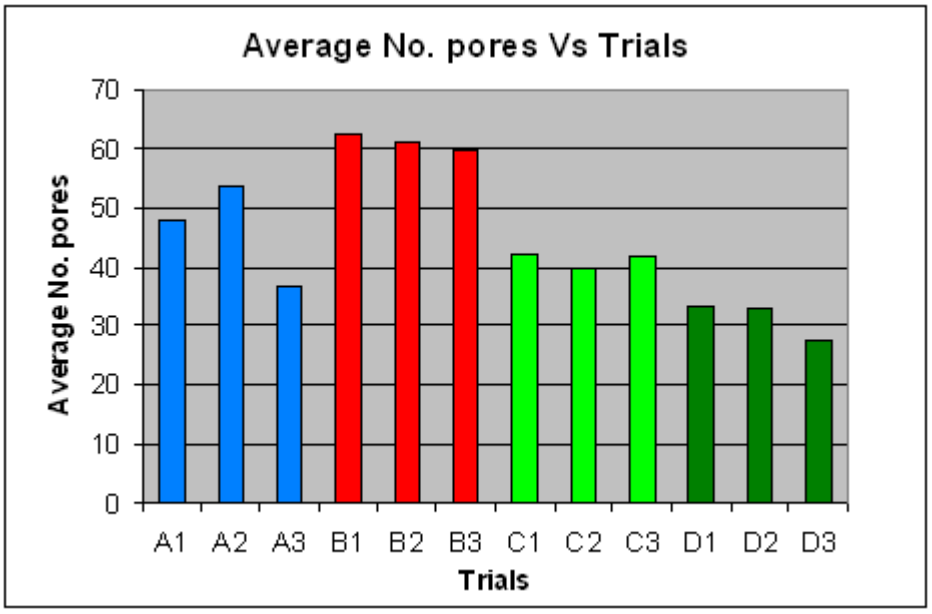

Figure 127: Average No. of porosities showing 27 % reduction in No. of pores in scenario C and 53 % reduction in scenario D compared to scenario B

9 Conclusion

Aluminium A356 alloy was cast in a ceramic mold and cooled from one end using a copper chill. Different casting cooling conditions were analysed using fixed and movable chills by measuring multiple thermal histories and air gap signals and plotted from Figure 42 to Figure 53. A computer model was created using ProCAST^{TM} and interfacial heat transfer coefficients were calculated using an inverse modelling technique. Micro-structural analyses of the sample castings were performed at different distances from the interface of the casting-chill and the corresponding secondary dendrite arm spacings are plotted in Figure 77

From this work following findings are made

1. It was previously believed that a fixed chill design with cooling (scenario A) would extract heat more effectively than without cooling. However, the presented experiments have proven that it actually becomes ineffective after a rapid development of an initial air gap. This is believed to be as a result of sudden freezing of the metal as the casting comes in contact with the water cooled chill.

2. The air gap formation can be reduced using a movable chill and higher heat removal rate could be achieved, thereby reducing the solidification time and hence improving the productivity of a given casting. The effective cooling with movable chill with cooling has increased by 40 % compared to fixed chill which is currently being used in the industry.

3. The size of SDAS was reduces from 76.99 μm (average SDAS of condition B) in fixed chill with cooling to 51.87 μm (average SDAS of condition D) in case of movable chill with cooling. The results show that the size of SDAS in with movable chills can be reduced by up to 26 % compared to fixed chills. Further it is observed that dendrite arm spacing can be refined by effective heat transfer during initial stage of solidification as in scenario D. The SDAS sizes are reduced to 32 % compared to scenario B.

4. The number of porosity (> 10 μm) in castings produced under condition C and D are less than condition B and A. This indicates that better quality casting can be

produced by new improved cooling technique. The average number of porosity has reduced by 27 % in scenario C and 50 % in scenario D compared to scenario B.

10 Future development

From the current research it can be seen that movable cooling chills are more effective in extracting heat from the casting. The quality of casting with a movable chill has improved in terms of microstructure and porosity. However a perfect contact (between casting and chill) has not been achieved by movable chills. Further work needs to be done to measure, model and improve the quality of contact between the casting and the chill. Industrial trials need to be conducted to study the cooling effectiveness of movable chills in overall castings as much as localised regions. Also it would be necessary to understand the impact of the new cooling technique on complicated casting geometries.

Further work also needs to be done to develop a control mechanism that could sense air gap formation at the interface and provide a quick response signal to an actuator to provide adequate displacement to the movable chill. Such systems could be based on air gap formation, temperature or time.

Development of such improved cooling technique would provide casting die designers more flexibility not only in terms of complex geometrical shapes but also better control of the solidification sequence in a given casting thus allowing it solidify in a directional manner and improving the structural integrity of the casting. From this research it can also be seen that the solidification time can be reduced by fast and effective cooling which could reduce the production time.

Appendices

Appendix A Composition of alloy used

Alloy specification	Al	Si	Fe	Cu	Mg	Zn	Ti
A356	91.75 %	6.5-7.5 %	0.2 %	0.05 %	0.05 %	0.05%	0.2 %

Table 9: Composition of alloy used

Appendix B Composition of the mold

Mold Composition (Dense fused silica)	
Silicon Dioxide (SiO_2)	99.60%
Aluminium Oxide (Al_3O_2)	0.30%
Titanium Dioxide (TiO_2)	0.01%
Iron Oxide (Fe_2O_3)	0.02%
Calcium Oxide(CaO)	0.02%
Magnesium Oxide (MgO)	0.02%

Table 10: Mold composition

Appendix C Physical Properties of the mold

Bulk density	1760 - 1950 kg/m³	114 - 118 lbs/ft³
Peak temperature	1650°C	3000°F
Sustained loads	1090°C	2000°F
Coefficient of thermal expansion	0.5 - 0.7 x 10^{-6} mm/ mm/°C	0.3 - 0.4 x 10-6 in/in/°F (max.)
Modulus of rupture	17 - 20 x 10^6 N/m²	2500 - 2900 lbs/in²
Cold crushing strength	48 - 51 x 10^6 N/m²	7000 - 7500 lbs/in²
Thermal conductivity	0.8 W/(m . K) at 13°C mean	5.8 BTU-in/hr/ft²/°F at 55°F mean
Apparent porosity	8% - 10%	

Figure 128: Properties of dense fused silica mold (reproduced from Pyrotek manual)

Appendix D Drawings of mold chill assembly

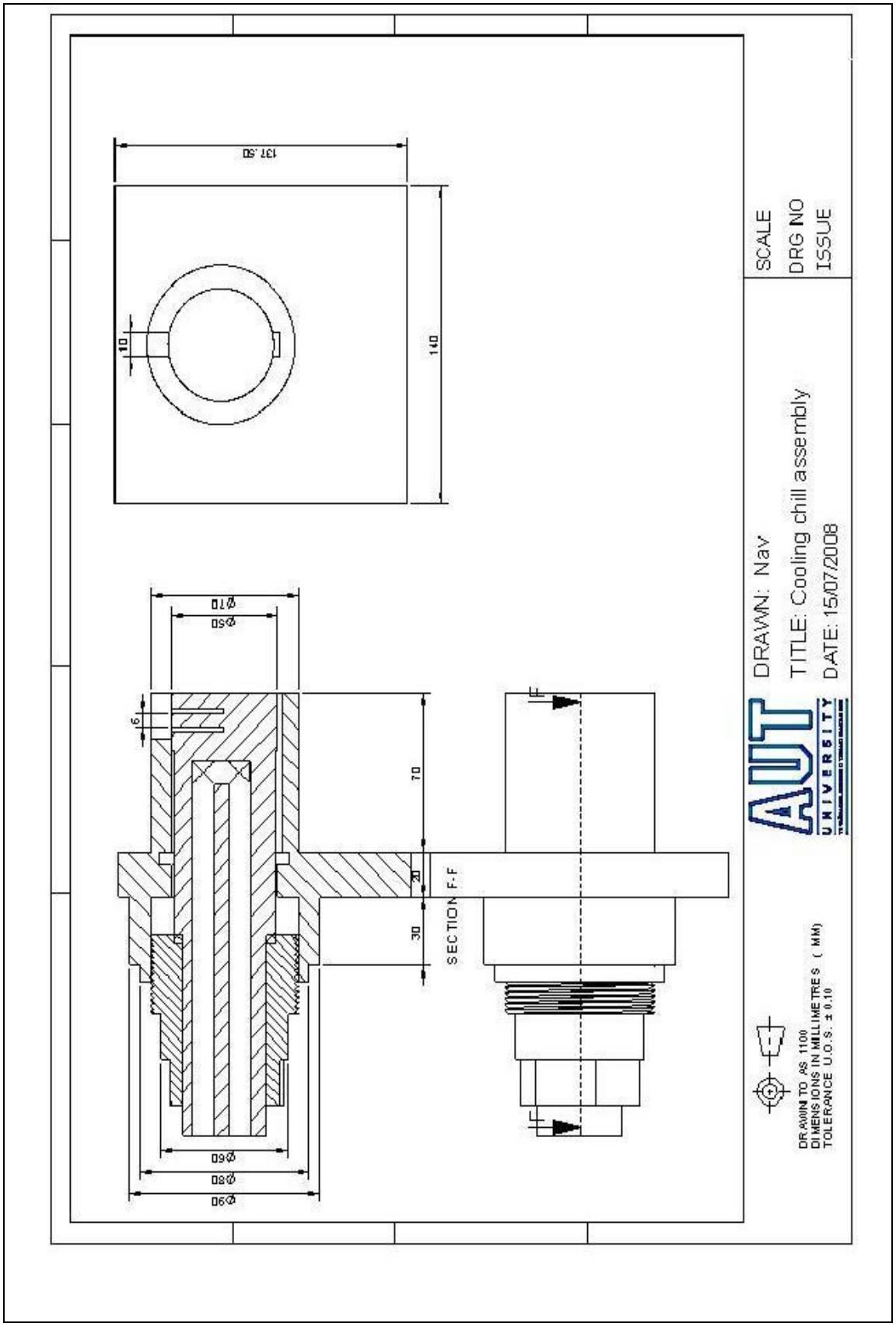

Figure 129: cooling chill assembly

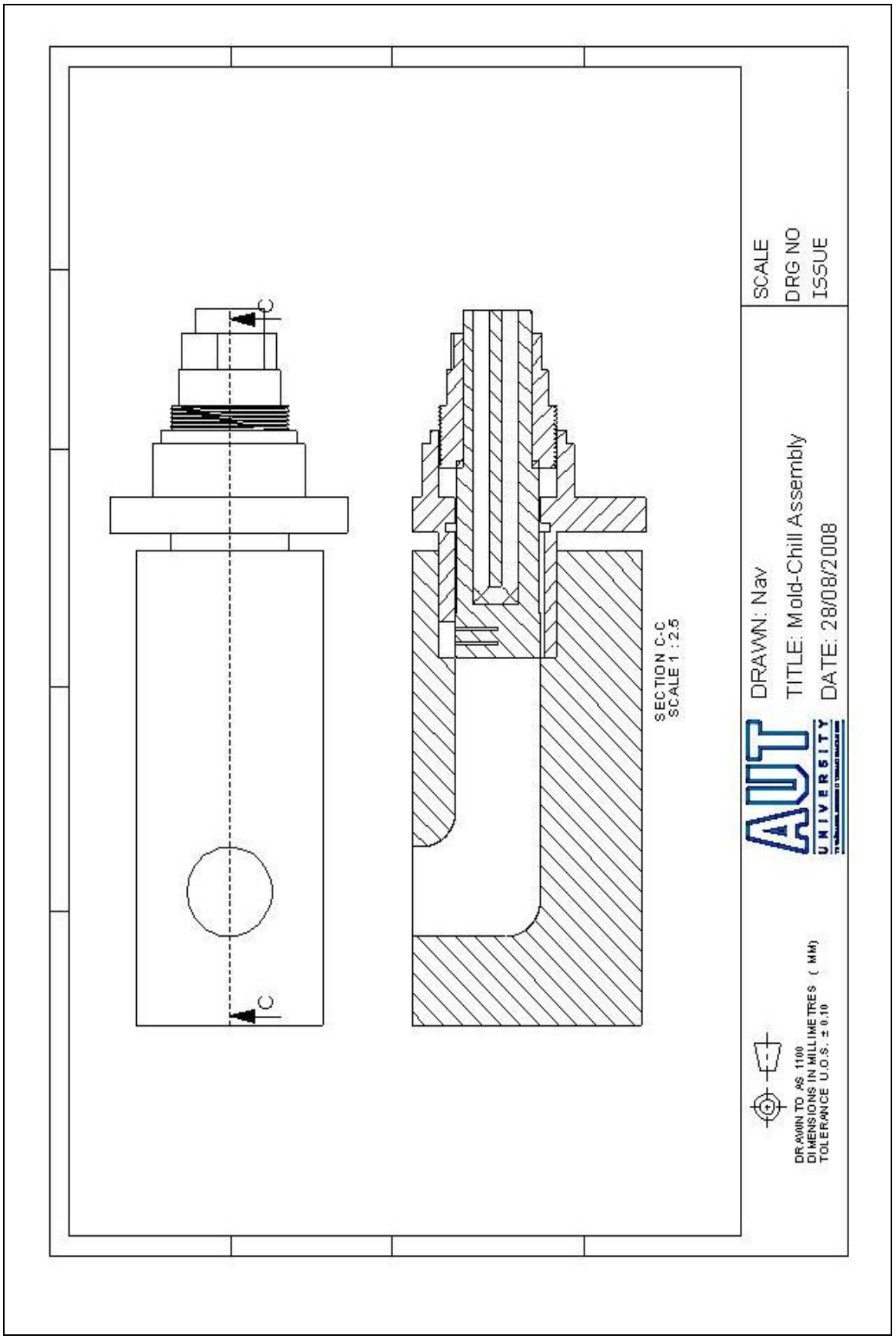

Figure 130: Chill mold assembly

Appendix E Air gap signals

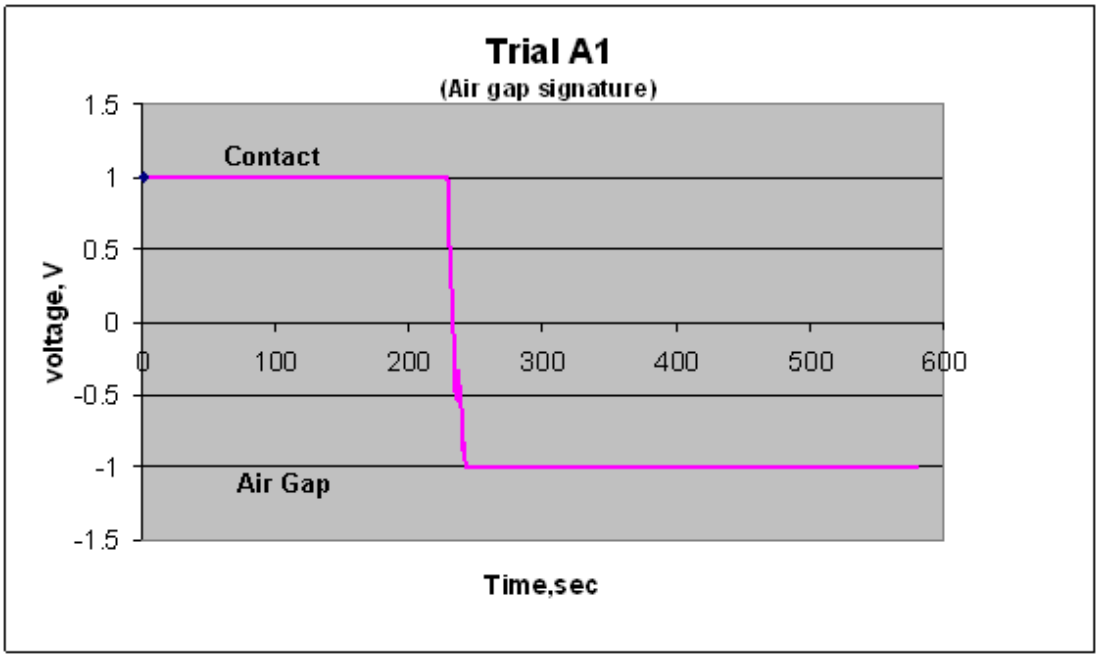

Figure 131: Air gap signal for Trial A1

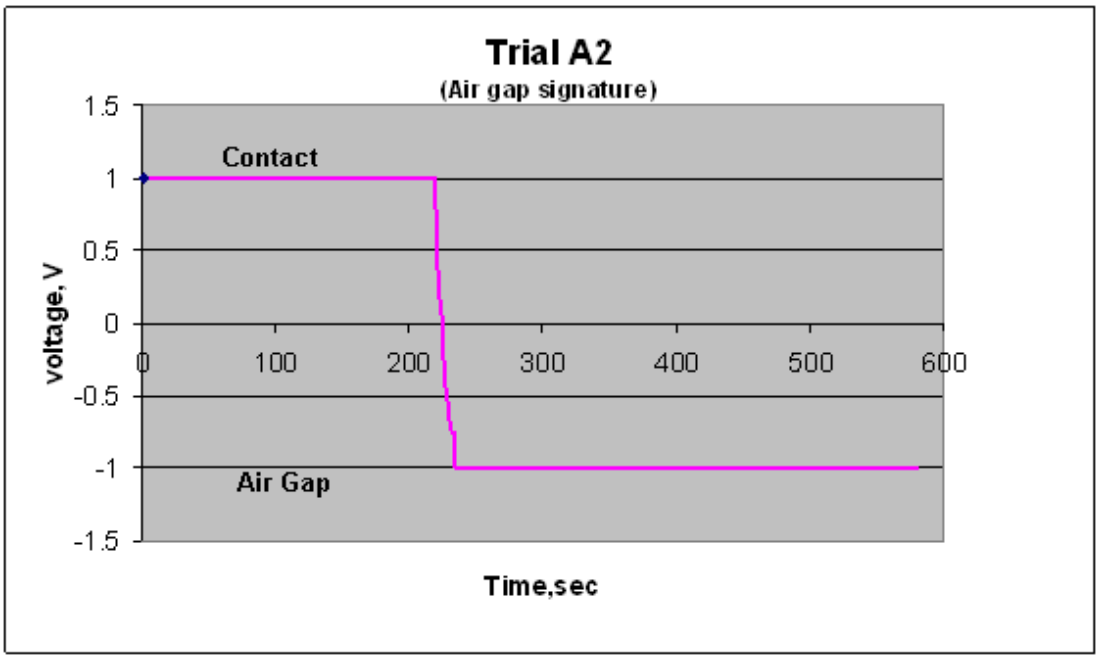

Figure 132: Air gap signal for Trial A2

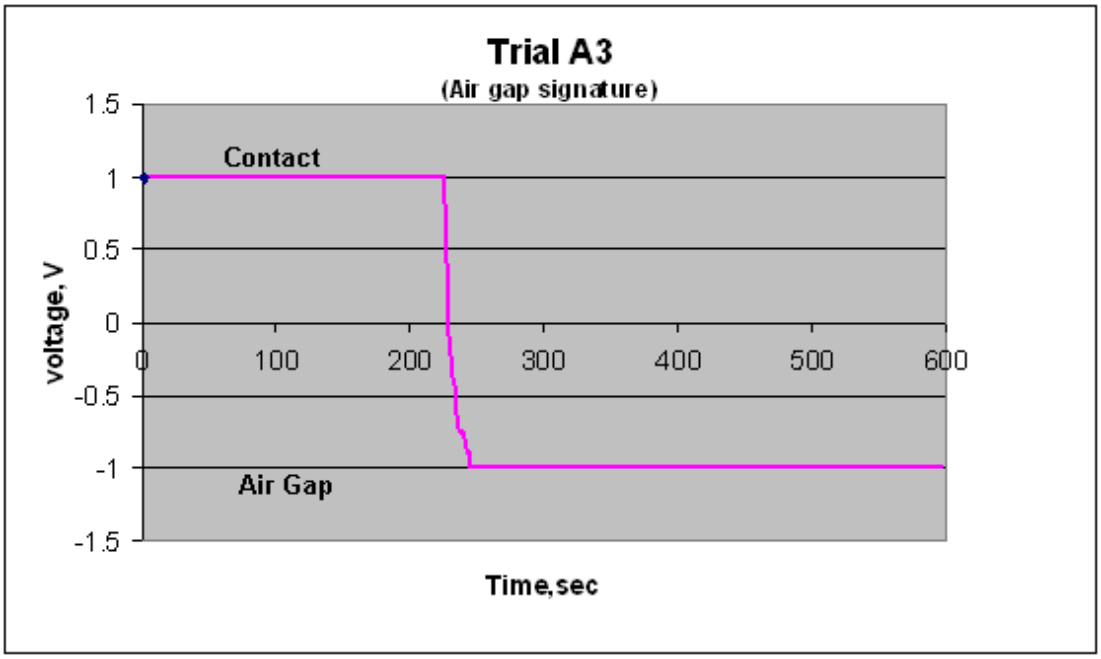

Figure 133: Air gap signal for Trial A3

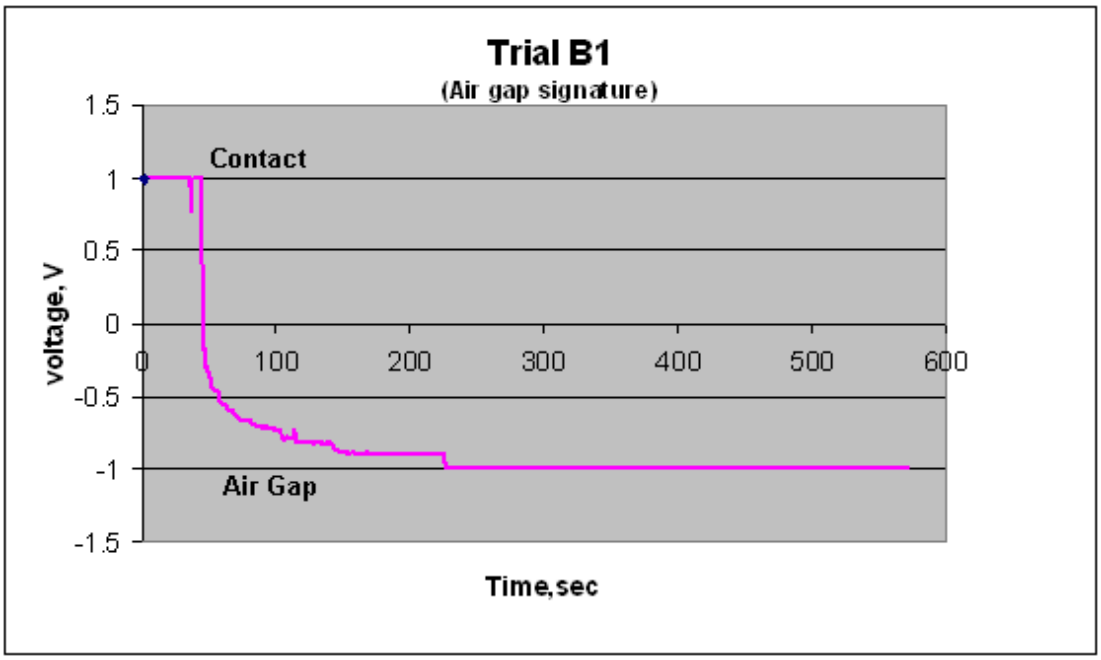

Figure 134: Air gap signal for Trial B1

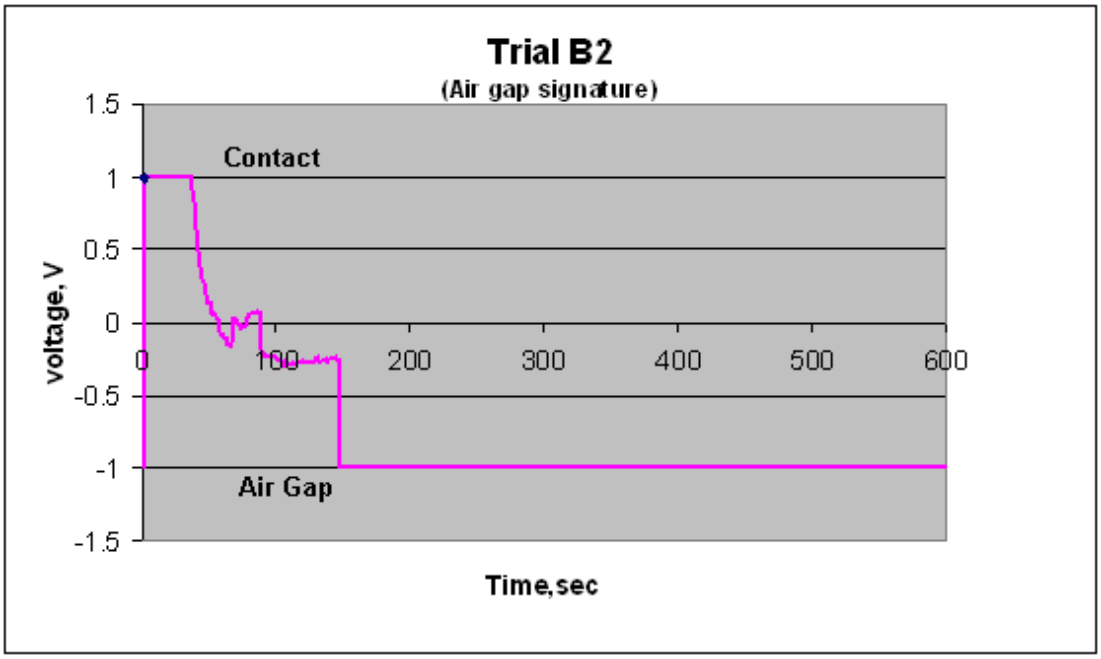

Figure 135: Air gap signal for Trial B2

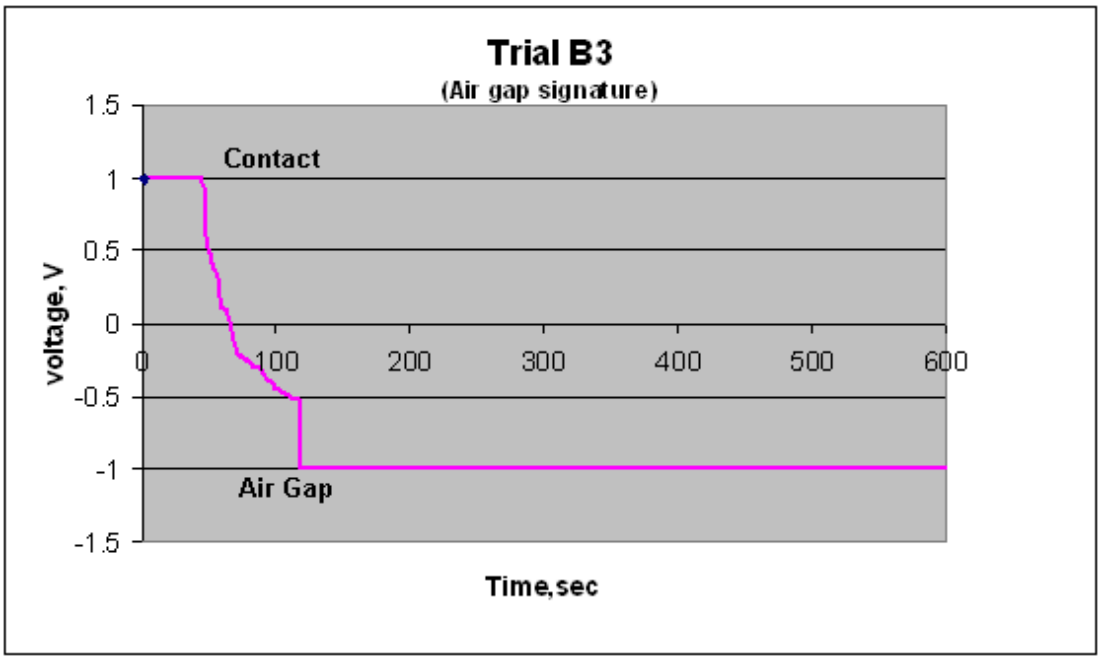

Figure 136: Air gap signal for Trial B3

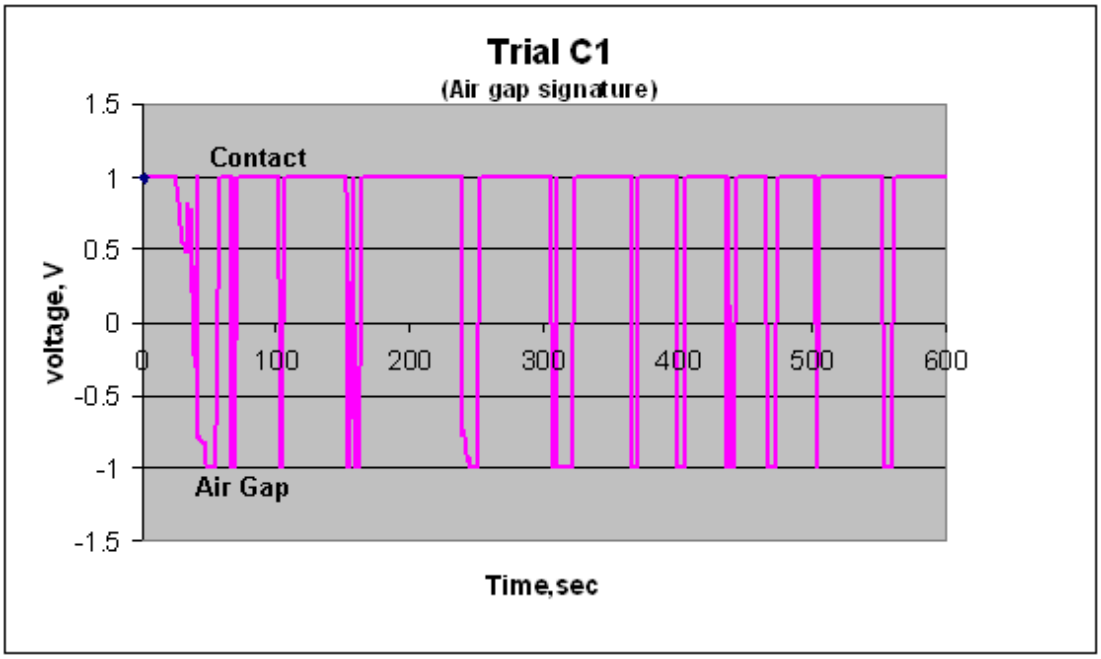

Figure 137: Air gap signal for Trial C1

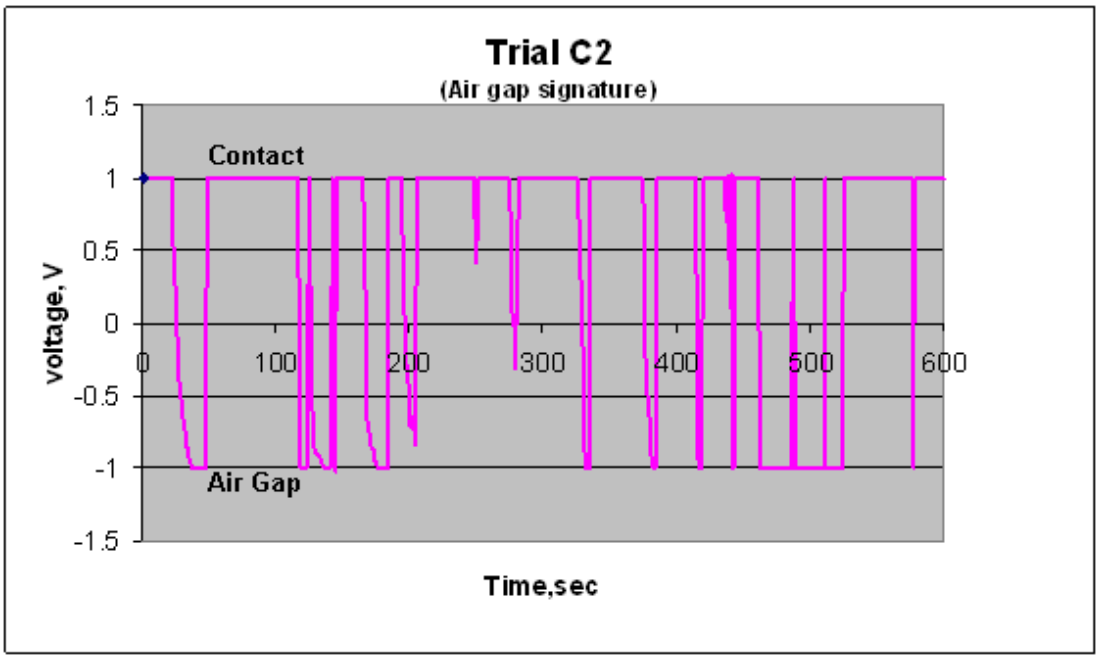

Figure 138: Air gap signal for Trial C2

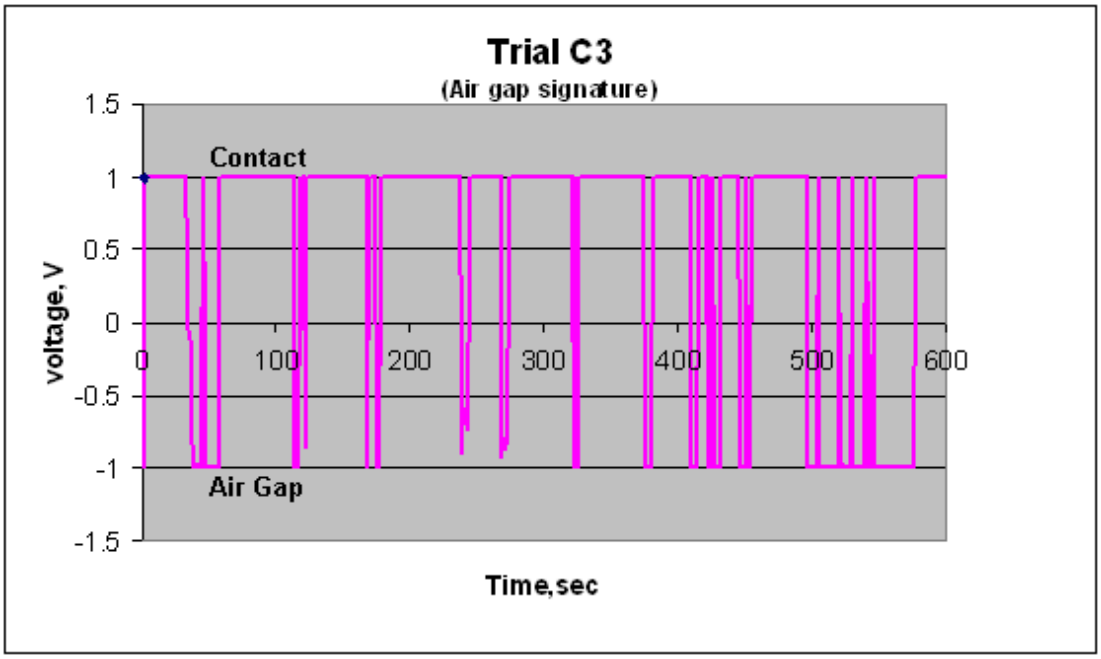

Figure 139: Air gap signal for Trial C3

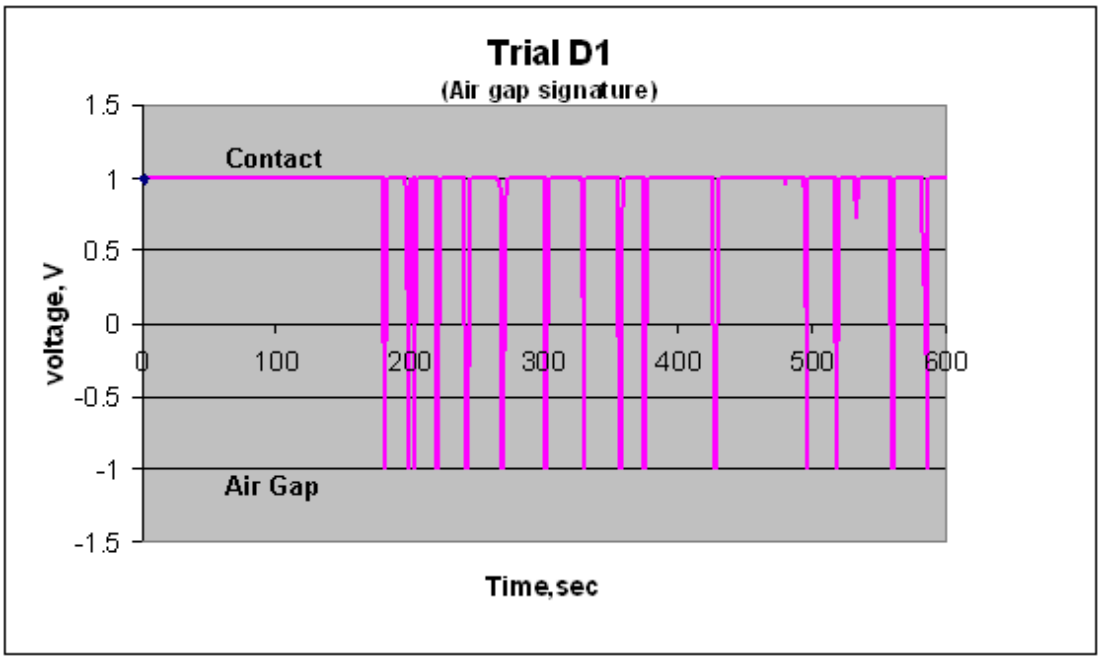

Figure 140: Air gap signal for Trial D1

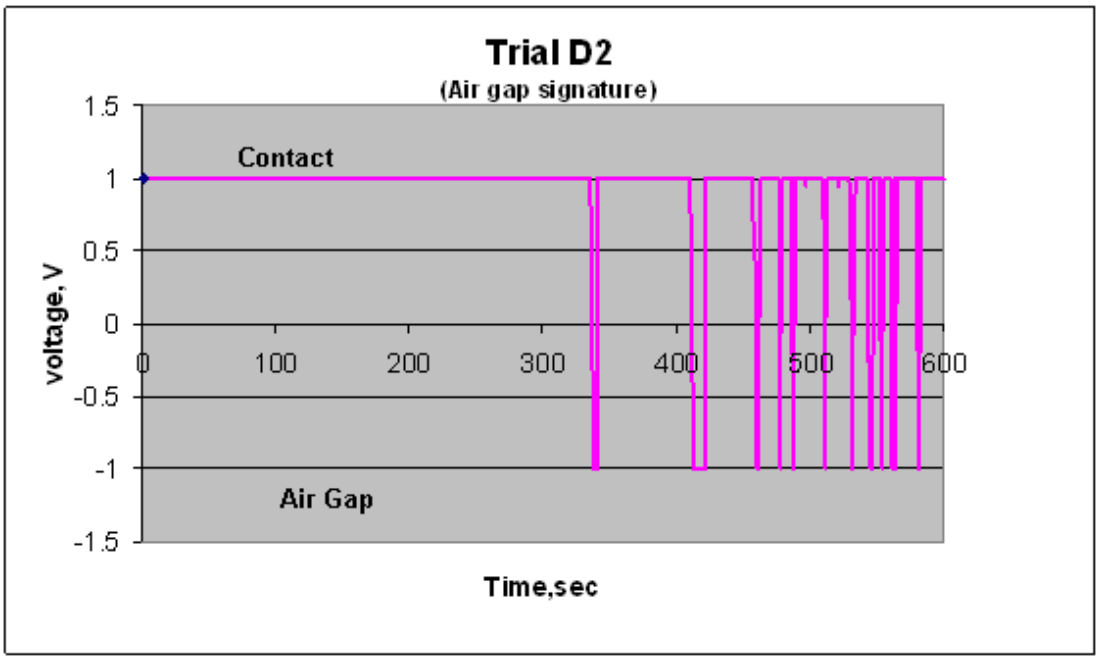

Figure 141: Air gap signal for Trial D2

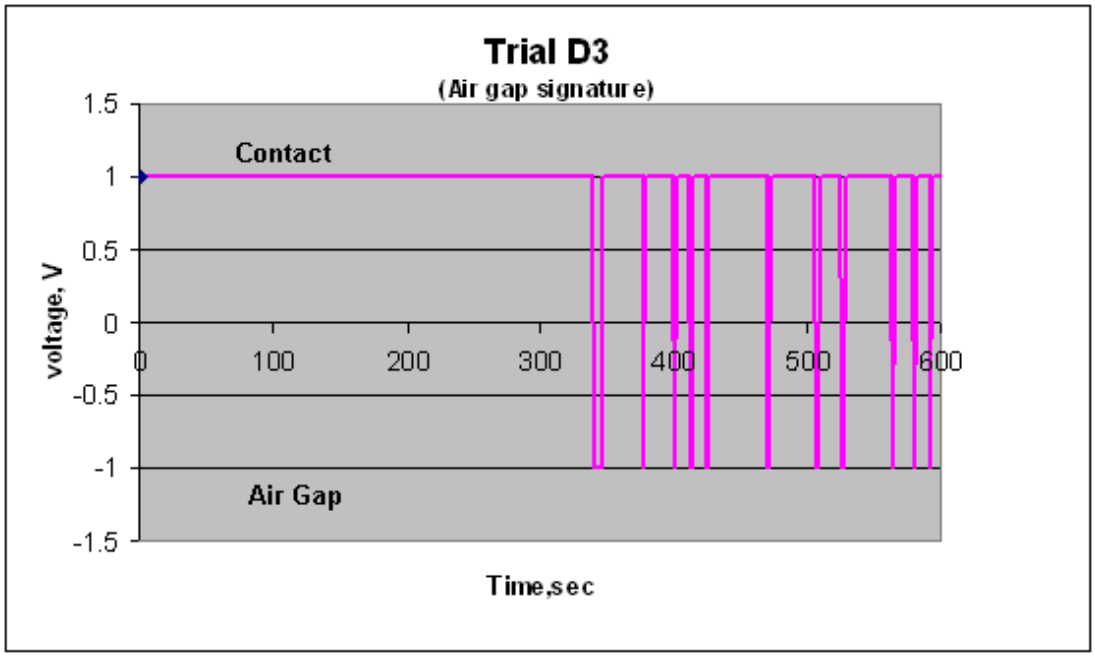

Figure 142: Air gap signal for Trial D3

Appendix F SDAS vs. Interface distance for different trials

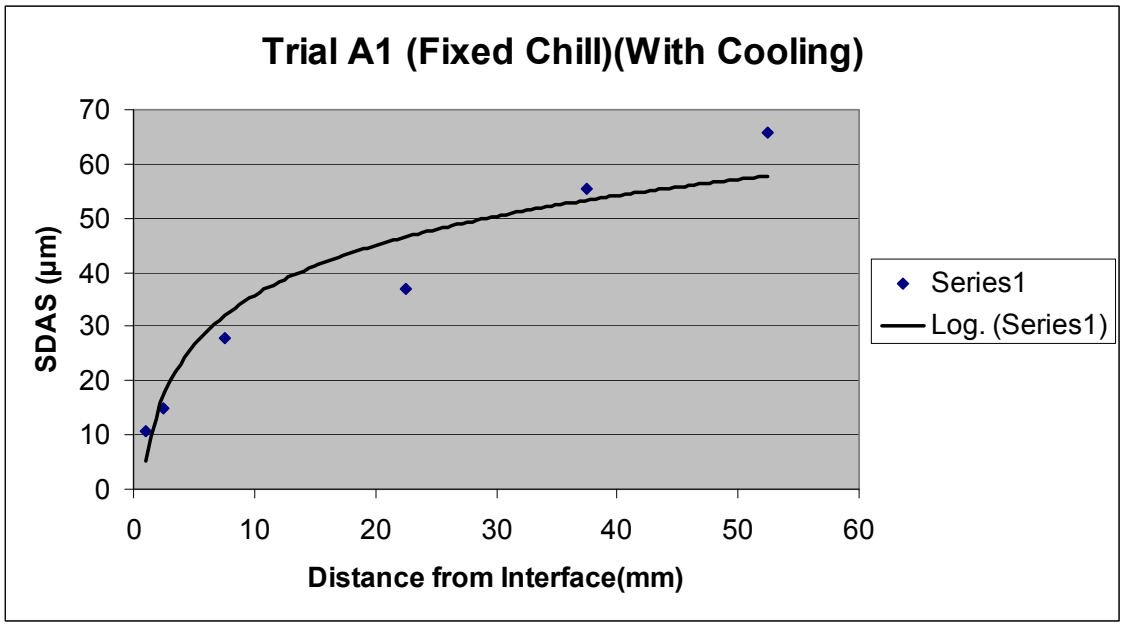

Figure 143: Average SDAS vs. Interface Distance for Trial A1

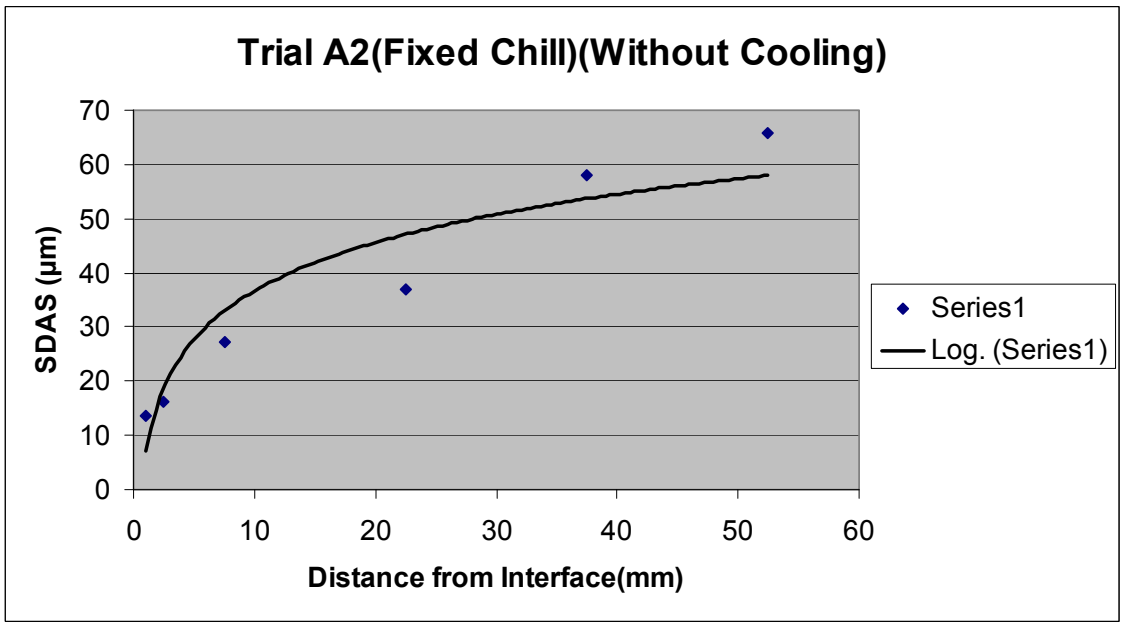

Figure 144: Average SDAS vs. Interface Distance for Trial A2

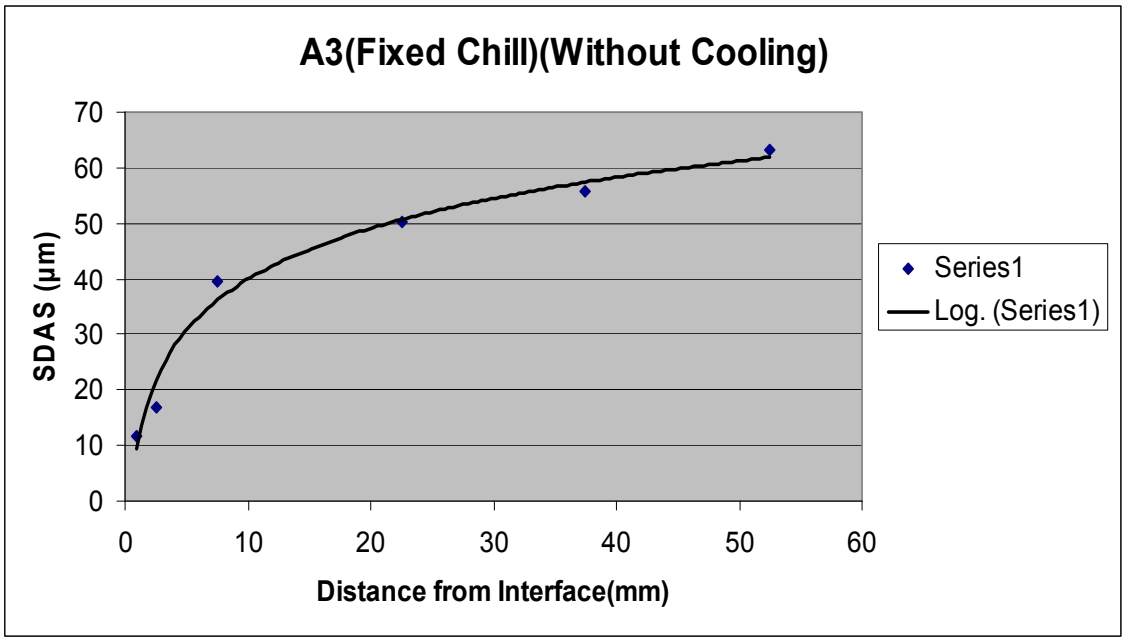

Figure 145: Average SDAS vs. Interface Distance for Trial A3

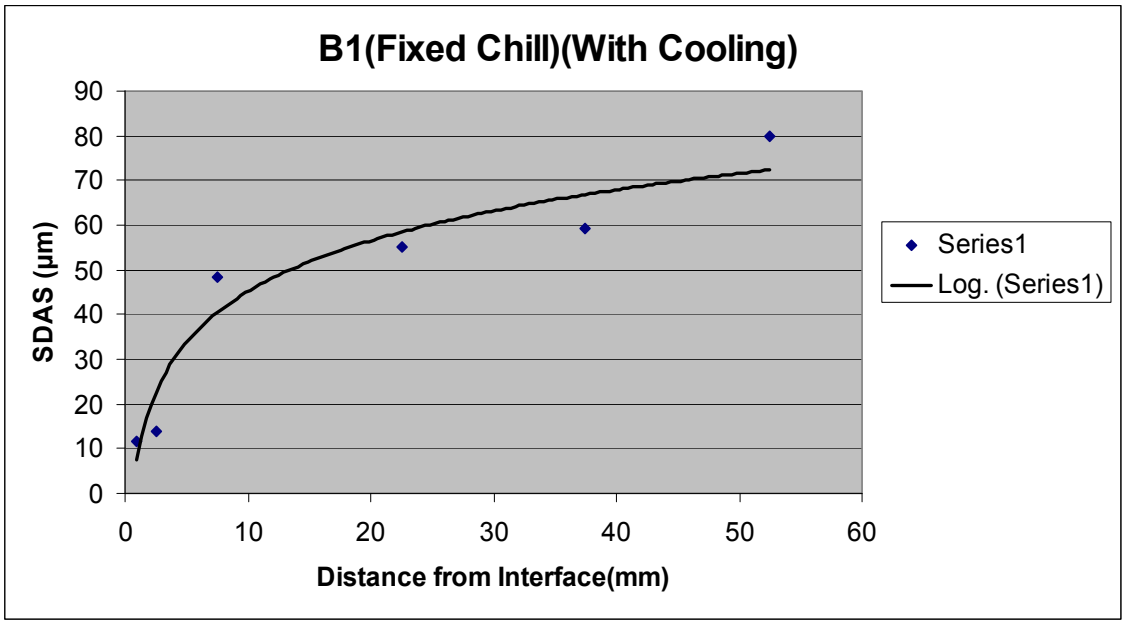

Figure 146: Average SDAS vs. Interface Distance for Trial B1

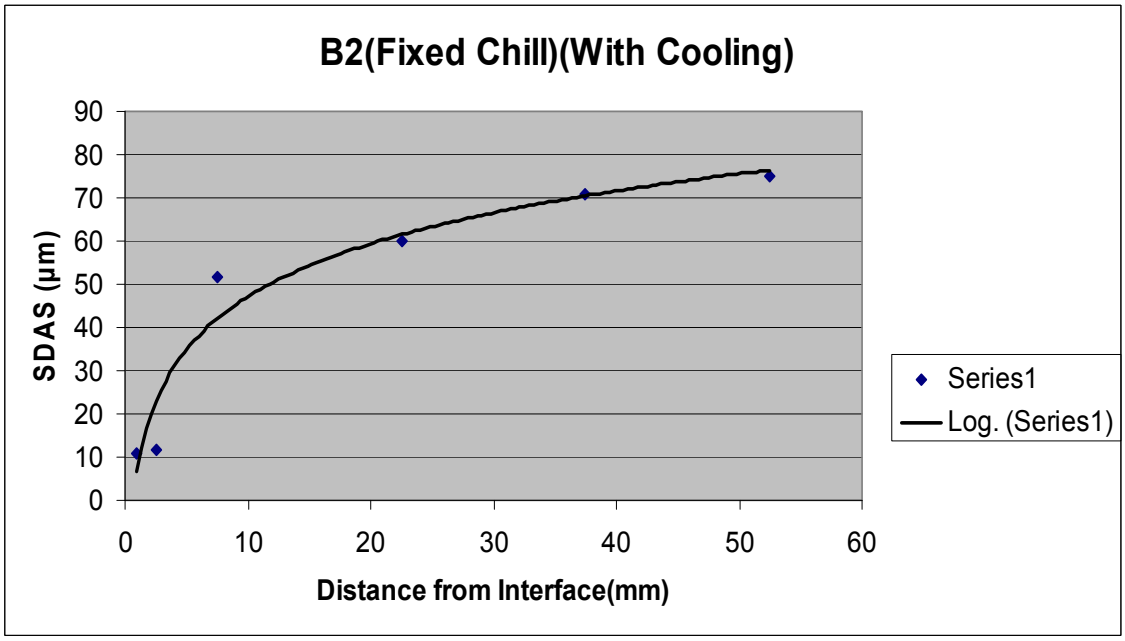

Figure 147: Average SDAS vs. Interface Distance for Trial B2

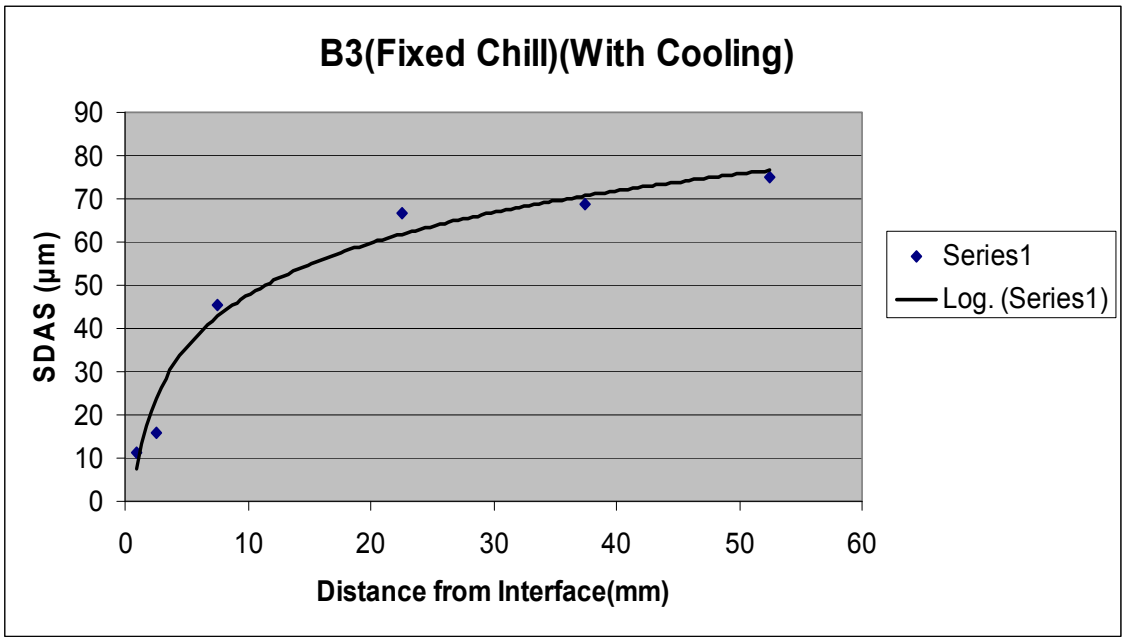

Figure 148: Average SDAS vs. Interface Distance for Trial B3

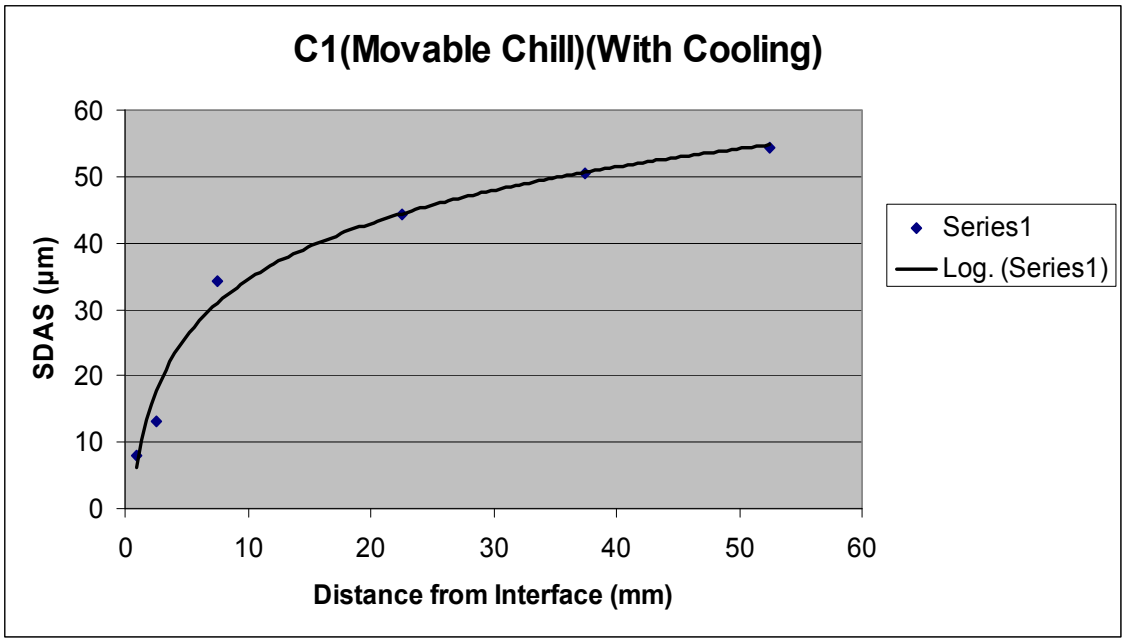

Figure 149: Average SDAS vs. Interface Distance for Trial C1

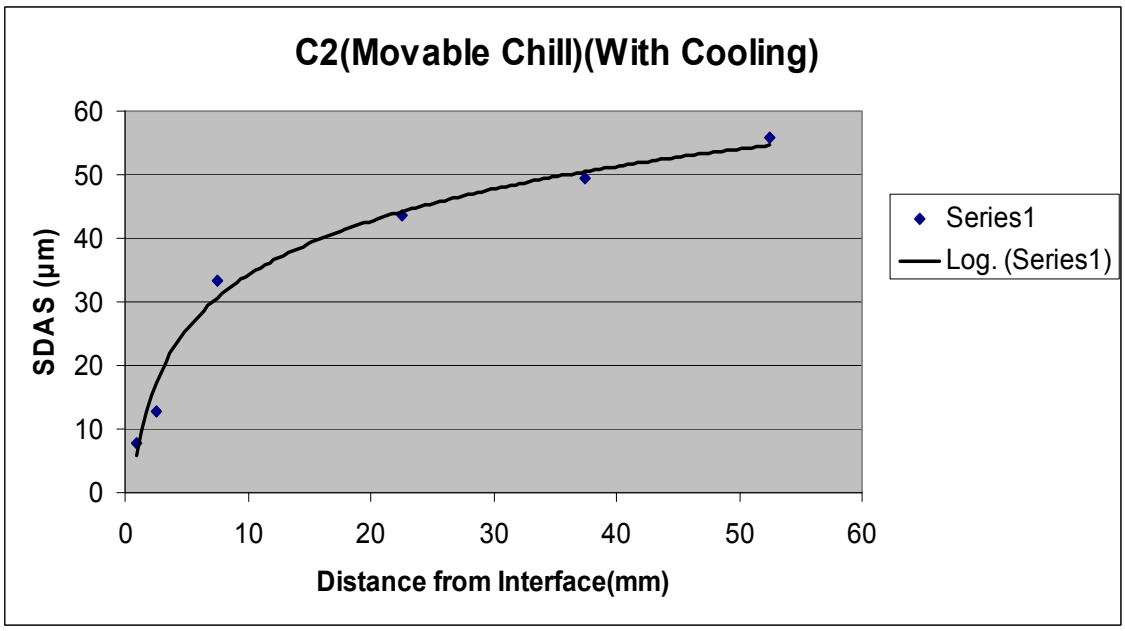

Figure 150: Average SDAS vs. Interface Distance for Trial C2

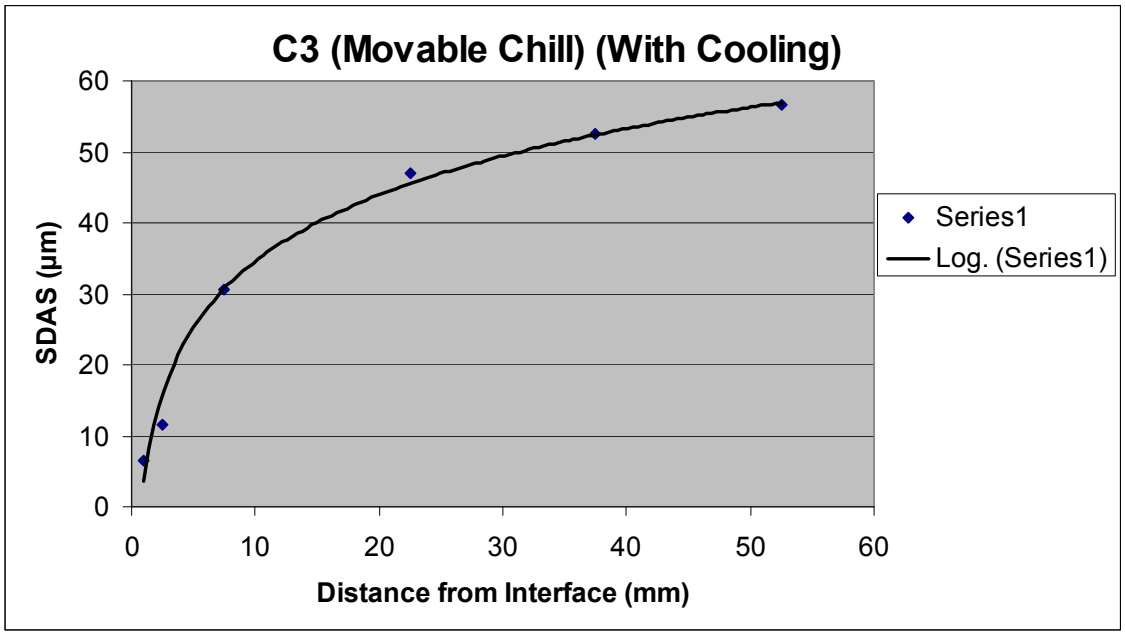

Figure 151: Average SDAS vs. Interface Distance for Trial C3

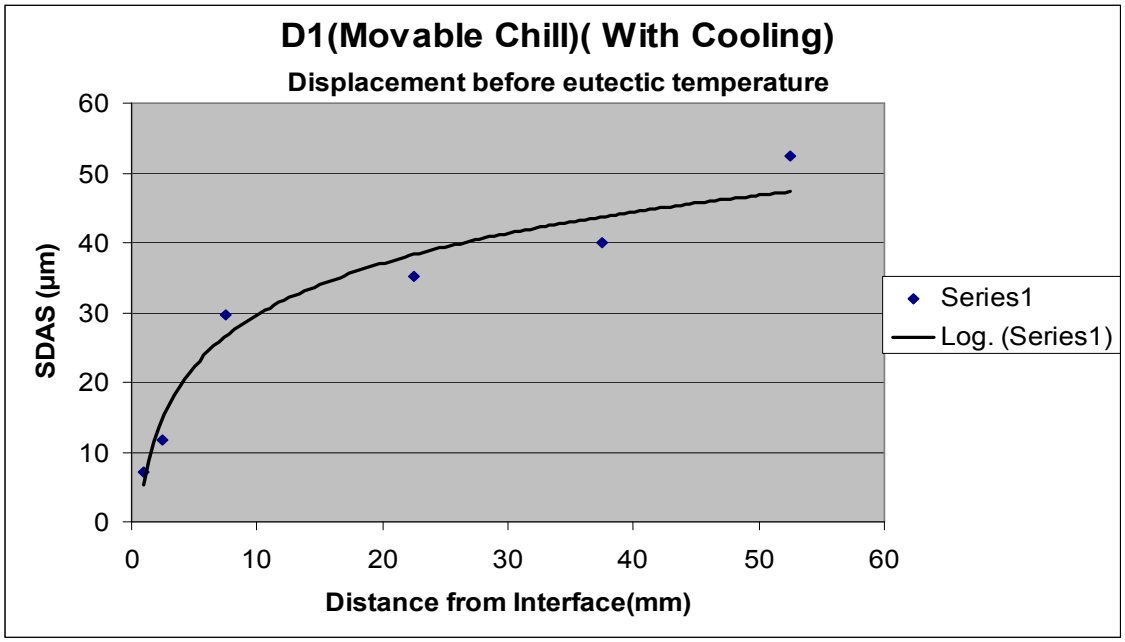

Figure 152: Average SDAS vs. Interface Distance for Trial D1

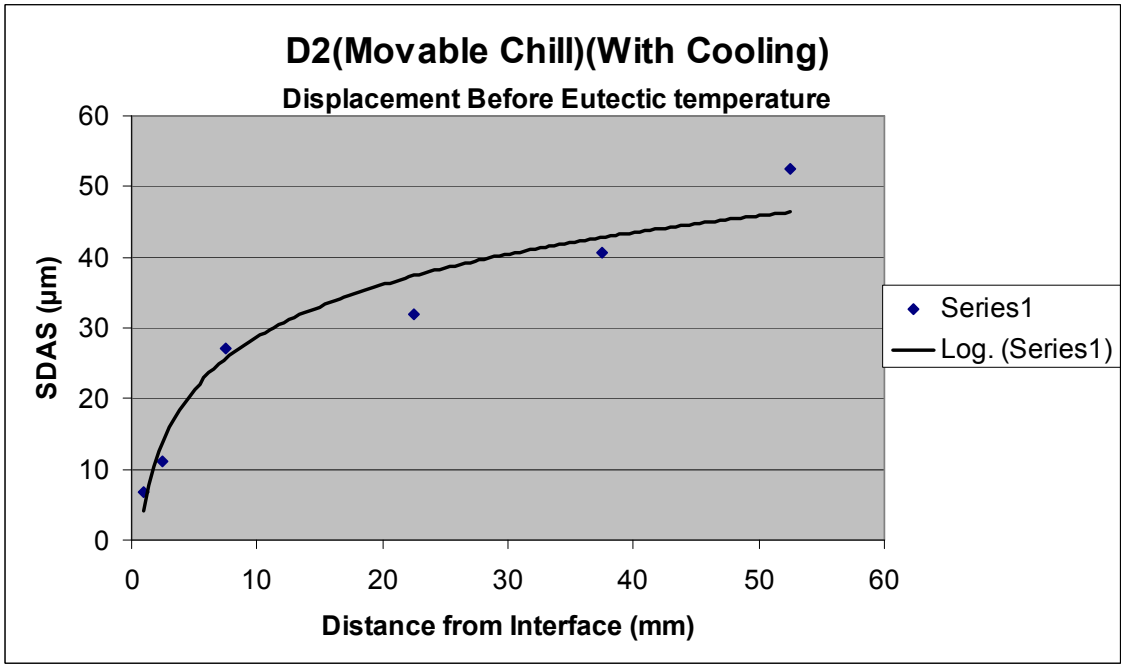

Figure 153: Average SDAS vs. Interface Distance for Trial D2

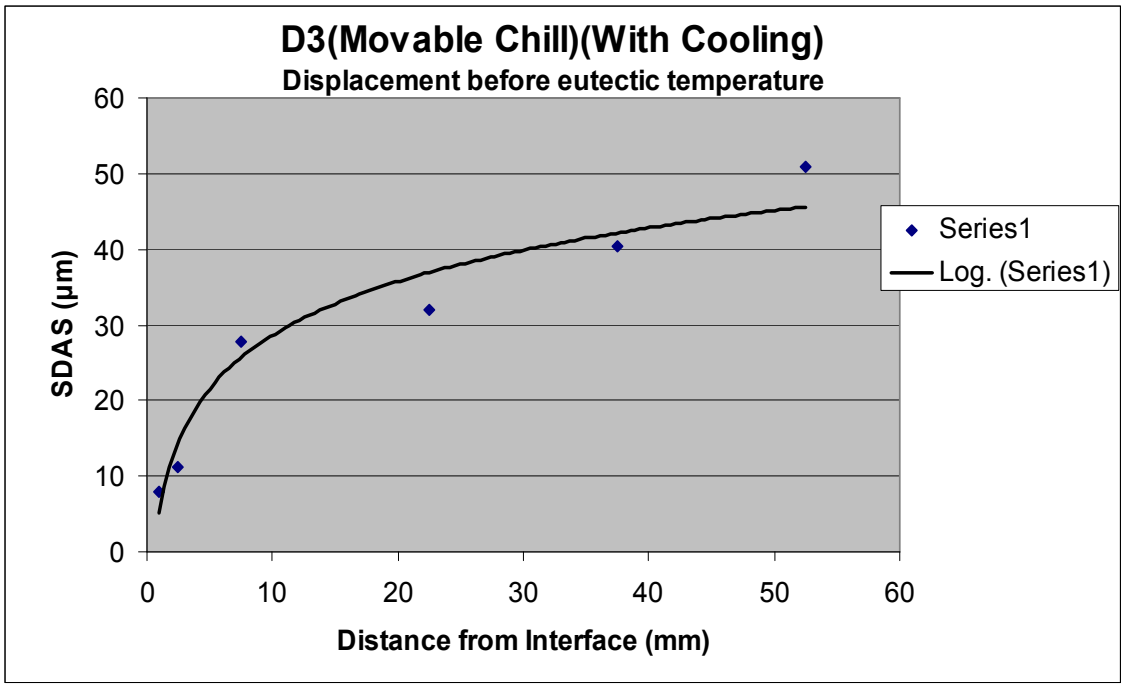

Figure 154: Average SDAS vs. Interface Distance for Trial D3

References

1. E. Paul DeGarmo, *Materials and Processes in Manufacturing*. 9 ed. 1974: Macmillan.
2. K.G Swift, *Process selection: from design to manufacture*, ed. 2nd. 2003: Butterworth-Heinemann.
3. P. Beeley, *Foundry Technology*, ed. Second. 2001: Butterworth-Heinemann 75-80.
4. Eds. G. Hirt, A.R., & A. Buhrig-Polaczek, Aachen Germany & Liege, *Semi-Solid Processing of Alloys and Composites*. 2008: Belgium.
5. D.P.K Singh, Mallinson G.D. & Panton S.M. *Reducing the cycle time in die casting using solidification Modelling and optimisation technique*. in *Proceeding of international Modelling: Casting, Welding and Advanced Solidification Processes*. 1998. San Diego,USA.
6. D.P.K. Singh, G.D. Mallinson., S. M. Panton, and N. Palle,, *Die Design Strategy forImproved Productivity and Quality in Die Casting.* AFS Transactions, 1999. **107**(99-25): p. 127-133.
7. W.D. Griffiths, *A model of interfacial heat transfer coefficients for the Aluminum gravity Die Casting process.* Metallurgical and Material Transactions, 2004.
8. S Song ,MM Yovanovich, F.O. Goodman, *Thermal gap conductance of conforming surfaces in contact.* Transactions of the ASME Journal of Heat Transfer, 1993: p. 533–540.
9. G.H. Ayers, *Cylindrical thermal contact conductance*, in *Mechanical Engineering*. 2003, A&M University: Texas.
10. J. Savage, *The problem of rupture of the billet in the continuous casting of steel*, Journal of steel and iron institute, 1962: p. 41.
11. M. Prates, *Variables Affecting the nature of chill-zone.* Metallurgical Transactions, 1972. **3A**: p. 1501.
12. R.D Pehlke, and K. Ho, *Transient methods for determination of metal-mould interfacial heat transfer.* AFS transactions, 1984(92): p. 587–597.
13. J.V. Beck, *The nonlinear inverse heat conduction problem.* ASME paper, 1965. **65-HT-40**.

14. K. Ho, and R. D Pehlke, *Metal-mould interfacial heat transfer.* Metal Transactions, 1985. **16B**: p. 585–594.
15. N. Prabhu, *One-Dimensional Predictive Model for Estimation of Interfacial Heat Transfer Coefficient During Solidification of Cast Iron in Sand Mould.* Materials Science technology, 2002. **18**: p. 804-810.
16. N.S. Eduardo, N. Cheung, C.A. Santos, Amauri G. *The variation of the Metal/Mold Heat Transfer Coefficient along the cross section of cylindrical shaped castings*, in *Design and Optimization Symposium*, Rio de Janeiro, Brazil 2004.
17. C.A. Santos, *Determination of transient interfacial heat transfer coefficients in chill mold castings*. 2000, Department of Materials Engineering, State University of Campinas.
18. Incropera, *Fundamentals of Heat and Mass Transfer*, ed. 5. 2002: John Wiley & Sons.
19. Doutre. *Advances in Industrial Materials*. in *TMS of CIM*. 1998: p. 289–301. Canada.
20. X. Wan, *Using Helium to Increase the Heat transfer at the Metal/Mold Interface in Permanent Mold Casting*, AFS transactions, 2004: p. 193–207.
21. A. Stavros, and C Horazio, *Comparisons of the Effects of Air and Helium on Heat Transfer at the Metal-Mold Interface.* Minerals, Metals & Materials Society, 2008: p. 457-468.
22. K.E. Metzloff, *The Effect of Helium Injection in Industrial Trials on Aluminum Permanent Mold Castings.* American Foundry Society, 2009.
23. V.A Carrig, T.T. Nguyen and G. deLooze, *Study on Squeeze Pins in Gravity Die Casting*. 2002, Technical report CSIRO Manufacturing Science & Technology.
24. S.M.H Mirbagheri, *Modelling of metal–mold interface resistance in the A356 Aluminium alloy casting process*, in *Department of Mining and Metallurgical Engineering*. 2007, Amirkabir University of Technology: Tehran.
25. J.P. Holman, *Heat transfer* 1981, New York: McGraw-Hill.
26. I.J.D Sully, *The Thermal Interface between Castings and Chill Molds.* AFS transactions, 1976. **84**: p. 735-747.
27. J.V. Beck, *Function Specification Method for the Solution of the Solution of the Inverse Heat Conduction Problem,* 1995 IPNet Digest, p.45-53,

28. O.M. Alifanov, , *Inverse heat transfer problems*. 1994, New York: Springer-Verlag.
29. M.N. Özışık, *Inverse Heat Transfer: Fundamentals and Applications*. 2000: Taylor & Francis.
30. A.N. Tikhonov, *Inverse problems in heat conduction.* Journal of engineering physics, 1975. **1**(29): p. 816-820.
31. W. J. Minkowycz, E. Sparrow, and J. Murthy, *Handbook of Numerical Heat Transfer*, ed. S. Edition. 1988., p-134-149
32. O.R. Burggraff, *An exact solution of the inverse problem in heat conduction theory and application.* J. Heat Transfer 1964. **86**: p. 373–382.
33. G, Stolz. Jr., *Numerical solution to an inverse problem of heat conduction for simple shapes.* J. Heat Transfer, 1960. **82**: p. 20-26.
34. E.M. Sparrow, *The inverse problem in transient heat conduction.* ASME journal of applied mechanics, 1964. **86**: p. 369-375.
35. M. Imber, J. Khan, *Prediction of transient temperature distributions with embedded thermocouples.* AIAA Journal, 1972. **10**: p. 784-789.
36. J. Taler, , *A semi-numerical method for solving inverse heat conduction problem.* Heat and mass transfer, 1996. **31**: p. 105-111.
37. J.V.Beck, *Surface heat flux determination using an intergral method.* Nuclear Engineering design, 1968. **7**: p. 170-178.
38. B.F. Blackwell, *Effecient technique for the numerical solution of the one-dimensional inverse problem of heat conduction.* Numerical heat transfer, 1981. **4**: p. 229-238.
39. P.S. Hore, *Application of finite element method to the inverse heat conduction problem.* ASME paper, 1977.
40. B. Bass, *Application of the finite element method to the nonlinear inverse heat conduction problem using Beck's second method.* Transactions of the ASME, 1980. **102**: p. 168-176.
41. X. Ling, *A noniterative finite element method for inverse heat conduction problems.* Int. journal of numerical method in engineering, 2003. **56**: p. 1315-1334.
42. A. Venkatesan, *Simulation of casting solidification and its grain structure prediction using FEM.* Journal of Materials Processing Technology, 2004(168): p. 10-15.

43. M. Trovant and S. Argyropolis, *Computational fluid dynamics and heat/mass transfer modeling in the metallurgical Industry*. 1996, Canadian Institute of Mining: Montreal.
44. Ansara, A Dinsdale, M. Rand, *Thermochemical Database for Light Metal Alloys*, ed. 1. Vol. 2. 1998.
45. D.G. Eskin, *Physical Metallurgy of Direct Chill Casting of Aluminum Alloys* 2008: CRC Press.
46. J. Kim, *Effect of Solidification Mechanism on the Pororsity Formation in Aluminum-silicon Alloys*. 1996: University of Wisconsin. 298.
47. M.C. Fleming, *Silver Annivesary Paper*. American Foundry Society Transactions, 1995. **2**.
48. D.H. Kirkwood, *A simple model for dendrite arm coarsening during solidification*. in *Materials Science and Engineering*. 1985.
49. J.G. Kaufman, *Alluminium Alloy Casting*. 2004: American Foundry Society. 55-97.
50. J. Wang, , S.X. He, B.D. Sun, M. Nishio, *Evolution of the rheocasting structure of A356 alloy investigated by large-scale crystal orientation observation.* Journnal of Material processing, 2003(141): p. 29-34.
51. H.C. Liao, Y. Sun, G.X Sun, *Correlation between mechanical properties and amount of dendritic $_7$ -Al phase in as-cast near-eutectic Al–11.6%Si alloys modified with strontium.* materials Science Engineering, 2002. **B**(335): p. 62-66.
52. X. Jian, H. Xu, T.T. Meek, Q. Han, *Effect of power ultrasound on solidification of aluminum A356 alloy.* Material Letter, 2005(59): p. 190–193.
53. B.J. Jung., C.H. Jung, T.K Han, Y.H. Kim, *Electromagnetic stirring and Sr modification in A356 alloy.* Journal of Materials Processing Technology, 2001(111): p. 69–73.
54. G. K. Upadhya , S. Das, U. Chandra and A. J. Paul, *Modelling the investment casting process: a novel approach for view factor calculations and defect prediction.* Applied Mathematical Modelling, 1995. **19**(6): p. 354-362.
55. C.M. Winnie, *Thermomechanical analyses of metal solidifiaction process*. 1995, Massachussets Institute of Technology.
56. R.W. Lewis and P. M. Robertson, *Finite element of solidification problems.* Applied science research, 1987. **G1**(44): p. 92.

57. J. D. Zhu, S.L. Cockcroft , and D.M. Maijer, *Modeling of micro-porosity formation in A356 aluminium alloy casting.* Metallurgical and Materials Transactions, 2006. **37**.
58. E.T. George, *Quenching and the control of distortion*. 1995: ASM Heat Treating Society. 525-550.
59. E.T. George, *Modeling and Simulation for Material Selection and Mechanical Design*. Vol. 1. 2003: Dekker Mechanical Engineering.
60. S.K. Das, *Modeling and Optimization of Direct Chill Casting to Reduce Ingot Cracking*. 2006, University of Kentucky. p. 12-18.
61. Y. Nishida, W. Droste and S Engler, *The Air Gap Formation Process at the Casting Mold Interface and the Heat Transfer Mechanism through the Gap.* metallurgical and Material Transactions, 1986. **17B**: p. 833-845.
62. D. Gunasegaram, J. V Touw and T Nguyen, *Heat Transfer at Metal-Mould Interfaces*. in *Casting and Solidification of Light Alloys*. 1995. Queensland, Australia.
63. D.R. Durham and J.T. Berry, *Role of the Mold/Metal Interface during Solidification of a Pure Metal against a Chill.* AFS transactions, 1974. **82**: p. 101.
64. R.C. Sun, *Simulation and Study of Surface Conductance of Heat Flow in the Early Stage of Casting.* AFS Cast Metal Research Journal, 1973. **6**: p. 117-128.
65. H. F. Bishop, F.A. Brant, and W.S. Pellini, *Solidification of Steel against Sand and Chill Walls.* AFS Transactions, 1951. **59**: p. 435-449.
66. W. J. Minkowycz, E. M. Sparrow, and J. Y. Murthy, *Heat Transfer and Microstructure During the Early Stages of Metal Solidification.* Metal Matellurgical Transactions, 1995. **26 B**: p. 361-382.
67. M. Prates, J. Fissolo, and H. Biloni, *Flow Parameters affecting the Uni-directional Solidification of Pure Metals.* Metal Matellurgical Transactions, 1972. **2A**: p. 1419-1425.
68. F. Michel, P. R Louchez., and F.H Samuel, *Heat Transfer Coefficient (H) during Solidification of Al-Si Alloys: Effect of Mold Temperature, and Coating Type and Thickness*, in *99th AFS Casting Congress*. 1995: Kansas City, Missouri.
69. P. Schmidt, *Experimental validation of heat transfer*. 1994, The Royal Institute of Technology: Stockholm.

70. M. Carroll, C. Walsh, and M. Makhlouf. *Determination of the effective interfacial heat transfer coefficient between metal mold and aluminium alloy castings*. in *AFS CastEXPO and Casting Congress*. 1999. St Louis, MO.
71. M. Krishnan and D.G.R. Sharma, *Extraction of Heat from Casting by Metallic Molds.* Indian Foundry Journal 1991. **13**(13-21).
72. A.C. Rapier, T.M. Jones, and J.E. McIntosh, *The Thermal Conductance of Uranium Dioxide Stainless Steel Interfaces.* international journal of heat and mass transfer, 1963. **6**: p. 397-416.
73. M. Bamburger and I. Prinz, *Heat Transfer between Hot Metal and Cooling Water-The Effect of Water Temperature.* International Foundry Congress, 1980. **47**: p. 502-520.
74. J. Wang, S.H., B. Guo, M. Nishio, *Grain refinement of Al–Si alloy (A356) by melt thermal treatment.* Journal of Materials Processing Technology, 2003(141): p. 29–34.
75. T. Nguyen, D. Gunasegaram, L. Luo and R. Esdaile. *Heat Transfer in Permanent Mold Casting*. in *Proc. Materials Solutions Conf.* 1998 on Aluminium Casting Tech.
76. Y. S. Lerner, and T M Westendorf, *Cooling Systems for Permanent Mold Castings.* Foundry Management and Technology, 1996: p. 81-91.
77. Nara, N., *Die Design and Cooling System Design for Low Pressure Aluminum Alloy Wheel Castings*. 1996, Ford Scientific Research Laboratory.
78. J. Langlais, T. Bourgeois, Y. Caron, G. Beland, and D Beland, *Measuring the Heat Extraction Capacity of DC Casting Cooling Water.* Light Metals, 1995: p. 979-986.
79. J W Yeh, and S.H. Jong., *The Cast Structure of a 7075 Alloy Produced by a Water Cooling Centrifugal Casting Method.* Metal Metallurgical Transactions, 1994. **25A**: p. 643-650.
80. R. Fletcher, *Practical Methods of Optimization: Unconstrained Optimization*. 1980, NY: Wiley and Sons.
81. D.R. Poirier and E.J. Poirier, *Fundamentals of Heat Transfer.* TMS proceedings, 1992.
82. D. Gunasegaram, J. Van der Touw, and T. Nguyen, *Heat Transfer at Metal-Mould Interfaces*. in *Casting and Solidification of Light Alloys*. 1995. Queensland, Australia.

83. S.N. Kulkarni, K. Radhakrishna., *Evaluation of metal–mould interfacial heat transfer during the solidification of aluminium–4.5% copper alloy castings cast in CO2–sand moulds.* Materials Science-Poland, 2005.

84. S.A. Argyropoulos, A.C. Mikrovas, and D.A. Doutre, *Dimensionless correlations for forced convection in liquid metals,* Metallurgical and Material Transactions, 2001. **32**(B): p. 239–246.

85. D.P.K. Singh, *Casting Die Design for Optimised Solidification*. 1999, The University of Auckland. p. 52-55.

86. P Manilal, D.P.K Singh .and Z.W. Chen, *Computer Modeling and Experimentation for Thermal Control of Dies in Permanent Mold Casting*, in *Proceedings of AFS Casting Congress*. 2003.

87. C.J. Chen, *Theoretical Error Analysis of Temperature Measurement by an Embedded Thermocouple.* Letters in Heat and Mass Transfer, 1974. **1,2**: p. 171 - 180.

88. W. H. Coleman, *Experimentation and Uncertainty Analysis for Engineers*, ed. 2nd. 1999: John Wiley & Sons.

89. M.H Attai, *Distortion in thermal field around inserted thermocouples in experimental interfacial studies.* Journal of Manufacturing Science and Engineering, 2002. **124**: p. 135-145.

90. J.R. Lee, *Effect of Cooling Circuit Duration on Formation of Solidification Shrinkage in A356 Cast Alloy Wheels*. 2006, Masters Thesis, AUT University.